BEILSTEIN JOURNAL OF NANOTECHNOLOGY

Nanotribology

Edited by Enrico Gnecco, Susan Perkin, Andrea Vanossi and Ernst Meyer

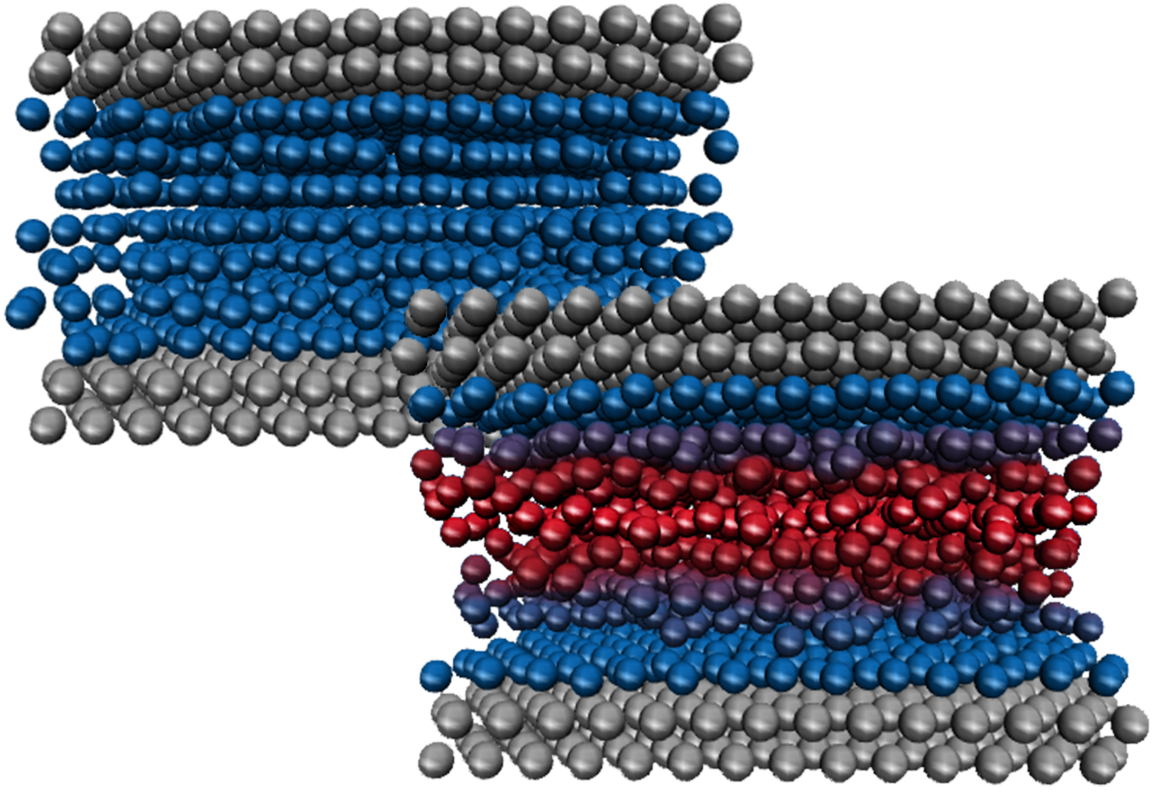

Imprint

Beilstein Journal of Nanotechnology
www.bjnano.org
ISSN 2190-4286
Email: journals-support@beilstein-institut.de

The *Beilstein Journal of Nanotechnology* is published by the Beilstein-Institut zur Förderung der Chemischen Wissenschaften.

Beilstein-Institut zur Förderung der Chemischen Wissenschaften
Trakehner Straße 7–9
60487 Frankfurt am Main
Germany
www.beilstein-institut.de

BEILSTEIN JOURNAL OF NANOTECHNOLOGY

Nanotribology

Enrico Gnecco*[1], Susan Perkin[2], Andrea Vanossi[3,4] and Ernst Meyer[5]

Editorial

Open Access

Address:
[1]Otto Schott Institute of Materials Research (OSIM), Friedrich Schiller University Jena, Löbdergraben 32, 07743 Jena, Germany, [2]Department of Chemistry, Physical and Theoretical Chemistry Laboratory, University of Oxford, Oxford OX1 3QZ, United Kingdom, [3]CNR-IOM Democritos National Simulation Center, Via Bonomea 265, 34136 Trieste, Italy, [4]International School for Advanced Studies (SISSA), Via Bonomea 265, 34136 Trieste, Italy, and [5]Department of Physics, University of Basel, Klingelbergstr. 82, CH-4056 Basel, Switzerland

Email:
Enrico Gnecco* - enrico.gnecco@uni-jena.de

* Corresponding author

Keywords:
nanotribology; nanoadhesion; nanofriction

Beilstein J. Nanotechnol. **2018,** *9,* 2330–2331.
doi:10.3762/bjnano.9.217

Received: 22 August 2018
Accepted: 25 August 2018
Published: 28 August 2018

This article is part of the Thematic Series "Nanotribology".

Editor-in-Chief: T. Schimmel

Nanotribology is a young and dynamic field of research which aims to investigate friction, wear and adhesion phenomena down to the nanometer scale. Since these phenomena occur in all natural, artificial or conceptual situations involving two surfaces (at least) in contact or in close proximity to each other, it is not surprising that, knowingly or not, many physicists, materials scientists, mechanical engineers or chemists have to contend with these topics sooner or later in their careers.

This Thematic Series is intended as an "invitation to nanotribology" addressed to the attentive readership of the *Beilstein Journal of Nanotechnology*. The first goal of this Thematic Series is simply to make more colleagues and students aware of the existence of this fascinating subject, which, in spite of its universality, is often considered as a niche topic even at prestigious scientific conferences. The second goal, which is closely related to the first one, is to provide fresh examples of the most recent advancements in the field worldwide. This is substantiated in a series of ten original contributions whose authors are quite well distributed around the world (from India, China, Argentina, Cameroon, Russia and USA back to many countries in Old Europe).

The covered topics include lubrication, surface preparation and theoretical models of friction at the nanoscale. Regarding the first topic, this Thematic Series gives examples of cutting-edge aqueous solutions including nanodiamonds [1] and novel materials such as nitrogen-doped graphene oxide [2] and imidazolium-based ionic liquids [3] used as additives to mineral oils. Standard large-scale applications to steel surfaces, but also to a material of key importance in micro- and nanoelecromechanical systems, i.e., silicon oxide, are recognized. The quality of the surface condition is addressed experimentally by the example of cryogenically treated martensitic stainless steel [4] and theoretically by an analysis of the influence of micro-dimple textures on hydrodynamic lubrication [5]. On a more fundamental level, different authors have modeled the influence of electrical double layers on hydrodynamic lubrication [6], the

occurrence of a second-order phase transition in ultrathin lubricant films [7] and the velocity dependence of dry friction on crystal surfaces at the atomic scale [8].

While many experimental techniques for materials characterization are those typical of surface science (e.g., X-ray diffraction, SEM, TEM, XPS and Raman spectroscopy), more specific to nanotribology are nanoindenters, nanotribometers, quartz force microbalance and especially atomic force microscopy (AFM), which, without a doubt, has triggered a true revolution in our understanding of friction at the atomic scale. This is exemplified by the lattice resolved friction force images on oxidized silicon surfaces in the tribochemistry study presented by the Bennewitz group [9]. On a larger scale, alternative surface scan methods (e.g., circular mode AFM) for investigation of abrasive wear are proposed by Noel et al. [10].

Considering the interdisciplinary nature of the subject, and the variety of materials, lubricants, and possible applications, the previous examples, in spite of their high quality, are still not enough to achieve our goals. For this reason, the research articles in this Thematic Series are complemented by a rather comprehensive but concise review paper [11], which was born out of the collaboration of nine researchers (experimentalists and theoreticians) within the European COST Action MP 1303 “Understanding and Controlling Nano and Mesoscale Friction”, which ran from 2013 to 2017. Here the covered topics include but are not limited to controlled manipulation of nanoparticles, optically trapped colloidal and ionic systems, superlubricity of graphene, sliding friction of organic molecules, charge density waves, and perspectives of tuning friction using photo-assisted reactions.

Hopefully, new ideas and further research work will be stimulated from this Thematic Series, which could not have come to light without the contributions of all authors and the constant support from the Beilstein-Institut and specifically, Dr. Wendy Patterson and Dr. Uli Fechner.

Enrico Gnecco, Susan Perkin, Andrea Vanossi, and Ernst Meyer

Jena, Oxford, Trieste and Basel, August 2018

ORCID® iDs

Enrico Gnecco - https://orcid.org/0000-0002-3053-923X

References

1. Curtis, C. K.; Marek, A.; Smirnov, A. I.; Krim, J. *Beilstein J. Nanotechnol.* **2017,** *8,* 2045–2059. doi:10.3762/bjnano.8.205
2. Chandrabhan, S. R.; Jayan, V.; Parihar, S. S.; Ramaprabhu, S. *Beilstein J. Nanotechnol.* **2017,** *8,* 1476–1483. doi:10.3762/bjnano.8.147
3. Amorim, P. M.; Ferraria, A. M.; Colaço, R.; Branco, L. C.; Saramago, B. *Beilstein J. Nanotechnol.* **2017,** *8,* 1961–1971. doi:10.3762/bjnano.8.197
4. Prieto, G.; Bakoglidis, K. D.; Tuckart, W. R.; Broitman, E. *Beilstein J. Nanotechnol.* **2017,** *8,* 1760–1768. doi:10.3762/bjnano.8.177
5. Li, K.; Jing, D.; Hu, J.; Ding, X.; Yao, Z. *Beilstein J. Nanotechnol.* **2017,** *8,* 2324–2338. doi:10.3762/bjnano.8.232
6. Jing, D.; Pan, Y.; Wang, X. *Beilstein J. Nanotechnol.* **2017,** *8,* 1515–1522. doi:10.3762/bjnano.8.152
7. Lyashenko, I. A.; Borysiuk, V. N.; Popov, V. L. *Beilstein J. Nanotechnol.* **2017,** *8,* 1889–1896. doi:10.3762/bjnano.8.189
8. Apostoli, C.; Giusti, G.; Ciccoianni, J.; Riva, G.; Capozza, R.; Woulaché, R. L.; Vanossi, A.; Panizon, E.; Manini, N. *Beilstein J. Nanotechnol.* **2017,** *8,* 2186–2199. doi:10.3762/bjnano.8.218
9. Petzold, C.; Koch, M.; Bennewitz, R. *Beilstein J. Nanotechnol.* **2018,** *9,* 1647–1658. doi:10.3762/bjnano.9.157
10. Noel, O.; Vencl, A.; Mazeran, P. E. *Beilstein J. Nanotechnol.* **2017,** *8,* 2662–2668. doi:10.3762/bjnano.8.266
11. Vanossi, A.; Dietzel, D.; Schirmeisen, A.; Meyer, E.; Pawlak, R.; Glatzel, T.; Kisiel, M.; Kawai, S.; Manini, N. *Beilstein J. Nanotechnol.* **2018,** *9,* 1995–2014. doi:10.3762/bjnano.9.190

License and Terms

BEILSTEIN JOURNAL OF NANOTECHNOLOGY

Development of a nitrogen-doped 2D material for tribological applications in the boundary-lubrication regime

Shende Rashmi Chandrabhan[1], Velayudhanpillai Jayan[2], Somendra Singh Parihar[2] and Sundara Ramaprabhu[*1]

Full Research Paper

Open Access

Address:
[1]Department of Physics, Alternative Energy and Nanotechnology Laboratory, Nano Functional Materials Technology Centre, Indian Institute of Technology Madras, Chennai, Tamil Nadu 600036, India and [2]Nano & Applied Coating Material Laboratory, NTPC Energy Technology Research Alliance (NETRA), NTPC Ltd, E3, Ecotech II, Greater Noida 201306, Uttar Pradesh, India

Email:
Sundara Ramaprabhu[*] - ramp@iitm.ac.in

* Corresponding author

Keywords:
friction; lubrication; nanolubricant; nitrogen-doped reduced graphene oxide; tribology; wear

Beilstein J. Nanotechnol. **2017,** *8,* 1476–1483.
doi:10.3762/bjnano.8.147

Received: 14 March 2017
Accepted: 27 June 2017
Published: 17 July 2017

This article is part of the Thematic Series "Nanotribology".

Guest Editor: E. Gnecco

Abstract

The present paper describes a facile synthesis method for nitrogen-doped reduced graphene oxide (N-rGO) and the application of N-rGO as an effective additive for improving the tribological properties of base oil. N-rGO has been characterized by different characterization techniques such as X-ray diffraction, scanning electron microscopy, transmission electron microscopy, X-ray photoelectron spectroscopy and Raman spectroscopy. N-rGO-based nanolubricants are prepared and their tribological properties are studied using a four-ball tester. The nanolubricants show excellent stability over a period of six months and a significant decrease in coefficient of friction (25%) for small amounts of N-rGO (3 mg/L). The improvement in tribological properties can be attributed to the sliding mechanism of N-rGO accompanied by the high mechanical strength of graphene. Further, the nanolubricant is prepared at large scale (700 liter) and field trials are carried out at one NTPC thermal plant in India. The implementation of the nanolubricant in an induced draft (ID) fan results in the remarkable decrease in the power consumption.

Introduction

Advances in machine technology necessitate the reduction in energy loss by improving the tribological performance. This energy loss is caused primarily by friction and wear. The employment of lubricants in machines reduces friction and wear, which results in energy saving. However, the tribological performance of conventional lubricants (water and oil) fails to meet the demand of newly developed mechanical technologies. Recent development in lubricant technology reveals that the

tribological performance of conventional lubricants can be improved by the addition of the solid particles [1-6]. When boundary lubrication occurs the asperities of the sliding surfaces are in direct contact with each other despite the presence of lubricant. Thus, the load is actually carried by the surface asperities [7]. The addition of solid particles is advantageous in the boundary-lubrication regime since the solid particles can move to the surface-contact region and improve the lubrication. This type of lubricants makes use of the ball-bearing mechanism and the high mechanical strength of solid additives.

Several studies have been carried to investigate the tribological performance of lubricant after the addition of solid particles. Initially, most of the studies were concentrated on the carbon C_{60} molecules as additive in lubricant oil [8-10]. Subsequently, researchers studied the tribological properties of carbon-based additives such as graphite [1], graphene [2,6], carbon spheres [11,12] and carbon nanotubes [13-15]. In addition, several reports are available on the tribological properties of nanolubricant based on metals [16], metal oxides [17,18], MoS_2 [4,19], boron [20] and WS_2 [21]. Among all the solid additives, 2D graphene is a promising material to improve the tribological performance because of its high surface area to volume ratio and excellent mechanical strength. Lin et al. studied the tribological properties of modified graphene platelets dispersed in oil and shows that the graphene platelets improved the wear resistance and load-carrying capacity of the machine after the modification [22]. Song et al. compared the tribological properties of multiwalled carbon nanotubes and graphene oxide nanosheets as additives for water-based lubricants and found that graphene oxide nanosheets improved the tribological properties more than the carbon nanotubes [23]. Zhang et al. studied the tribological properties of an oil lubricant with oleic acid-modified graphene and obtained 17% and 14% reduction in coefficient of friction (COF) and wear scar diameter (WSD), respectively [24]. Berman et al. studied the friction and wear characteristics of 440C steel test pairs lubricated with graphene and found a remarkable reduction in COF (from ca. 1 to ca. 0.15) and wear [25]. In addition, there are several studies carried out on reduced graphene oxide and revealed that the graphene is the most promising material for enhancing the tribological performance [6,22,23,26-38]. Recently, Jaiswal et al. reported the tribological study on TiO_2-reinforced boron/nitrogen co-doped graphene oxide and revealed that the doping of reduced graphene oxide with heteroatoms (nitrogen, boron, co-doped nitrogen/boron) successively enhanced the antiwear properties [39]. Considering aforesaid facts, the present work describes the facile synthesis of nitrogen-doped reduced graphene oxide (N-rGO) where the surface of graphene sheet is modified by doping with nitrogen, which results in an excellent stability in base oil. Moreover, the nanolubricants prepared by dispersing a very small amount of N-rGO (3 mg/L) show a significant decrease in the COF (25%) and WSD (15%) and these are the lowest values ever reported for COF for such a small amount of N-rGO. The present work not only describes the tribological performance of the nanolubricant but also reports the application of the developed nanolubricant in an induced draft (ID) fan and thus proves the potential towards commercialization. The implementation of the prepared nanolubricants in the ID fan results a remarkable reduction in the power consumption.

Experimental

Synthesis of N-rGO

The synthesis of graphene oxide using Hummers method is described in Supporting Information File 1. Nitrogen-doped reduced graphene oxide (N-rGO) was prepared from melamine and GO. Melamine was used as nitrogen precursor. For this, the GO and melamine were mixed thoroughly in 1:1 ratio. The GO and melamine mixture was loaded into a tubular furnace. Initially, argon gas was flushed inside the furnace for 10 min to create an inert atmosphere. Afterwards, the temperature of the furnace was raised to 500 °C and hydrogen gas was flowed through for 30 min. At this temperature, GO was exfoliated into few-layered reduced graphene oxide (r-GO). Further, the temperature of furnace was increased to 700 °C. At this temperature, melamine was decomposed completely resulting in the uniform doping of nitrogen in graphene. The final sample is labeled as N-rGO. Figure 1 shows the schematic for the synthesis of N-rGO.

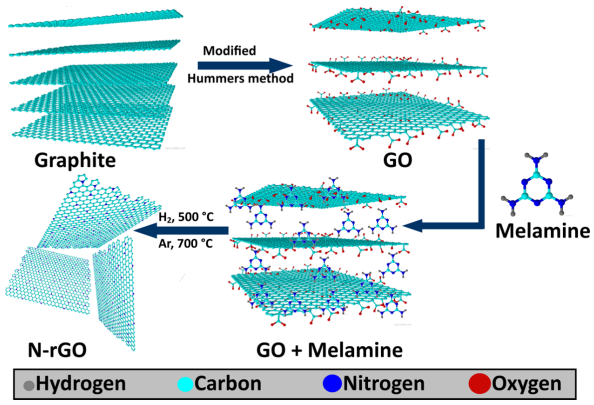

Figure 1: Schematic illustration for the synthesis of N-rGO.

Characterization techniques

The powder X-ray diffraction (XRD) patterns were recorded in the range of $2\theta = 5°$ to $2\theta = 90°$ using a Rigaku X-ray diffractometer. Raman scattering spectra of graphite, GO and N-rGO were collected by using a WITec Raman spectrometer equipped with Nd:YAG laser ($\lambda = 532$ nm). The surface morphology of the sample was analyzed by using field-emission scanning elec-

tron microscopy (FEI quanta FEG200). Transmission electron microscopy images were taken using transmission electron microscope (JEOL JEM-2010F) operated at 200 keV. X-ray photoelectron spectroscopy was performed to confirm the presence of various elements. Nanolubricants were prepared by using a probe sonicator (Sonics, 500 W).

Tribological testing

The tribological properties of nanolubricants were studied using a four-ball tester (Magnum Engineers, Bengaluru, India). The test balls are made of chrome steel alloy having a diameter of 12.7 mm according to ANSI standard. The measurements were performed according to ASTM 5183 standard.

Nanolubricant preparation

Nanolubricants were prepared by dispersing N-rGO in oil using probe sonication. The probe sonication was done for 30 min with a 20 kHz frequency and a power of 500 W (20%) using probe sonicator. Different nanolubricants with different amounts of N-rGO were prepared and the stability of these nanolubricants was checked by probing the settlement after one-month time. Figure 2 shows the photographs of nanolubricants prepared in base oil with different amounts of N-rGO with a minimum of 3 mg/L and a maximum of 12.5 mg/L. The N-rGO lubricants have a good stability as seen in Figure 2.

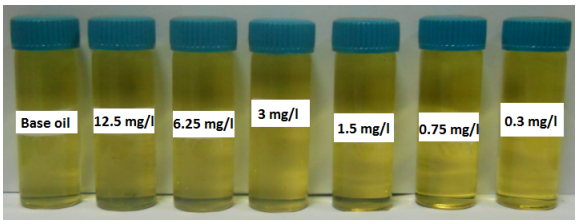

Figure 2: N-rGO dispersion nanolubricant at different concentration.

Friction and wear test

The COF and wear test of N-rGO nanolubricant was studied by using a four-ball tester. In a four-ball tribotester, an upper ball rotates with a specific speed against the three stationary balls at an applied load. This rotation results in the friction and wears at the contact points of the three stationary balls. For the present study, the friction and wear tests were carried out at a rotating speed of 600 rpm by applying a constant load of 400 N. The tests were carried out for 60 min at 75 °C. Before carrying out the measurements, the four test balls were ultrasonicated in ethanol for 10 min and dried. The other components were cleaned with ethanol and the cleaned three test balls were clamped together in the ball-pot assembly. The test balls were covered with nanolubricant for measurements. The fourth ball was clamped in the upper holder and the constant load of 400 N was applied. Figure 3 represents the schematic of the ball-pot assembly in a four-ball tester.

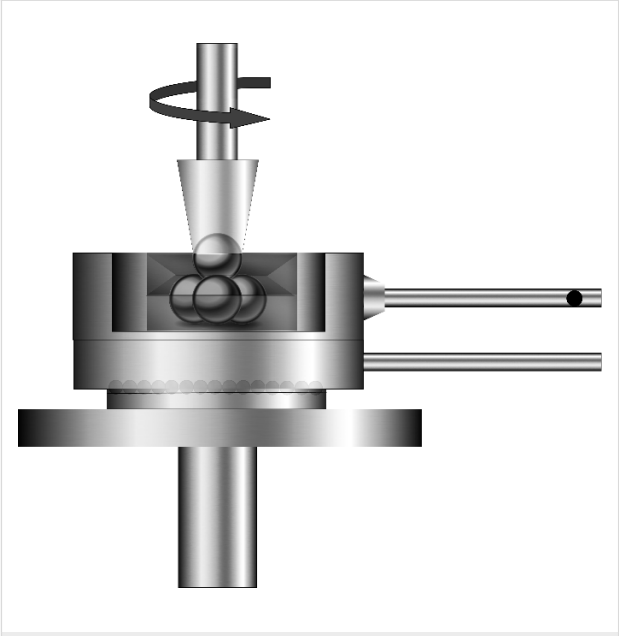

Figure 3: Schematic of the ball-pot assembly in a four-ball tester.

Results and Discussion

Materials characterization

The XRD patterns of graphite, GO and N-rGO are depicted in Figure S1 (Supporting Information File 1). The intense crystalline peak of graphite occurs at ca. 26°, which is the characteristic peak of hexagonal graphite with a *d*-spacing of 0.34 nm. Upon conversion of graphite into GO, the peak position shifts to ca. 11° corresponding to an interlayer spacing of 0.79 nm. This increase in *d*-spacing can be attributed to the intercalation of –OH and –COOH functional groups in the graphite layers. N-rGO shows a broad peak from ca. 15° to 36° with a *d*-spacing of 0.37 nm. The decrease in the interlayer spacing from 0.79 to 0.37 nm suggests the removal of oxygen-containing functional groups from the GO interlayer during exfoliation [40]. This broad peak is also indicative of a loss of the long-range order in graphene.

Raman spectroscopic measurements (Figure S2, Supporting Information File 1) were performed at low laser intensities in order to avoid the burning of samples. A highly intense peak is observed for graphite at 1589 cm^{-1} corresponding to the G band. The lack of D band peaks in graphite implies that the graphite is defect-free. A shift of the G band of GO located at 1610 cm^{-1} is observed [40]. However, after reduction and nitrogen doping, the peak corresponding to the G band shifted back to 1589 cm^{-1}, close to the value of graphite. The presence of the D band, with an intensity comparable to that of the

G band, in case of GO and N-rGO suggests that defects are created during the chemical treatment.

SEM and TEM images of the N-rGO are shown in Figure S3 (Supporting Information File 1). N-rGO exhibits a wrinkled surface, which can be attributed to the rapid removal of functional groups during exfoliation. The size of N-rGO sheets is of a few square micrometers. The samples for TEM analysis are prepared by dispersing small amount of N-rGO in 2-propanol. The dispersion is ultrasonicated for 10 min and then drop-cast over a carbon-coated copper grid (200 mesh). TEM images shown in Figure S3c,d (Supporting Information File 1) reveal that N-rGO has few layers and shows folding at some places.

In order to confirm the nitrogen doping in N-rGO, X-ray photoelectron spectroscopy was carried out. The XPS survey spectrum of N-rGO confirms the presence of carbon (87.5 atom %), oxygen (8.9 atom %) and nitrogen (3.6 atom %) (Figure S4, Supporting Information File 1). The high-resolution C 1s spectra show three components corresponding to sp^2 C=C bonds (at 284.6 eV), sp^2 C=N bonds (at 285.9 eV) and sp^3 C–N bonds (at 288.8 eV). The peaks at 285.9 and 288.8 eV can be assigned to oxygen-containing functional groups, i.e., C=O and C–OH, respectively [41]. The high-resolution N 1s spectrum of N-rGO is deconvoluted into three peaks corresponding to graphitic N (at 401.1 eV), pyridinic N (at 398.2 eV) and pyrrolic N (at 400.1 eV).

Optimization of additive

In order to optimize the concentration of additive, the nanolubricants were prepared with various concentrations and tested their tribological properties. Figure 4 and Figure 5 give the change in the COF as a function of the concentration of additive (N-rGO) at the ASTM standard. One can see that the optimum amount of the additive (N-rGO) is 3 mg/L for which the maximum decrease of COF was obtained. COF decreases from 0.225 (base oil) to 0.170 (3 mg/L of N-rGO), which is a reduction of about 25%. The excessive additive in base oil increases the COF of nano-lubricant (Figure 5). For comparison, the COF at higher concentrations of N-rGO is shown in Figure 5. The COF increases with increasing concentration of N-rGO additive. This increase can be attributed to the formation of aggregates between the contact surfaces resulting in poor lubrication. These measurements suggest that the optimum amount of additive is 3 mg/L, which is the concentration used in all further experiments.

Figure 6 shows the measurements of COF with base oil and the nanolubricant with N-rGO (3 mg/L). The COF of nanolubricant is lower than that of base oil. For 2D nanostructures, the improvement in tribological properties is well understood as

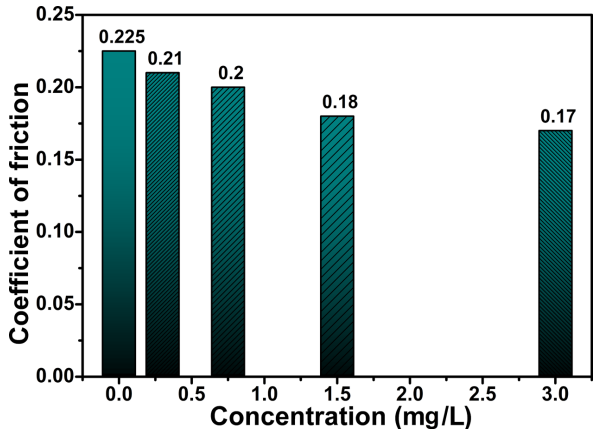

Figure 4: Coefficient of friction at low N-rGO concentrations.

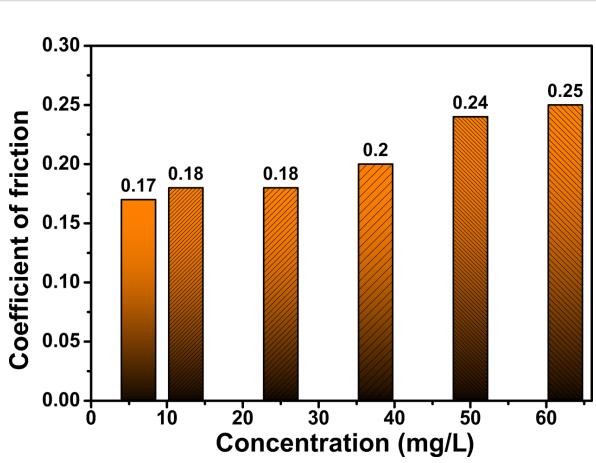

Figure 5: Coefficient of friction at high N-rGO concentrations.

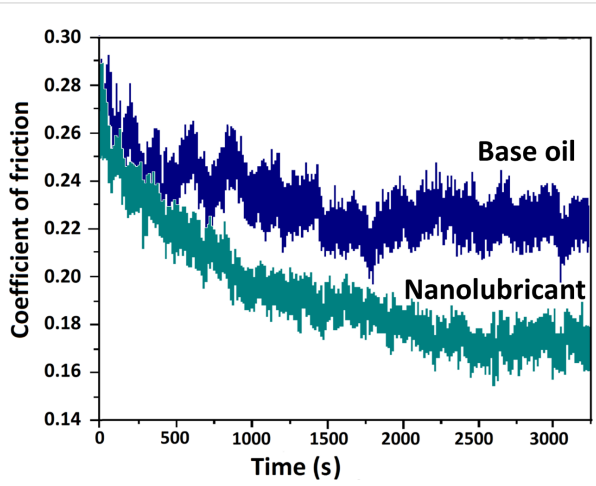

Figure 6: Variation of COF over time for base oil and nanolubricant with N-rGO (3 mg/L).

sliding mechanism. The significant decrease in the COF for N-rGO dispersed nanolubricant can be ascribed to the layered morphology of N-rGO, which allows the easy intrusion in the friction interfaces. In the boundary-lubrication regime, friction surfaces are in direct contact with each other and the presence of N-rGO sheets between the moving contact surfaces avoids the direct contact and thus reduces the COF.

WSD of the test ball with base oil and N-rGO nanolubricant is shown in Figure 7. With N-rGO (3 mg/L) oil the WSD is reduced to 200 µm from 230 µm for base oil (15% reduction). The significant decrease in WSD can be attributed to the easy penetration of N-rGO sheets into the contact points [2,39], which reduces the direct contact between the rough surfaces.

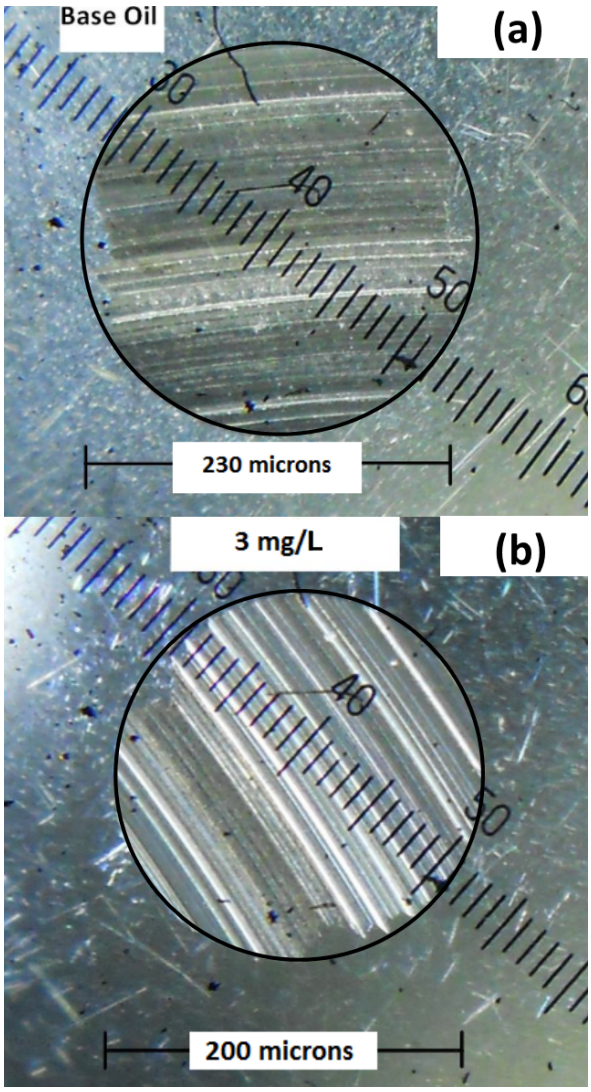

Figure 7: Wear scar diameter (WSD) of stainless steel balls lubricated with (a) base oil and (b) N-rGO nanolubricant (3 mg/L).

The measured temperature as a function of the gradually increased normal load during the experiment is plotted and compared in Figure 8 for base oil and N-rGO oil. The temperature increased to 62.5 °C for base oil while for N-rGO nanolubricant, the temperature increased to 47.5 °C at 1400 N. This indicates that the developed N-rGO based nanolubricant not only reduces the COF, but also acts as heat transfer fluid and decreases the temperature at friction interfaces.

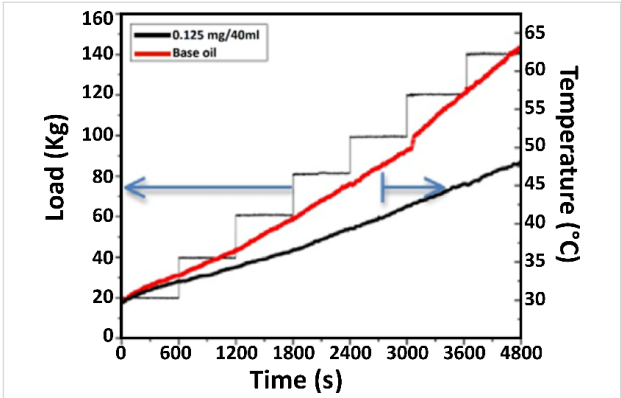

Figure 8: Comparison of the measured temperature of base oil and N-rGO (3 mg/L) nanolubricant as a function of the load.

Application of the nanolubricant in induced draft (ID) fans

Stable nanolubricants were prepared in large scale (700 liter) for field trial at a power plant of the National Thermal Power Corporation (NTPC) in India. The study was performed on two different induced draft (ID) fans (A and B) on two different channels (Ch 1 and Ch 2) using an energy management system. Initially, the data were recorded for 80 days at an interval of 1 h before the base oil was replaced with the nanolubricant during an overhaul. Figure 9a,b show the variation of unit load and current in fan A and fan B for Ch 1 and Ch 2 with base oil. Figure 9a shows that the average current in Fan A and Fan B (Ch 1) is about 255 A. From Figure 9b, it is observed that the current in fan A and fan B (in Ch 2) is not exactly equal. The average value of the current of fan A turned out to be 245 A whereas the average value of the current of fan B was 265 A.

The lubricant in fan A was then replaced with the N-rGO nanolubricant while the lubricant in ID fan B remained base oil in both channels. Figure 9c,d show the variation of unit load and current in Ch 1 and Ch 2 after replacing the lubricant in fan A. It is clear that the current in fan A is lower than current in fan B. For Ch 1, the average value of current for fan A and fan B was 250 A and 265 A. Similarly for Ch 2, the average value of current for fan A was 240 A whereas for fan B it was 275 A. Thus, the difference in current between fan A and fan B was increased from 20 A to 35 A in Ch 2.

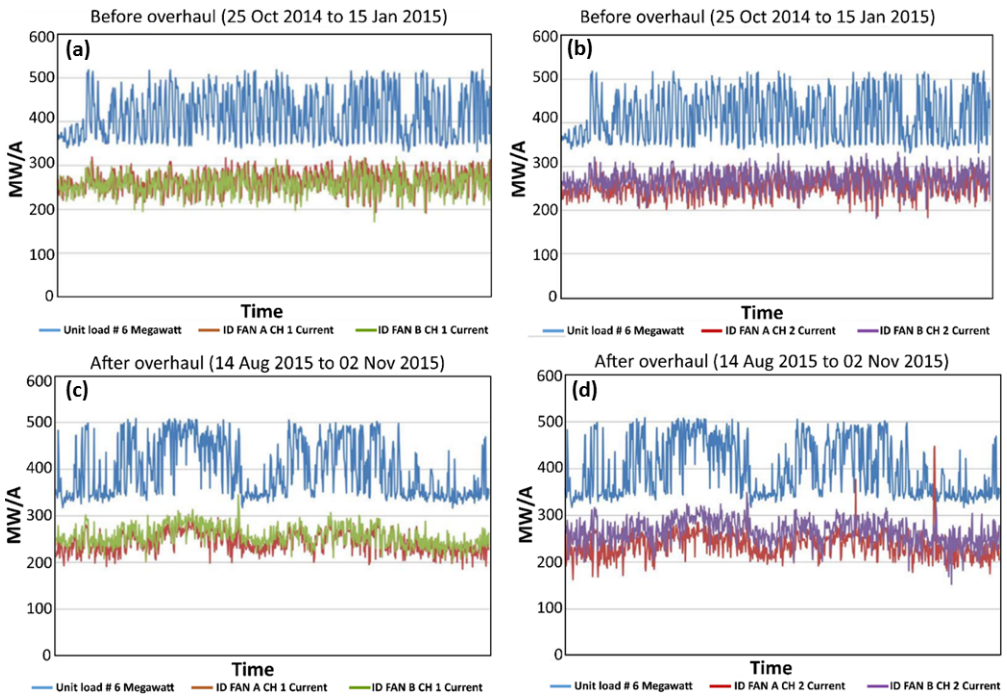

Figure 9: Unit load and current of ID fan A and B for (a) Ch 1, (b) Ch 2 before overhaul (replacement of base oil with nanolubricant), (c) Ch 1 and (d) Ch 2 after overhaul.

In summary, before the overhaul for Ch 1 there was no difference in current but after deployment of N-rGO nanolubricant the difference observed was 15 A. In case of Ch 2, before overhaul the difference was 20 Amp, which increased to 35 Amp after the implementation of nanolubricant. So, in conclusion the average difference due to the application of nanolubricant is 15 A for both channels.

Table 1 shows the power consumed by fan A and fan B for each month. It is very clear that the power consumed by fan A was considerably lower than that consumed by fan B for both channels. Figure 10 shows the total power consumption of fan A (Ch 1 and 2) and fan B (Ch 1 and 2).

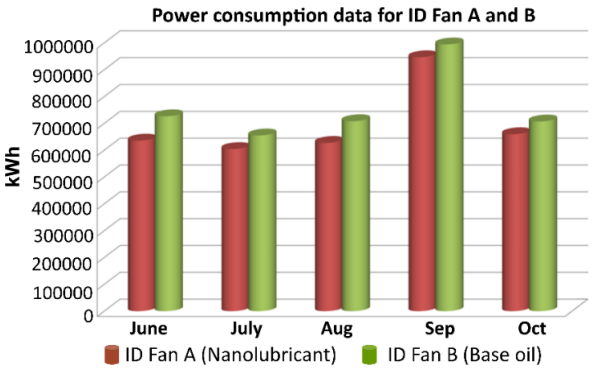

Figure 10: Power Consumption data for ID Fan A and B for few months.

Table 1: Power consumption of ID fans A and B over several months.

	June (kWh)	July (kWh)	Aug (kWh)	Sep (kWh)	Oct (kWh)
ID fan A (Ch 1)	309457.92	294362.11	305819.70	461072.16	318319.49
ID fan A (Ch 2)	326387.20	310225.23	321657.49	485770.78	341571.97
ID Fan B (Ch 1)	366251.52	330099.71	357024.60	501537.57	356346.24
ID fan B (Ch 2)	360467.45	324949.28	351382.42	492960.35	350942.59
ID fan A (Ch 1 + Ch 2)	635845.12	604587.34	627477.19	946842.94	659891.46
ID fan B (Ch 1 + Ch 2)	726718.98	655048.99	708407.02	994497.92	707288.83
difference (B − A)	90873.856	50461.651	80929.829	47654.976	47397.376

Conclusion

The present work describes the synthesis of N-rGO and a nanolubricant prepared by dispersing different amounts of nanoparticles in base oil. The study of tribological properties shows the significant decrease in COF when the nanolubricant is used. The measurement of COF was carried out for different concentrations of N-rGO and the maximum decrease in COF (25%) was obtained for a concentration of 3 mg/L. Moreover, the WSD for nanolubricant was reduced considerably compared to the base oil. The field study of nanolubricant in ID fans shows that there is remarkable decrease in the power consumption after the application of the nanolubricant. Thus, N-rGO nanolubricants are very promising for the tribological application due to the considerable improvement of tribological properties.

Supporting Information

Supporting Information File 1

Additional experimental data.
[http://www.beilstein-journals.org/bjnano/content/supplementary/2190-4286-8-147-S1.pdf]

Acknowledgements

This research work is supported by NTPC Ltd and authors are grateful to NTPC management for permission to publish this work. The help received from plant engineers is thankfully acknowledged.

References

1. Huang, H. D.; Tu, J. P.; Gan, L. P.; Li, C. Z. *Wear* **2006,** *261,* 140–144. doi:10.1016/j.wear.2005.09.010
2. Eswaraiah, V.; Sankaranarayanan, V.; Ramaprabhu, S. *ACS Appl. Mater. Interfaces* **2011,** *3,* 4221–4227. doi:10.1021/am200851z
3. Wu, Y. Y.; Tsui, W. C.; Liu, T. C. *Wear* **2007,** *262,* 819–825. doi:10.1016/j.wear.2006.08.021
4. Kalin, M.; Kogovšek, J.; Remškar, M. *Wear* **2012,** *280–281,* 36–45. doi:10.1016/j.wear.2012.01.011
5. Sunqing, Q.; Junxiu, D.; Guoxu, C. *Wear* **1999,** *230,* 35–38. doi:10.1016/S0043-1648(99)00084-8
6. Ota, J.; Hait, S. K.; Sastry, M. I. S.; Ramakumar, S. S. V. *RSC Adv.* **2015,** *5,* 53326–53332. doi:10.1039/c5ra06596h
7. Hamrock, B. J.; Schmid, S. R.; Jacobson, B. O. *Fundamentals of Fluid Film Lubrication,* 2nd ed.; Dekker: Basel, Switzerland, 2004. doi:10.1201/9780203021187
8. Grobert, N.; Terrones, M.; Osborne, A. J.; Terrones, H.; Hsu, W. K.; Trasobares, S.; Zhu, Y. Q.; Hare, J. P.; Kroto, H. W.; Walton, D. R. M. *Appl. Phys. A: Mater. Sci. Process.* **1998,** *67,* 595–598. doi:10.1007/s003390050828
9. Blau, P. J.; Haberlin, C. E. *Thin Solid Films* **1992,** *219,* 129–134. doi:10.1016/0040-6090(92)90732-Q
10. Thundat, T.; Warmack, R. J.; Ding, D.; Compton, R. N. *Appl. Phys. Lett.* **1993,** *63,* 891–893. doi:10.1063/1.109892
11. Alazemi, A. A.; Etacheri, V.; Dysart, A. D.; Stacke, L.-E.; Pol, V. G.; Sadeghi, F. *ACS Appl. Mater. Interfaces* **2015,** *7,* 5514–5521. doi:10.1021/acsami.5b00099
12. St. Dennis, J. E.; Jin, K.; John, V. T.; Pesika, N. S. *ACS Appl. Mater. Interfaces* **2011,** *3,* 2215–2218. doi:10.1021/am200581q
13. Vakili-Nezhaad, G. R.; Dorany, A. *Chem. Eng. Commun.* **2009,** *196,* 997–1007. doi:10.1080/00986440902797865
14. Yang, Y.; Grulke, E. A.; Zhang, Z. G.; Wu, G. *J. Appl. Phys.* **2006,** *99,* 114307. doi:10.1063/1.2193161
15. Liu, L.; Fang, Z.; Gu, A.; Guo, Z. *Tribol. Lett.* **2011,** *42,* 59–65. doi:10.1007/s11249-011-9749-y
16. Tarasov, S.; Kolubaev, A.; Belyaev, S.; Lerner, M.; Tepper, F. *Wear* **2002,** *252,* 63–69. doi:10.1016/S0043-1648(01)00860-2
17. Hernández Battez, A.; González, R.; Viesca, J. L.; Fernández, J. E.; Díaz Fernández, J. M.; Machado, A.; Chou, R.; Riba, J. *Wear* **2008,** *265,* 422–428. doi:10.1016/j.wear.2007.11.013
18. Alves, S. M.; Mello, V. S.; Faria, E. A.; Camargo, A. P. P. *Tribol. Int.* **2016,** *100,* 263–271. doi:10.1016/j.triboint.2016.01.050
19. Ye, P.; Jiang, X.; Li, S.; Li, S. *Wear* **2002,** *253,* 572–575. doi:10.1016/S0043-1648(02)00042-X
20. Greco, A.; Mistry, K.; Sista, V.; Eryilmaz, O.; Erdemir, A. *Wear* **2011,** *271,* 1754–1760. doi:10.1016/j.wear.2010.11.060
21. Zhang, L. L.; Tu, J. P.; Wu, H. M.; Yang,, Y. Z. *Mater. Sci. Eng., A* **2007,** *454–455,* 487–491. doi:10.1016/j.msea.2006.11.072
22. Lin, J.; Wang, L.; Chen, G. *Tribol. Lett.* **2011,** *41,* 209–215. doi:10.1007/s11249-010-9702-5
23. Song, H.-J.; Li, N. *Appl. Phys. A: Mater. Sci. Process.* **2011,** *105,* 827–832. doi:10.1007/s00339-011-6636-1
24. Zhang, W.; Zhou, M.; Zhu, H.; Tian, Y.; Wang, K.; Wei, J.; Ji, F.; Li, X.; Li, Z.; Zhang, P. *J. Phys. D: Appl. Phys.* **2011,** *44,* 205303. doi:10.1088/0022-3727/44/20/205303
25. Berman, D.; Erdemir, A.; Sumant, A. V. *Carbon* **2013,** *59,* 167–175. doi:10.1016/j.carbon.2013.03.006
26. Song, H.-J.; Jia, X.-H.; Li, N.; Yang, X.-F.; Tang, H. *J. Mater. Chem.* **2012,** *22,* 895–902. doi:10.1039/c1jm13740a
27. Bai, G.; Wang, J.; Yang, Z.; Wang, H.; Wang, Z.; Yang, S. *RSC Adv.* **2014,** *4,* 47096–47105. doi:10.1039/C4RA09488C
28. Ye, X.; Ma, L.; Yang, Z.; Wang, J.; Wang, H.; Yang, S. *ACS Appl. Mater. Interfaces* **2016,** *8,* 7483–7488. doi:10.1021/acsami.5b10579
29. Liu, Y.; Wang, X.; Pan, G.; Luo, J. *Sci. China: Technol. Sci.* **2013,** *56,* 152–157. doi:10.1007/s11431-012-5026-z
30. Kandanur, S. S.; Rafiee, M. A.; Yavari, F.; Schrameyer, M.; Yu, Z.-Z.; Blanchet, T. A.; Koratkar, N. *Carbon* **2012,** *50,* 3178–3183. doi:10.1016/j.carbon.2011.10.038
31. Kinoshita, H.; Nishina, Y.; Alias, A. A.; Fujii, M. *Carbon* **2014,** *66,* 720–723. doi:10.1016/j.carbon.2013.08.045
32. Llorente, J.; Román-Manso, B.; Miranzo, P.; Belmonte, M. *J. Eur. Ceram. Soc.* **2016,** *36,* 429–435. doi:10.1016/j.jeurceramsoc.2015.09.040
33. Liang, H.; Bu, Y.; Zhang, J.; Cao, Z.; Liang, A. *ACS Appl. Mater. Interfaces* **2013,** *5,* 6369–6375. doi:10.1021/am401495y
34. Tai, Z.; Chen, Y.; An, Y.; Yan, X.; Xue, Q. *Tribol. Lett.* **2012,** *46,* 55–63. doi:10.1007/s11249-012-9919-6
35. Zhang, Y.; Tang, H.; Ji, X.; Li, C.; Chen, L.; Zhang, D.; Yang, X.; Zhang, H. *RSC Adv.* **2013,** *3,* 26086–26093. doi:10.1039/c3ra42478b
36. Berman, D.; Erdemir, A.; Sumant, A. V. *Carbon* **2013,** *54,* 454–459. doi:10.1016/j.carbon.2012.11.061

37. Huang, T.; Xin, Y.; Li, T.; Nutt, S.; Su, C.; Chen, H.; Liu, P.; Lai, Z. *ACS Appl. Mater. Interfaces* **2013,** *5,* 4878–4891. doi:10.1021/am400635x
38. Pu, J.; Wan, S.; Zhao, W.; Mo, Y.; Zhang, X.; Wang, L.; Xue, Q. *J. Phys. Chem. C* **2011,** *115,* 13275–13284. doi:10.1021/jp111804a
39. Jaiswal, V.; Kalyani; Umrao, S.; Rastogi, R. B.; Kumar, R.; Srivastava, A. *ACS Appl. Mater. Interfaces* **2016,** *8,* 11698–11710. doi:10.1021/acsami.6b01876
40. Kaniyoor, A.; Baby, T. T.; Ramaprabhu, S. *J. Mater. Chem.* **2010,** *20,* 8467–8469. doi:10.1039/c0jm01876g
41. Li, B.; Dai, F.; Xiao, Q.; Yang, L.; Shen, J.; Zhang, C.; Cai, M. *Energy Environ. Sci.* **2016,** *9,* 102–106. doi:10.1039/C5EE03149D

License and Terms

BEILSTEIN JOURNAL OF NANOTECHNOLOGY

The effect of the electrical double layer on hydrodynamic lubrication: a non-monotonic trend with increasing zeta potential

Dalei Jing[1], Yunlu Pan[*2] and Xiaoming Wang[*3]

Full Research Paper

Open Access

Address:
[1]School of Mechanical Engineering, University of Shanghai for Science and Technology, Shanghai, 200093, P. R. China, [2]Key Laboratory of Micro-Systems and Micro-Structures Manufacturing, Ministry of Education and School of Mechatronics Engineering, Harbin Institute of Technology, Harbin, 150001, P. R. China, and [3]School of Electrical Engineering and Automation, Harbin Institute of Technology, Harbin, 150001, P. R. China

Email:
Yunlu Pan[*] - yunlupan@hit.edu.cn; Xiaoming Wang[*] - kazen_6@163.com

* Corresponding author

Keywords:
electrical double layer; electroviscous effect; hydrodynamic lubrication; zeta potential

Beilstein J. Nanotechnol. **2017,** *8,* 1515–1522.
doi:10.3762/bjnano.8.152

Received: 29 April 2017
Accepted: 07 July 2017
Published: 25 July 2017

This article is part of the Thematic Series "Nanotribology".

Guest Editor: E. Gnecco

Abstract

In the present study, a modified Reynolds equation including the electrical double layer (EDL)-induced electroviscous effect of lubricant is established to investigate the effect of the EDL on the hydrodynamic lubrication of a 1D slider bearing. The theoretical model is based on the nonlinear Poisson–Boltzmann equation without the use of the Debye–Hückel approximation. Furthermore, the variation in the bulk electrical conductivity of the lubricant under the influence of the EDL is also considered during the theoretical analysis of hydrodynamic lubrication. The results show that the EDL can increase the hydrodynamic load capacity of the lubricant in a 1D slider bearing. More importantly, the hydrodynamic load capacity of the lubricant under the influence of the EDL shows a non-monotonic trend, changing from enhancement to attenuation with a gradual increase in the absolute value of the zeta potential. This non-monotonic hydrodynamic lubrication is dependent on the non-monotonic electroviscous effect of the lubricant generated by the EDL, which is dominated by the non-monotonic electrical field strength and non-monotonic electrical body force on the lubricant. The subject of the paper is the theoretical modeling and the corresponding analysis.

Introduction

As one of the oldest techniques in modern engineering, lubrication is widely recognized and has inspired significant scientific interest [1-4]. The use of a layer of lubricant film, either in solid or fluid state, between frictional pairs can effectively reduce friction and wear. With respect to fluid lubrication, it can be divided into various regimes or states based on the thickness of

the lubricant film, such as dry friction with a lubricant film thickness of ≈1–10 nm, boundary lubrication (≈1–50 nm), thin film lubrication (≈10–100 nm) and fluid film lubrication (≈0.1–100 μm) [3,5]. Considering the small dimension of the fluid lubrication film (on the micro/nanoscale in the thickness direction), the chemical and physical properties of the solid–lubricant interface play an important role on the lubrication. Among these interfacial properties, the effect of charged frictional pair–lubricant interface and the resulting electrical double layer (EDL) within the lubricant have been recognized and studied [5-13]. The generation of surface charge at the frictional pair–lubricant interface is wide, especially for the frictional pairs of ceramics which have numerous applications of water as a lubricant.

EDL is a physical structure spontaneously formed near the charged solid–liquid interface due to the electrostatic interaction between the charged interface and free ions within the liquid when the interface is charged due to different mechanisms [14-17]. To explain the effect of the EDL on the hydrodynamic lubrication, one of the fundamental mechanisms is the influence of the EDL on the apparent viscosity of the lubricant, which is referred as the electroviscous effect [17]. Although the applications and studies of lubrication theory have a history dating back to hundreds of years, the role of surface-charge-induced EDL on the lubrication is a relatively new field. This role was first considered for the study of thin film lubrication by Bike and Prieve [6]. Following them, Zhang and Umehara [7] introduced the effect of the EDL on modifying the conventional Reynolds equation, analyzing the hydrodynamic lubrication. They found that the minimum lubricant film thickness increased with the increasing absolute value of zeta potential (an important parameter of EDL to manifest the surface charge at the solid–liquid interface). Li [9] theoretically studied the combined roles of EDL and surface roughness on the hydrodynamic lubrication. Huang and his colleagues [8,10,13] systematically studied the effects of EDL on the hydrodynamic lubrication or elasto-hydrodynamic lubrication, where the effect of zeta potential was analyzed. All these studies revealed that the EDL can significantly affect the lubrication capacity, especially when the Debye length (an important parameter to manifest the thickness of the EDL) of the EDL is similar to the thickness of the lubricant film.

To investigate the role on the hydrodynamic lubrication played by the EDL, it is needed to obtain the electrical potential and ion concentration within the lubricant affected by the EDL. In the previous theoretical studies regarding the effect of the EDL on the hydrodynamic lubrication, the EDL-affected electrical potential and ion concentration were mainly obtained on the basis of solving the linear Poisson–Boltzmann equation (PBE), which is a simplified mathematical model under the assumption of the Debye–Hückel approximation (DHA) [6-11]. It should be noted that zeta potential must be strictly limited to a small range (normally, the magnitude of zeta potential should be smaller than 25 mV) in these analyses based on DHA, otherwise, an unallowable error can be introduced [17-22]. In such a small range of zeta potentials, the literature mainly revealed that the effect that the zeta potential has on lubrication, including minimum film thickness, pressure and load capacity, was a change in the form of a monotonic trend [6-11]. Actually, it was reported that the magnitude of zeta potential could be up to several hundred millivolts [23-25]. However, there are fewer studies regarding the dependence of the lubrication on the EDL with zeta potential (over a wide range) without the application of the DHA. Without the implementation of the DHA, Chakraborty and Chakraborty [12] carried out theoretical work to study the effect of the zeta potential in a range from −25. 9 to −77.6 mV on lubrication, with the additional consideration of the finite size of the ions. They found that the effect of the zeta potential on the load capacity resulted in a non-intuitive trend with increasing magnitude of zeta potential; however, further details and explanation were not given. In addition, the electroviscous effect is dependent on the electrical conductivity of the lubricant [26,27], which inevitably affects the hydrodynamic lubrication. However, most of the previous theoretical works neglected the variation of electrical conductivity of the lubricant considering the effect of the EDL.

To solve these problems, this paper presents a theoretical study on the effect of the EDL on the hydrodynamic lubrication with the additional consideration of the effect of the EDL on the electrical conductivity of the lubricant. The electrical potential and ion concentration distribution within the EDL are obtained by solving the nonlinear PBE without the use of the DHA. On the basis of these assumptions, the effect of the zeta potential on the apparent viscosity of the lubricant is first studied and analyzed. Then, by combining the effects of the EDL on the electrical conductivity and apparent viscosity of the lubricant, the conventional Reynolds equation is modified to study the effect of the EDL on the load capacity of hydrodynamic lubrication. In addition, the dependence of the apparent viscosity and load capacity on the bulk ion concentration of lubricant and lubricant film thickness are also investigated. The underlying mechanisms of these issues are analyzed.

Theoretical Modeling

To analyze the effect of the EDL on the hydrodynamic lubrication, a hydrodynamic lubrication model in a 1D slider bearing with the effect of the EDL is considered. The physical model is shown in Figure 1. For the physical model in Figure 1, when the lubricant comes in contact with the slider bearing, two separate

EDLs form near the upper solid–lubricant interface and the lower solid–lubricant interface. The following assumptions are made to carry out the modeling.

1. Both of these two bearing surface–lubricant interfaces are negatively charged and have the same zeta potential, ζ.
2. The lubricant film thickness is much larger than the Debye length, thus, the two EDLs are non-overlapped.
3. The no slip condition of the velocity is considered.
4. The lubricant is an incompressible Newtonian fluid in the steady laminar state. Inertial force is neglected when compared with viscous force.

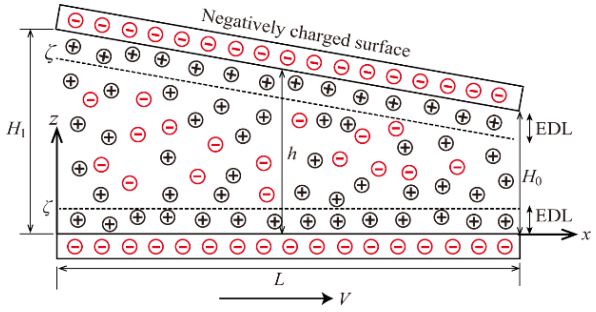

Figure 1: The schematic of hydrodynamic lubrication in a 1D slider bearing considering the effect of the EDL. *h* is a variable to indicate the lubricant film thickness, H_0 and H_1 are the lubricant film thickness at the outlet and inlet of bearing, respectively, *L* is the length of the bearing, *V* is the sliding velocity of the lower bearing surface, and *x* and *z* are the coordinate axes.

To analyze the hydrodynamic lubrication under the effect of the EDL, the electrical potential within the EDL should first be analyzed. Normally, the nonlinear PBE is an effective tool to obtain the electrical potential within the EDL. However, it should be noted that the classical PBE is derived based on the assumption that the free ions in the lubricant are point-like. Under this assumption, the number density of the counter-ions adjacent to the interface can be infinitely large based on the PBE when the ion concentration and/or zeta potential is large enough, which is not valid for the actual situation. Thus, the steric effect has been proposed and introduced to correct the classical PBE [12,28,29]. Based on the previous studies, in a certain range of zeta potential whose magnitude is normally smaller than 300 mV for a dilute solution, the classical PBE can still effectively predict the electrical potential and ion concentration within an EDL with an allowable error when comparing with the prediction of theoretical model considering the steric effect [28]. Based on this analysis, in the present work, the PBE is still used to analyze the electrical potential distribution within the EDL. Furthermore, the zeta potential is strictly chosen during the simulation to reduce the error.

By solving the nonlinear PBE, the electrical potential φ of a non-overlapped EDL in the lubricant with a certain thickness of *h* can be derived as [12,17,27],

$$\varphi=\frac{2k_BT}{ce}\ln\left\{\frac{\left[1+e^{-\kappa z}\tanh\left(\frac{ce\zeta}{4k_BT}\right)\right]}{\left[1-e^{-\kappa z}\tanh\left(\frac{ce\zeta}{4k_BT}\right)\right]}\right\}z\in\left[0,\frac{h}{2}\right]$$
$$\varphi=\frac{2k_BT}{ce}\ln\left\{\frac{\left[1+e^{\kappa(z-h)}\tanh\left(\frac{ce\zeta}{4k_BT}\right)\right]}{\left[1-e^{\kappa(z-h)}\tanh\left(\frac{ce\zeta}{4k_BT}\right)\right]}\right\}z\in\left[\frac{h}{2},h\right] \quad (1)$$

where $\kappa=[2n_0c^2e^2/(\varepsilon\varepsilon_0k_BT)]^{1/2}$ (n_0 is the original bulk ion concentration of the lubricant, *c* is the chemical valence of free ions in the lubricant, *e* is the elementary charge, ε is the lubricant's relative permittivity, and ε_0 is vacuum's absolute dielectric constant) is the reciprocal of the Debye length, *z* is the coordinate perpendicular to the lower bearing surface, ζ is the zeta potential at the solid–liquid interface and *h* is the lubricant film thickness.

By solving the modified Navier–Stokes equation describing the velocity field of the lubricant flowing in a 1D parallel plate channel with a height of *h* under the combined actions of the EDL, the driving pressure and the lower sliding wall with a velocity of *V*, the velocity field v and the relevant volume flow rate of the lubricant *Q* can be derived as,

$$v=\frac{1}{2\mu}\frac{dp}{dx}\left(z^2-hz\right)+\frac{(h-z)V}{h}+\frac{\varphi-\zeta}{\mu}\varepsilon\varepsilon_0E_x$$
$$Q=B\int_0^h v\,dz \quad (2)$$

where μ is lubricant's dynamic viscosity, d*p*/d*x* is pressure gradient, *V* is the sliding velocity of the lower surface, E_x is the electrical field strength within the flowing EDL, and *B* is the width of the channel that is assumed to be much larger than the height of the channel.

For a steady lubricant flow, the electrical field strength E_x can be obtained on the basis of when the total current within the lubricant is zero [17,30]. There are three kinds of electrical current induced by the EDL: the streaming current, the conduction current and the sliding-wall-induced current, which can be expressed in the following forms, respectively [17,30],

$$I_s = B\int_0^h \rho_e v\,dz$$
$$I_c = hB\lambda_{ave}E_x + 2B\lambda_s E_x \quad (3)$$
$$I_w = BV\sigma$$

where I_s is the streaming current, I_c is the conduction current, I_w is the sliding-wall-induced current, $\rho_e = ce(n_+ - n_-)$ is the local net ionic charge density within the EDL, λ_{ave} is the average bulk electrical conductivity of the lubricant, λ_s is the surface electrical conductivity of the lubricant that is neglected here, and $\sigma = -\varepsilon\varepsilon_0(d\varphi/dz)_{z=0}$ is the surface charge density at the lower bearing surface. Based on the zero net current in the steady state, the electrical field strength E_x can be given as,

$$E_x = \frac{\frac{\varepsilon\varepsilon_0}{\mu}\frac{dp}{dx}\left(-\int_0^h z\frac{d\varphi}{dz}dz\right) + \frac{h}{2}\int_0^h \frac{d\varphi}{dz}dz) + \frac{\varepsilon\varepsilon_0 V}{h}\int_0^h \frac{d\varphi}{dz}dz}{h\lambda_{ave} + \frac{(\varepsilon\varepsilon_0)^2}{\mu}\int_0^h\left(\frac{d\varphi}{dz}\right)^2 dz}. \quad (4)$$

Based on the previous studies, the bulk electrical conductivity of the lubricant under the influence of the EDL increases with the increasing absolute value of the zeta potential [26,27]. Hence, the EDL-dependent electrical conductivity of the lubricant must be considered during the analysis of the electroviscous effect and hydrodynamic lubrication. The average bulk electrical conductivity under the influence of the EDL can be obtained as [26,27,31],

$$\lambda_{ave} = \frac{1}{h}\int_0^h \lambda dz = \frac{c^2e^2An_0}{RT}\left[D_+\int_0^h e^{-\frac{ce\varphi}{k_BT}}dz + D_-\int_0^h e^{\frac{ce\varphi}{k_BT}}dz\right], \quad (5)$$

where A is Avogadro constant, D_+ is counter-ion's diffusion constant, D_- is co-ion's diffusion constant, R is molar gas constant, n_+ is counter-ion's concentrations and n_- is co-ion's concentration in the following equations.

$$n_\pm = n_0\exp\left(\mp\frac{ce\varphi}{k_BT}\right) \quad (6)$$

Normally, the electroviscous effect can be characterized by the apparent viscosity of the lubricant. Based on the apparent viscosity, the effect of the EDL on the flow can also be expressed by the following equation.

$$\mu_a\frac{d^2v_a}{dz^2} = \frac{dp}{dx} \quad (7)$$

where μ_a is the lubricant's apparent viscosity under the effect of the EDL, and v_a is the apparent velocity field across the lubricant in the following equation,

$$v_a = \frac{1}{2\mu_a}\frac{dp}{dx}\left(z^2 - hz\right) + \frac{(h-z)V}{h}. \quad (8)$$

Using the apparent viscosity, the flow rate of the lubricant can be expressed as,

$$Q_a = B\int_0^h v_a dz. \quad (9)$$

In practice, the flow rates in Equation 3 and Equation 8 are the same, thus, the apparent viscosity of the lubricant under the influence of the EDL can be expressed as,

$$\mu_a = \frac{\mu\frac{dp}{dx}\frac{h^3}{12}}{\frac{dp}{dx}\frac{h^3}{12} - \varepsilon\varepsilon_0 E_x\left(\int_0^h \varphi dz - \zeta h\right)}. \quad (10)$$

after obtaining the electrical potential within the EDL and apparent viscosity of the lubricant under the influence of the EDL. The effect of the EDL on the hydrodynamic lubrication can be derived as follows. Under the assumption of an incompressible lubricant, the mass conservation law gives the following modified Reynolds equation, which includes the effect of the EDL [7],

$$\frac{\partial}{\partial x}\left(\frac{h^3}{12\mu_a}\frac{dp}{dx}\right) = -\frac{V}{2}\frac{\partial h}{\partial x}. \quad (11)$$

The hydrodynamic load capacity of the lubricant can be obtained by integrating the pressure over the 1D slider bearing length [7],

$$W = \int_0^L p\,dx = \frac{1}{\alpha}\int_{H_0}^{H_1} p\,dh, \quad (12)$$

where L is the 1D slider bearing length, α is the slope of the upper bearing surface and H_0 and H_1 are the lubricant film thicknesses at the outlet and inlet of bearing, respectively. While solving for the hydrodynamic load capacity, the following pressure boundary conditions were used:

$$p|_{h=H_0,H_1} = 0. \quad (13)$$

Results and Discussion

After establishing the theoretical model regarding the effect of the EDL on the hydrodynamic lubrication, NaCl solution was chosen as the lubricant to carry out the analysis. The diffusion constants of Na^+ and Cl^- are 1.334×10^{-9} m^2/s and 2.032×10^{-9} m^2/s, respectively [32]. To maintain the validity of the nonlinear PBE [28,29], the zeta potential is limited to a range from 0 mV to −250 mV.

Electrical potential within the EDL

Figure 2 shows the dimensionless electrical potential within the EDL as a function of dimensionless lubricant film thickness. To illustrate the differences induced by the DHA, the curves shown in Figure 2 are obtained by applying both the linear PBE and the nonlinear PBE, respectively. "Linear PBE" in the figure means the electrical potential is obtained on the basis of the linear PBE, while "Nonlinear PBE" means the electrical potential is obtained on the basis of the nonlinear PBE. Because the zeta potential at both the lower and upper bearing surfaces are the same, the electrical potential distribution within the EDL is symmetric. Hence, only half of the dimensionless electrical potential curves are given in Figure 2. It can be seen that the dimensionless electrical potentials obtained by the linear PBE remained constant with different values of zeta potential. Furthermore, there is a larger difference between the dimensionless electrical potentials obtained by the linear PBE and the nonlinear PBE when the zeta potential value is larger. Thus, the EDL-dependent lubrication analysis, based on the linear PBE, should be strictly limited to a small zeta potential range, otherwise, a large error will be introduced. To reduce this error when the magnitude of the zeta potential is large, the nonlinear PBE is used in present work to carry out the EDL-dependent lubrication analysis.

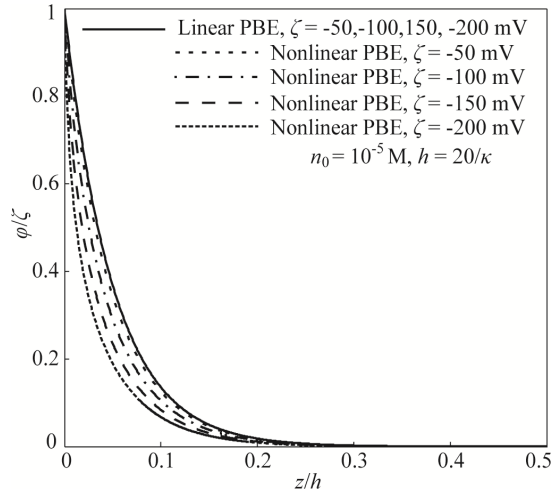

Figure 2: Dimensionless electrical potential distribution obtained by solving the linear PBE and the nonlinear PBE (the model used in present work).

On the basis of the nonlinear PBE, Figure 2 shows that the dimensionless electrical potential decreases with an increase in the absolute value of the zeta potential. That is, the electrical potential shows a faster reduction. The mechanism for this phenomenon is described as follows. For the case of the zeta potential with a larger absolute value, there is a larger surface charge density at the bearing surface–lubricant interface. This results in a larger local net ionic charge density near the interface by attracting many more counter ions to close the interface, leading to a faster reduction of dimensionless electrical potential.

Non-monotonic electroviscous effect

Figure 3 shows variations of the EDL-dependent apparent viscosity of lubricant based on different assumptions and models. The label "changed λ" in the figure means that the variation of electrical conductivity with the zeta potential is considered during the analysis of apparent viscosity, while "constant λ" in the figure means that the influence of the zeta potential on the electrical conductivity is neglected during the analysis and the electrical conductivity is assumed to be a constant. From Figure 3, it can be found that there are large differences for the apparent viscosities of the lubricant based on different assumptions and models, especially when the absolute value of the zeta potential is large enough (up to hundreds of millivolts). When a constant electrical conductivity and the linear PBE based on DHA are used to analyze the effect of the zeta potential on the

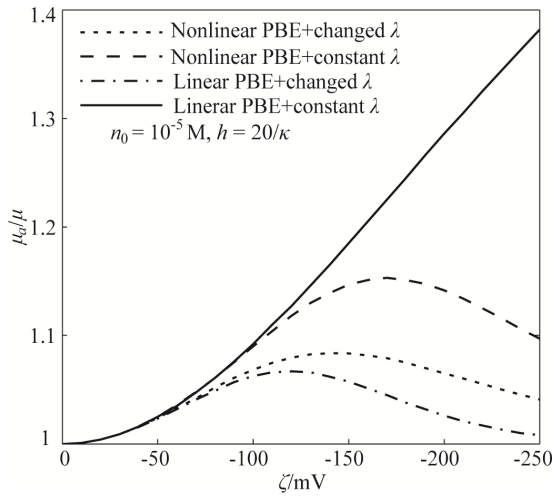

Figure 3: The effect of the zeta potential on the apparent viscosity of the lubricant based on different assumptions and theoretical models. The "Nonlinear PBE+changed λ" case is the model established in the present work.

apparent viscosity, it can be found that the apparent viscosity of the lubricant monotonically increases with the increasing absolute value of the zeta potential. This holds even when the absolute value of the zeta potential is large (up to hundreds of millivolts), as seen by the solid line in Figure 3. This result is similar to the result reported by Li and Jin [11]. However, for the other three groups of results based on different assumptions, all of the three apparent viscosities show non-monotonic variations with the increasing absolute value of the zeta potential. Figure 3 shows that the theoretical model should be carefully established to guarantee the validity of EDL-induced apparent viscosity of the lubricant. It is believed that the theoretical model based on the nonlinear PBE and changed electrical conductivity is much more reasonable, and this is the model established and used in the present work.

On the basis of the nonlinear PBE and modified electrical conductivity, Figure 4 shows the effect of the zeta potential of the EDL on the apparent viscosity of the lubricant and the dependence of the EDL-induced apparent viscosity on the lubricant film thickness and ion concentration of the lubricant. Figure 4 shows that the zeta potential leads to an increase in the apparent viscosity. More interestingly, the EDL-enhanced apparent viscosity shows a non-monotonic trend from increasing to decreasing with the gradually increasing absolute value of the zeta potential, that is, the electroviscous effect exhibits a non-monotonic characteristic.

The non-monotonic electroviscous effect has been systematically studied in our previous study and can be analyzed on the basis of the modified Navier–Stokes equation [27,33-35]. Based on the previous studies, the electrical body force applied on the flowing lubricant is dominated by the electrical field strength, which has a non-monotonic behavior with the increasing magnitude of the zeta potential. This non-monotonic electrical field strength leads to a non-monotonic electrical field force on the lubricant, which then results in a non-monotonic variation of the velocity and a non-monotonic electroviscous effect. In addition, the apparent viscosity increases with decreasing lubricant film thickness and decreasing ion concentration. These dependences of the electroviscous effect on the lubricant film thickness and ion concentration can also be explained on the basis of electrical field force applied on the lubricant, and have been studied in our previous works [27,33-35].

Non-monotonic hydrodynamic load capacity of the lubricant

Based on the influence of the EDL on the apparent viscosity, the effect of the EDL on the hydrodynamic load capacity of the lubricant can be analyzed. Figure 5 shows the effect of the EDL on the hydrodynamic load capacity of lubricant based on different theoretical models and different assumptions. W_0 is the hydrodynamic load capacity without the effect of the zeta potential. W is the hydrodynamic load capacity with the effect of the zeta potential. Figure 5 shows that there are large differences for the hydrodynamic load capacity of the lubricant based on different models when the absolute value of the zeta potential is large enough. For example, when a constant electrical conductivity and the linear PBE are applied, the hydrodynamic load capacity of the lubricant monotonically increases with increasing absolute value of the zeta potential, even when the absolute value of the zeta potential is large. This result is simi-

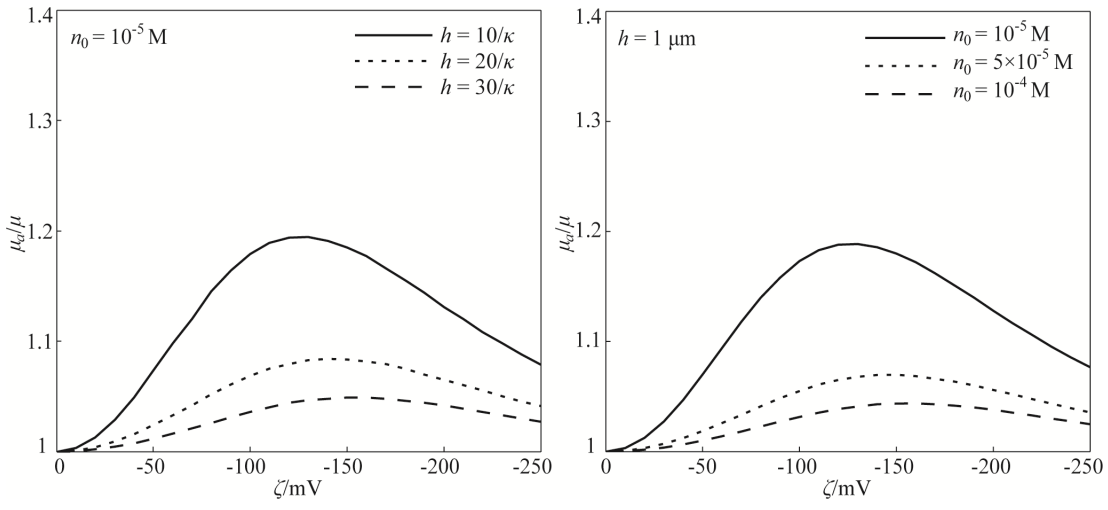

Figure 4: The effect of the zeta potential on the apparent viscosity of the lubricant and the dependence of the EDL-induced apparent viscosity on the lubricant film thickness and ion concentration of the lubricant based on the model of nonlinear PBE and modified electrical conductivity.

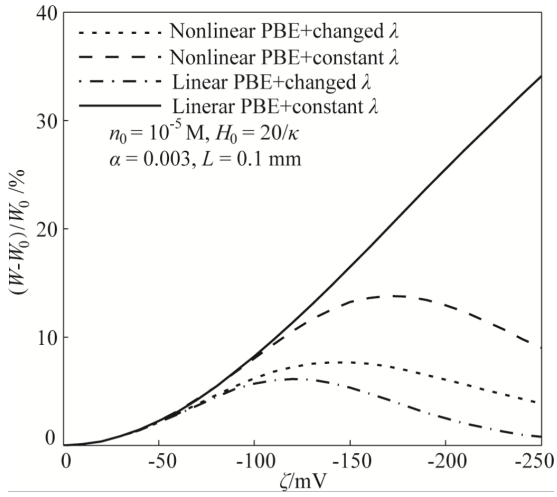

Figure 5: Comparison of the hydrodynamic load capacity of the lubricant including the effect of the zeta potential based on different assumptions and theoretical models. The "Nonlinear PBE+changed λ" is the model established and used in the present work.

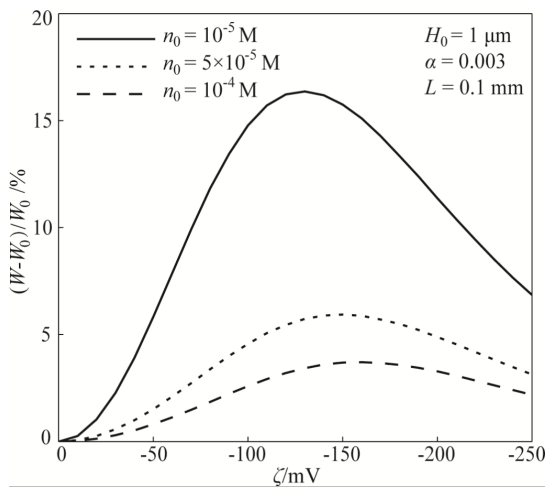

Figure 6: The effect of zeta potential on the hydrodynamic load capacity of the lubricant and the dependence of the hydrodynamic load capacity on the ion concentration based on the model of nonlinear PBE and varying electrical conductivity.

lar to the reports of Li and Jin [11]. However, the other three types of hydrodynamic load capacities show non-monotonic variations with increasing zeta potential. The variation of the hydrodynamic load capacity is consistent with the variation of apparent viscosity. Among these models, the theoretical model based on the nonlinear PBE and varied electrical conductivity should be the most reasonable one, and this is the model used in the present work.

Figure 6 shows the influence of the zeta potential of the EDL on the hydrodynamic load capacity of the lubricant based on the nonlinear PBE and changed electrical conductivity. It can be concluded from Figure 6 that, although the EDL can enhance the hydrodynamic load capacity, the hydrodynamic load capacity shows a non-monotonic trend changing from enhancement to attenuation with the gradually increasing absolute value of the zeta potential. There is a non-monotonic relationship between the hydrodynamic load capacity and the zeta potential of the EDL. This result is similar to the result of Chakraborty and Chakraborty [12]. By considering the steric effect, they also found that the hydrodynamic load capacity followed a non-intuitive trend with increasing magnitude of zeta potential. The variation of the hydrodynamic load capacity with zeta potential is consistent with the variation of the apparent viscosity with zeta potential. A larger apparent viscosity leads to a stronger hydrodynamic load capacity. In addition, Figure 6 shows that the hydrodynamic load capacity increases with the decreasing ion concentration. This is because under the condition of a fixed lubricant film dimension, a smaller ion concentration of lubricant means a larger Debye length, and a larger range to affect the lubrication.

Conclusion

In this paper, the effect of the zeta potential of the non-overlapped EDL on the hydrodynamic lubrication of a 1D slider bearing is theoretically studied on the basis of the nonlinear PBE without the use of the DHA. By considering the EDL-dependent bulk electrical conductivity, the effect of the EDL on the apparent viscosity of the lubricant was first studied to modify the classical Reynolds equation. Then, the effect of the zeta potential on the hydrodynamic lubrication was studied and analyzed based on the modified Reynolds equation.

The present study reveals that the apparent viscosity of the lubricant first increases and then decreases with the gradually increasing absolute value of zeta potential. The non-monotonic apparent viscosity including the effect of the zeta potential is dependent on the electrical field force applied on the lubricant, which is dominated by the non-monotonic electrical field strength. Being consistent with the variation in the apparent viscosity of the lubricant, the hydrodynamic load capacity of the lubricant under the effect of the EDL in a 1D slider bearing also shows a non-monotonic trend, changing from enhancement to attenuation with the gradually increasing absolute value of zeta potential. In addition, the hydrodynamic load capacity of the lubricant increases with decreasing ion concentration under the condition of fixed lubricant film thickness. Furthermore, the assumptions of DHA and constant electrical conductivity of the lubricant should be carefully applied to guarantee the validity of the hydrodynamic lubrication analysis.

The present work shows that the effect of a surface-charge-induced EDL on the hydrodynamic lubrication exhibits a non-

monotonic behavior. The load capacity of a micro/nanometer sliding bearing firstly increases followed by a decrease with increasing absolute value of the zeta potential. Thus, an effective control of the surface charge or zeta potential at the bearing wall–lubricant interface can be a potential method to optimize the hydrodynamic lubrication capacity.

Acknowledgements

The authors gratefully acknowledge the financial support of the National Natural Science Foundation of China (No. 51505292 & No. 51505108) and the Young Teachers Training Program of Shanghai, China (No. ZZsl15025).

References

1. Reynolds, O. *Philos. Trans. R. Soc. London* **1886,** *177,* 157–234. doi:10.1098/rstl.1886.0005
2. Dowson, D. *History of Tribology,* 2nd ed.; Professional Engineering Publishing: London, United Kingdom, 1998.
3. Bhushan, B. *Introduction to Tribology,* 1st ed.; John Wiley & Sons: New York, U.S.A, 2002.
4. Bhushan, B. *Nanotribology and Nanomechanics – An Introduction,* 1st ed.; Springer: Heidelberg, Germany, 2005.
5. Xie, G.; Guo, D.; Luo, J. *Tribol. Int.* **2015,** *84,* 22–35. doi:10.1016/j.triboint.2014.11.018
6. Bike, S. G.; Prieve, D. C. *J. Colloid Interface Sci.* **1990,** *136,* 95–112. doi:10.1016/0021-9797(90)90081-X
7. Zhang, B.; Umehara, N. *JSME Int. J., Ser. C* **1998,** *41,* 285–290. doi:10.1299/jsmec.41.285
8. Wong, P. L.; Huang, P.; Meng, Y. *Tribol. Lett.* **2003,** *14,* 197–203. doi:10.1023/A:1022320531293
9. Li, W. L. *Tribol. Lett.* **2005,** *20,* 53–61. doi:10.1007/s11249-005-7792-2
10. Bai, S.; Huang, P.; Meng, Y.; Wen, S. *Tribol. Int.* **2006,** *39,* 1405–1412. doi:10.1016/j.triboint.2005.12.004
11. Li, W.-L.; Jin, Z. *Proc. Inst. Mech. Eng., Part J* **2008,** *222,* 109–120. doi:10.1243/13506501JET369
12. Chakraborty, J.; Chakraborty, S. *Phys. Fluids* **2011,** *23,* 082004. doi:10.1063/1.3624615
13. Zuo, Q.; Huang, P.; Su, F. *Tribol. Int.* **2012,** *49,* 67–74. doi:10.1016/j.triboint.2011.12.021
14. Hunter, R. J. *Zeta Potential in Colloid Science;* Academic Press: London, United Kingdom, 1981.
15. Israelachvili, J. *Intermolecular and Surface Forces,* 2nd ed.; Academic Press: : London, United Kingdom, 1991.
16. Hunter, R. J. *Foundations of Colloid Science;* Oxford University Press: New York, U.S.A., 2001.
17. Li, Q. D. *Electrokinetics in Microfluidics;* Academic Press: Oxford, United Kingdom, 2004.
18. Burgreen, D.; Nakache, F. R. *J. Phys. Chem.* **1964,** *68,* 1084–1091. doi:10.1021/j100787a019
19. Rice, C. L.; Whitehead, R. *J. Phys. Chem.* **1965,** *69,* 4017–4024. doi:10.1021/j100895a062
20. Mala, G. M.; Li, D.; Dale, J. D. *Int. J. Heat Mass Transfer* **1977,** *40,* 3079–3088. doi:10.1016/S0017-9310(96)00356-0
21. Yang, J.; Kwok, D. Y. *Langmuir* **2003,** *19,* 1047–1053. doi:10.1021/la026201t
22. Jamaati, J.; Niazmand, H.; Renksizbulut, M. *Int. J. Therm. Sci.* **2010,** *49,* 1165–1174. doi:10.1016/j.ijthermalsci.2010.01.008
23. Wright, P. B.; Lister, A. S.; Dorsey, J. G. *Anal. Chem.* **1997,** *69,* 3251–3259. doi:10.1021/ac9613186
24. Deshiikan, S. R.; Papadopoulos, K. D. *Colloid Polym. Sci.* **1998,** *276,* 117–124. doi:10.1007/s003960050218
25. Ren, L.; Li, D.; Qu, W. *J. Colloid Interface Sci.* **2001,** *233,* 12–22. doi:10.1006/jcis.2000.7262
26. Ban, H.; Lin, B.; Song, Z. *Biomicrofluidics* **2010,** *4,* 014104. doi:10.1063/1.3328091
27. Jing, D.; Bhushan, B. *Beilstein J. Nanotechnol.* **2015,** *6,* 2207–2216. doi:10.3762/bjnano.6.226
28. Kilic, M. S.; Bazant, M. Z.; Ajdari, A. *Phys. Rev. E* **2007,** *75,* 021502. doi:10.1103/PhysRevE.75.021502
29. Khair, A. S.; Squires, T. M. *J. Fluid Mech.* **2009,** *640,* 343–356. doi:10.1017/S0022112009991728
30. Soong, C. Y.; Wang, S. H. *J. Colloid Interface Sci.* **2003,** *265,* 202–213. doi:10.1016/S0021-9797(03)00513-7
31. Moorfe, J. H.; Spencer, N. D. *Encyclopedia of Chemical Physics and Physical Chemistry;* Institute of Physics Pub: Bristol, United Kingdom, 2001.
32. Haynes, M. W. *Handbook of Chemistry and Physics,* 96th ed.; CRC Press, Inc.: Boca Raton, FL, U.S.A., 2015.
33. Jing, D.; Pan, Y. *Int. J. Heat Mass Transfer* **2016,** *101,* 648–655. doi:10.1016/j.ijheatmasstransfer.2016.05.087
34. Jing, D.; Pan, Y.; Wang, X. *Int. J. Heat Mass Transfer* **2017,** *108,* 1305–1313. doi:10.1016/j.ijheatmasstransfer.2016.12.090
35. Jing, D.; Pan, Y.; Wang, X. *Int. J. Heat Mass Transfer* **2017,** *113,* 32–39. doi:10.1016/j.ijheatmasstransfer.2017.05.061

License and Terms

BEILSTEIN JOURNAL OF NANOTECHNOLOGY

Nanotribological behavior of deep cryogenically treated martensitic stainless steel

Germán Prieto[*1,2,§], Konstantinos D. Bakoglidis[3], Walter R. Tuckart[1,2] and Esteban Broitman[3]

Full Research Paper

Open Access

Address:
[1]Grupo de Tribología, Departamento de Ingeniería, Universidad Nacional del Sur, Bahía Blanca, Buenos Aires, Argentina, [2]Consejo Nacional de Investigaciones Científicas y Técnicas, CABA, Argentina and [3]IFM, Linköping University, SE581 83 Linköping, Sweden

Email:
Germán Prieto[*] - german.prieto@uns.edu.ar

* Corresponding author
§ Full postal address: Av. Alem 1253, Bahía Blanca, Buenos Aires, Argentina, CP 8000.

Keywords:
carbide refinement; cryogenic treatments; friction; nanoindentation; nanoscratch; wear-resistance improvement

Beilstein J. Nanotechnol. **2017,** *8,* 1760–1768.
doi:10.3762/bjnano.8.177

Received: 10 February 2017
Accepted: 10 August 2017
Published: 25 August 2017

This article is part of the Thematic Series "Nanotribology".

Guest Editor: E. Gnecco

Abstract

Cryogenic treatments are increasingly used to improve the wear resistance of various steel alloys by means of transformation of retained austenite, deformation of virgin martensite and carbide refinement. In this work the nanotribological behavior and mechanical properties at the nano-scale of cryogenically and conventionally treated AISI 420 martensitic stainless steel were evaluated. Conventionally treated specimens were subjected to quenching and annealing, while the deep cryogenically treated samples were quenched, soaked in liquid nitrogen for 2 h and annealed. The elastic–plastic parameters of the materials were assessed by nanoindentation tests under displacement control, while the friction behavior and wear rate were evaluated by a nanoscratch testing methodology that it is used for the first time in steels. It was found that cryogenic treatments increased both hardness and elastic limit of a low-carbon martensitic stainless steel, while its tribological performance was enhanced marginally.

Introduction

AISI 420 is a martensitic stainless steel, commonly used in pumping applications in the petrochemical industry, oil extraction and energy generation. As a result, components made of AISI 420 are subjected to severe mechanical and tribological solicitations. Therefore, the enhancement of wear resistance of this steel is of technological and industrial interest.

Although enhancing the wear resistance of steel alloys by means of cryogenic processing has been known since at least the last three decades [1], the metallurgical phenomena responsible for this modifications are still under discussion. The main operative mechanisms during the cryogenic treatment of steels discussed in the current state-of-the-art

literature are: transformation of retained austenite [2-4], carbide refinement [5-7] and plastic deformation of virgin martensite [8,9].

Because of the high hardenability of low-carbon AISI 420 stainless steel, both transformation of retained austenite and plastic deformation of virgin martensite do not seem to be operative during cryogenic cooling. The main effect observed in AISI 420 after cryogenic processing is a strong reduction in carbide size and a more even dispersion of them in the martensitic matrix [10]. This carbide refinement improved the macroscale wear resistance of the material by 35% under lubricated and by 90% under dry sliding conditions compared to the conventionally treated specimens [11]. A slight reduction in the macroscale friction coefficient has also been observed [11] and an increase in fracture toughness (ca. 30%) was reported in deep cryogenically treated specimens [12].

Nanotribological tests, such as the nanoscratch technique described in [13], can be used for studying the influence of microstructural features on the frictional and wear behavior of a material, thanks to the small size of the tip counterpart, and applied loads in the order of micronewtons. A nanotribological approach is necessary, as most engineering surfaces begin to contact at the tip of asperities, whose dimensions are at the nanometric scale. However, so far the majority of the research efforts available in the open literature were focused on the micro- and nanotribological evaluation of Si and single metals for microelectromechanical system (MEMS) applications [14,15] and carbon-based coatings [16-18]. Although, there is an incipient amount of nanotribological studies performed in engineering steels [19-24].

Tribometers built on nanoindentation-based equipments, such as triboindenters, made possible the study of friction and wear at small contact scales. This kind of equipment can be used to simulate a single sharp asperity sliding over a surface while simultaneously controlling with high precision the applied force, and measuring the topographical modifications and the friction forces.

The purpose of this paper is to deepen the understanding of the influence of cryogenic treatments on the wear resistance and the mechanical properties of a low-carbon AISI 420 martensitic stainless steel evaluated at very small scales.

Experimental

The material used in this study was a low-carbon AISI 420 martensitic stainless steel. Its chemical composition is presented in Table 1 and was determined using an Spectro SPECTROMAXx optical emission spectrometer.

AISI 420 specimens were pre-heated at 830 °C for 10 min, followed by quenching in oil from 1030 °C, and afterwards annealed at 410 °C for 10 min with furnace cooling. This group was identified as conventionally heat-treated (CHT). The other group of specimens was quenched in oil from 1030 °C and immediately afterwards soaked in liquid nitrogen, at an equilibrium temperature of −196 °C. The cooling rate was set at 0.45 °C/s and the soaking time at cryogenic temperature was of 2 h. Finally, the specimens were annealed at 410 °C for 10 min and slowly cooled inside the furnace (Figure 1). This latter group was identified as deep cryogenically treated (DCT). The austenization, quenching and annealing of the specimens was performed in argon atmosphere in order to prevent decarburation. The selection of the heat-treatment parameters was based in the results of our previous work [10].

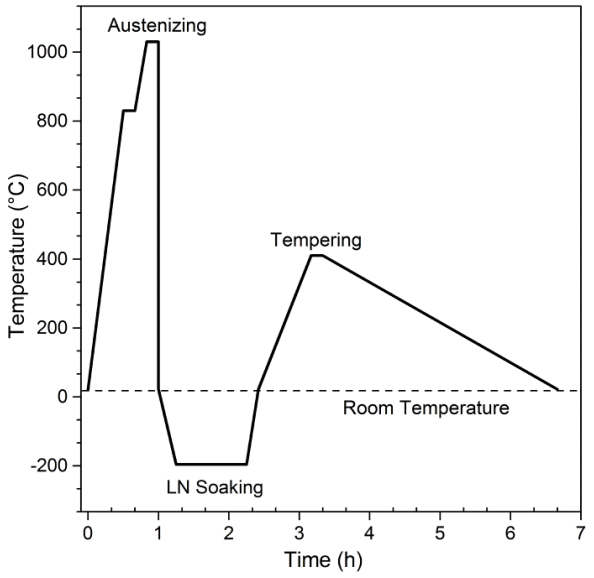

Figure 1: Representation of the applied cryogenic treatment.

Scanning electron microscopy (SEM) was used to characterize the resulting microstructures after each heat treatment (JEOL JSM-35CF). The volume fraction of carbides was estimated

Table 1: Chemical composition of AISI 420.

element	C	Cr	Mn	Si	P	S	Fe
content in AISI 420 (wt %)	0.17	12.83	0.76	0.55	0.05	0.017	balance

from the SEM micrographs using Delesse's principle for stereographic relationships [25].

All specimens were included in carbon-filled bakelite using a Buehler SIMPLIMET 3 hot press, and then were polished with a Struers TEGRAMIN-30 automatic polishing machine, employing diamond suspensions down to 0.25 μm in particle size. The obtained roughness parameters, measured with a Hysitron TI950 triboindenter, were: R_a = 15 ± 3.2 nm, R_z = 98 ± 18 nm, R_t = 125 ± 31 nm. The polished specimens were ultrasonically cleaned with acetone and isopropyl alcohol for 5 min and then placed onto the stage of the triboindenter to perform nanoindentation and nanotribological tests.

Nanoindentation tests

A Hysitron TI950 triboindenter was employed for performing nanoindentation measurements, using a three-plate capacitive transducer. This transducer can act both as the actuator and the sensing device and allows for the application of normal forces up to 10 mN. The triboindenter utilizes the Oliver and Pharr (O&P) method [26] as the standard procedure to interpret the data from nanoindentations. According to [26], hardness (H) is defined as:

$$H = \frac{P}{A}, \tag{1}$$

where P is the maximum normal load and A is the contact area between the tip and the specimen. The contact area can be related to the contact stiffness by using Sneddon's law [27]:

$$E_r = \frac{\sqrt{\pi}}{2}\frac{S}{\sqrt{A}}. \tag{2}$$

Nanoindentation tests were performed using a Berkovich diamond tip, with an apex radius of ca. 100 nm. Penetration depths of 50, 100, and 200 nm were set. A 3 × 4 array of indentations was performed in the specimens at each penetration depth, spaced at 20 μm from each other. The significance of the obtained results was determined by analysis of variance (ANOVA), using the statistical software INFOSTAT [28].

When carrying out nanoindentations in an elastic–plastic material like a metal, it tends to accumulate around the indenter, forming a pile-up that is higher than the sample surface. This phenomenon can lead to the underestimation of the true contact area and a significant deviation of calculated hardness and elastic modulus from their real values. The formation of pile-ups during nanoindentation of steels has been studied by several researchers [29-31].

Our approach was to compare the conventional O&P method with the one proposed by Joslin and Oliver (J&O) [32]. The J&O method utilizes the ratio between the hardness and the square of the elastic modulus (H/E^2) as an independent characteristic parameter. The proposed method utilizes the maximum force applied during the test (P) and the calculated contact stiffness (S) from the nanoindentation data. S is defined as the slope of the unloading curve ($\partial P/\partial h$), evaluated at the point of maximum force. Both P and S and can be determined without knowledge of the exact geometry of the diamond tip or the shape and size of the indentation. The values of P and S are related through the following equation [32]:

$$\frac{H}{E_r^2} = \left(\frac{4}{\pi}\right)\left(\frac{P}{S^2}\right), \tag{3}$$

where E_r is the relative elastic modulus, defined as

$$\frac{1}{E_r} = \left[\left(\frac{1-\nu_s^2}{E_s}\right) + \left(\frac{1-\nu_i^2}{E_i}\right)\right]. \tag{4}$$

E_s and ν_s are Young's modulus and Poisson's ratio of the sample, and E_i and ν_i are Young's modulus and Poisson's ratio of the indenter (E_i = 1140 GPa, ν_i = 0.07).

This approach does not allow for the simultaneous determination of E and H, but several researchers [33,34] have reported P/S^2 (i.e., H/E_r^2) as a useful characterizing parameter, even when the development of pile-up is considerable [35].

Nanotribology tests

In order to evaluate the frictional behavior of the samples and their wear resistance, microscale friction tests were performed. The experimental setup followed the guidelines of the test procedure proposed by Broitman and Flores [13]. In this method, a probe is continuously scanning a track in a reciprocal movement, as shown in Figure 2. In our work, a 1 mN load was applied in a stroke length of 5 μm for 31 cycles to evaluate the evolution of the friction coefficient, and a load of 3 μN in a stroke of 10 μm for 12 scanning cycles was used to evaluate the surface roughness. The obtained topographic information at the low load is used to calculate the wear rate and roughness evolution, while the force transducers measure the friction force variations at the higher applied loads. The method utilizes a MatLab® script to eliminate the thermal drift. The software output gives the resulting friction coefficient, track roughness, and wear rate as a function of the number of cycles of the probe. The wear volume is estimated considering the projected area A of the tip as a function of the penetration depth (h):

$A = (2Rh - h^2)$, where R is the tip radius. The volume of the displaced material during each cycle is calculated as the sum of areas at the different penetration depths of the track. Additionally, the evolution of the average trench roughness (R_a) is calculated after every cycle as $100 \times R_a/R_0$, where R_0 is the average roughness before the first test cycle. It should be pointed out that, in this method, the wear is calculated after the elastic recovery of the surface took place.

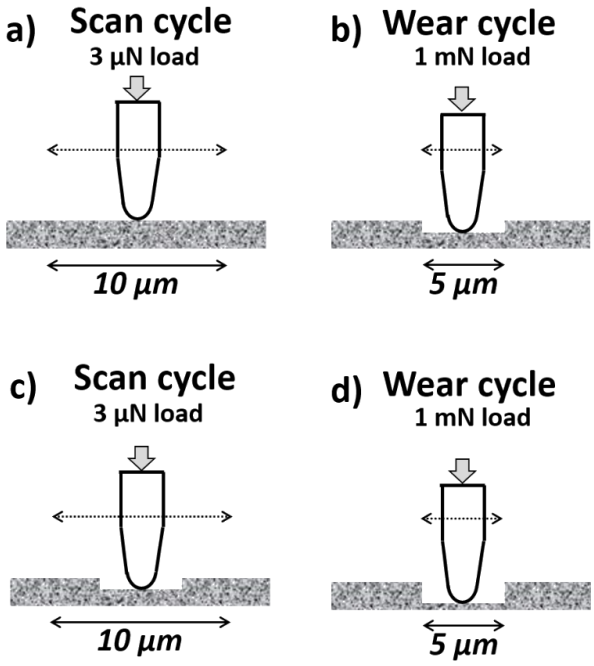

Figure 2: Schematics of the used scratch method to measure friction and wear: (a) pre-scan to get the initial topographical profile; (b) first cycle of wear; (c) post-scan to get the new topographical profile; (d) three cycles of wear. The processes (c) and (d) are repeated ten times. Reprinted with permission from [13], copyright 2015 AIP Publishing LLC.

For the nanoscratch tests, a conical diamond tip with an apex radius of 5 µm was employed. The applied normal load was set at 1000 µN and each reported value corresponds to the average of at least three valid tests. The theoretical Hertzian contact pressure was estimated at 10.7 GPa.

In order to evaluate if the scratch tests were generating wear and not only plastically deforming the surfaces, the elastic recovery (ER) was calculated for each sample by nanoindentation using the same tip and normal load as in the scratch tests. ER is calculated as the ratio between the maximum (h_t) and the residual (h_r) height as follows:

$$\mathrm{ER} = \left(\frac{h_t - h_r}{h_t} \right) \times 100. \quad (5)$$

Results and Discussion

Microstructural characterization

SEM micrographs of the specimens after the heat treatments are shown in Figure 3. It can be seen that in both cases the microstructure consisted of a martensitic matrix with precipitated globular carbides. The application of the cryogenic treatment generated a strong reduction in the size of carbides and an increase in the amount of particles, changing the mean carbide diameter of 0.9 µm for CHT specimens to 0.4 µm in DCT samples. The volume fraction of carbides was estimated to be 16.8% in CHT specimens, whereas for the DCT ones it was 11.9%. Similar reductions of the carbide size were reported by Das and co-workers [3,36].

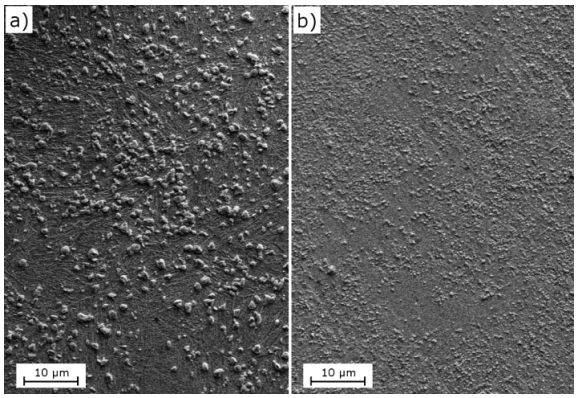

Figure 3: SEM image of a) CHT specimen and b) DCT specimen, showing a martenstic matrix with precipitated globular carbides.

Nanoindentation tests

A summary of the results from the nanoindentation tests performed with the Berkovich tip is shown in Table 2. It can be seen that the residual height (h_r) was smaller for DCT specimens at all penetration depths, meaning that they had a larger amount of elastic recovery during unloading also depicted by the higher values of the h_r/h_t ratios. The ANOVA test indicated that these differences were statistically significant. Furthermore, the ANOVA analysis of the maximum applied load (P_{max}) for each penetration depth has shown no statistically significant differences for both CHT and DCT specimens. According to Bolshakov and Pharr [37], the h_r/h_t ratios are in all cases at the limit of applicability of the O&P method, i.e., above ca. 0.7 in materials that develop pile-ups. The maximum penetration depth has been predefined by the displacement control condition, and the force required to reach each depth was the same for both groups of specimens. Hence, the DCT samples must have a higher elastic limit [38,39].

The aforementioned phenomenon can be seen more clearly from the analysis of the contact stiffness, as DCT specimens

Table 2: Summary of nanoindentation results.

penetration depth (nm)	residual height (nm)		maximum force (μN)		h_r/h_t		contact stiffness (μN/nm)	
	CHT	DCT	CHT	DCT	CHT	DCT	CHT	DCT
50	34.5 ± 0.9	32.6 ± 1.2	887 ± 51	877 ± 48	0.651	0.690	75.6 ± 1.8	65.1 ± 1.7
100	74.6 ± 1.7	71.8 ± 1.2	2122 ± 137	2153 ± 99	0.719	0.746	108.7 ± 2.3	87.9 ± 2.4
200	153.6 ± 1.9	145.0 ± 2.7	5788 ± 259	5983 ± 276	0.725	0.768	160.9 ± 2.4	126.9 ± 1.8

showed significantly smaller values of contact stiffness (S) at all penetration depths. If we assume that the elastic modulus does not change with the application of cryogenic treatments, then it follows from Equation 2 that the true contact area between the indenter and the specimen has to be smaller in the DCT samples. This smaller contact area can be accounted by a higher amount of elastic recovery (as evidenced by the residual height) and also by the formation of smaller pile-ups.

In order to characterize the resistance of the material to plastic deformation, the parameter H/E_r^2 has been calculated by two different approaches (Table 3). It can be seen that there is no significant difference between the methods, which could mean that pile-up is not so severe, at least at penetration depth of 50 and 100 nm. At 200 nm, pile-up influence shows a marked increase, as h_f/h_{max} is higher than 0.7. However, the values from Table 3 are useful for comparison purposes between CHT and DCT specimens. The values of H/E_r^2 for cryogenically treated specimens were ca. 30% higher than those of the conventionally treated samples at penetration depths of 50 and 100 nm, independently of the calculation method. At 200 nm, this difference is 56% when applying the O&P method and 67% with the J&O method. These results also support the hypothesis that the cryogenic treatment increased the elastic limit of the specimens.

The reduction of the carbide volume fraction in DCT specimens can be associated to a higher amount of undissolved carbon in the martensitic matrix. In addition, cryogenic treatments also increase residual stresses in the martensitic matrix, as we were able to measure in our previous work using X-ray diffractometry [10]. These residual stresses can be associated to a higher dislocation density, which in turn has been identified by Kehoe and Kelly [40] as the main factor affecting the strength of martensite materials with equal amounts of carbon. Due to the small scale of the test, the analysis primarily yields information regarding the metallic matrix. As carbides are much harder than martensite, it can be expected that they would sink into the matrix if they are hit by the diamond tip. As a result, the measured stiffness will be slightly higher than during indenting a "pure" matrix. The variations that we observe in the values of H/E_r^2 are then the result of hitting areas where the carbide is closer or further than in the other points.

With respect to the possible influence of the native oxide films, stainless steels develop oxide films of ca. 2 nm in thickness [41,42], thus its influence can be neglected as the penetration depths are much larger.

Nanoscratch tests

Prior to the execution of the nanoscratch tests, we performed indentations with the conical indenter (apex radius ca. 100 μm) at the same normal load (1000 μN) that we used in the wear cycles. In Figure 4 it can be seen that the elastic recoveries for all samples was above 85% and that there was no significant difference between CHT and DCT specimens. These high values of elastic recovery are useful in order to evaluate whether we are effectively removing material during the nanoscratch test or whether we are plastically deforming the surface.

Figure 5 shows the evolution of the wear coefficient during a complete run of the wear test. It can be seen that cryogenically treated specimens exhibited marginally lower wear rates during the initial stage of the tests.

Table 3: Comparison of the H/E_r^2 values obtained by the Oliver & Pharr and Joslin & Oliver methods.

penetration depth (nm)	H/E_r^2 (GPa^{-1} × 10^{-4})			
	Oliver & Pharr		Joslin & Oliver	
	CHT	DCT	CHT	DCT
50	2.12 ± 0.10	2.82 ± 0.19	1.98 ± 0.10	2.64 ± 0.18
100	2.45 ± 0.13	3.15 ± 0.16	2.29 ± 0.12	2.95 ± 0.15
200	3.14 ± 0.11	4.92 ± 0.24	2.85 ± 0.14	4.75 ± 0.26

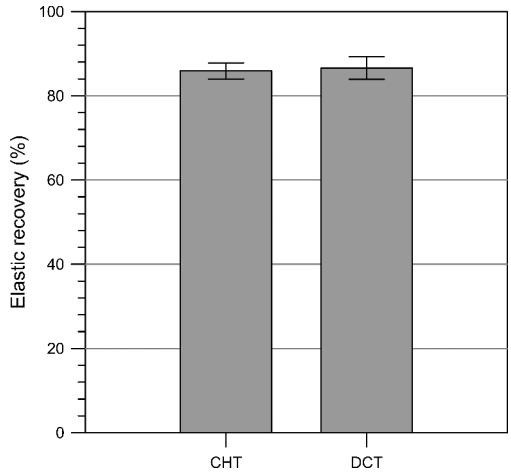

Figure 4: Elastic recovery values for nanoindentations performed with a conical indenter ($r \approx 100$ µm) at 1000 µN of normal load.

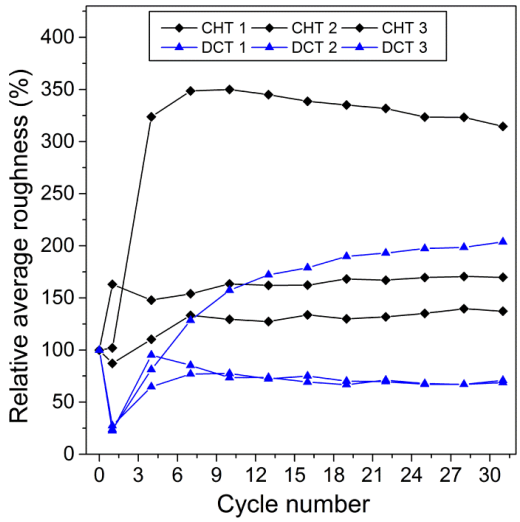

Figure 6: Evolution of the relative average roughness after each test cycle.

Cryogenically treated specimens had a lower amount of total wear (Figure 5b), although this difference was only marginal. Figure 6 shows the evolution of roughness for three complete test runs of each type of specimens. It can be seen that DCT specimens had a lower average roughness, and in two runs roughness reached a steady state after running-in, while for the CHT specimens, the first two runs showed an increasing trend and the third one had a marked increase (over 300%) from the initial roughness and a slight reduction afterwards. These differences in the roughness evolution could be associated to the modification of the elastic limit of the cryogenically treated specimens. Again, the effect of the oxide films can be neglected as they wear out after two or three cycles.

As a nanoscratch test is essentially an abrasion test using a single asperity, our results confirm that the increase in hardness shown by the DCT specimens led to a higher wear resistance following the classical approach of Rabinowicz [43].

Regarding the evolution of the friction coefficient (CoF), Figure 7 shows that it slightly diminished towards the end of the tests, mainly due to wear and deformation of asperities of the surface of the track (Figure 8) [44]. The level of friction reduction was between 2 and 5%. Similarly to the behavior of the wear coefficient, DCT specimens performed better than CHT samples. This difference was more pronounced during the

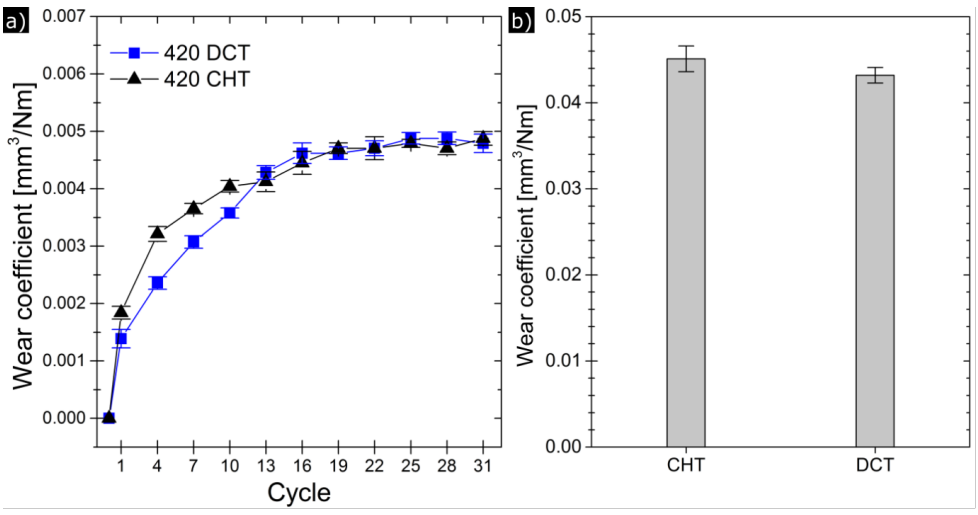

Figure 5: a) Evolution of wear coefficient during the tests at 1000 µN of applied normal load and b) cumulative wear coefficient.

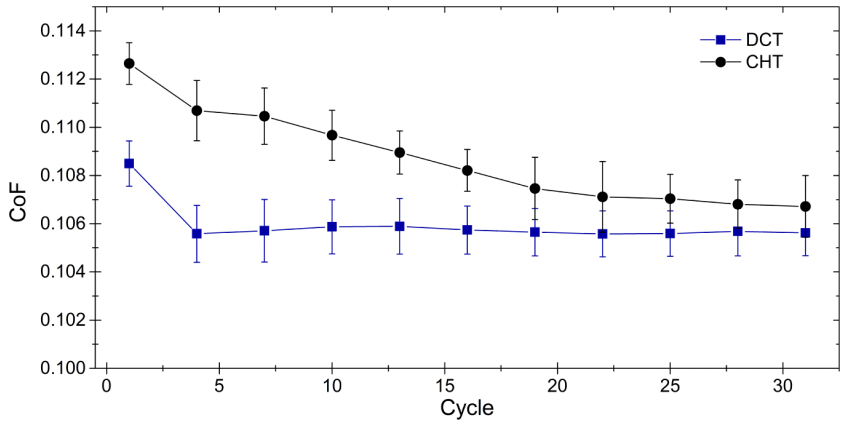

Figure 7: Evolution of the friction coefficient during the nanowear test.

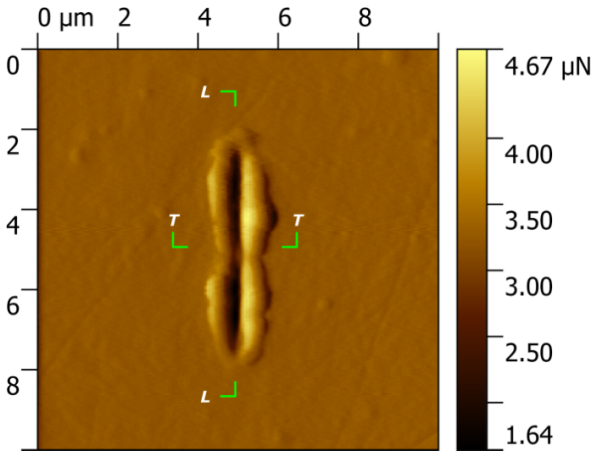

Figure 8: Scanning probe microscopy (SPM) image after 30 cycles of nanoscratch testing in a DCT specimen. The depth profiles below in Figure 9 were taken in the longitudinal (L–L) and transversal (T–T) directions.

initial passes of the test. However, the improvement of the friction behavior for DCT specimens should be considered marginal.

The evolution of the wear and friction coefficients (Figure 5 and Figure 7) shows that DCT specimens exhibit a marginally improved tribological behavior, i.e., less friction and wear than CHT specimens during the first passes of the diamond tip. We attribute this behavior mainly to the increased hardness and elastic limit of the martensitic matrix. Similarly, Xie et al. [45] has reported that a hardness increase implies a higher elastic shakedown limit of the material and a reduction of the friction coefficient.

Figure 8 shows a scanning probe microscopy (SPM) image of a DCT specimen after a nanoscratch test, where the formation of the wear track can be clearly seen. Material pile-up is visible at both sides of the trench, as well as at the entry and exit edges. The wear scar presents the typical features of an abrasion test performed in a ductile material.

Figure 9a presents the initial (black line) and the final (red line) longitudinal profiles of a DCT specimen, showing the formation of the trench. The total wear volume is the result of the combined adhesion, ploughing effect and cutting effects during the sliding process. The final profile of the scar reveals the probable presence of a subsuperficial carbide (Figure 9a), which did not wear as much as the metallic matrix due to its higher hardness. In the transversal profile (Figure 9b), material pile-up at the edges of the track can be clearly seen, in agreement with the plastic deformation observed in the nanoindentation tests.

It is interesting to compare the nanoscratch results with those from macroscopic tests reported by Prieto and Tuckart [11]. In that work, wear occurred mainly by delamination, driven by ratcheting, while in this present work wear is mainly abrasive. In [11], the smaller carbides in DCT specimens delayed the subsuperficial cracking due to a reduction in the stress concentration effect. Instead, in this present work wear tests were reciprocal, therefore ratcheting was not operative and the carbides played a secondary role in the wear response of the material. This was also a consequence of the scale of the wear tracks, which we infer were of the order of the distance between carbides.

The combination of nanoindentation and nanoscratch tests allowed us to have a better understanding of the role of the martensitic matrix and its contribution to the wear resistance of the material. This contribution could not be analyzed in the macroscopic tests performed in [11] due to the large scale of the tribological interactions and the type of sliding conditions.

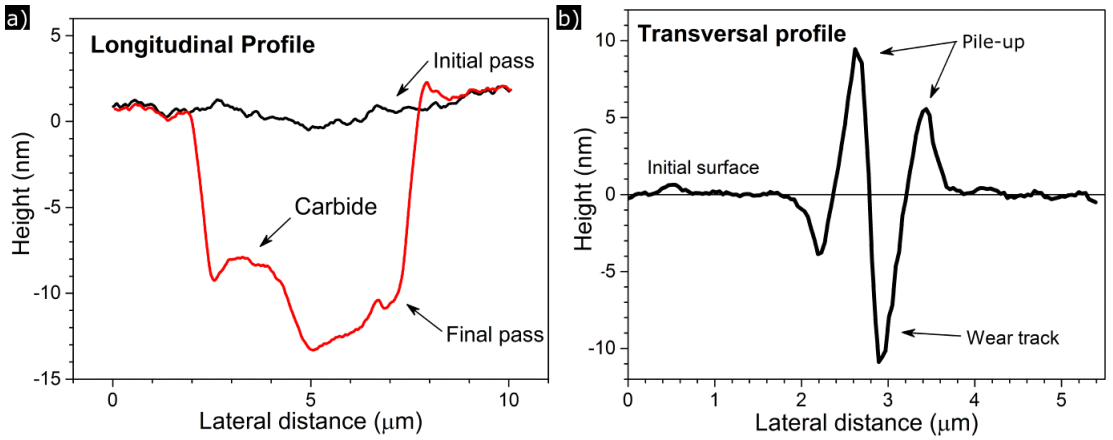

Figure 9: Depth profiles after a wear test in a DCT specimen in the a) longitudinal and b) transversal directions. The formation of the wear groove and the pile-ups around the track can be seen, as well as the probable revelation of a subsuperficial carbide.

Conclusion

Considering the results obtained from the study of the mechanical and tribological properties of a cryogenically treated martensitic AISI 420 stainless steel, we conclude that cryogenically treated specimens show a higher amount of undissolved carbon in the martensitic matrix, therefore leading to an increased hardness and elastic limit in comparison with the conventionally treated ones.

The carbide refinement developed in cryogenically treated specimens had a marginal contribution in preventing abrasive wear at the small scale of our test. Instead, we propose that the improved mechanical resistance of the cryogenically treated martensite was responsible for the reduction in friction and the marginal decrease in the wear coefficient.

Acknowledgments

G. Prieto and W. R. Tuckart would like to thank the Universidad Nacional del Sur and the Consejo Nacional del Investigaciones Científicas y Técnicas for the provision of funding (Grant PICT-0616-2013). K. D. Bakoglidis acknowledges financial support from VINN Excellence Center Functional Nanoscale Materials (FunMat, Grant #2005-02666). E. Broitman acknowledges the financial support from the Swedish Government Strategic Research Area in Materials Science on Functional Materials at Linköping University (Faculty Grant SFO-Mat-LiU No.2009-00971).

References

1. Barron, R. F. *Cryogenics* **1982,** *22,* 409–413. doi:10.1016/0011-2275(82)90085-6
2. Bensely, A.; Prabhakaran, A.; Mohan Lal, D.; Nagarajan, G. *Cryogenics* **2005,** *45,* 747–754. doi:10.1016/j.cryogenics.2005.10.004
3. Das, D.; Dutta, A. K.; Ray, K. K. *Mater. Sci. Eng., A* **2010,** *527,* 2182–2193. doi:10.1016/j.msea.2009.10.070
4. Leskovšek, V.; Kalin, M.; Vižintin, J. *Vacuum* **2006,** *80,* 507–518. doi:10.1016/j.vacuum.2005.08.023
5. Meng, F.; Tagashira, K.; Sohma, H. *Scr. Metall. Mater.* **1994,** *31,* 865–868. doi:10.1016/0956-716X(94)90493-6
6. Collins, D. N.; Dormer, J. *Int. Heat Treat. Surf. Eng.* **2008,** *2,* 150–154. doi:10.1179/174951508X446376
7. Xie, C.-h.; Huang, J.-w.; Tang, Y.-f.; Gu, L.-n. *Trans. Nonferrous Met. Soc. China* **2015,** *25,* 3023–3028. doi:10.1016/S1003-6326(15)63929-2
8. Tyshchenko, A. I.; Theisen, W.; Oppenkowski, A.; Siebert, S.; Razumov, O. N.; Skoblik, A. P.; Sirosh, V. A.; Petrov, Yu. N.; Gavriljuk, V. G. *Mater. Sci. Eng., A* **2010,** *527,* 7027–7039. doi:10.1016/j.msea.2010.07.056
9. Gavriljuk, V. G.; Theisen, W.; Sirosh, V. V.; Polshin, E. V.; Kortmann, A.; Mogilny, G. S.; Petrov, Yu. N.; Tarusin, Ye. V. *Acta Mater.* **2013,** *61,* 1705–1715. doi:10.1016/j.actamat.2012.11.045
10. Prieto, G.; Perez Ipiña, J. E.; Tuckart, W. R. *Mater. Sci. Eng., A* **2014,** *605,* 236–243. doi:10.1016/j.msea.2014.03.059
11. Prieto, G.; Tuckart, W. R. Wear behavior of cryogenically treated AISI 420 martensitic stainless steel. In *VIII Iberian Conference on Tribology,* Cartagena, Spain, June 18–19, 2015; Ballest Jiménez, A. E.; Rodríguez Espinosa, T.; Serrano Saurín, N.; Pardilla Arias, J.; Olivares Bermúdez, M. D., Eds.; Universidad Politécnica de Cartagena: Spain, 2015; pp 68–75.
12. Prieto, G.; Tuckart, W. R.; Ipiña, J. E. P. *Mater. Technol. (Ljubljana, Slovenia)* **2017,** *51,* 591–596.
13. Broitman, E.; Flores-Ruiz, F. J. *J. Vac. Sci. Technol., A* **2015,** *33,* 043201. doi:10.1116/1.4921584
14. Bhushan, B. *Wear* **2005,** *259,* 1507–1531. doi:10.1016/j.wear.2005.01.010
15. Broitman, E.; Flores-Ruiz, F. J.; Di Giulio, M.; Gontad, F.; Lorusso, A.; Perrone, A. *J. Vac. Sci. Technol., A* **2016,** *34,* 21505. doi:10.1116/1.4936080
16. Charitidis, C. A. *Int. J. Refract. Met. Hard Mater.* **2010,** *28,* 51–70. doi:10.1016/j.ijrmhm.2009.08.003

17. Broitman, E.; Hultman, L. Advanced carbon-based coatings. In *Comprehensive Materials Processing;* Hashmi, S.; Batalha, G. F.; Van Tyne, C. J.; Yilbas, B., Eds.; Elsevier: Oxford, United Kingdom, 2014; pp 389–412. doi:10.1016/B978-0-08-096532-1.00428-3
18. Bakoglidis, K. D.; Glenat, H.; Greczynski, G.; Schmidt, S.; Grillo, S.; Hultman, L.; Broitman, E. *Wear* **2017,** *370–371,* 1–8. doi:10.1016/j.wear.2016.11.005
19. Wang, X. Y.; Li, D. Y. *Wear* **2003,** *255,* 836–845. doi:10.1016/S0043-1648(03)00055-3
20. Degiampietro, K.; Colaço, R. *Wear* **2007,** *263,* 1579–1584. doi:10.1016/j.wear.2006.10.020
21. Colaço, R. *Wear* **2009,** *267,* 1772–1776. doi:10.1016/j.wear.2008.12.024
22. Graça, S.; Vilar, R.; Colaço, R. *Wear* **2010,** *268,* 931–938. doi:10.1016/j.wear.2009.12.019
23. Lafaye, S.; Troyon, M. *Wear* **2006,** *261,* 905–913. doi:10.1016/j.wear.2006.01.036
24. Gåård, A.; Karlsson, P.; Krakhmalev, P.; Broitman, E. *Adv. Mater. Res.* **2015,** *1119,* 70–74. doi:10.4028/www.scientific.net/AMR.1119.70
25. Underwood, E. E. *Quantitative stereology;* Addison-Wesley Pub. Co.: Boston, MA, U.S.A., 1970.
26. Oliver, W. C.; Pharr, G. M. *J. Mater. Res.* **1992,** *7,* 1564–1583. doi:10.1557/JMR.1992.1564
27. Sneddon, I. N. *Int. J. Eng. Sci.* **1965,** *3,* 47–57. doi:10.1016/0020-7225(65)90019-4
28. *INFOSTAT,* version 2011e; Universidad Nacional de Córdoba: Córdoba, Argentina, 2012.
29. Han, C.-F.; Lin, J.-F. *IEEE Trans. Nanotechnol.* **2008,** *7,* 256–265. doi:10.1109/TNANO.2008.917853
30. Mirshams, R. A.; Srivastava, A. K. *Adv. Mater. Res.* **2013,** *853,* 143–150. doi:10.4028/www.scientific.net/AMR.853.143
31. Cabibbo, M.; Ricci, P. *Metall. Mater. Trans. A* **2013,** *44,* 531–543. doi:10.1007/s11661-012-1375-2
32. Joslin, D. L.; Oliver, W. C. *J. Mater. Res.* **1990,** *5,* 123–126. doi:10.1557/JMR.1990.0123
33. Page, T. F.; Pharr, G. M.; Hay, J. C.; Oliver, W. C.; Lucas, B. N.; Herbert, E.; Riester, L. *Mater. Res. Soc. Symp. Proc.* **1998,** *522,* 53. doi:10.1557/PROC-522-53
34. Saha, R.; Nix, W. D. *Acta Mater.* **2002,** *50,* 23–38. doi:10.1016/S1359-6454(01)00328-7
35. Chen, Z.; Gandhi, U.; Lee, J.; Wagoner, R. H. *J. Mater. Process. Technol.* **2016,** *227,* 227–243. doi:10.1016/j.jmatprotec.2015.08.024
36. Das, D.; Ray, K. K. *Mater. Sci. Eng., A* **2012,** *541,* 45–60. doi:10.1016/j.msea.2012.01.130
37. Bolshakov, A.; Pharr, G. M. *J. Mater. Res.* **1998,** *13,* 1049–1058. doi:10.1557/JMR.1998.0146
38. Cheng, Y. T.; Cheng, C. M. *Polym. Prepr. (Am. Chem. Soc., Div. Polym. Chem.)* **2000,** *41,* 1476–1477.
39. Cheng, Y.-T.; Cheng, C.-M. *Mater. Sci. Eng., R* **2004,** *44,* 91–149. doi:10.1016/j.mser.2004.05.001
40. Kehoe, M.; Kelly, P. M. *Scr. Metall.* **1970,** *4,* 473–476. doi:10.1016/0036-9748(70)90088-8
41. Marcus, P.; Grimal, J. M. *Corros. Sci.* **1992,** *33,* 805–814. doi:10.1016/0010-938X(92)90113-H
42. Maurice, V.; Yang, W. P.; Marcus, P. *J. Electrochem. Soc.* **1998,** *145,* 909–920. doi:10.1149/1.1838366
43. Rabinowicz, E. *Friction and wear of materials;* Wiley: Hoboken, NJ, U.S.A., 1995.
44. Holmberg, K.; Ronkainen, H.; Laukkanen, A.; Wallin, K. *Surf. Coat. Technol.* **2007,** *202,* 1034–1049. doi:10.1016/j.surfcoat.2007.07.105
45. Xie, Y.; Williams, J. A. *Wear* **1996,** *196,* 21–34. doi:10.1016/0043-1648(95)06830-9

License and Terms

BEILSTEIN JOURNAL OF NANOTECHNOLOGY

Stick–slip boundary friction mode as a second-order phase transition with an inhomogeneous distribution of elastic stress in the contact area

Iakov A. Lyashenko*[1,2], Vadym N. Borysiuk[1,2] and Valentin L. Popov[1,3,4]

Full Research Paper

Open Access

Address:
[1]Technische Universität Berlin, 10623 Berlin, Germany, [2]Sumy State University, 40007 Sumy, Ukraine, [3]National Research Tomsk State University, 634050 Tomsk, Russia, and [4]National Research Tomsk Polytechnic University, 634050 Tomsk, Russia

Email:
Iakov A. Lyashenko* - nabla04@ukr.net

* Corresponding author

Keywords:
boundary friction; dimensionality reduction; numerical simulation; shear stress and strain; stick–slip motion; tribology

Beilstein J. Nanotechnol. **2017,** *8,* 1889–1896.
doi:10.3762/bjnano.8.189

Received: 23 April 2017
Accepted: 16 August 2017
Published: 08 September 2017

This article is part of the Thematic Series "Nanotribology".

Guest Editor: E. Gnecco

Abstract

This article presents an investigation of the dynamical contact between two atomically flat surfaces separated by an ultrathin lubricant film. Using a thermodynamic approach we describe the second-order phase transition between two structural states of the lubricant which leads to the stick–slip mode of boundary friction. An analytical description and numerical simulation with radial distributions of the order parameter, stress and strain were performed to investigate the spatial inhomogeneity. It is shown that in the case when the driving device is connected to the upper part of the friction block through an elastic spring, the frequency of the melting/solidification phase transitions increases with time.

Introduction

The boundary friction mode occurs in tribological systems when the thickness of the lubricant layer separating two contacting surfaces is significantly smaller than the typical size of the surface roughness. At such a system configuration, the lateral motion of the friction surface is followed by a contact interaction between the asperities. A specific case of boundary friction is friction between two atomically flat surfaces separated by a layer of lubricant with thickness of a few atomic diameters [1,2], or even monolayers [3]. Such type of friction mode plays an important role in applied mechanics as it often occurs in nanometer-sized tribological systems that are commonly used in aerospace technologies, computer memory devices and electronic positioning systems [4]. Various experimental research has shown that in the boundary friction mode, the lubricant can undergo periodic phase transitions between the structure states which may lead to the stick–slip motion with non-monotonic time dependence of the friction force [1,2,4,5]. Stick–slip motion is known to cause fast destruction of the contact parts of microscopic devices, which is why it receives significant attention from the scientists and engineers.

The boundary friction mode can be described within the framework of several theoretical models [6-12] where lubricant melting is described either as a first-order [8,9], or a second-order [10,11] phase transition. It is worth mentioning that in three-dimensional systems, melting always appears as a first-order phase transition [13], while in the systems with confined lubricant, second-order phase transitions were observed in both numerical [14-16] and theoretical [10] studies. Moreover, recent experimental investigations [5] have shown that melting as a first-order phase transition is not possible for boundary lubricants consisting of spherically shaped molecules. However for the polymeric lubricant materials, first-order phase transition may occur [17].

In our previous work [18] we studied the stick–slip boundary friction mode considering lubricant melting as both first and second-order phase transitions with an inhomogeneous distribution of elastic stress in a contact area. This obtained results have shown that the melting begins at the edge of a contact area and propagates to its center, and the wave of melting is followed by a wave of recrystallization. Such inhomogeneous behavior was also observed in experiments [19,20]. However, in [18] we consider the motion of the friction surfaces with constant relative velocity, while in the real experiments, the driving device is applied to the upper surface through the elastic spring [1,4,6]. In such an experimental configuration, the velocities of the friction surface and driving device are not equal, which significantly affects the friction mode. In the present paper, we study this situation using a previously developed technique [18]. In our research we use a thermodynamic approach, as proposed in [10], which gives relevant physical results. The dependence of the order parameter on elastic strain in the lubricant layer, obtained using the above-mentioned thermodynamic approach, agrees with the similar data obtained from computational studies [14-16]. Moreover, strain–stress curves obtained in [10] are confirmed by experimental data [21].

Results and Discussion

We consider a simplified case where the properties of the lubricant are independent of pressure and its behavior can be described within a thermodynamic approach [10]. Assuming that the melting of the lubricant develops as a second-order phase transition (which follows from the computer simulations [14,15] and experimental investigations [5]), the free-energy density can be written in the form [10]:

$$f = \alpha\left(T - T_{\mathrm{c}}\right)\varphi^2 + \frac{a}{2}\varphi^2\varepsilon_{\mathrm{el}}^2 + \frac{b}{4}\varphi^4 \qquad (1)$$

where T is the temperature of the lubricant; T_{c} is the critical temperature; $\varepsilon_{\mathrm{el}}$ is the shear component of the elastic stress; α, a and b are positive constants. The order parameter φ is a periodic component of the microscopic density of the material: in a solid-like state of the lubricant $\varphi > 0$, while in a liquid-like state $\varphi = 0$.

Using Equation 1 and the definition $\tau = \partial f / \partial\varepsilon_{\mathrm{el}}$ [10,22] shear stresses that appear in the lubricant can be written in the form:

$$\tau = a\varphi^2\varepsilon_{\mathrm{el}} = \mu\varepsilon_{\mathrm{el}} \qquad (2)$$

where we have introduced the shear modulus of the lubricant μ, that takes nonzero values only in solid-like states. The stationary values of the order parameter φ_0 can be estimated from the condition $\partial f / \partial\varphi = 0$ in the following form:

$$\varphi_0 = \sqrt{\frac{2\alpha(T_{\mathrm{c}} - T) - a\varepsilon_{\mathrm{el}}^2}{b}}. \qquad (3)$$

According to Equation 3, the stationary value of the order parameter φ_0 decreases with the growth of both temperature T and elastic strain $\varepsilon_{\mathrm{el}}$. When the strain exceeds a critical value

$$\varepsilon_{\mathrm{el}} > \varepsilon_{\mathrm{el,c}} = \sqrt{\frac{2\alpha(T_{\mathrm{c}} - T)}{a}}, \qquad (4)$$

stationary values of the order parameter φ_0 and shear modulus μ_0 (according to Equation 2) equal to zero and the lubricant melts. In the case $\varepsilon_{\mathrm{el}} < \varepsilon_{\mathrm{el,c}}$ as defined by Equation 4, the stationary stress in the lubricant can be expressed as

$$\tau_0 = \frac{a\varepsilon_{\mathrm{el}}\left[2\alpha(T_{\mathrm{c}} - T) - a\varepsilon_{\mathrm{el}}^2\right]}{b}. \qquad (5)$$

Equation 5 describes the strain–stress curve defined by the expansion parameters. However, it is more convenient to use experimentally observable values of the maximum stress $\tau^{\max}$ and strain $\varepsilon_{\mathrm{el}}^{\max}$. The relation between the expansion parameters α, a and b and values of $\tau^{\max}$ and $\varepsilon_{\mathrm{el}}^{\max}$ can be estimated from Equation 5 in the following form [18]:

$$\frac{4\alpha(T_{\mathrm{c}} - T)a}{3b} = \frac{\tau^{\max}}{\varepsilon_{\mathrm{el}}^{\max}}, \quad \frac{2a^2}{b} = \frac{\tau^{\max}}{\left(\varepsilon_{\mathrm{el}}^{\max}\right)^3}. \qquad (6)$$

To study the kinetics of the lubricant we employed the Ginzburg–Landau–Khalatnikov evolutionary equation for the order parameter in the form:

$$\frac{\partial \varphi}{\partial t} = -\gamma \frac{\partial f}{\partial \varphi} + \xi(t) \tag{7}$$

where γ is the kinetic parameter that defines the inertial properties of the system, ξ(*t*) represents random processes in the heat fluctuation of a small amplitude which cannot significantly affect the system behavior. Nevertheless, it is necessary to take them into account due to the peculiarities of the further numerical calculations [23]. In explicit form, Equation 7 can be written as

$$\dot{\varphi} = -\gamma\varphi\left(2\alpha(T - T_c) + a\varepsilon_{el}^2 + b\varphi^2\right) + \xi(t). \tag{8}$$

The thermodynamic approach described above can be used to investigate the boundary friction mode with different geometrical shapes of the contact area. In the present work we consider a tribological system as shown in Figure 1.

As can be seen from Figure 1, a cylindrically shaped flat-ended stamp with radius a_0 is in contact with a lower surface through the lubricant layer with thickness h_0. The materials of the top and bottom surfaces have the shear moduli G_1,G_2 and Poisson ratios ν_1,ν_2, respectively. This configuration can be reduced to the contact of a rigid stamp with half-space characterized by an effective shear modulus [24]

$$G^* = \left(\frac{2-\nu_1}{4G_1} + \frac{2-\nu_2}{4G_2}\right)^{-1}. \tag{9}$$

Assuming that the upper stamp has mass *m*, and the coordinate of the stamp center is *X*, let us consider the situation where the stamp is driven by a spring with the constant stiffness *K*. The free end of the spring moves with a constant velocity V_0. Thus, the equation of motion for the upper friction block with mass *m* has the following form [4]:

$$m\ddot{X} = K\left(V_0 t - X\right) - F_x \tag{10}$$

where *t* is the time, and F_x is the friction force between two contacting surfaces. The magnitude of the friction force F_x depends on the properties of the system shown in Figure 1.

As the upper stamp moves, local displacements of its surface in the contact area with a lubricant are defined by a radial distribution $u_x^{(0)}(r)$, where *r* is the radial coordinate. Denoting the corresponding local displacements of a bottom surface as $u_x^{(3D)}(r)$, we can define the local shear strain in the lubricant layer as a function of the radial coordinate *r*:

$$\varepsilon(r) = \frac{u_x^{(0)}(r) - u_x^{(3D)}(r)}{h_0}. \tag{11}$$

Knowing the distribution of strain ε(*r*) and order parameter φ(*r*) we can obtain the distribution of the stress in the lubricant according to Equation 2:

$$\tau(r) = a\varepsilon_{el}(r)[\varphi(r)]^2. \tag{12}$$

The distribution of the displacements $u_x^{(3D)}(r)$ in Equation 11 is defined by shear stress. In our further investigations we will use the method of dimensionality reduction (MDR) [24-26], which allows us to reduce the three-dimensional problem (with general coordinate *r*) to an equivalent one-dimensional (coordinate *x*) with a possible reverse transition.

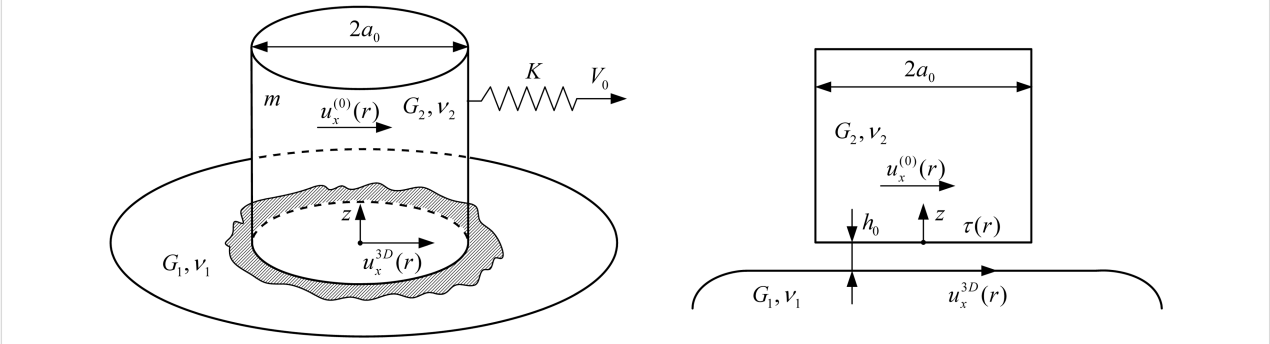

Figure 1: Geometrical scheme of the system under investigation. Stamp of a cylindrical shape with radius a_0, made of material with shear modulus of G_2 and Poisson ratio ν_2, placed over the material with elastic parameters G_1,ν_1. Upper and lower friction blocks are separated by a layer of lubricant with thickness h_0.

Within the MDR technique, a one-dimensional distribution of the force density can be defined from the known distribution $\tau(r)$ as:

$$q(x) = 2\int_{x}^{a_0} \frac{r\tau(r)\mathrm{d}r}{\sqrt{r^2 - x^2}}. \quad (13)$$

From the obtained $q(x)$, the one-dimensional distribution of the displacements $u_x^{(1D)}(r)$ can be calculated as:

$$u_x^{(1D)}(x) = \frac{q(x)}{G^*} \quad (14)$$

and the distribution $u_x^{(3D)}(r)$ can be obtained from the equation:

$$u_x^{(3D)}(r) = \frac{2}{\pi}\int_{0}^{r} \frac{u_x^{(1D)}(x)\mathrm{d}x}{\sqrt{r^2 - x^2}}. \quad (15)$$

The elastic component of the friction force in the system can be defined in two ways (in one-dimensional and three-dimensional interpretations):

$$F_x = 2\int_{0}^{a_0} q(x)\,\mathrm{d}x = 2\pi\int_{0}^{a_0} \tau(r) r\,\mathrm{d}r. \quad (16)$$

The aim of the present work is to take into account the elastic properties of the contacting materials in simulation of the kinetics of the boundary friction in the system shown in Figure 1. Let us introduce the brief algorithm of the simulation scheme. First, we need to set the initial distributions $u_x^{(0)}(r) = 0$ and $u_x^{(3D)}(r) = 0$. After that, the procedure described in Equation 11–Equation 15 is repeated in loops and for every value of $\varepsilon(r)$ a related value of the order parameter is calculated from Equation 8.

The displacement of upper stamp X can be estimated from the numerical solution of Equation 10 with friction force F_x calculated from Equation 16. With incremental growth of the upper friction block, coordinate X values of the distribution $u_x^{(0)}(r)$ are also incremented by the same magnitude. Thus, at the beginning of motion, $u_x^{(0)}(r,t) \equiv X(t)$. However, $u_x^{(0)}(r)$ is set to zero when the lubricant melts (in numerical scheme $u_x^{(0)}(r_i) = 0$ when $\varphi(r_i) < 0.01$ [18]).

In numerical calculations integrals of Equation 13, Equation 15 and Equation 16 were replaced by corresponding sums, while coordinates x and r were divided into N segments. All calculated distributions depending on radius r (or coordinate x), were computed at the points $r_i = ia_0 / N$ ($x_i = ia_0 / N$), where $i \in [0, N-1]$. In our simulation we set the time step to be $\Delta t = 10^{-8}$ s and number of segments $N = 2000$.

Figure 2 shows the results of a numerical simulation of the shifting of the free end of the spring with constant velocity V_0 at constant system parameters.

An analogous dependence was described in [18], where the motion of a stamp with constant velocity was considered. Such configuration relates to the case where the spring, shown in Figure 1, is replaced by the rigid coupler. However, in real ex-

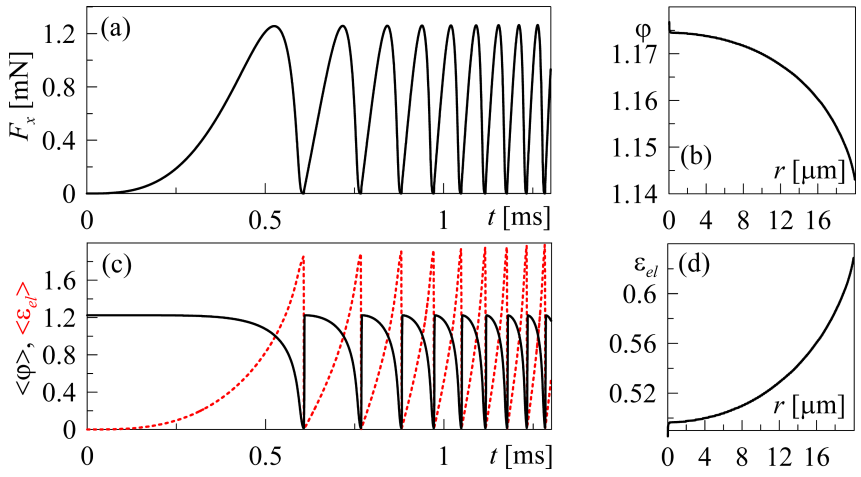

Figure 2: (a) Kinetic dependence of the friction force $F_x(t)$, calculated at parameters $\tau^{max} = 10^6$ Pa, $\varepsilon_{el}^{max} = 1.0$, $a = 10^6$ Pa, $h_0 = 10^{-7}$ m, $\gamma = 10$ (Pa·s)$^{-1}$, $a_0 = 2{\cdot}10^{-5}$ m, $G^* = 10^9$ Pa, $K = 500$ N/m, $m = 0.1$ kg, $V_0 = 1$ m/s. (b) Spatial distribution of the order parameter $\varphi(r)$ in the moment of time $t = 1.3$ ms, related to final point of the dependence shown in Figure 2a. (c) Time dependence of the mean values of the order parameter <φ> (solid line) and elastic strain <ε_{el}> (dashed line). (d) Spatial distribution of the elastic strain $\varepsilon_{el}(r)$ at $t = 1.3$ ms.

periments, the spring (finite stiffness) between the stamp and the driving device always exists.

The dependence shown in Figure 2 allows us to conclude that the stick–slip mode, with increasing frequency of the melting/solidification phase transitions, is established in the system. The growth of the frequency is caused by the increasing tension of the driving spring $\Delta X = V_0 t - X$ and the elastic force $F_u = K(V_0 t - X)$. The shear velocity of the upper stamp $V = \dot{X}$ also increases according to Equation 10, while the time interval, during which the elastic stress ε_{el} exceeds the critical value, is reduced.

As it is follows from Figure 2b,d, melting of the lubricant occurs at the edge of the contact area and propagates to the center; this situation was observed earlier in theoretical [18,27] and experimental [19] research. It is worth mentioning that before the first melting, the dependencies $F_x(t)$, $\langle\varphi\rangle(t)$ and $\langle\varepsilon_{el}\rangle(t)$ show the transition mode where monotonic growth of the friction force F_x and mean value of elastic strain $\langle\varepsilon_{el}\rangle$ as well as $\langle\varphi\rangle$ are significantly slower. The corresponding time interval from the beginning of motion to the first melting is the largest due to the presence of the spring between the stamp and driving device [4]. Such a transition mode was not observed in [18] as the stamp was moving with constant velocity V from the very beginning of motion.

Additional time dependence of the order parameter $\varphi(t)$ obtained for different values of the radial coordinate r is shown in Figure 3.

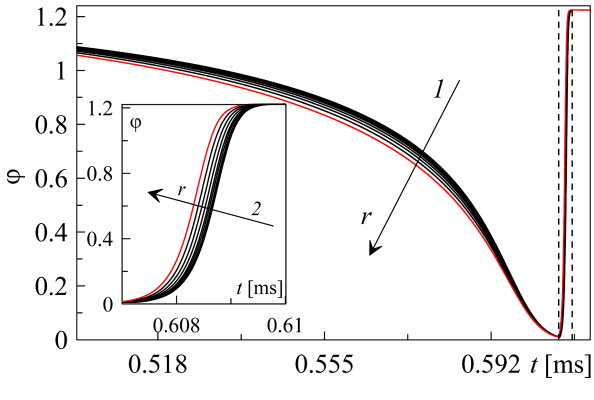

Figure 3: (a) Time dependence of the order parameter $\varphi(t)$, calculated using the same parameters as in Figure 2 and corresponding to the melting process (arrow 1) before the first dashed line and to the recrystallization process (arrow 2) after the first dashed line for different values of the radial coordinate r. Arrows show the increment of a radial coordinate r from 2 to 18 μm, with a step of 2 μm. Inset shows the time interval between two dashed lines.

As it can be seen from Figure 3, melting begins at the edge of the contact area and is immediately followed by recrystallization. We also conclude that the inhomogeneous distribution of the parameters weakly affects the behavior of the considered tribological system in contrast to the case of a first-order phase transition, where the influence of inhomogeneity is significantly stronger [18].

The developed theoretical model of the boundary friction allows investigating of the influence of the temperature of the lubricant on the melting process. It is worth mentioning that the influence of the temperature was studied in a previous work [18] for the case where the stamp was moving with a constant velocity, and here we will discuss an analogous investigation for the system with the spring. As the coefficient

$$A = \frac{2\alpha(T_c - T)a}{b} \tag{17}$$

is the only parameter in the model that depends on the temperature T, the variations of this coefficient can be considered as variations of the temperature of the lubricant. As it follows from the definition, the coefficient A decreases with temperature increase. The dependence in Figure 2 is obtained using the parameters $\tau^{max} = 10^6$ Pa and $\varepsilon_{el}^{max} = 1.0$, which corresponds to the value of $A = 1.5 \cdot 10^6$ Pa according to Equation 6. Figure 4 shows the time dependence of the friction force with monotonically decreasing coefficient A according to the relaxation law

$$A = A_0 \exp\left(-t / \tilde{t}\right) \tag{18}$$

where A_0 is the initial value of coefficient A at time $t = 0$, while $\tilde{t}$ is the relaxation time. Equation 18 relates to the increase of the lubricant temperature.

The temperature of the lubricant can vary during the natural heat exchange with the environment (friction surfaces are considered as a thermostat) [28]. As it follows from Figure 4, the higher temperature of the lubricant leads to the reduced amplitude of the friction force, elastic stress and order parameter, which was previously observed in [18]. However, in the considered case, the frequency of the phase transitions increase with time due to the presence of the spring, as shown in Figure 1. Complete melting of the lubricant occurs at $A = 2\alpha(T_c - T)a / b \leq 0$ (not shown in the figure) and is followed by a sliding mode with zero friction force $F_x = 0$ (only the elastic component of the friction force is considered within the proposed model).

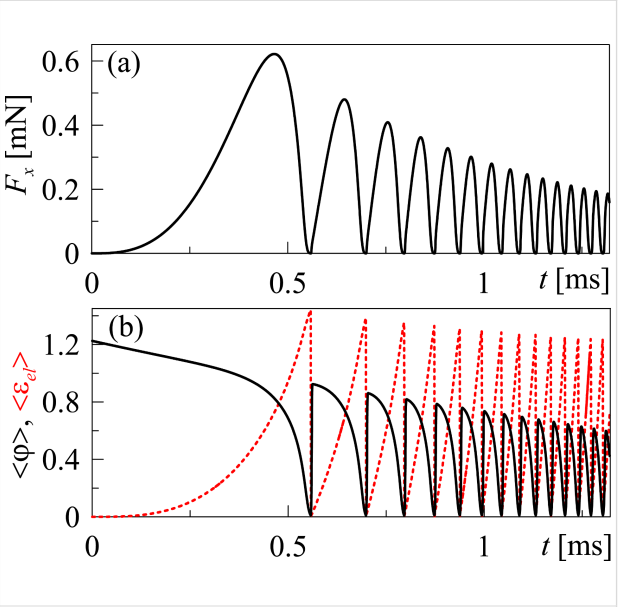

Figure 4: (a) Time dependence of the friction force F_x (Equation 16) using the parameters of Figure 2 and an increasing temperature according to Equation 18 using the parameters $A_0 = 1.5 \cdot 10^6$ Pa and $\tilde{t} = 10^{-3}$s. (b) Mean values of the order parameter <φ> and elastic strain <ε_{el}> are according to the parameters of Figure 4a.

Let us note that all presented dependencies relate to the particular situation where elastic stress increases according to Equation 11. However, in various experimental and theoretical studies, the boundary friction mode develops through an alternative mechanism where elastic stress, which cause the melting of a lubricant, can also exist in a liquid-like state [4,9,23]. At these conditions of time dependence, the friction force has a saw-like form and melting of the lubricant occurs when the shear velocity V exceeds some critical value. After the lubricant is melted, the elastic friction force becomes equal to zero, i.e. $F_x = 0$.

In the proposed model, we consider a quasi-static case where the elastic strain is defined by the displacement of the friction surfaces (see Equation 11) instead of the shear velocity V. Moreover, in the case of quasi-static contact, the viscous friction force is not considered, while in the standard dynamic model, it plays significant role [9]. Note however, that in most cases, the boundary lubricant layers will exhibit non-Newtonian behavior, so obtaining the dependence of viscous friction force on shear velocity may represent another difficult challenge [29]. Thus, in our model, the increase in the shear velocity V causes the increase in the frequency of phase transitions, and a critical value of V related to the complete melting of the lubricant is not observed. However, it is worth mentioning that the developed approach allows us to investigate the physical processes directly in the contact area, which is not possible within standard models.

The dependence of the friction force F_x on the coordinate of the upper friction block X as shown in Figure 5 corresponds to the data from Figure 2a and Figure 4a.

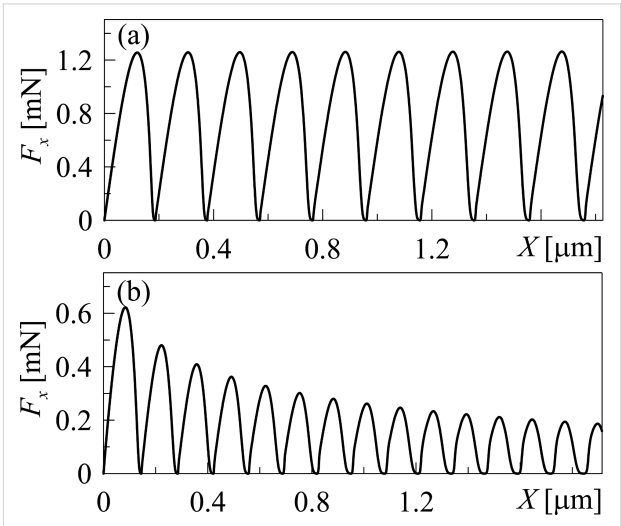

Figure 5: (a) Dependence of the friction force F_x on the stamp coordinate X (upper friction surface), corresponding to Figure 2a. (b) Dependence of the friction force F_x on the stamp coordinate X, corresponding to Figure 4a.

As it can be seen from Figure 5, $F_x(X)$ is periodical (with damping oscillations in the second case, as the amplitude of the friction force decreases in time due to the heating of the lubricant). The presented dependencies have a regular form in contrast to the data in Figure 2 and Figure 4, where the frequency of the phase transitions increases with time. Different forms of the obtained dependencies can be explained as follows. Let us recall that in our simulations we introduced the constant velocity of the free edge of the spring V_0 (see Figure 1). The velocity of the stamp center $V = \dot{X}$ is calculated from Equation 10 and does not coincide with the velocity V_0 mostly due to the presence of the friction force F_x (Equation 16). After the motion has begun, the tension of the spring and related growth of the elastic force causes the growth of the upper stamp velocity V. The lubricant melts in certain regions of the contact area where elastic stress, $\varepsilon_{el}(r)$, exceed a critical value, $\varepsilon_{el,c}$ (Equation 4). As the velocity of the upper stamp V grows, the time needed for the elastic stress to reach the critical value $\varepsilon_{el,c}$ decreases. Thus, the frequency of the phase transitions in Figure 2 and Figure 4 increases in time. However, strains (Equation 11) are determined by the magnitude of the displacement of the upper stamp over the bottom surface after another melting and subsequent solidification (when the lubricant solidifies after melting, strain is equal to zero for the subsequent growth according to Equation 11). Thus, the upper stamp, after another solidification of the lubricant, must pass approximately the same distance before the next melting, as is depicted in

Figure 5. This situation confirms the assumption that the frequency of the phase transitions increases (as it is shown in Figure 2 and Figure 4) due to the increase in the strain rate.

Conclusion

We have presented the dynamical simulation of the boundary friction between a cylindrically shaped stamp and a flat surface. Using the method of dimensionality reduction (MDR) we have studied the stick–slip friction mode that occurs in the tribological system under shear deformation. The MDR approach allowed us to describe the situation in which elastic stress, strain and order parameter are spatially distributed within contact area. The established stick–slip mode is characterized by continuous phase transitions between solid-like and liquid-like states of the lubricant, which were described as the second-order phase transitions between kinetic states of friction. Within the performed numerical simulation it is shown that an increase of the lubricant temperature leads to smaller amplitudes of the friction force, elastic stress and order parameter, while the frequency of phase transitions increases due to the presence of the spring. It is worth mentioning that the spatial distribution of elastic stress considered in the presented study will always occur in tribological systems with analogous geometrical shape of the contact area; thus, the developed approach can be an additional tool in various experimental investigations for contact problems of this type.

Acknowledgements

This work was supported in part by Tomsk State University, Academic D.I. Mendeleev Fund Program and the Deutsche Forschungsgemeinschaft. I.A.L. and V.N.B. are grateful to the Ministry of Education and Science of Ukraine for financial support under the project for young scientists “Thermodynamic theory of the phase transitions between structural states of the boundary lubricant with spatial inhomogeneity” (Project No. 0116U006818).

References

1. Zhang, J.; Meng, Y. *Friction* **2015,** *3,* 115–147. doi:10.1007/s40544-015-0084-4
2. Krim, J. *Adv. Phys.* **2012,** *61,* 155–323. doi:10.1080/00018732.2012.706401
3. Bruschi, L.; Fois, G.; Pontarollo, A.; Mistura, G.; Torre, F.; Buatier de Mongeot, C.; Borango, R.; Buzio, R.; Valbusa, U. *Phys. Rev. Lett.* **2006,** *96,* No. 216101. doi:10.1103/PhysRevLett.96.216101
4. Yoshizawa, H.; Israelachvili, J. *J. Phys. Chem.* **1993,** *97,* 11300–11313. doi:10.1021/j100145a031
5. Kienle, D. F.; Kuhl, T. L. *Phys. Rev. Lett.* **2016,** *117,* No. 036101. doi:10.1103/PhysRevLett.117.036101
6. Carlson, J. M.; Batista, A. A. *Phys. Rev. E* **1996,** *53,* 4153–4165. doi:10.1103/PhysRevE.53.4153
7. Filippov, A. E.; Klafter, J.; Urbakh, M. *Phys. Rev. Lett.* **2004,** *92,* No. 135503. doi:10.1103/PhysRevLett.92.135503
8. Aranson, I. S.; Tsimring, L. S.; Vinokur, V. M. *Phys. Rev. B* **2002,** *65,* No. 125402. doi:10.1103/PhysRevB.65.125402
9. Lyashenko, I. A.; Khomenko, A. V. *Tribol. Lett.* **2012,** *48,* 63–75. doi:10.1007/s11249-012-9939-2
10. Popov, V. L. *Tech. Phys.* **2001,** *46,* 605–615. doi:10.1134/1.1372955
11. Popov, V. L. *Solid State Commun.* **2000,** *115,* 369–373. doi:10.1016/S0038-1098(00)00179-4
12. Persson, B. N. J. *Phys. Rev. B* **1994,** *50,* 4771–4786. doi:10.1103/PhysRevB.50.4771
13. Landau, L. D. *Sov. Phys. – JETP* **1937,** *7,* 627.
14. Bock, H.; Schoen, M. *J. Phys.: Condens. Matter* **2000,** *12,* 1545–1568. doi:10.1088/0953-8984/12/8/301
15. Schoen, M.; Hess, S.; Diestler, D. J. *Phys. Rev. E* **1995,** *52,* 2587–2602. doi:10.1103/PhysRevE.52.2587
16. Bordarier, P.; Schoen, M.; Fuchs, A. H. *Phys. Rev. E* **1998,** *57,* 1621–1635. doi:10.1103/PhysRevE.57.1621
17. Braun, O. M.; Naumovets, A. G. *Surf. Sci. Rep.* **2006,** *60,* 79–158. doi:10.1016/j.surfrep.2005.10.004
18. Lyashenko, I. A.; Filippov, A. E.; Popov, M.; Popov, V. L. *Phys. Rev. E* **2016,** *94,* No. 053002. doi:10.1103/PhysRevE.94.053002
19. Bayart, E.; Svetlizky, I.; Fineberg, J. *Phys. Rev. Lett.* **2016,** *116,* No. 194301. doi:10.1103/PhysRevLett.116.194301
20. Pierno, M.; Bruschi, L.; Mistura, G.; Paolicelli, G.; di Bona, A.; Valeri, S.; Guerra, R.; Vanossi, A.; Tosatti, E. *Nat. Nanotechnol.* **2015,** *10,* 714–718. doi:10.1038/nnano.2015.106
21. Reiter, G.; Demirel, A. L.; Peanasky, J.; Cai, L.; Granick, S. In *Physics of Sliding Friction;* Persson, B. N. J.; Tosatti, E., Eds.; NATO Advanced Studies Institute, Series E: Applied Science, Vol. 311; Kluwer: Dordrecht, Netherlands, 1996; pp 119 ff.
22. Pogrebnjak, A. D.; Bratushka, S. N.; Beresnev, V. M.; Levintant-Zayonts, N. *Russ. Chem. Rev.* **2013,** *82,* 1135–1159. doi:10.1070/RC2013v082n12ABEH004344
23. Lyashenko, I. A. *Tech. Phys.* **2011,** *56,* 869–876. doi:10.1134/S1063784211060168
24. Popov, V. L.; Heß, M. *Method of dimensionality reduction in contact mechanics and friction;* Springer: Berlin, Germany, 2015. doi:10.1007/978-3-642-53876-6
25. Popov, V. L.; Hess, M. *Facta Univ., Ser.: Mech. Eng.* **2014,** *12,* 1–14.
26. Hess, M.; Popov, V. L. *Facta Univ., Ser.: Mech. Eng.* **2016,** *14,* 251–268.
27. Slutsker, J.; Thornton, K.; Roytburd, A. L.; Warren, J. A.; McFadden, G. B. *Phys. Rev. B* **2006,** *74,* No. 014103. doi:10.1103/PhysRevB.74.014103
28. Kisiel, M.; Pellegrini, F.; Santoro, G. E.; Samadashvili, M.; Pawlak, R.; Benassi, A.; Gysin, U.; Buzio, R.; Gerbi, A.; Meyer, E.; Tosatti, E. *Phys. Rev. Lett.* **2015,** *115,* No. 046101. doi:10.1103/PhysRevLett.115.046101
29. Vågberg, D.; Olsson, P.; Teitel, S. *Phys. Rev. E* **2017,** *95,* No. 052903. doi:10.1103/PhysRevE.95.052903

BEILSTEIN JOURNAL OF NANOTECHNOLOGY

Imidazolium-based ionic liquids used as additives in the nanolubrication of silicon surfaces

Patrícia M. Amorim[1,2], Ana M. Ferraria[3], Rogério Colaço[4], Luís C. Branco[2] and Benilde Saramago[*1]

Full Research Paper

Open Access

Address:
[1]Centro de Química Estrutural, Instituto Superior Técnico, Universidade de Lisboa, Av. Rovisco Pais, 1049-001 Lisboa, Portugal, [2]LAQV-REQUIMTE, Departamento de Química, Faculdade de Ciências e Tecnologia, Universidade Nova de Lisboa, Campus da Caparica, 2829-516 Caparica, Portugal, [3]Centro de Química-Física Molecular and Institute of Nanoscience and Nanotechnology, Instituto Superior Técnico, Universidade de Lisboa, Av. Rovisco Pais, 1049-001 Lisboa, Portugal and [4]IDMEC-Instituto de Engenharia Mecânica, Departamento de Engenharia Mecânica, Instituto Superior Técnico, Universidade de Lisboa, Av. Rovisco Pais, 1049-001 Lisboa, Portugal

Email:
Benilde Saramago[*] - b.saramago@tecnico.ulisboa.pt

* Corresponding author

Keywords:
additives; ionic liquids; lubricants; nanotribology; silicon

Beilstein J. Nanotechnol. **2017,** *8,* 1961–1971.
doi:10.3762/bjnano.8.197

Received: 12 May 2017
Accepted: 31 August 2017
Published: 20 September 2017

This article is part of the Thematic Series "Nanotribology".

Guest Editor: E. Gnecco

Abstract

In recent years, with the development of micro/nanoelectromechanical systems (MEMS/NEMS), the demand for efficient lubricants of silicon surfaces intensified. Although the use of ionic liquids (ILs) as additives to base oils in the lubrication of steel/steel or other types of metal/ metal tribological pairs has been investigated, the number of studies involving Si is very low. In this work, we tested imidazolium-based ILs as additives to the base oil polyethylene glycol (PEG) to lubricate Si surfaces. The friction coefficients were measured in a nanotribometer. The viscosity of the PEG + IL mixtures as well as their contact angles on the Si surface were measured. The topography and chemical composition of the substrates surfaces were determined with atomic force microscopy (AFM) and X-ray photoelectron spectroscopy (XPS), respectively. Due to the hygroscopic properties of PEG, the first step was to assess the effect of the presence of water. Then, a series of ILs based on the cations 1-ethyl-3-methylimidazolium [EMIM], 1-butyl-3-methylimidazolium [BMIM], 1-ethyl-3-vinylimidazolium [EVIM], 1-(2-hydroxyethyl)-3-methylimidazolium [C_2OHMIM] and 1-allyl-3-methylimidazolium [AMIM] combined with the anions dicyanamide [DCA], trifluoromethanesulfonate [TfO], and ethylsulfate [$EtSO_4$] were added to dry PEG. All additives (2 wt %) led to a decrease in friction coefficient as well as an increase in viscosity (with the exception of [AMIM][TfO]) and improved the Si wettability. The additives based on the anion [$EtSO_4$] exhibited the most promising tribological behavior, which was attributed to the strong interaction with the Si surface ensuring the formation of a stable surface layer, which hinders the contact between the sliding surfaces.

Introduction

The use of ILs as neat lubricants was first proposed by Ye et al. in 2001 [1]. Since then, many investigations confirmed the good performance of ILs and their potential to substitute traditional lubricants in specific applications due to their peculiar properties. However, the price of ILs compared with that of commercial oils does not make them commercially competitive. Thus, the possibility of using ILs as additives to base lubricants rose as an attractive alternative from the economical point of view, and it has been pointed out in previous studies [2,3]. The first investigation reporting the use of ILs as additives is, to our knowledge, the work of Phillips et al. [4], who added imidazolium-based ILs to water for the lubrication of ceramics. Other investigators followed this idea and added imidazolium-based ILs to base oils to lubricate steel/aluminum contacts [5-7] and steel/steel contacts [8-13]. Jiménez and Bermúdez [7] tested two ILs with the short alkyl chain imidazolium cation [EMIM], and the anions tetrafluoroborate [BF_4] and bis(trifluoromethylsulfonyl)imide [NTf_2] mixed with propylene glycol dioleate to lubricate Al alloys. There was no impact on the friction coefficient but the wear rate was reduced significantly. The group of Liu [9-13] extensively investigated the role of ILs formed by imidazolium-based cations and the anions [BF_4], hexafluorophosphate [PF_6] and [NTf_2] as additives to PEG and polyurea grease in the lubrication of steel/steel pairs, at room temperature and high temperatures. Recently, Pejaković et al. [14] tested several imidazolium sulfate ILs and found significant improvement of the tribological behavior of the same type of sliding pairs when 1-ethyl-3-methylimidazolium octylsulfate was added to the model lubricant fluid (glycerol). They attributed this to sulfur species in the tribofilm. Gusain et al. [15] synthesized bis-imidazolium ILs that proved to be efficient as additives to PEG in the lubrication of the same type of sliding pairs. Other ILs, namely those based on phosphonium [16,17] and ammonium [18-20] cations, have been tested as lubricant additives as described in recent reviews.

In most cases, the studies involved steel/steel or other types of metal/metal tribological pairs. However, the need for efficient lubrication of silicon surfaces rose with the development of micro/nanoelectromechanical systems (MEMS/NEMS) [21]. These miniaturized devices demand lubricants of high performance because the large surface-to-volume ratios may cause serious adhesion and friction problems, the so-called stiction. ILs stand up as promising lubricants for this type of systems, all the more so since ILs are conductive liquids, leading to the minimization of the contact resistance between sliding surfaces, which is required for various electrical applications. Several authors have successfully tested pure ILs as lubricants for Si surfaces [22-26]. However, to our knowledge, the only reports on the efficient behavior of ILs as oil additives to lubricate Si surfaces were recently published by the group of T. Atkin [27,28]. They studied the lubrication of silica surfaces at the macro- and the nanoscale with mixtures of trihexyl(tetradecyl)-phosphonium bis(2,4,4-trimethylpentyl)phosphinate and apolar base oils, such as octane and hexadecane. Macroscale studies were done with a pin-on-disk tribometer under loads of 2 N and 10 N, while an atomic force microscope was used in the nanoscale investigation. Different lubrication regimes were observed at both scales: boundary lubrication at the nanoscale and mixed lubrication the macroscale. In the former case, lubricity was a function of the density of the adsorbed layer; in the latter one, the friction performance depended on the load: at low loads, the mixtures oil–IL were more efficient than the pure oil, while, at high loads, only concentrated oil–IL mixtures led to efficient lubrication.

In this work, we went back to imidazolium-based ILs and tried to improve their tribological performance as additives through the introduction of adequate functional groups both in the cation and in the anion. First, we investigated the influence of the presence of water in the base oil (PEG) through the comparison of the behavior of dry and water-equilibrated mixtures. Then, a series of ILs based on the cations [EMIM], [BMIM], [EVIM], [C_2OHMIM] and [AMIM] and the anions [DCA], [TfO], [$EtSO_4$] were used as additives in PEG to lubricate Si surfaces using a nanotribometer. Figure 1 illustrates the structures of the studied ILs.

As far as we know, the lubricant properties of these pure ILs on silicon-based materials were never investigated, with the exception of [EMIM][$EtSO_4$]. The reason should be the poor results obtained by other authors with similar ILs. Xie et al. [24] found a deficient lubrication performance of [EMIM][BF_4], which was attributed to the small alkyl chain length on the imidazolium ring. Mo et al. [23] studied the lubricant properties of ILs based on the cation EMIM containing methyl, hydroxy, nitrile, and carboxyl groups deposited by dip-coating on Si surfaces. They found favorable friction reduction with [C_2OHMIM][Cl] being the least efficient IL. In contrast, promising results were obtained with [EMIM][$EtSO_4$], which were attributed to the presence of a stable tribofilm resulting from specific interaction between the [$EtSO_4$] anion and the silicon surface [26,29].

The PEG + IL mixtures were characterized with respect to their viscosity and substrate wettability. The topography and chemical composition of the substrates surfaces were determined with atomic force microscopy (AFM) and X-ray photoelectron spectroscopy (XPS), respectively. Correlations between the obtained friction coefficients and the surface properties as well as

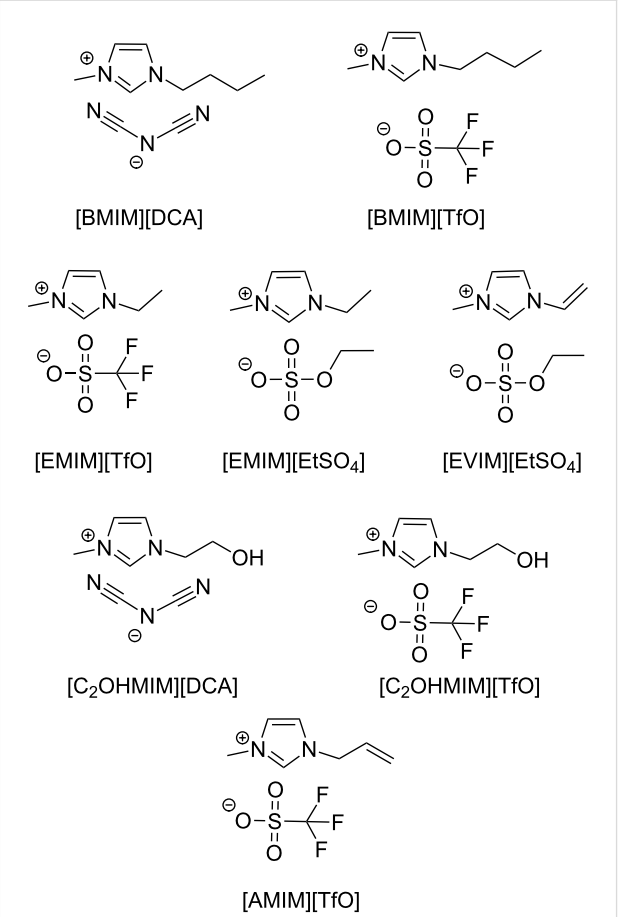

Figure 1: Structure of the studied ILs.

the lubricants viscosity were attempted in order to understand the mechanism involved in the lubrication process.

Results and Discussion

Friction and wear under dry conditions

For comparison purposes, a set of nanotribological tests were done under dry conditions in a nitrogen stream using substrates and counter bodies similar to those used in the lubricated tests, the same normal load and scanning speed. The number of cycles used was 3100. In these tests it was observed that, after a very short running in period, the friction coefficient (CoF) stabilizes at a value of 0.7. Clear wear tracks could be observed, even with unaided eye, after the nanotribological tests under dry conditions. The AFM observation of these worn surfaces (Figure 2) reveals the existence of parallel grooves with peak-to-valley depths of approximately 500 nm, typical of severe abrasive conditions caused on the Si surface by the steel counter body.

Effect of water in the lubricants

Most ILs and PEG itself are very hygroscopic liquids the water content of which may increase during the tribological applications under ambient conditions. Thus, it is important to know the influence of water on the tribological performance of pure PEG and its mixtures. Two types of PEG and PEG mixtures were tested: the liquids equilibrated with the atmosphere, here designated as humid, and the dry liquids, which were submitted to a vacuum drying process. Three ILs based on hydrophobic ([TfO]) and hydrophilic ([DCA]) anions were chosen as testing liquids to prepare the mixtures: [EMIM][TfO], [BMIM][TfO] and [BMIM][DCA]. The values of the viscosity, η, at 25 °C and the water content of humid and dry liquids (PEG and PEG + IL mixtures) are presented in Table 1.

The presence of water decreases the viscosity of PEG and its mixtures by about 5 mPa·s. Addition of ILs increases the viscosity of humid and dry PEG in a similar fashion.

The first observation to retain from the nanotribological tests is the fact that, under the tested conditions, no wear was observed in any of the samples tested under lubricated conditions, either with PEG and with PEG+IL mixtures. In what concerns the CoF, the values are plotted in Figure 3. The values of CoF obtained with both humid and dry liquids are plotted as a function

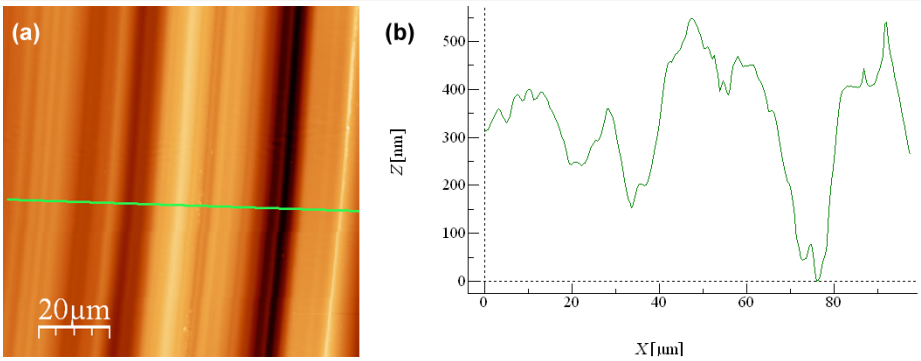

Figure 2: (a) AFM observation of the worn surface of Si submitted to nanotribological tests under dry conditions and (b) height profile of the worn region.

Table 1: Viscosity, η, at 25 °C and water content of dry and humid liquids.

PEG + IL additive	humid liquids		dry liquids	
	η/mPa·s	water content/ppm	η/mPa·s	water content/ppm
PEG	36	4466	40	200–500
PEG + [EMIM][TfO]	48	3932	53	568
PEG + [BMIM][TfO]	47	3970	52	674
PEG + [BMIM][DCA]	52	4061	56	552

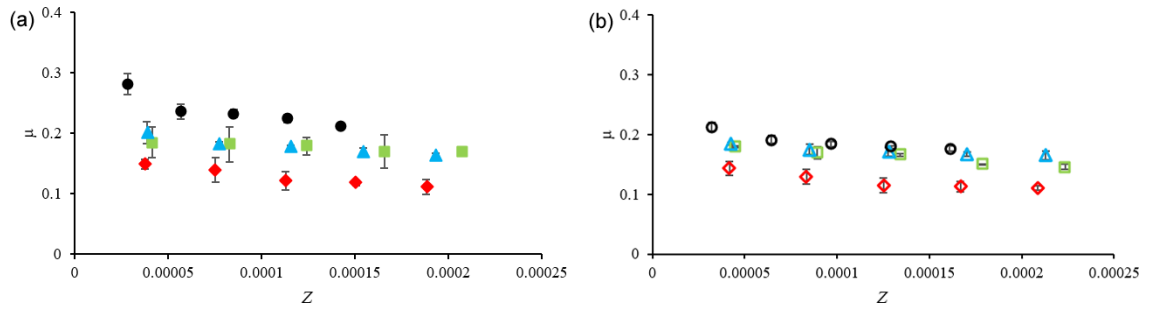

Figure 3: CoF as a function of the Sommerfeld parameter, *Z*, for (a) humid and (b) dry PEG (black circle) and PEG + [EMIM][TfO] (blue triangle), PEG + [BMIM][TfO] (red diamond), and PEG + [BMIM][DCA] (green square).

of the Sommerfeld parameter $Z = \eta \cdot r \cdot v$ (Stribeck curves), where F is the applied force, r is the radius of the counterbody, and v is the velocity.

The main difference occurs between humid and dry PEG: The presence of water slightly increases the friction coefficient. Similar results were reported by the group of Spencer who found that water negatively affects the lubrication efficiency of ILs, at both the nanoscale [30] and the macroscale [31]. They used an extended surface force apparatus to study the influence of water on the structure of the nanoconfined films of ILs containing both hydrophilic ([$EtSO_4$]) and hydrophobic (trifluorophosphate) anions. Water had different effects on both types of ILs: In hydrophilic ILs water hydrated the anions, while in hydrophobic ILs, it mainly hydrated the substrate surface. However, in both cases, ambient humidity was found to disturb the ion-pair coordination, which resulted in an increase in friction [31]. Tests carried out at macroscale showed the same effect when using hydrophobic imidazolium-based ILs to lubricate silica/silicon pairs at a small applied load (0.5 N). Under these conditions, low friction and no detectable wear in a nitrogen atmosphere was detected; in humid air, wear and friction increased, which was attributed to the disruption of lubricant film, leading to contact between the sliding surfaces [32]. Recently, the same group reported somewhat different results when studying the tribological behavior of silica/silicon pairs lubricated with [EMIM][$EtSO_4$] with a pin-on-disk tribometer at high load (4.5 N) [32]. They studied the effect of ambient humidity and found a decrease in friction and wear of both counterparts when water was present in the IL which they attributed to the formation of a ductile layer of hydrated silica which resulted in the smoothing of the silica surface.

The increase in the viscosity of the dry liquids may also influence the tribological behavior, because in a mixed lubrication regime a more viscous lubricant would be more efficient in keeping the surfaces apart. Addition of ILs led to a decrease in friction, more significant for wet PEG, which should result from the formation of a boundary film as well as from the increase in the viscosity. In dry conditions an adsorbed layer of cations is expected; in wet conditions, adsorbed water may be present when the ILs are hydrophobic (TfO-based) or a layer of adsorbed cations and anions for hydrophilic ILs [31].

The contact angles of humid and dry PEG and their mixtures with ILs on the silicon substrates are presented in Figure 4. In both cases, addition of the ILs to PEG increased the wettability confirming the preferential interaction of the IL ions with the silicon surface. The contact angles of the humid liquids are lower than those of the dry liquids, which should result from the preferential adsorption of water molecules on the Si surface. The reduction of the contact angle in the presence of water is more significant for the PEG+IL mixtures than for pure PEG, which suggests that in the former case the water molecules being preferentially attached to the IL anions by H-bonds have a higher tendency to concentrate at the surface.

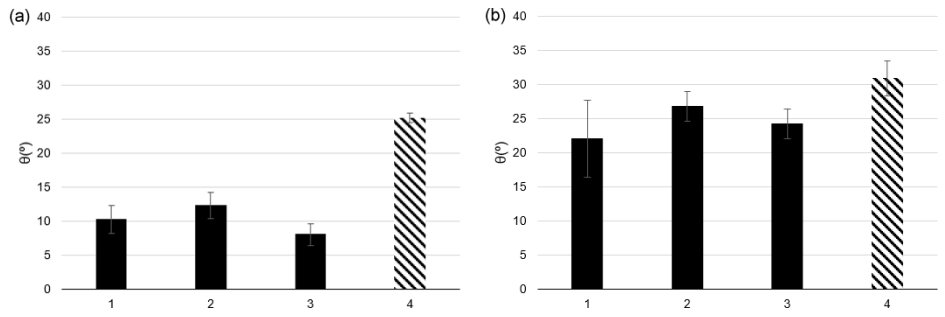

Figure 4: Contact angles of (a) humid and (b) dry PEG + [BMIM][DCA] (1), PEG + [BMIM][TfO] (2), PEG + [EMIM][TfO] (3), and PEG (4) on silicon substrates. The error bars correspond to standard deviations ($n \geq 7$).

The correlation of the tribological performance with the substrate wettability is not a straightforward issue. In principle, for a boundary/mixed lubrication regime, a good wettability of the substrates should be important to keep a stable lubricating film. However, Borruto et al. [33] found that water lubrication in the mixed/hydrodynamic regime was most effective when pins and discs were made of materials of different wettability. In particular, when the counterbody was very hydrophilic and the disk very hydrophobic a stable layer of water remained between the sliding surfaces. In our case, the presence of water had a stronger effect on the CoF of pure PEG the wettability of which was the least affected. When comparing the different mixtures, both in dry or wet state, no correlation seems to exist between the substrate wettability and the tribological behavior, which is not unexpected considering the similarity of the corresponding contact angles.

Effect of IL cation and anion

The ILs presented in Figure 1 were mixed with PEG (2 wt %) to prepare the mixtures used in the nanotribological tests. The choice of this concentration was based on preliminary tests using weight percentages of 1 wt %, 2 wt % and 5 wt %, which showed similar results for 2 wt % and 5 wt %. The characterization of the PEG + IL mixtures with respect to the viscosity, η, at 25 °C, water content and contact angle on the silicon surface is described in Table 2.

The viscosity of the mixtures is considerably higher than that of PEG, except for PEG + [AMIM][TfO]. PEG + [EVIM][$EtSO_4$] stands out as the most viscous mixture. All mixtures present lower contact angles than pure PEG (31°) on the silicon substrate, including those based on the hydrophobic [TfO] anion, especially when the cation contains hydroxy or allyl groups in the side chain.

In order to investigate the effect of the cation and the anion of the IL additive on the tribological performance of the PEG mixtures, we compared the CoFs obtained with PEG and with PEG+IL mixtures grouped according to the anion: ILs based on the hydrophobic [TfO] anion coupled with [EMIM], [BMIM], [AMIM] and [C_2OHMIM]; ILs based the hydrophilic [DCA] anion coupled with [BMIM] and [C_2OHMIM]; ILs based on the hydrophilic [$EtSO_4$] anion coupled with [EMIM] and [EVIM]. The results are presented in Figure 5.

Analysis of Figure 5 indicates the presence of a mixed-lubrication regime, except for PEG + [EVIM][$EtSO_4$] due to its high viscosity. Among the TfO-based additives (Figure 5a), the one with cation [EMIM] (shorter side chain) led to the worst results: It had almost no effect, in particular, at higher velocities. Addition to PEG of other cations with short side chains but functional groups (hydroxy or allyl), respectively, [C_2OHMIM] and [AMIM], led to a slight decrease in friction. Cation [BMIM]

Table 2: Viscosity, η, at 25 °C, water content and contact angle of PEG + IL mixtures.

PEG + IL additive	η/mPa·s	water content/ppm	contact angle/°
PEG + [EMIM][TfO]	53	568	24 ± 2
PEG + [BMIM][TfO]	52	675	27 ± 2
PEG + [C_2OHMIM][TfO]	55	466	15 ± 1
PEG + [AMIM][TfO]	40	406	17 ± 1
PEG + [BMIM][DCA]	56	552	22 ± 6
PEG + [C_2OHMIM][DCA]	52	560	17 ± 2
PEG + [EMIM][$EtSO_4$]	53	432	17 ± 2
PEG + [EVIM][$EtSO_4$]	75	480	19 ± 3

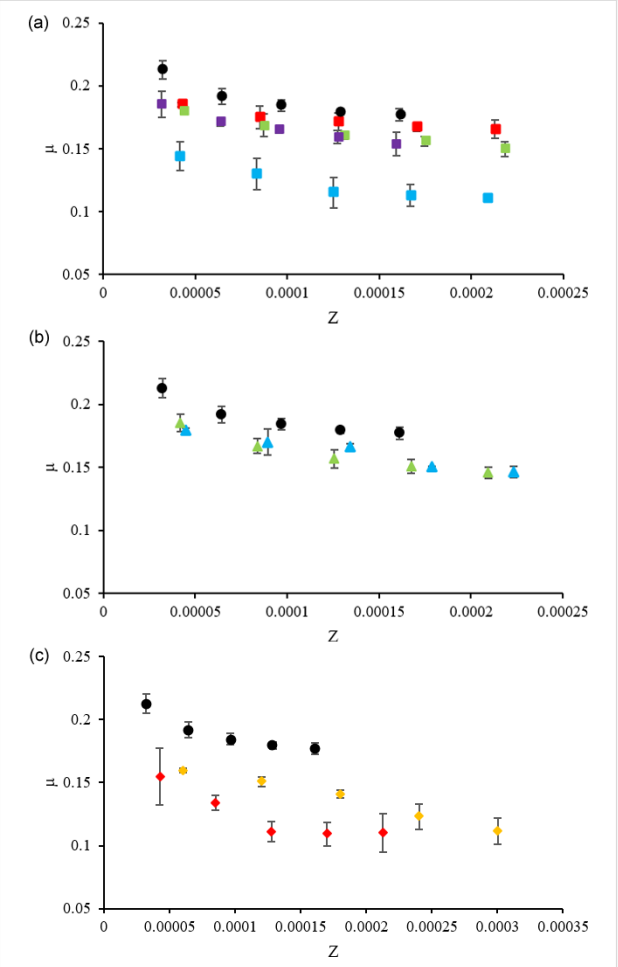

Figure 5: CoF vs Sommerfeld parameter, *Z*, for (a) TfO-based, (b) DCA-based and (c) $EtSO_4$-based ILs mixed with PEG: PEG (black circles), PEG + [EMIM][TfO] (red squares), PEG + [BMIM][TfO] (blue squares), PEG + [C_2OHMIM][TfO] (green squares), PEG + [AMIM][TfO] (purple squares), PEG + [BMIM][DCA] (blue triangles), PEG + [C_2OHMIM][DCA] (green triangles), PEG + [EMIM][$EtSO_4$] (red diamonds), PEG + [EVIM][$EtSO_4$] (yellow diamonds).

with a longer side chain induced a significant decrease in friction, despite the fact that it presents the highest contact angle. Comparison of the DCA-based additives (Figure 5b) shows that all combinations ([BMIM] and [C_2OHMIM]) led to similar small decreases in CoF. Finally, the $EtSO_4$-based additives (Figure 5c) led to accentuated decreases in friction but the behavior of both cations was different. While [EVIM][$EtSO_4$] led to a linear decrease of CoF with increasing *Z*, with [EMIM][$EtSO_4$] a constant CoF was obtained for intermediate values of *Z*. This difference may be attributed to the higher viscosity of the former one which may contribute for the stability of the boundary layer at high sliding speeds.

To further understand the differences in behavior of the PEG/IL mixtures in the lubrication of the Si surface, AFM observation of some of the Si surfaces was done. After the nanotribological tests, tracks could be observed on the surfaces; however these tracks disappeared after washing the samples, demonstrating that no wear occurred. Figure 6 shows the AFM images of samples submitted to nanotribological tests (3100 cycles), before washing: Figure 6a shows the sample tested with pure PEG; Figure 6b shows the sample submitted to tribological tests performed with the mixture PEG + [EMIM][TfO], which presents a CoF similar to that of pure PEG (Figure 5a); Figure 6c shows the sample tested with the mixture PEG + [EMIM][$EtSO_4$], which presents a lower CoF. Outside the sliding region an adsorbed layer with some agglomerates of the lubricant is present in all the samples. Moreover, AFM observation shows the following:

- Figure 6a**:** PEG adsorbs to the surface forming an adsorbed layer of approximately 3 nm of height. This layer is continuously removed by the sliding movement of the counter body. Nevertheless, PEG decreases the CoF and impairs the wear of the Si surface.

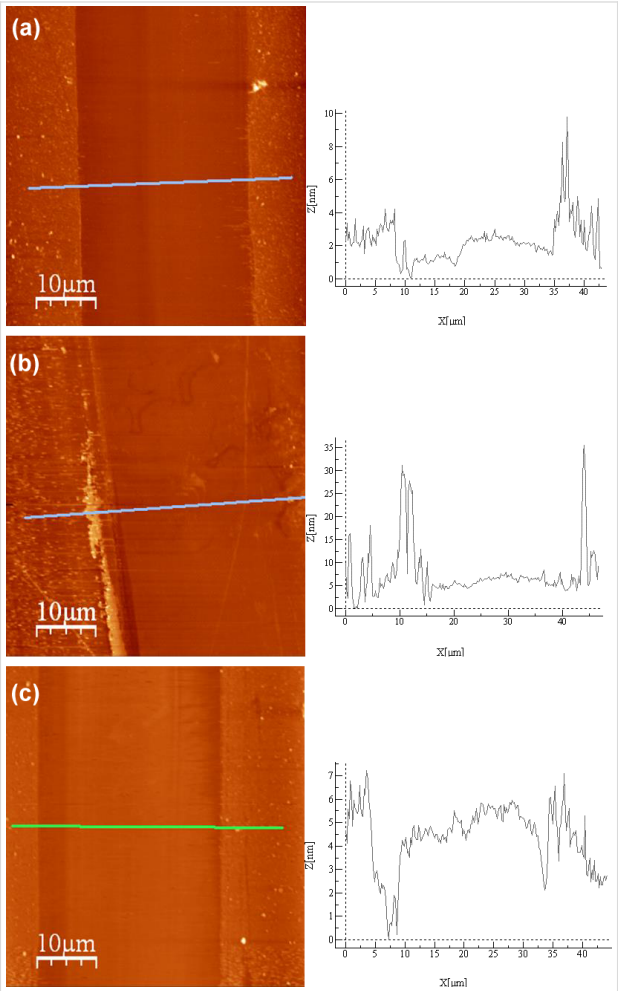

Figure 6: AFM images and height profiles of the sliding tracks in (a) dry PEG, (b) PEG + [EMIM][TfO] and (c) PEG + [EMIM][$EtSO_4$].

- Figure 6b**:** The surface of the samples submitted to tests with PEG + [EMIM][TfO] is similar to the surface of samples tested with PEG. Both the morphology of the layer and the depth of the sliding track (3–4 nm in average) are comparable to what can be observed in PEG samples, the main difference being the formation of some ridges at the periphery of the tracks, caused by the accumulation of the removed layer.
- Figure 6c**:** The adsorbed layer of PEG + [EMIM][$EtSO_4$] is similar in morphology to the previous ones. However, in this case, the adsorbed layer is only partially removed in the periphery of the sliding tracks, indicating that the adhesion of PEG to the Si surface is enhanced by the presence of 2 wt % of [EMIM][$EtSO_4$].

Therefore, the AFM results indicate that, although the adsorbed lubricant film is partially removed by the sliding action of the counterbody, in general, this removal is only partial and wear protection by the lubricants is ensured. The AFM observations also indicate that, when [EMIM][$EtSO_4$] is added to PEG, the adsorbed layer is thicker which may explain the smaller CoF measured.

XPS was used to analyze the Si surfaces after contacting with PEG and with two mixtures exhibiting the best and the worst nanotribological performance, respectively, PEG + [EMIM][$EtSO_4$] and PEG + [EMIM][TfO] (see Figure 5). Adsorption of PEG to the Si surface was attested by the peak centered at about 287 eV assigned to carbon singly bound to oxygen (C–O) (Figure 7a), confirming the AFM observation. Another peak of C 1s, much smaller, is present at ca. 285 eV and may be assigned to hydrocarbon-like contaminations on the Si surface. In the case of the IL mixtures, no important differences exist among the C 1s signals: Two peaks may be fitted in the same positions, the intensity of the aliphatic carbon being lower in the PEG + [EMIM][$EtSO_4$] sample. The most intense XPS sulfur peak is the S 2p (S $2p_{3/2}$ + S $2p_{1/2}$), which is superposed to the Si 2s plasmon loss. Comparison was, therefore, based on the S 2s peaks. In both samples, the signal to noise ratio is very poor (Figure 7b). Anyway, the smoothed data (full black lines) show different S 2s peaks in the sample treated with PEG + [EMIM][TfO] and with PEG + [EMIM][$EtSO_4$]. In the former case, the peak centered at 232.9 eV, assigned to the sulfonate group in TfO, is broad but rather symmetrical. In the latter case, at least two peaks may be identified, one at higher energy (ca. 234 eV) assigned to sulfate, and the other one at lower energy similar to that of SO_3 in TfO. This suggests that the anion $EtSO_4$ is more affected by the presence of the substrate than the anion TfO. Finally, the spectra reveal a single N 1s peak centered at 402.1 eV, which is assigned to the nitrogen atoms with delocalized charge in the imidazolium ring of both [EMIM][$EtSO_4$] and [EMIM][TfO] (Figure 7c). To further

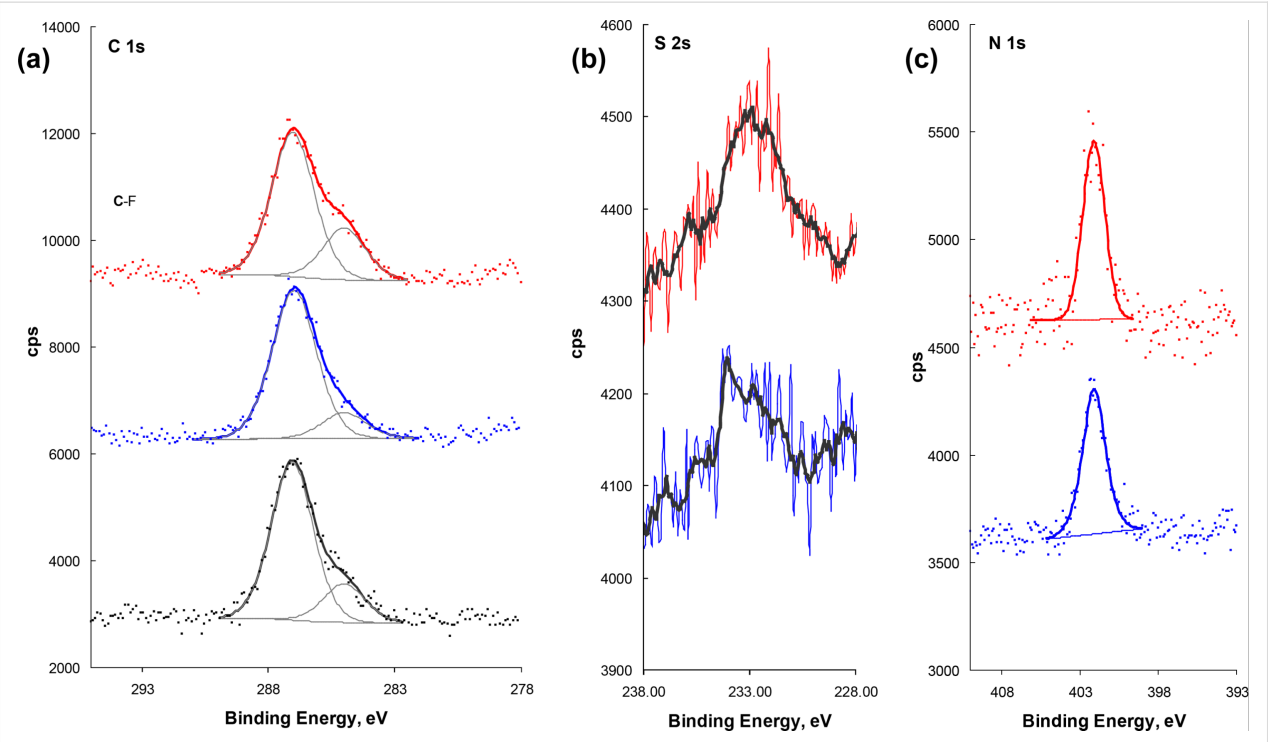

Figure 7: XPS regions of (a) C 1s, (b) S 2s, and (c) N 1s for, from bottom to top, in (a) Si/PEG, Si/PEG + [EMIM][$EtSO_4$] and Si/PEG + [EMIM][TfO], and in (b) and (c) Si/PEG + [EMIM][$EtSO_4$] and Si/PEG+[EMIM][TfO]. The solid black line in (b) represents the smoothed data.

support this idea, quantitative atomic ratios were calculated and are given in Table 3.

Table 3: XPS atomic ratios for the Si samples coated with PEG, PEG + [EMIM][$EtSO_4$] and PEG + [EMIM][TfO].

	PEG + [EMIM][$EtSO_4$]	PEG + [EMIM][TfO]	PEG
C–O/Si	0.41 ± 0.01	0.43 ± 0.01	0.46 ± 0.01
N/C–O	0.13 ± 0.01	0.16 ± 0.01	—
S/C–O	0.042 ± 0.004	0.066 ± 0.007	—

The C–O/Si values given in Table 3 show that the amount of PEG on the Si surfaces exposed to the PEG + IL mixtures is slightly lower than that on the surface exposed to pure PEG, especially when the IL is [EMIM][$EtSO_4$]. This result may be interpreted that either a smaller amount of polymer is adsorbed on the surface, or the same amount exists but PEG is more aggregated. The N/C–O and the S/C–O ratios suggest that less IL seems to exist in the sample coated with PEG + [EMIM][$EtSO_4$] than in the sample coated with PEG + [EMIM][TfO]. Since the expected ratios should be similar in both cases, these results are compatible with stratification of the surface layers to some extent, with [EMIM][$EtSO_4$] being closer to the Si surface than [EMIM][TfO]. This supports the interpretation given above for the large asymmetry of the S 2s peak in the former case. Stratification of ILs near solid surfaces, namely alumina and silica, was detected by several authors using atomic force microscopy imaging and MD simulations, even in the absence of long alkyl side chains [34,35]. However, stratification may lead to large distortions of the XPS atomic ratios when compared to the stoichiometric ones [36], thus no further quantitative analysis was performed.

Overall, these results seem to indicate a stronger interaction between [EMIM][$EtSO_4$] and the surface compared with that of [EMIM][TfO], which leads to the greater stability of the adsorbed layer and the better tribological behavior of the additive [EMIM][$EtSO_4$].

The efficiency of ILs based on the anion $EtSO_4$ as pure lubricants was already reported in the literature [26,29]. However, to our knowledge, this is the first time that these ILs are successfully tested as additives to base lubricants. Strong adsorption of [$EtSO_4$] on the surface oxide that covers the Si substrate should be responsible for this behavior. The S–O bond of this anion is known to interact with the silica surface to yield Si–O–S bonds, while the Si-OH groups were not found to give a significant contribution [37]. In this case, the positive role of the [$EtSO_4$] anion seems to overlap the poor efficiency of the [EMIM] cation. Other authors [38,39] tested the frictional behavior of ILs composed of the cation [EMIM] and the sulfur-based anions, methylsulfate ([$MeSO_4$]), *n*-buthylsulfate ([*n*-$BuSO_4$]) and octylsulfate ([$OcSO_4$]), as oil additives to lubricate steel surfaces and got different results. They found that friction did not improve with respect to that obtained with the base oil (glycerol), except under high shear conditions. Among the three ILs, the one based on [*n*-$BuSO_4$] was the best, because it promoted a more complete covering of the substrate surface [38]. Later, they repeated the experiments keeping constant the molar fraction instead of the weight fraction of the additive and found that the mixtures with [EMIM][$OcSO_4$] performed better because they formed thicker, more compact surface films. However, comparison with pure glycerol did not show a significant improvement [39]. All these results indicate the beneficial influence of the presence of IL additives depends strongly on the chemical nature of both ILs and the substrate. Enhanced interactions between the cation and or the anion and the hydrophilic silicon substrate, due to van der Waals forces (long side chains), hydrogen bonding (ethanol functional groups) and, more importantly, chemical bonding involving the hydrophilic sulfate and Si, promote the formation of an ordered surface layer, which helps to hinder the contact between the sliding surfaces.

Conclusion

A series of imidazolium-based ILs was tested as additives to the base oil PEG in the lubrication of Si surfaces: [EMIM][TfO], [BMIM][TfO], [C_2OHMIM][TfO], [AMIM][TfO], [BMIM][DCA], [C_2OHMIM][DCA], [EMIM][$EtSO_4$] and [EVIM][$EtSO_4$]. The presence of water in PEG, equilibrated with the ambient atmosphere, worsened its tribological performance. However, contrary to what occurs in the tests under dry conditions, all the tested lubricants are efficient to impair wear under the tested conditions. A small percentage (2 wt %) of ILs was sufficient to induce a decrease in CoF, which was most significant in the case of those containing the anion [$EtSO_4$]. XPS analysis of the silicon surfaces after exposure to PEG + IL mixtures containing the anions [$EtSO_4$] and [TfO], respectively, leading to the best and the worst tribological behavior in what concerns CoF, confirmed the stronger interaction with [$EtSO_4$]. The excellent results obtained with [EMIM][$EtSO_4$] and [EVIM][$EtSO_4$] encourage a deeper research on this type of additives with the objective of substituting the traditional oils in microelectronics lubrication.

Experimental

Materials

The following reagents were used: 1-methylimidazole (Alfa Aesar, 99%), 1-vinylimidazole (Sigma-Aldrich, 99%), allyl bromide (BHD, 99%), diethyl sulfate (Acros Organics, 99%), sodium dicyanamide (Aldrich, ≥97%). The solvents used for reaction media and/or purification processes are the following:

dichloromethane (Carlo Erba Reagents, 99.9%), ethanol (LabChem), acetone (LabChem), acetonitrile (Carlo Erba Reagents, 99.8%), diethyl ether (LabChem, 99.9%). The reagent sodium trifluoromethanesulfonate, and the ILs [EMIM][TfO], [EMIM][$EtSO_4$], [BMIM][TfO], [BMIM][DCA], [C_2OHMIM][TfO], and [C_2OHMIM][DCA] were kindly provided by Solchemar company (Portugal). The purity of these ILs is greater than 98%, according to the supplier. The commercial lubricant PEG 200 is from FLUKA (Sigma-Aldrich), ref: 81150. The substrates used for tribological tests and contact angle measurements are silicon wafers b100N with 0.5 mm of thickness and a roughness below 0.1 nm. Stainless steel AISI 316L spheres with 3 mm of diameter were used as counter bodies.

Methods

Synthesis of ionic liquids

[AMIM][Br]: 1-Methylimidazole (14.0 mL, 176 mmol) was dissolved in 50 mL of acetone in a round-bottomed flask. This flask was submerged in ice and allyl bromide (15.2 mL, 211 mmol) was slowly added with stirring under an inert atmosphere. After the addition, the flask was fitted with a reflux condenser, removed from ice and kept at room temperature overnight. The next day, the mixture was kept at 40 °C for 5 h. In the end of the reaction the solvent was evaporated and the crude was washed with diethyl ether (5 × 5 mL under vigorous stirring) and then dried in vacuum at 85 °C for 3 days. The pure product was obtained as a viscous brown liquid (31 g, 87%).

^{1}H NMR (DMSO-d_6, 400 MHz) δ 3.90 (s, 3H), 4.94 (d, J = 8.00 Hz, 2H), 5.32 (m, 2H), 6.04 (m, 1H), 7.86 (d, J = 4.00 Hz, 2H), 9.42 ppm (s, 1H).

[AMIM][TfO]: [AMIM][Br] (8 g, 39.4 mmol) was dissolved in 50 mL of ethanol in an Erlenmeyer flask. Sodium triflate (7.8 g, 45.3 mmol) was also dissolved in 50 mL of ethanol, added to the previous solution and kept at room temperature under stirring for 24 h. In the end of the reaction the solvent was evaporated and the crude was dissolved in dichloromethane in which the sodium bromide precipitates. The solution was filtered and, after evaporation of dichloromethane, dried in vacuum at 85 °C for 3 days. The pure product was obtained as a brown viscous liquid (8.4g, 78%).

^{1}H NMR (DMSO-d_6, 400 MHz) δ 3.87 (s, 3H), 4.84 (d, J = 4.00 Hz, 2H), 5.33 (m, 2H), 6.04 (m, 1H), 7.70 (d, J = 4.00 Hz, 2H), 9.09 ppm (s, 1H); ^{19}F NMR (DMSO-d_6, 282 MHz) δ −77.99, −77.62 ppm; FTIR (KBr) ṽ: 518.86, 575.30, 642.20, 759.40, 848.18, 949.20, 995.75, 1033.18, 1166.81, 1261.74, 1426.68, 1573.08, 1643.73, 2361.52, 3115.17, 3156.87, 3511.69 cm^{-1}; Anal. calcd for $C_8H_{11}F_3N_2O_3S{\cdot}H_2O$: C, 33.10; H, 4.51; N, 9.65; found: C, 33.24; H, 4.08; N, 9.57.

[EVIM][$EtSO_4$]: 1-Vinylimidazole (1.9 mL, 21.3 mmol) was dissolved in 20 mL of acetonitrile in a round-bottomed flask. Diethyl sulfate (3.6 mL, 27.6 mL) was slowly added at room temperature under stirring. After the addition, the flask was fitted with a reflux condenser for 48 h at 60 °C. In the end of the reaction the solvent was evaporated and the crude was washed with diethyl ether (5 × 5 mL under vigorous stirring) and then dried in vacuum at 85 °C for 3 days. The pure product was obtained as a viscous brown liquid (5.2 g, 99%).

^{1}H NMR (DMSO-d_6, 400 MHz) δ 1.10 (t, J = 12.00 Hz, 3H), 1.44 (t, J = 12.00 Hz, 3H), 3.79 (t, J = 12.00 Hz, 2H), 4.24 (m, 2H), 5.39 (m, 1H), 5.95 (m, 1H), 7.28 (m, 1H), 7.94 (s, 1H), 8.19 (s, 1H), 9.50 ppm (s, 1H); FTIR (KBr) ṽ: 585.28, 620.68, 781.43, 847.05, 919.84, 959.21, 1013.61, 1060.70, 1118.96, 1173.10, 1389.78, 1453.22, 1552.34, 1574.08, 1655.44, 2361.69, 2988.76, 3145.11, 3437.22 cm^{-1}; Anal. calcd for $C_8H_{14}N_2O_4S{\cdot}(1.1H_2O)$: C, 37.82; H, 6.43; N, 11.03; found: C, 37.85; H, 6.33; N, 10.53.

Characterization of IL mixtures

The water weight fraction of PEG and of the mixtures PEG + ILs, after being submitted to the vacuum drying process at 50 °C and 85 °C, respectively, was checked by Karl Fischer (coulometric) titration. The viscosity of PEG and its mixtures with the ILs was measured with a viscometer DV-II+Pro (Brookfield) at 25 °C. All measurements were done in triplicate. The temperature uncertainty was ±0.02 °C, while the precision of the dynamic viscosity measurements was ±0.5%.

The contact angle measurements on Si substrates were done with the sessile-drop method using the equipment described previously [40]. The Si substrates were submitted to a careful cleaning procedure: 2 × 15 min sonication in a detergent solution intercalated with 10 min sonication in water, followed by 3 × 10 min sonication in water, rinsing with distilled and deionized water, drying with nitrogen and finally drying for 2 h inside a vacuum oven at room temperature. The liquid drops were generated using a micrometric syringe from Gilmont inside an ambient chamber model 100-07-00 (Ramé-Hart, Succasunna, NJ, USA) at 20 °C. During the experiments, the chamber was continuously flushed with dry nitrogen, to minimize water absorption by the liquids. The images of drops were obtained with a video camera (jAi CV-A50, Barcelona, Spain) mounted on a microscope Wild M3Z (Leica Microsystems, Wetzlar, Germany) and analyzed by running the ADSA (Axisymmetric Drop Shape Analysis, Applied Surface Thermodynamics Research Associates, Toronto, Canada) software.

Nanotribological tests

The coefficients of friction (CoFs) were measured in a nanotribometer (CSM Instruments, Peseux, Switzerland) using PEG and PEG + ILs as lubricants. The Si substrates, previously cleaned as described above, were placed at the bottom of a liquid cell and a few drops of the lubricant were deposited on top to ensure complete coverage of the substrate surface. The amplitude of the reciprocal movement of the counter body (stainless steel sphere) on the Si surface was 0.5 mm and a force of 15 mN was applied. The sliding speed was varied between 0.4 and 2.0 $cm \cdot s^{-1}$, i.e., the nanotribological tests were carried out at low sliding speeds (low Sommerfeld numbers), corresponding to boundary or mixed-lubrication regimes. The number of cycles varied from 200 for the determination of CoF to 3100 for the observation of the substrates with AFM. Each test was repeated, at least, three times. The experiments were done at room temperature under a flow of dry nitrogen. The evolution of CoF with time was followed in all experiments and completely steady values were obtained after a few seconds meaning that the running in period was very short.

Microscopic observations

The surfaces of Si substrates after the nanotribological tests (3100 cycles) were observed with an optical microscope and then analyzed with an atomic force microscope (AFM) (NanoSurf Easyscan 2) using Si tips (c = 0.2 $N \cdot m^{-1}$, f_0 = 25 kHz) at a constant contact force of 20 nN, in contact mode. The images were obtained through the WSxM 5.0 Develop 4.0 software.

XPS determinations

The Si substrates were immersed in PEG and PEG + IL for 40 min, which is the duration of the longer friction tests and then dried with a flux of Ar prior to XPS analysis. Spectra were acquired at TOA = 0° (relative to normal) with the Mg Kα X-ray source of a KRATOS XSAM800. Data treatment details were given in a previous work [41]. The sensitivity factors used for quantification analysis were: 0.318 for C 1s, 0.391 for S 2s, 0.736 for O 1s, 0.505 for N 1s and 0.371 for Si 2p.

Acknowledgements

This research was supported by the projects UID/QUI/00100/2013, UID/QUI/50006/2013, UID/NAN/50024/2013 and PEst-C/LA0006/2013. L. C. Branco thanks to financial support of FCT/MCTES (IF/0041/2013/CP1161/CT00). A.M. Ferraria acknowledges FCT for the fellowship SFRH/BPD/108338/2015. The NMR spectrometers are part of The National NMR Facility, supported by FCT/MCTES (RECI/BBB-BQB/0230/2012). The help of Mariana Freire in the measurement of contact angles is acknowledged. A.M. Botelho de Rego is acknowledged for fruitful discussion of the XPS data.

References

1. Ye, C.; Liu, W.; Chen, Y.; Yu, L. *Chem. Commun.* **2001,** *21,* 2244–2245. doi:10.1039/b106935g
2. Tang, Z.; Li, S. *Curr. Opin. Solid State Mater. Sci.* **2014,** *18,* 119–139. doi:10.1016/j.cossms.2014.02.002
3. Zhou, Y.; Qu, J. *ACS Appl. Mater. Interfaces* **2017,** *9,* 3209–3222. doi:10.1021/acsami.6b12489
4. Phillips, B. S.; Mantz, R. A.; Trulove, P. C.; Zabinski, J. S. *ACS Symp. Ser.* **2005,** *901,* 244–253. doi:10.1021/bk-2005-0901.ch019
5. Jiménez, A. E.; Bermúdez, M. D.; Iglesias, P.; Carrión, F. J.; Martínez-Nicolás, G. *Wear* **2006,** *260,* 766–782. doi:10.1016/j.wear.2005.04.016
6. Jiménez, A.-E.; Bermúdez, M.-D. *Wear* **2008,** *265,* 787–798. doi:10.1016/j.wear.2008.01.009
7. Jiménez, A.-E.; Bermúdez, M.-D. *Tribol.-Mater., Surf. Interfaces* **2012,** *6,* 109–115. doi:10.1179/1751584X12Y.0000000011
8. Hernández Battez, A.; González, R.; Viesca, J. L.; Blanco, D.; Asedegbega, E.; Osorio, A. *Wear* **2009,** *266,* 1224–1228. doi:10.1016/j.wear.2009.03.043
9. Cai, M.; Zhao, Z.; Liang, Y.; Zhou, F.; Liu, W. *Tribol. Lett.* **2010,** *40,* 215–224. doi:10.1007/s11249-010-9624-2
10. Cai, M.; Liang, Y.; Yao, M.; Xia, Y.; Zhou, F.; Liu, W. *ACS Appl. Mater. Interfaces* **2010,** *2,* 870–876. doi:10.1021/am900847j
11. Zhang, H.; Xia, Y.; Yao, M.; Jia, Z.; Liu, Z. *Tribol. Lett.* **2009,** *36,* 105–111. doi:10.1007/s11249-009-9465-z
12. Cai, M.; Liang, Y.; Zhou, F.; Liu, W. *ACS Appl. Mater. Interfaces* **2011,** *3,* 4580–4592. doi:10.1021/am200826b
13. Cai, M.; Liang, Y.; Zhou, F.; Liu, W. *Wear* **2013,** *306,* 197–208. doi:10.1016/j.wear.2012.09.001
14. Pejaković, V.; Tomastik, C.; Dörr, N.; Kalin, M. *Tribol. Int.* **2016,** *97,* 234–243. doi:10.1016/j.triboint.2016.01.034
15. Gusain, R.; Gupta, P.; Saran, S.; Khatri, O. P. *ACS Appl. Mater. Interfaces* **2014,** *6,* 15318–15328. doi:10.1021/am503811t
16. Hernández Battez, A.; Bartolomé, M.; Blanco, D.; Viesca, J. L.; Fernández-González, A.; González, R. *Tribol. Int.* **2016,** *95,* 118–131. doi:10.1016/j.triboint.2015.11.015
17. Gutierrez, M. A.; Haselkorn, M.; Iglesias, P. *Lubricants* **2016,** *4,* 14–26. doi:10.3390/lubricants4020014
18. Gusain, R.; Bakshi, P. S.; Panda, S.; Sharma, O. P.; Gardas, R.; Khatri, O. P. *Phys. Chem. Chem. Phys.* **2017,** *19,* 6433–6442. doi:10.1039/C6CP05990B
19. Khatri, P. K.; Joshi, C.; Thakre, G. D.; Jain, S. L. *New J. Chem.* **2016,** *40,* 5294–5299. doi:10.1039/C5NJ02225H
20. Barnhill, W. C.; Luo, H.; Meyer, H. M., III; Ma, C.; Chi, M.; Papke, B. L.; Qu, J. *Tribol. Lett.* **2016,** *63,* 22–33. doi:10.1007/s11249-016-0707-6
21. Bhushan, B. Nanotribology and Nanomechanics of MEMS/NEMS and BioMEMS/BioNEMS Materials and Devices. In *Nanotribology and Nanomechanics - An introduction,* 4th ed.; Bhushan, B., Ed.; Springer: Berlin, Germany, 2017; pp 797–907. doi:10.1007/978-3-319-51433-8_16
22. Yu, B.; Zhou, F.; Mu, Z.; Liang, Y.; Liu, W. *Tribol. Int.* **2006,** *39,* 879–887. doi:10.1016/j.triboint.2005.07.039
23. Mo, Y.; Zhao, W.; Zhu, M.; Bai, M. *Tribol. Lett.* **2008,** *32,* 143–151. doi:10.1007/s11249-008-9371-9
24. Xie, B.; Wang, Q.; Si, L.; Liu, S.; Li, G. *Tribol. Lett.* **2009,** *36,* 247–257. doi:10.1007/s11249-009-9480-0
25. Mo, Y.; Huang, F.; Zhao, F. *Surf. Interface Anal.* **2011,** *43,* 1006–1014. doi:10.1002/sia.3684

26. Cosme, J.; Bastos, P. D. A.; Catela, I.; Silva, D.; Colaço, R.; Branco, L. C.; Saramago, B. *ChemistrySelect* **2016,** *1,* 3612–3617. doi:10.1002/slct.201600880
27. Li, H.; Cooper, P. K.; Somers, A. E.; Rutland, M. W.; Howlett, P. C.; Forsyth, M.; Atkin, R. *J. Phys. Chem. Lett.* **2014,** *5,* 4095–4099. doi:10.1021/jz5021422
28. Li, H.; Somers, A. E.; Howlett, P. C.; Rutland, M. W.; Forsyth, M.; Atkin, R. *Phys. Chem. Chem. Phys.* **2016,** *18,* 6541–6547. doi:10.1039/C5CP07061A
29. Perkin, S.; Albrecht, T.; Klein, J. *Phys. Chem. Chem. Phys.* **2010,** *12,* 1243–1247. doi:10.1039/B920571C
30. Espinosa-Marzal, R. M.; Arcifa, A.; Rossi, A.; Spencer, N. D. *J. Phys. Chem. C* **2014,** *118,* 6491–6503. doi:10.1021/jp5000123
31. Arcifa, A.; Rossi, A.; Espinosa-Marzal, R. M.; Spencer, N. D. *J. Phys. Chem. C* **2014,** *118,* 29389–29400. doi:10.1021/jp505998k
32. Arcifa, A.; Rossi, A.; Espinosa-Marzal, R. M.; Spencer, N. D. *ACS Appl. Mater. Interfaces* **2016,** *8,* 2961–2973. doi:10.1021/acsami.5b09370
33. Borruto, A.; Crivellone, G.; Marani, F. *Wear* **1998,** *222,* 57–65. doi:10.1016/S0043-1648(98)00256-7
34. Köhler, R.; Restolho, J.; Krastev, R.; Shimizu, K.; Lopes, J. N. C.; Saramago, B. *J. Phys. Chem. Lett.* **2011,** *2,* 1551–1555. doi:10.1021/jz2005682
35. Shimizu, K.; Pensado, A.; Malfrey, P.; Padua, A. A. H.; Canongia Lopes, J. N. *Faraday Discuss.* **2012,** *154,* 155–169. doi:10.1039/C1FD00043H
36. Raposo, M.; Lourenço, J. M. C.; Botelho do Rego, A. M.; Ferraria, A. M.; Ribeiro, P. A. *Colloids Surf., A* **2012,** *412,* 1–10. doi:10.1016/j.colsurfa.2012.05.005
37. Gupta, A. K.; Verma, Y. L.; Singh, R. K.; Chandra, S. *J. Phys. Chem. C* **2014,** *118,* 1530–1539. doi:10.1021/jp408142a
38. Pejaković, V.; Kalin, M. *Lubr. Sci.* **2015,** *27,* 463–477. doi:10.1002/ls.1289
39. Pejaković, V.; Igartua, A.; Kalin, M. *Lubr. Sci.* **2015,** *27,* 489–503. doi:10.1002/ls.1292
40. Restolho, J.; Mata, J. L.; Saramago, B. *J. Colloid Interface Sci.* **2009,** *340,* 82–86. doi:10.1016/j.jcis.2009.08.013
41. Ferraria, A. M.; Boufi, S.; Battaglini, N.; Botelho do Rego, A. M.; Vilar, M. R. *Langmuir* **2010,** *26,* 1996–2001. doi:10.1021/la902477q

License and Terms

BEILSTEIN JOURNAL OF NANOTECHNOLOGY

A comparative study of the nanoscale and macroscale tribological attributes of alumina and stainless steel surfaces immersed in aqueous suspensions of positively or negatively charged nanodiamonds

Colin K. Curtis[1], Antonin Marek[2], Alex I. Smirnov[2] and Jacqueline Krim[*1]

Full Research Paper

Open Access

Address:
[1]Department of Physics, North Carolina State University, Raleigh, NC 27695, USA and [2]Department of Chemistry, North Carolina State University, Raleigh, NC 27695, USA

Email:
Jacqueline Krim[*] - jkrim@ncsu.edu

* Corresponding author

Keywords:
additives; alumina; aqueous colloids; fractal; friction; lubricants; nanodiamond; nanotribology; quartz crystal microbalance; stainless steel

Beilstein J. Nanotechnol. **2017,** *8,* 2045–2059.
doi:10.3762/bjnano.8.205

Received: 27 May 2017
Accepted: 05 September 2017
Published: 29 September 2017

This article is part of the Thematic Series "Nanotribology".

Guest Editor: E. Gnecco

Abstract

This article reports a comparative study of the nanoscale and macroscale tribological attributes of alumina and stainless steel surfaces immersed in aqueous suspensions of positively (hydroxylated) or negatively (carboxylated) charged nanodiamonds (ND). Immersion in −ND suspensions resulted in a decrease in the macroscopic friction coefficients to values in the range 0.05–0.1 for both stainless steel and alumina, while +ND suspensions yielded an increase in friction for stainless steel contacts but little to no increase for alumina contacts. Quartz crystal microbalance (QCM), atomic force microscopy (AFM) and scanning electron microscopy (SEM) measurements were employed to assess nanoparticle uptake, surface polishing, and resistance to solid–liquid interfacial shear motion. The QCM studies revealed abrupt changes to the surfaces of both alumina and stainless steel upon injection of –ND into the surrounding water environment that are consistent with strong attachment of NDs and/or chemical changes to the surfaces. AFM images of the surfaces indicated slight increases in the surface roughness upon an exposure to both +ND and −ND suspensions. A suggested mechanism for these observations is that carboxylated −NDs from aqueous suspensions are forming robust lubricious deposits on stainless and alumina surfaces that enable gliding of the surfaces through the −ND suspensions with relatively low resistance to shear. In contrast, +ND suspensions are failing to improve tribological performance for either of the surfaces and may have abraded existing protective boundary layers in the case of stainless steel contacts. This study therefore reveals atomic scale details associated with systems that exhibit starkly different macroscale tribological properties, enabling future efforts to predict and design complex lubricant interfaces.

Introduction

Interest in nanoparticles as eco-friendly lubricant additives has grown tremendously in recent years [1,2]. The field is driven in a large part by a pressing need to replace hazardous additive materials in present-day oil-based lubrication technologies and to eliminate the serious environmental risks associated with oil leakage and disposal [3-5]. Water-based lubricant systems are a particularly attractive target for nanoparticulate additives since conventional oil additives generally fail to improve tribological performance in aqueous environments. Numerous studies of nanoparticulate additives to oil-based systems have been reported in the literature, with many displaying significant improvements in macroscopic friction and wear rates [6]. Water-based suspensions have received far less attention [1,2,7-9]. Although the low shear strength of water is beneficial in the hydrodynamic regime of lubrication, under normal loads it also enables contact between opposing surfaces. Nanoparticulate additives have the potential to overcome this deficiency, by penetrating into contacts where they may form boundary films and/or act as rolling or sliding spacers (Figure 1) [6,10,11]. As such, nanoparticles exhibit a great potential for replacement of the centuries-old oil-based lubricating technologies.

Tribological studies of water-based nanoparticle suspensions reported to date have mostly involved NDs. Reductions in kinetic friction coefficients μ_k by factors of 5–20 have been reported for metallic [7], ceramic [8], and semiconducting materials [2]. It is likely that the literature is reporting primarily on those nanoparticle additives with a beneficial tribological performance. Identification of nanoparticulate additives that are detrimental and/or have no effect have received much less attention even though such data are exceptionally useful for the purposes of evaluating test models [12]. Liu et al. recently investigated the tribological performance of steel/gold contacts in water using both nano- and macroscale measurements and found the contact to be highly sensitive to the sign of the charge on the NDs in suspension [9]. The authors suggested that the −ND suspensions were more likely to improve the tribological performance in macroscale settings than the +ND suspensions, and speculated that the electrostatic properties of the materials in contact might play a role. Generally, NDs require surface chemical treatments in order to be electrically charged in aqueous suspensions so as to inhibit aggregation via a mutual electrostatic repulsion, similar to other nanoparticles [2,9,13-15]. These chemical treatments are well known, however, to impact the friction coefficients in humid and dry environments for standard tip on disk geometries [16,17]. The surface chemical treatments employed in the production of the ND might therefore dominate the tribological performance. The surface charges on ND are also expected to affect the interfacial solid–fluid slip lengths attributes, and therefore the apparent fluid viscosity, via electroviscous and/or steric mechanisms [18-20]. Fundamental studies at the nanoscale are clearly essential at this time in order for the field to progress and for accurate model predictions to be developed.

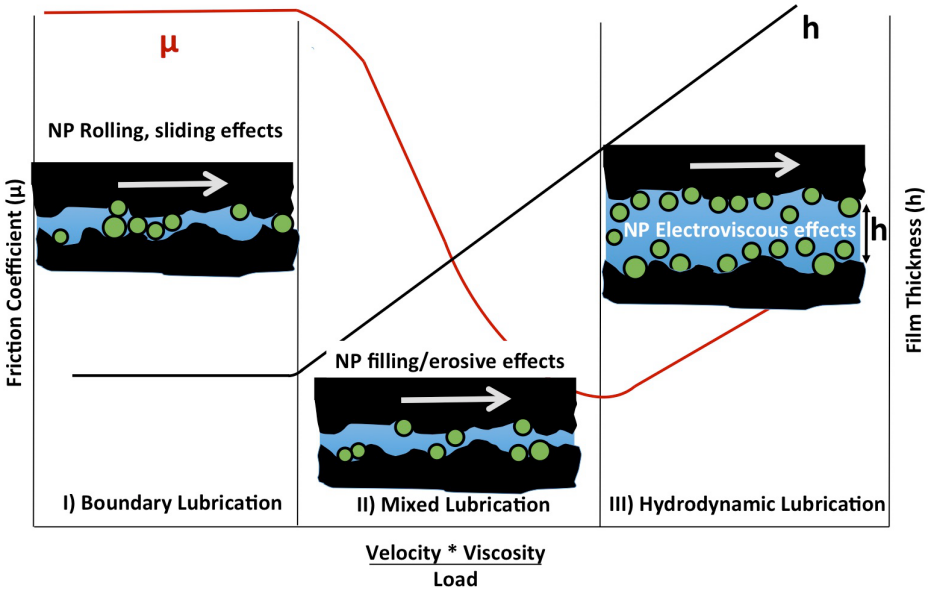

Figure 1: Friction coefficient plotted as a function of fluid viscosity and shear velocity divided by load (Stribeck curve). NPs present in a fluid could impact the tribological performance in all three lubrication regimes, for example by forming lubricious surface coatings or acting as rolling or sliding spacers at the contacts. In addition they may potentially fill or erode the contacts and/or cause the solid–fluid interfacial slip attributes to change via electroviscous and/or steric mechanisms. See text for further discussion.

QCM is emerging as an ideal tool for studying the fundamental mechanisms associated with nanoparticle lubrication [9]. While historically it was developed as a time standard and a deposition rate monitor for thin films [21], it has rapidly expanded in recent years to a broad range of applications through simultaneously monitoring of changes in frequency and quality factors [22-26]. It has become well known as a nanotribological technique for studying uptake and sliding friction levels of films in both in vacuum and liquid environments [23-25]. When immersed in liquid, it can be used to probe frictional drag forces and interfacial effects at complex solid–liquid interfaces [19,27] including those of a biological origin [18,22]. Given that the transverse shear speed of the oscillating QCM electrode is generally in the range of mm/s to m/s [23], it can readily be compared to conditions of macroscopic friction measurements. In addition, QCM experiments can be performed using an electrode in a rubbing contact with another macroscopic surface, for example a ball bearing [9,26], yielding important information on the shear strength and friction coefficients associated with macroscopic contacts.

For the present study, the QCM technique was employed to perform a comparative analysis of the tribological parameters of aqueous suspensions of either positively (hydroxylated) or negatively charged (carboxylated) NDs for the surfaces with contrasting electrical properties, namely insulating ceramic (alumina) and electrically conducting (stainless steel) surfaces immersed in suspensions of either positively (hydroxylated) or negatively charged (carboxylated) NDs (Figure 2).

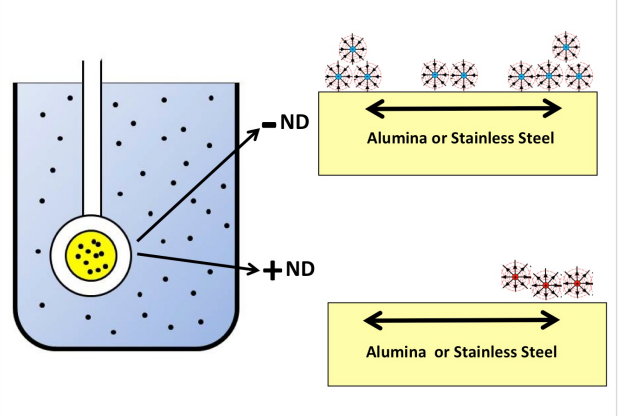

Figure 2: Schematic of a QCM immersed in aqueous suspensions of −ND and +ND, for sliding friction studies on materials with contrasting electrical properties, namely alumina and stainless steel. Adapted with permission from [9], copyright 2015, Royal Society of Chemistry.

The QCM measurement experiments were complemented by AFM and SEM measurements of the surface topography before and after the ND exposure, as well as macroscale measurements of μ_k. The materials were inspired by Liu et al.'s suggestion that differences in the tribological properties between +ND and −ND suspensions might originate in electrostatic effects [9], since the electrical charge carriers in the QCM electrodes might respond differently to positively and negatively charged nanoparticles. Would the effect therefore be absent for insulating materials? Was the explanation viable given the symmetry of electrostatic forces?

As will be reported, beneficial tribological behaviors were observed for immersion of stainless steel or alumina samples in −ND suspensions, while either neutral (alumina) or detrimental (stainless steel) behaviors were observed for immersion in +ND suspensions. This yields an exceptional opportunity for cross-comparisons with atomic scale tribological probes. At the atomic scale, the QCM and microscopy studies indicated uptake of particles, along with the potential presence of lubricious slurry for the −ND suspensions, somewhat analogous to boundary lubrication and steric repulsion effects by mucinous glycoproteins boundary layers in aqueous biological settings [18]. Such behavior was not observed for the +ND suspensions. The nanoscale mechanisms associated with effective lubrication therefore include boundary film deposits in combination with low interfacial resistance to shear motion in the suspension.

Materials and Methods

Materials

Aqueous suspensions of 5 nm detonation NDs with oppositely charged zeta potentials were purchased from Adamas Nanotechnologies (Raleigh, NC). All other chemicals were purchased from Sigma-Aldrich (St. Louis, MO) or Acros Organics (Morris Plains, NJ). The −ND samples were carboxylated [2,28], (part# ND5nmNH20) and as manufactured have an average particle size of 5 nm and a zeta potential of −50 mV [29]. The +ND samples were hydroxylated in the course of a reduction reaction [28], (part# ND5nmPH20) and, as manufactured, have an average particle size of 5 nm and a zeta potential of +45 mV. The suspensions were employed as received from the manufacturer in the form of 1 wt % slurries in DI water, and stored without exposure to light. The suspensions were diluted tenfold by volume in advance of experiments using DI water to yield 0.1 wt % suspensions employed in all measurements. While both stock and the diluted suspensions were found to be stable over a short storage up to 1 month, some slow agglomeration has been observed over a prolonged storage (e.g., see [9,29]).

Macroscale friction measurements were performed with ball-on-disk contacts of like materials. Alumina (Al_2O_3) ball and the disk contacts were purchased from PCS Instruments (London, United Kingdom), with respective part #'s MTMB3/4AL2O3 and MTMD3/4AL2O3.

Stainless steel (AISI 52100) polished ball and the disk contacts were also purchased from PCS Instruments (London, United Kingdom), with respective part #'s BALLD and MTMPD. Unpolished 304 stainless steel penny washers (part # HYW-M10-45-A2) were purchased from AccuGroup, (Huddersfield, United Kingdom) (304 stainless steel is also referred to as A2 stainless steel) and were employed as disks for selected measurements. Before the macroscale friction measurements all surfaces were cleaned in ethanol and then DI water.

5 MHz polished QCM crystals (1" diameter) with either stainless steel (SS304; part number QM1022) or aluminium (part number QM1010) electrodes on the liquid facing side were purchased from Fil-Tech (Boston, MA). The QCM's were specifically designed for operating with one surface immersed in a liquid at a fundamental transverse shear mode. The aluminum QCM samples were anodized using a literature method that grows an alumina layer at the rate of 2 μm/h [30]. For these results, the liquid side QCM electrode was connected as the anode and the sample was then immersed into 4 wt % oxalic acid solution maintained at 0 °C. A cathode was placed in the bath and an electric potential of 40 V was applied between the anode and the cathode. Anodization was halted at 3 min yielding an approximately 100 nm thick Al_2O_3 layer. After the anodization procedure, the samples were thoroughly rinsed with DI water before mounting the sample within the flow cell.

Macroscale friction measurements

Macroscopic scale friction coefficient measurements were performed with a MTM2 Mini-Traction Machine (PCS Instruments, London, UK). The apparatus is capable of measuring frictional properties of both lubricated and unlubricated contacts under either both sliding and rolling conditions. Its test specimens consist of a 19.05 mm (3/4 inch) ball and a 46 mm diameter disc. The ball is loaded against the face of the disc and the ball and disk are driven independently to create a mixed rolling/sliding contact. Force transducers measure the frictional forces, and additional sensors are present to measure the loading force and lubricant temperature in real time. For the measurements reported here, the setting were adjusted to a normal load of 4 N with a ball rolling speed of 200 mm/s and a slide to roll ratio of 90%, which resulted in a smooth friction coefficient versus time signal for both stainless steel and alumina contacts. Lubrication under such conditions allows one to probe of the ability of nanoparticulates to penetrate the contacts when they are introduced to fluids surrounding a contact [10].

A series of alumina–alumina and stainless steel ball on disk combinations were studied, ranging from pristine as-manufactured samples to samples that had experienced multiple exposures to DI water and ND suspensions. Contacting materials included both the alumina and stainless steel substrates obtained directly from the instrument manufacturer or stainless steel penny washers situated in place of the disk while in contact with the stainless steel ball.

Atomic force microscopy and scanning electron microscopy characterization of surface topology

Surface topology characterization of the QCM electrodes was performed with an Asylum Research MFP 3D AFM equipped with silicon nitride tips (part#NCHV-A, Bruker AFM Probes, Camarillo, CA) and operated in a tapping mode. The 1024 × 1024 images were recorded at a rate of 1 line/s yielding a height profile $h = h(x_i,y_i)$. The height profiles were quantified by the rms roughness value σ, which is virtually always dependent on the size of the area sampled below a characteristic lateral correlation length ξ. For a self-affine fractal surface the rms roughness increases with the lateral length of the sampled area as $\sigma \propto L^H$, where H is the roughness exponent whose value lies between 0 and 1. Fractal surfaces are often characterized by self-affine fractal dimension $D = 3 - H$ [31-33]. Self-affine surfaces have an upper horizontal cut-off length (the lateral correlation length (ξ)) above which the rms roughness saturates towards a value of σ_s and no longer exhibits fractal scaling. The surface roughness parameters (D, ξ and σ_s) reported herein were obtained from the log(σ) vs log(scan size) plot method as described by Krim and co-workers [32]. Previously, a detailed comparison of the results obtained by this method to several literature approaches yielded roughness parameters within experimental error of each other [33]).

Scanning electron microscope imaging was performed using an FEI Verios 460L field-emission microscope. A high resolution through-the-lens detector was used in a beam-deceleration mode for ultra-high resolution backscatter imaging of flat samples. For a typical SEM imaging, a whole QCM crystal (1" in diameter) was attached to a pin mount using a small piece of a double sided carbon tape. Sets of images at different magnifications ranging from 5×10^3 to 350×10^3 were recorded under typical settings of an accelerating voltage and a bias of 2.00 kV and 200 V, respectively.

Quartz crystal microbalance apparatus

QCM data were collected using a QCM100 (Stanford Research Systems, Sunnyvale, CA, USA) system. The system includes a controller, oscillator electronics and a Teflon holder and a flow cell that exposes one side of the crystal to approximately 0.15 mL of liquid, as well as providing mechanical support and electrical connections to the QCM electrode. All QCM experiments were carried out at room temperature and the temperature was stabilized by the thick, insulating polymer walls of the

flow-cell apparatus, as evidenced by the flatness in the frequency during initial and final water exposures. All liquids were kept adjacent to one another on the lab bench during the experiment to minimize temperature differences between them. A LabView (National Instruments, Austin, TX) PC-based data acquisition system was used to record both the crystal resonant frequency and the conductance voltage V_c, from the controller output. The conductance voltage, V_c, is related to the mechanical resistance, R_m, as $R_m = 10^{(4-V_c/5)} - 75$ [34]. Changes in mechanical resistance are directly proportional to changes in the inverse quality factor of the resonator, as will be described below.

Data were recorded as follows. The QCM sample was first placed into the flow-cell initially filled with ambient air. The system was operated continuously until the frequency and amplitude stabilized to less than 1 ppm/min. Once this stabilization occurred, DI water was injected into the flow-cell. Following 1 h water exposure, 10 mL of aqueous 0.1 wt % ND suspension was flushed into the flow-cell using a syringe pump. The use of a large excess of ND suspension ensured complete replacement of the DI water in the cell. Following 1 h of exposure to the ND suspension, 20 mL of DI water was flushed into the cell by a second syringe pump.

Quartz crystal microbalance data analysis

Analogous to the description in [9], changes in the resonant frequency, δf, and the inverse quality factor, $\delta(Q^{-1})$, of a QCM reflect changes in the mass and frictional energy losses of materials deposited onto its surface electrodes and/or drag forces and interfacial slippage of fluids that it is immersed in. For a QCM with one side immersed in a fluid with bulk density ρ_3 and viscosity η_3, the shifts in δf and $\delta(Q^{-1})$ associated with the presence of the liquid under no-slip boundary conditions are given by [35]:

$$\delta\left(Q^{-1}\right) = 2\alpha,\ \delta f = -f\alpha,\ \textit{where}\ \alpha = \sqrt{\frac{\rho_3\eta_3 f}{\pi\rho_q\mu_q}}, \quad (1)$$

where $\rho_q = 2.648$ g/cm^3 is the density and $\mu_q = 2.947 \times 10^{11}$ g/cm/s^2 is the shear modulus of quartz. Immersion of one side of a 5 MHz resonant frequency QCM in water at room temperature ($\rho_3 = 1$ g/cm^3, $\eta_3 = 0.01$ poise) results in a $\delta f = -714$ Hz drop in the resonant frequency and an increase of $\delta(Q^{-1}) = 2.85 \times 10^{-4}$ in the dissipation. For a QCM with quality factor $Q = 50{,}000$ in air this corresponds to a drop to $Q = 3{,}280$ after an immersion in water.

The viscous drag forces on the QCM electrode are mechanical in nature; a decrease in Q is manifested as an increase in the series resonant resistance R_m of the QCM resonator that can be measured electrically. For a QCM electrode exposed to a fluid from one side under non-slip conditions [36,37]:

$$\delta R_m = \frac{1}{8K^2C_0}\sqrt{\frac{\pi\rho_3\eta_3}{f\rho_q\mu_q}}, \quad (2)$$

where $K^2 = 7.74 \times 10^{-3}$ is the electromechanical coupling factor for the AT cut quartz (AT stands for temperature compensated transverse shear mode type A) and C_0 is the static capacitance of the QCM electrodes, including the parasitic capacitance associated with the connections to the oscillator circuit. A comparison of Equation 2 and Equation 3 reveals that δR_m is directly proportional to $\delta(Q^{-1})$: Both are reflective of the oscillator dissipative behaviour. For the QCM system employed here, the theoretical value for δR_m increase associated with the immersion of a 5 MHz resonant frequency QCM in water is approximately 300 Ω.

In practice, the frequency shifts observed upon immersion into a liquid environment are larger than those predicted by Equation 1 for perfectly planar QCM electrodes. This effect is attributed to the roughness of the surface electrode and can be minimized by using overtone polished crystals, but cannot be completely neglected because no surface has perfectly zero roughness. The magnitude of this contribution has been estimated to be in the range of 2–10% for materials with rms roughness of the same order as the QCM electrodes employed here [36-41]. Therefore, if a QCM surface immersed in a liquid becomes rougher or smoother while immersed in a liquid suspension of nanoparticles, its frequency will drop or increase in unison. A similar response is present also for the changes in the mechanical resistance.

In addition to the aforementioned contributions, nanoparticles may rigidly adhere to the surface when introduced into a liquid, resulting in further changes to the frequency and quality factor of the QCM in association with their mass loading effects. As originally reported by Sauerbrey, an additional rigidly adhering film deposited onto one side of a QCM will decrease its resonant frequency by [21]:

$$\delta f_{\text{film}} = -\left(\frac{m_f}{A}\right)\left(\frac{2f^2}{\sqrt{\rho_q\mu_q}}\right) = -2.264\times10^{-6}\left(\rho_2 f^2\right), \quad (3)$$

where $\rho_2 = (m_f/A)$ is the mass per unit area of the film in g/cm^2. This equation is the main basis for the use of QCM as a mass sensor in vacuum applications where the Equation 1 contribu-

tions from a surrounding fluid are absent. Martin et al. studied the effect of simultaneous mass and liquid loading on QCM and demonstrated that Equation 1 and Equation 3 can be added linearly to obtain the combined effect so long as the mass is not slipping on the surface electrode [36]. Therefore the frequency shift associated with mass uptake from a liquid is the same as mass uptake from a vacuum.

If the adsorbed particles slip on the QCM surface in a response to the oscillatory motion, and/or the no-slip boundary conditions are altered at the upper boundary of the film with the surrounding liquid, the magnitude of the frequency shift δf_{film} will be lower than that of a rigidly attached film [27,37,40]. These effects may cause the liquid's effective viscosity to appear to increase or decrease due to electroviscous or steric effects [19]. They will also be reflected in the QCM's quality factor, Q, since the friction associated with the oscillatory motion is manifested in the quality factor. Therefore, while the exact details of the complex solid–liquid–nanoparticle interface may be unknown, changes in the quality factor reflect outright the frictional resistance forces at the interface, and in particular whether the combined resistance to shear motion at the solid–liquid interface. Frequency shifts due to changes in temperature and/or stress on crystal by the added mass layer are expected to be very minimal for the present work, since the measurements were performed at constant room temperature.

Results

Macroscale friction measurements

Figure 3 shows representative data recorded in a macroscale friction experiment when the contacting surfaces become exposed to ND suspensions. The data reveal a clear difference between the surfaces exposed to +ND and −ND suspensions. Introduction of −ND suspensions consistently resulted in a substantial reductions in $\mu_{k,}$ to the range of 0.05–0.1 while +ND consistently resulted in a modest to substantial increases in μ_k. Substantial increases in μ_k were observed for the stainless steel surfaces exposed to the +ND suspensions while alumina surfaces showed only modest to negligible increases in μ_k. The data do not appear to correlate with the σ_s or fractal dimension D of the samples [42], which were measured by AFM to respectively be (6 nm, 2.4); (9 nm, 2.2); and (50 nm, 2.1) for the polished AISI 52100 stainless steel disk, 304 stainless steel penny washer, and alumina disk samples.

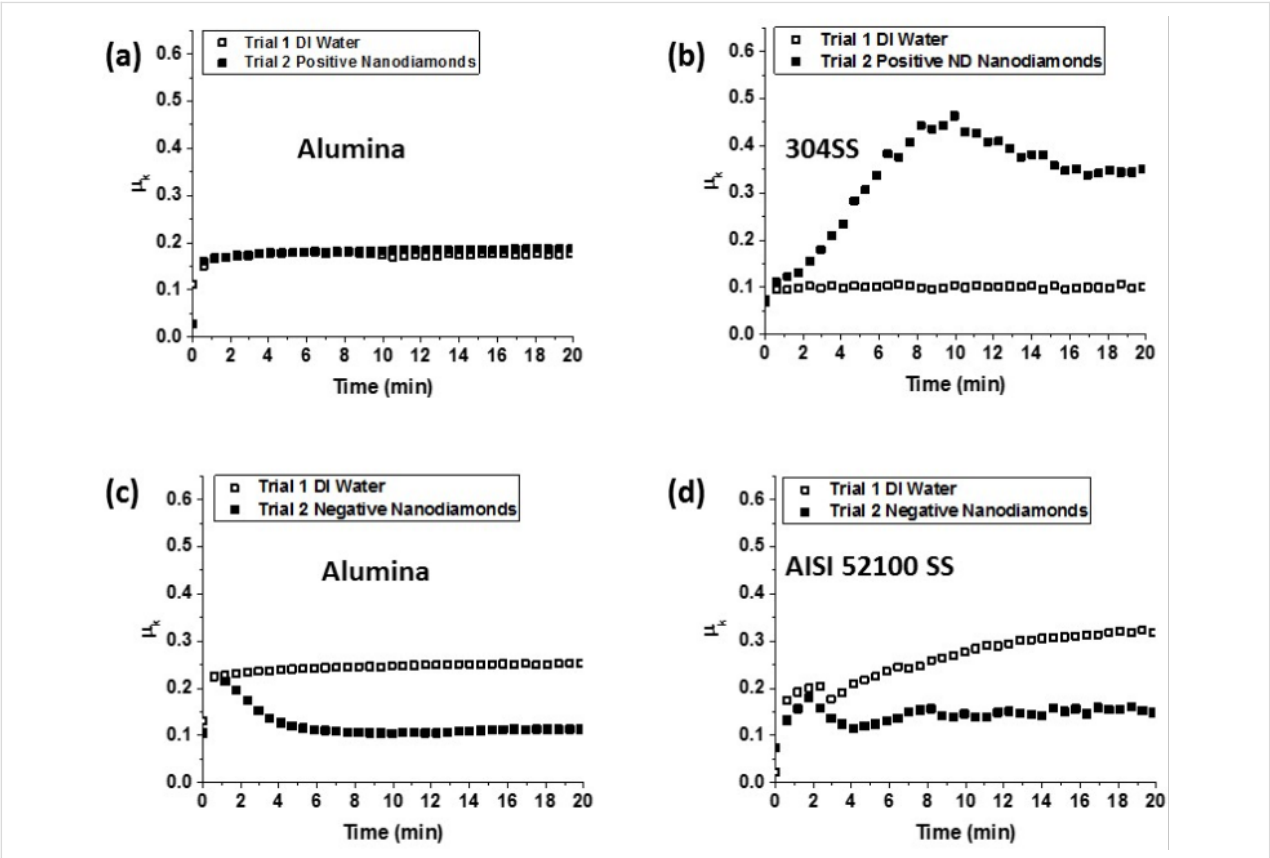

Figure 3: Representative friction coefficient versus time plots for alumina (left) and stainless steel (right) contacts lubricated with pure DI water (open squares), positively (a,b) and negatively (c,d) (filled squares) charged ND suspensions. Addition of −ND to water (c,d) consistently lowered the friction coefficient while addition of +ND to water consistently (a,b) failed to lower the friction coefficient.

After the experiments with ND suspensions, selected samples were removed, cleaned extensively in DI water in an ultrasonic bath, and then measured again. In these trials, μ_k remained unchanged for samples that had been exposed to +ND suspensions, and increased slightly for those which had been exposed to −ND suspensions. Exposure of the samples to a ND suspension of the opposite sign would, however, immediately alter the friction coefficient. For example, if a sample was immersed in a ND suspension with an opposite surface charge to its first exposure, μ_k would shift up or down depending on the sign of the ND charge in the second exposure.

The observations suggest that −ND have a strong affinity for the surfaces studied and act as passivation agents. They also reveal that −ND and +ND may act as neutralizing or removal agents for one another. In order to probe ND attachment/film formation and/or polishing effects for the surfaces as a whole and to separate this from effects confined within the contact region, AFM and QCM measurements were performed on surfaces exposed to ND suspensions in the absence of a contacting load. In the absence of a contact, the ND are still potentially abrasive, on account of the oscillatory nature of the QCM electrode and the associated high acceleration rates.

AFM and SEM measurements

AFM measurements of open surfaces exposed to ND suspensions were performed directly on samples employed for the QCM studies so as to be able to directly cross-reference results obtained from the two techniques. Images were recorded in air, after 1 h of QCM oscillation while immersed in water and after one hour of QCM oscillation while immersed in a ND suspension. The high frequency nature of the oscillation in the presence of the NDs slurries could potentially remove the electrode material but NDs might also attach to the surface. AFM measurements were recorded in at least triplicate for each unique solid:ND combination.

Figure 4 shows representative images of stainless steel 304 (left) and alumina (right) QCM electrodes after oscillating in DI water for 1 h, −ND and +ND suspensions for 1 h , and then rinsed in DI water. Images (b), (c) and (e) for alumina and SS304 surfaces immersed in −ND and SS304 surfaces immersed in +ND indicate changes to the surface electrodes, with (e) the alumina surfaces exposed to −ND exhibiting the most pronounced differences as compared to the water exposure only. Image (f) for alumina surfaces exposed to +ND meanwhile shows no visual evidence of NDs. The Figure 4 images do not specifically reveal whether substrate material was removed in a polishing process during immersion as has been clearly documented for gold QCM electrodes in aqueous suspensions of SiO_2 [43]. While alumina and SS304 may not be as susceptible to erosion and polishing as gold, NDs could potentially remove the electrode material by an accelerated penetration into surface asperities by the oscillatory action of the QCM [44-46].

Additional scanning electron microscopy (SEM) images (Figure 5) were recorded on the SS304 samples to further elucidate changes in the surface topology after exposure to NDs followed by rinsing in DI water. Alumina samples became rapidly charged upon an exposure to an electron beam (presumably due electrically isolating alumina layer still present on the electrode surface), preventing high quality SEM images from being recorded. Features associated with permanently adhering nanoparticles are present in the images for the samples exposed to ND. For the case of −ND exposure, the attached particles are clustered and the deposits are more uniformly distributed over the surface. The +ND exposure results in very sparse deposits, which form dendritic surface aggregates in regions where they are present.

The AFM and SEM data are consistent with the results from nanodiamond seeding literature [46], where it has been reported that the particle attachment density can, for example, vary from very low (10^8 cm^{-2}) for hydrogen treated nanodiamonds (+ND) to very high (10^{11} cm^{-2}) for oxidized nanodiamonds (−ND) on AlN substrates [47]. The data are also consistent with a report on a formation of ND clusters of ca. 23 nm in diameter on SiO_2 surfaces exposed to ND dispersions [48]. Clusters of this size are large enough to separate the surfaces employed for the Section ‘Macroscale friction measurements’.

In order to characterize adhesion of NDs to surfaces quantitatively, the QCM frequencies and resistances were compared for crystals exposed to air before and after the exposure to the ND suspensions (followed by a rinse in pure water). The results, summarized in Table 1, exhibit a decrease in frequency after the exposure to the suspensions regardless of the ND surface charge sign. While some of the downward shifts in frequency may be attributable to a variation in the uptake of particulate and physisorbed species from air, the net mass increase is consistent with the addition of NDs in levels that exceed the mass of any material removed from the QCM electrode arising from the potentially erosive action of the ND. Consistent with the images, a definitive mass uptake is present for the alumina sample immersed in the −ND suspension. Resistance shifts were virtually zero for the stainless steel samples and consistent with the rigidly attached NDs. The increase in resistance for the alumina samples immersed in +ND is consistent with the presence of poorly attached layers that are slipping on the surface. This might be attributable to loosely attached NDs or physisorbed

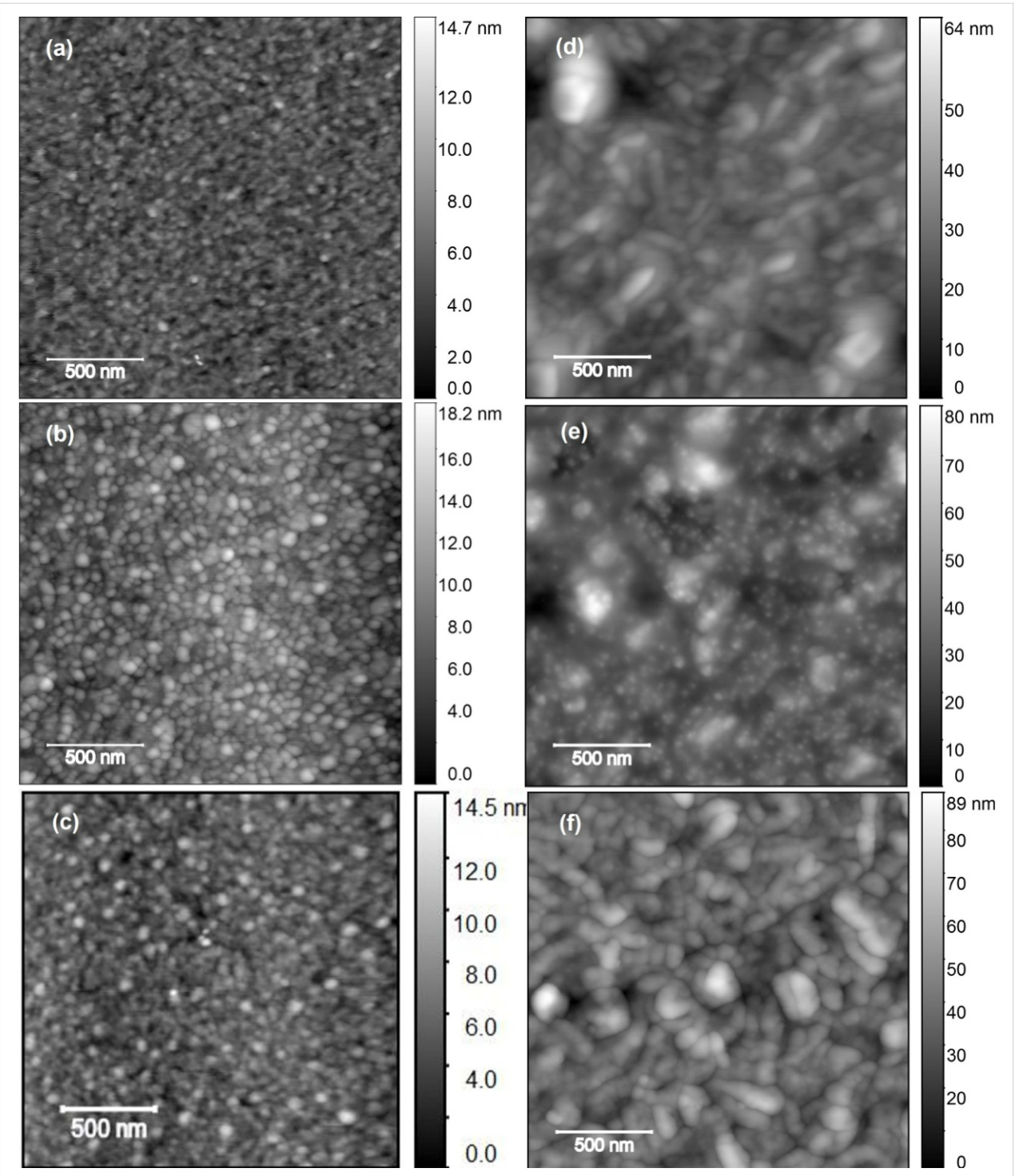

Figure 4: Representative AFM images of stainless steel 304 (left) and alumina (right) QCM electrodes after 1 h of oscillation in DI water (upper), −ND (middle) and +ND (lower) suspensions and then rinsing in DI water.

adsorbates, neither of which would be readily observed by AFM.

In order to convert the frequency shifts to particle density on the surface, we assume a cluster size of 25 nm and a packing fraction within the cluster of 0.7. The mass of each cluster would be $[(25\ \text{nm}/5\ \text{nm})^3] \times 0.7\ (2.29 \times 10^{-19}\ \text{g}/5\ \text{nm particle}) = 2 \times 10^{-17}$ g. A surface coverage of 10^{10} clusters per cm^2 therefore has a mass per unit area of $\rho_2 = 2 \times 10^{-7}$ g/cm^2, which corresponds to a decrease in the resonant frequency of 11.3 Hz (cf.

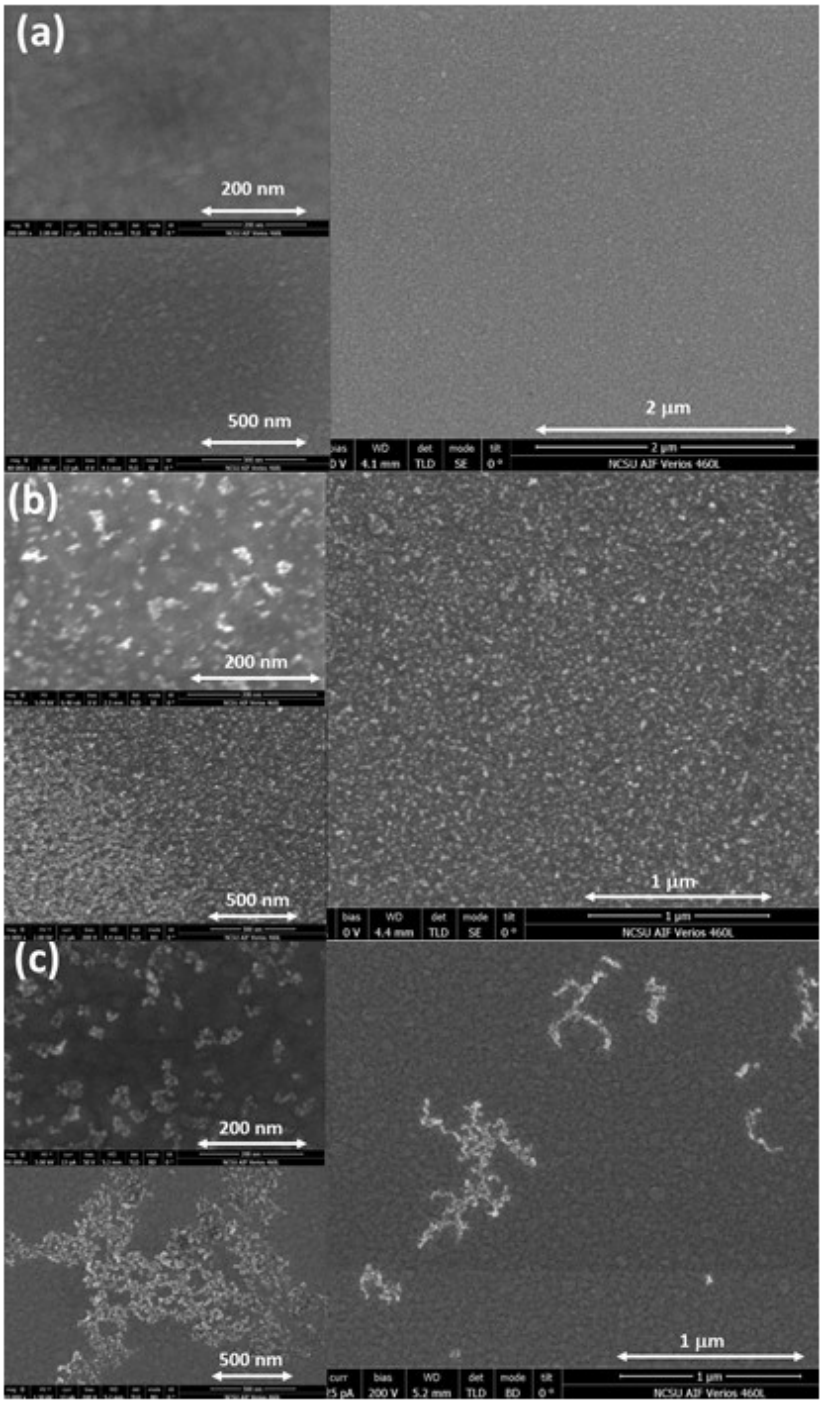

Figure 5: SEM images of SS304 QCM electrodes after oscillated in (a) water, (b) −ND, and (c) +ND suspensions for 1 h and then rinsed in DI water. See text for further details.

Equation 3). For comparison, a monolayer of spherical 5 nm diamond nanoparticles packed in the closest hexagonal arrangement (assuming diamond bulk density of 3.5 g/cm^3; mass per particle: 2.29×10^{-19} g) corresponds to 4.6×10^{12} ND/cm^2, $\rho_2 = 1.058 \times 10^{-6}$ g/cm^2 and a decrease in the resonant frequency of 59.8 Hz.

Graphs of log(σ) vs log(scan size) obtained from the AFM images shown in Figure 4 are presented in Figure 6. Each data point represents an average of multiple locations on the surface. The slope of a linear fit in lower length scale gives the roughness exponent (*H*), and an exponential fit for the larger length scale gives the asymptotic value of σ_s, as described earlier.

Table 1: QCM frequency (+/−15 Hz) and resistance shifts (+/−1 Ω) in air before and after 60 min of oscillation in aqueous ND suspensions. The equivalent surface coverage of 25 nm clusters is also reported (+/−1 × 10^{10} clusters/cm^2).

Sample	+ND suspension immersion		25 nm cluster coverage level	−ND suspension immersion		25 nm cluster coverage level
	δ*f* (Hz)	d*R* (Ω)	clusters/cm^2	δ*f* (Hz)	d*R* (Ω)	clusters/cm^2
alumina	−8	+15.5	0.7 × 10^{10}	−69	−1.6	6.1 × 10^{10}
SS304	−18	−0.1	1.6 × 10^{10}	−25	−0.1	2.2 × 10^{10}

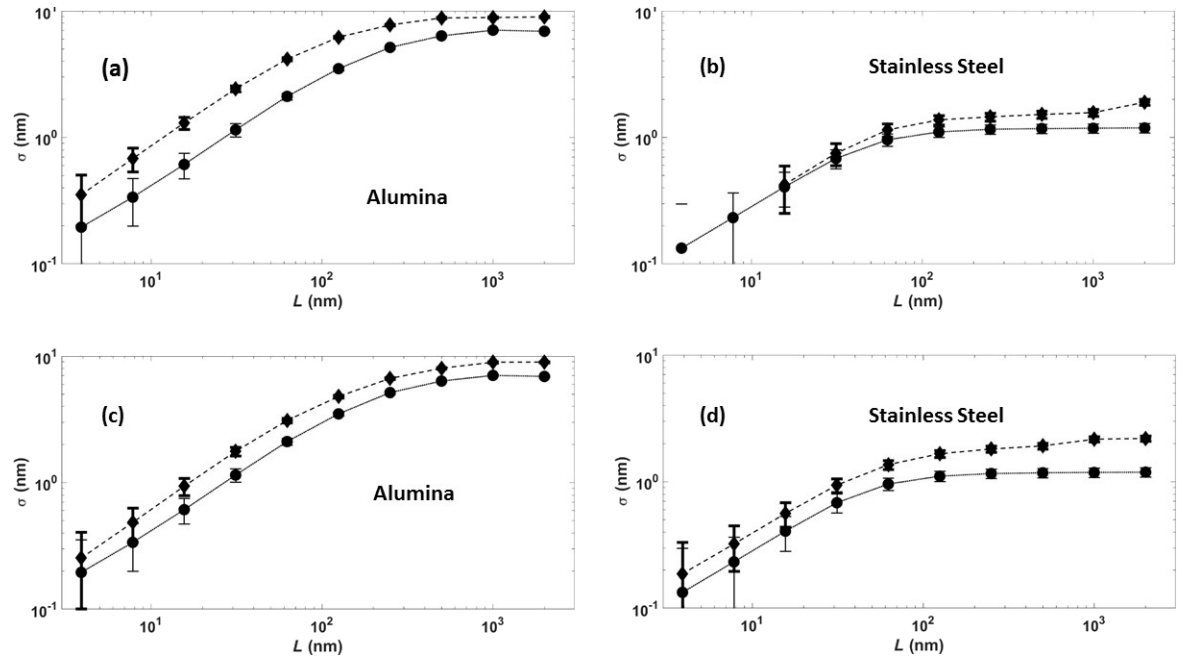

Figure 6: RMS roughness σ versus scan size *L* for QCM electrodes comprised of alumina (left) and stainless steel (right) after an oscillation for 1 h in DI water (solid lines) and after an oscillation for 1 h in suspensions of either positively (a),(b) or negatively (c),(d) (dashed lines) charged NDs. See text for details.

All samples exhibited increases in σ_s after an oscillation in ND suspensions (Table 2). Alumina surfaces, however, exhibited greater increases in σ_s than SS304. Only the SS304 sample exposed to +ND exhibited a change in *D*, increasing from 2.2 to 2.3, which corresponds to a more jagged surface texture [30]. It is interesting to note that this is the only surface studied that exhibited a striking increase in friction upon an exposure to the NDs.

QCM measurements

Frequency *f* and mechanical resistance *R* values of QCM relative to their initial values in air, *f*_air and *R*_air, are summarized in Figure 7. All QCM crystals were first exposed in DI water for 1 h followed by +ND or −ND dispersions for another 1 h and then returned to DI water for an additional 1 h. Fluid injections at 1 and 2 h in some cases caused temporary perturbations in *f* and *R* that serve as markers delineating the three

Table 2: Saturated rms roughness σ_s (+/−0.1 nm) and fractal dimension *D* (+/−0.05) of QCM electrodes after 1 h of oscillation in DI water or ND suspensions.

Samples	Pure DI water		+ND suspension		−ND suspension	
	σ_s (nm)	*D*	σ_s (nm)	*D*	σ_s (nm)	*D*
alumina	7.8	2.1	9.8	2.1	9.9	2.1
SS304	1.2	2.2	1.6	2.3	2.4	2.2

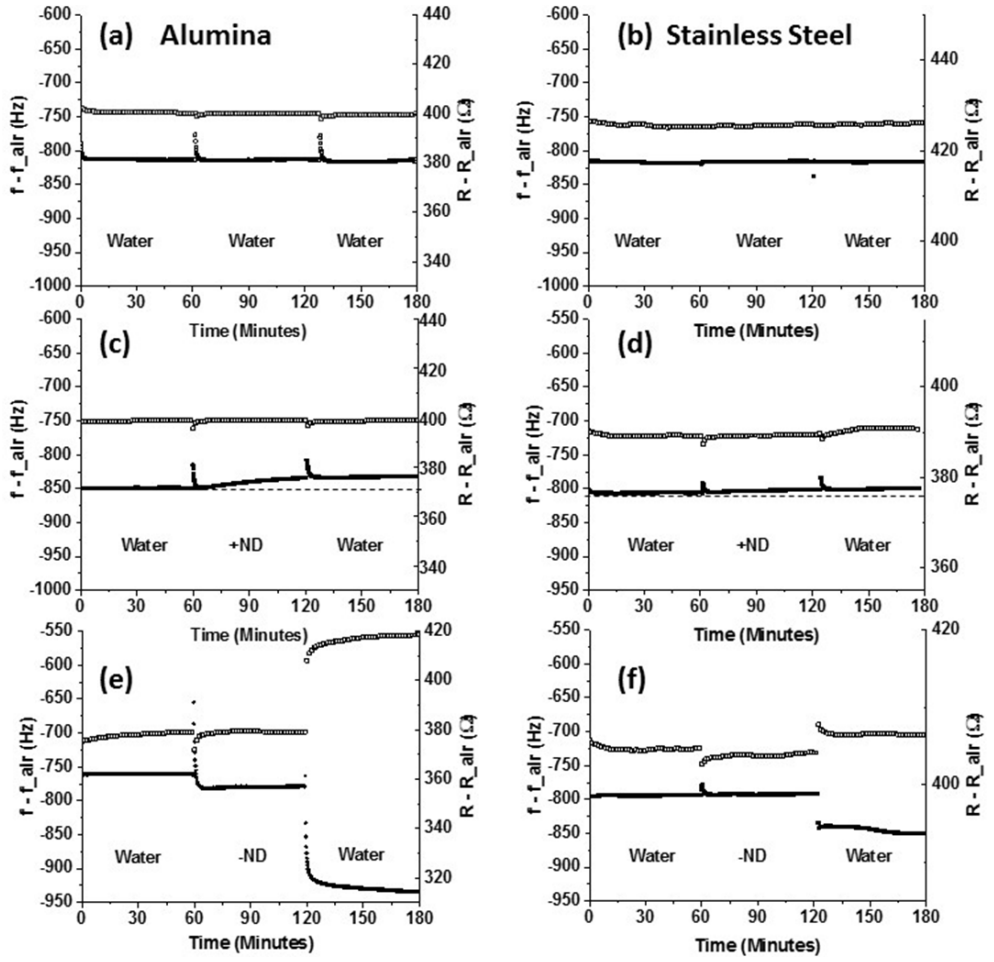

Figure 7: Time course of changes in mechanical resistance, *R* (top, open squares), and frequency *f* (bottom, filled squares), of QCM relative to air for SS304 (right) or alumna (left) electrode surfaces consequently exposed to DI water (a and b); +ND and water (c and d); −ND and water (e and f).

regimes of exposure. All experiments were conducted at in at least triplicate using new QCM crystals, and only minor differences were observed between the individual runs.

Control runs in DI water (i.e., no ND exposure) are displayed in Figure 7a and 7b for the alumina and SS304 electrodes. Only minimal changes in *f* and *R* are observed in the control runs, apart from the momentary perturbations occurring at the time of pure water injections. Also, the drops in *f* and *R* relative to those recorded air are larger than the theoretical values for perfectly planar surfaces, −714 Hz and 300 Ω. These large experimental shifts are attributable to the surface roughness of the electrodes.

Changes in *f* and *R* for the samples exposed to ND suspensions were found to be dependent on the ND surface charge. Both the alumina and SS304 samples exhibit a slow, yet a small increase in *f* upon an exposure to +ND suspension (Figure 7c and 7d) that ceases upon re-entry of DI water. Given the AFM results indicating that both surfaces become slightly rougher upon an exposure to +ND, the upward trend does not appear to be attributable to the surface polishing but rather some modest erosive effects. Virtually no changes in the resistance to shear motion at the solid liquid interface were observed upon an introduction of the +ND. Such changes might result from loosely bound particles enabling some decoupling of the mass of the fluid surrounding the QCM with no significant reductions in the friction energy losses at the interface.

In contrast, significant changes in both *f* and *R* observed upon an exposure of both types of surfaces to −NDs and consequent rinsing in DI water (Figure 7e and 7f). Specifically, upon exposing the QCM to −ND suspension both *f* and *R* abruptly drop for the alumina sample while for the SS304 sample the frequency is essentially unchanged while *R* drops abruptly. Upon rinsing, an abrupt drop in *f* and a rise in *R* are observed for both surfaces. The QCM data provide a clear evidence of the −ND exposure permanently altering the both surfaces. These surface

alterations appear to have a direct effect on the shear forces encountered at the solid–liquid interfaces. This global surface treatment may in fact provide a key piece of evidence to the fundamental mechanism underlying the friction reductions observed at the macroscale for the stainless steel and alumina surfaces immersed in −ND suspensions.

Discussion

The data reported here reveal key similarities and differences in both the macro- and nanotribological properties of stainless steel and alumina when exposed to ND aqueous dispersions. While Liu et al.'s suggestion that −ND dispersions are more likely to improve the tribological performance at the macroscale than the +ND dispersions [9] has been validated, the previous explanation of the underlying mechanism by strictly electrostatic appears to be somewhat simplistic within the context of simply comparing insulating alumina and conducting stainless steel surfaces.

For QCM electrodes coated with aluminum, the surface-exposed aluminum metal is readily oxidized to Al_2O_3 under ambient air. This surface layer of alumina is protecting the rest of metal from a further corrosion. In our experiments, the electrodes were additionally anodized for 3 min. This procedure is expected to yield approximately 50–100 nm thick Al_2O_3 layer. For Al_2O_3 is exposed to water one expect a formation of several aluminum hydroxide phases [49]. The presence of hydroxy (OH) groups on the alumina surface is affected by the oxide surface structure as well as other parameters with pH being the most important. Overall, the surface hydroxy groups determine electrostatic properties of the surface that, in turn, affect interactions of charged nanoparticles (NDs in this study) with the QCM alumina electrode.

In the past Cuddy et al. employed contact angle titration to determine Isoelectric points (IEPs) for five common (QCM) sensors [50]. Specifically, they reported a mildly basic IEP = 8.7 for Al_2O_3 sensors. Therefore, the QCM alumina surface is likely to be positively charged at the neutral pH of our experiments and this would explain a rapid uptake of negatively charged NDs on the electrode surface observed in our QCM experiments. Thus, this observation is in agreement with Liu's electrostatic hypothesis [9]. We note that recently an electrostatic self-assembly seeding of monosized individual diamond nanoparticles (obtained by a detonation method) on silicon dioxide surfaces has been reported [51]. Although the latter study employed an aqueous dispersion of positively charged NDs, the silica surface is expected to be charged negatively at normal pH (IEP = 3.9, [50]) providing the same short-range electrostatic forces responsible for the ND surface self-assembly.

The EIP of SS304 surfaces, however, is somewhat acidic but could vary over a broader range from ca. 3.2 to 5.0 depending on the sample surface treatment according literature data summarized in [52]. Thus, at neutral pH or at a somewhat acidic pH of the DI water absorbing CO_2 from air, the SS304 surface is expected to bare some negative change or no charge at all. Therefore, electrostatic interactions alone would not explain effects on −ND on tribological properties of SS304 surfaces.

One common feature observed in the data sets is that −ND dispersions produced through carboxylation consistently reduced the macroscopic friction coefficient relative to DI water by a factor of 2–5 for all stainless steel and alumina contacts studied and the value upon immersion consistently dropped into the range 0.05–0.1. QCM studies of stainless steel and alumina surfaces immersed in −ND dispersions meanwhile displayed behaviors consistent with a rapid uptake of −NDs, some slight but measurable increases in the surface roughness and distinct changes in the nature of the solid–liquid interfacial resistance to shear. These systems also exhibited an abrupt drop in f and an increase in R when re-exposed to pure DI water. The latter behavior is potentially explained by the suspended −ND nanoparticles acting as a lubricious slurry reducing resistance at the solid–liquid interface through potentially electrostatic repulsion with the rest of the −NDs in the surrounding suspension [20,43]. This suggestion, which is somewhat analogous to boundary lubrication and steric repulsion effects by mucinous glycoproteins boundary layers in aqueous biological settings [18], remains an intriguing possibility for the future investigations. The permanent changes observed in the surfaces morphology are likely associated with strong chemical attachment of −NDs in a manner distributed over the surface to form a more lubricous sliding interface than the bare surfaces alone.

It is notable that the literature on the contacts lubricated by aqueous ND suspensions for a range of materials reports the friction coefficients in the same range, 0.05–0.1, as observed here [2,7,8], while NDs similar to those employed here result in a markedly lower friction coefficients when treated with a dispersant so as to form colloids in oils [53]. This is consistent with a suggestion that the surface passivation treatments of NDs have great impact on the tribological properties. The notion is well known in the literature for diamond on diamond contacts in a variety of vacuum and humid environments [17,54-58]. The films of NDs strongly attached to surfaces are capable of providing both boundary lubrication and, potentially, a solid–liquid interface with a low resistance to shear. Therefore a custom design of nanolubrication systems by a proper chemical passivation of ND surfaces appears as a promising approach.

Hydroxylated NDs bearing a positive zeta potential in aquelus dispersion, produced no significant response in the frequency or resistance behavior of the QCM electrode covered with either alumina or SS304. While it is reasonable that the carboxylated −ND might exhibit more affinity to the alumina and stainless surfaces studied, one might conclude that the +ND suspensions would have little impact on the macroscale friction coefficients measured. But the friction increased significantly for the stainless steel materials. This may arise from corrosive and/or tribocorrosive effects at the macroscopic steel on steel interface being exacerbated by an abrasive action in the confined contact [59,60], a phenomena which was not probed by the AFM and QCM methods utilized here. It is notable that the changes in the QCM behavior upon immersion in +ND suspensions were very slow and gradual, in a stark contrast to the effects of the −ND suspensions. Detrimental wear at the macroscale might well out-pace any beneficial effects of ND for such liquid–solid interfaces.

We note that water was chosen as a liquid lubricant for this study so the results could be directly compared with preceding experiments of Liu et al. who employed QCM to investigate lubricating properties of aqueous suspensions of positively and negatively charged detonation nanodiamonds for gold electrode surfaces [9]. It is worthwhile to note that the methods described here are fully applicable to fluids other than water as long as the viscosity is sufficiently low for QCM to oscillate. Further studies will undoubtedly lead to a better understanding of third-body problems as well as improved design of the nanoparticle-based lubricants. Importantly, we have identified systems exhibiting beneficial, neutral, and detrimental tribology properties, facilitating additional experimental as well as theoretical studies from the first principles approach.

Conclusion

A comparative study of the nanoscale and macroscale tribological attributes of alumina and stainless steel surfaces immersed in positively (hydroxylated) or negatively (carboxylated) charged nanodiamond (ND) dispersion is reported here. The work has revealed key similarities and differences between the surfaces that are effectively or ineffectively lubricated by aqueous suspensions of ND. The principle observations and conclusions are as follows:

- Immersion in −ND aqueous dispersion consistently resulted in a reduction in μ_k, for the stainless steel and alumina samples studied, falling by a factor of 2–5 to a steady state value in the range 0.05–0.1.
- Immersion in +ND aqueous dispersion consistently increased μ_k, for the stainless steel contacts and resulted in little to no increases for the alumina contacts.
- QCM and AFM measurements documented a rapid change in the surfaces of both alumina and stainless steel upon an exposure to −ND, consistent with a strong attachment of particles to the surfaces.
- The surfaces, upon uptake of ND, were characterized by a low resistance to shear at the interface between the solid and the aqueous −ND dispersion.
- Negligible polishing and/or abrasive effects were observed for QCM electrode surfaces after oscillating in either +ND or −ND dispersions for 1 h. The roughness of all the surfaces increased slightly upon an exposure to ND suspensions. This could be attributed to an attachment of NDs to the surface and/or some erosion effects.
- The +ND nanoparticles were not observed to rigidly adhere to the surfaces, for example, as a chemically bound adlayer, but some limited evidence was present for a loose attachment to alumina and very low coverages of dendritic aggregates on stainless steel.
- A suggested mechanism for the observations is that carboxylated −NDs in an aqueous dispersion form robust, lubricious film deposits on stainless steel and/or alumina surfaces that are both readily replenished by the surrounding suspensions and also glide through it with a relatively low resistance to shear, potentially because of the repulsive electrostatic forces between the individual particles.

In summary, this study provides for atomic scale details associated with systems that exhibit radically different macroscale tribological properties. It also reveals a broad class of materials that will be of great value in enabling theoretical efforts to predict and model complex lubricant interfaces.

Acknowledgements

This work was supported by NSF DMR1535082. SEM studies were performed at the Analytical Instrumentation Facility (AIF) at North Carolina State University, which is supported by the State of North Carolina and the NSF (Award Number ECCS-1542015). The AIF is a member of the North Carolina Research Triangle Nanotechnology Network (RTNN), a site in the National Nanotechnology Coordinated Infrastructure (NNCI). We are grateful to B. Acharya, D. Berman, D. Brenner, J. A. Harrison and K. J. Wahl for useful discussions. M. Chestnut and B. Vasconcelos de Farias are respectively thanked for assistance with recording of the electron micrographs and macroscale tribology measurements.

References

1. Wu, H.; Zhao, J.; Xia, W.; Cheng, X.; He, A.; Yun, J. H.; Wang, L.; Huang, H.; Jiao, S.; Huang, L.; Zhang, S.; Jiang, Z. *Tribol. Int.* **2017,** *109,* 398–408. doi:10.1016/j.triboint.2017.01.013

2. Osawa, E. In *Handbook of Advanced Ceramics;* Somiya, S., Ed.; Academic Press, 2013; pp 89–102. doi:10.1016/B978-0-12-385469-8.00004-6
3. Torres-Sanchez, C.; Balodimos, N. *Packag. Technol. Sci.* **2017,** *30,* 209–218. doi:10.1002/pts.2294
4. Betton, C. I. *Chemistry and Technology of Lubricants;* Springer US: Boston, MA, 1994; pp 282–298. doi:10.1007/978-1-4615-3554-6_13
5. Mortier, R. M.; Fox, M. F.; Orszulik, S. T., Eds. *Chemistry and technology of lubricants;* Springer Netherlands: Dordrecht, 2010; Vol. 53.
6. Dai, W.; Kheireddin, B.; Gao, H.; Liang, H. *Tribol. Int.* **2016,** *102,* 88–98. doi:10.1016/j.triboint.2016.05.020
7. Alias, A. A.; Kinoshita, H.; Fujii, M. *J. Adv. Mech. Des., Syst., Manuf.* **2015,** *9,* No. 6. doi:10.1299/jamdsm.2015jamdsm0006
8. Liu, Y.; Wang, X.; Pan, G.; Luo, J. *Sci. China: Technol. Sci.* **2013,** *56,* 152–157. doi:10.1007/s11431-012-5026-z
9. Liu, Z.; Leininger, D.; Koolivand, A.; Smirnov, A. I.; Shenderova, O.; Brenner, D. W.; Krim, J. *RSC Adv.* **2015,** *5,* 78933–78940. doi:10.1039/C5RA14151F
10. Chiñas-Castillo, F.; Spikes, H. A. *J. Tribol.* **2003,** *125,* 552–557. doi:10.1115/1.1537752
11. Jacobson, S.; Hogmark, S. *Wear* **2009,** *266,* 370–378. doi:10.1016/j.wear.2008.04.035
12. Pieper, C.; Oschmann, T.; Markauskas, D.; Kempf, A.; Fischer, A.; Kruggel-Emden, H. *Chem. Eng. Technol.* **2016,** *39,* 1497–1508. doi:10.1002/ceat.201500647
13. Yang, N.; Foord, J. S.; Jiang, X. *Carbon* **2016,** *99,* 90–110. doi:10.1016/j.carbon.2015.11.061
14. Galli, G. Structure, Stability and Electronic Properties of Nanodiamonds. In *Computer-Based Modeling of Novel Carbon Systems and Their Properties;* Colombo, L.; Fasolino, A., Eds.; Carbon Materials: Chemistry and Physics, Vol. 3; Springer: Dordrecht, 2010; pp 37–56. doi:10.1007/978-1-4020-9718-8_2
15. Holt, K. B. *Philos. Trans. R. Soc., A* **2007,** *365,* 2845–2861. doi:10.1098/rsta.2007.0005
16. Brewer, N. J.; Beake, B. D.; Leggett, G. J. *Langmuir* **2001,** *17,* 1970–1974. doi:10.1021/la001568o
17. Konicek, A. R.; Grierson, D. S.; Gilbert, P. U. P. A.; Sawyer, W. G.; Sumant, A. V.; Carpick, R. W. *Phys. Rev. Lett.* **2008,** *100,* 235502. doi:10.1103/PhysRevLett.100.235502
18. Coles, J. M.; Chang, D. P.; Zauscher, S. *Curr. Opin. Colloid Interface Sci.* **2010,** *15,* 406–416. doi:10.1016/j.cocis.2010.07.002
19. Granick, S.; Zhu, Y.; Lee, H. *Nat. Mater.* **2003,** *2,* 221–227. doi:10.1038/nmat854
20. Jing, D.; Pan, Y.; Wang, X. *Beilstein J. Nanotechnol.* **2017,** *8,* 1515–1522. doi:10.3762/bjnano.8.152
21. Sauerbrey, G. *Z. Phys.* **1959,** *155,* 206–222. doi:10.1007/BF01337937
22. Qiao, X.; Zhang, X.; Tian, Y.; Meng, Y. *Appl. Phys. Rev.* **2016,** *3,* 031106. doi:10.1063/1.4963312
23. Krim, J. *Adv. Phys.* **2012,** *61,* 155–323. doi:10.1080/00018732.2012.706401
24. Pisov, S.; Tosatti, E.; Tartaglino, U.; Vanossi, A. *J. Phys.: Condens. Matter* **2007,** *19,* 305015. doi:10.1088/0953-8984/19/30/305015
25. Highland, M.; Krim, J. *Phys. Rev. Lett.* **2006,** *96,* 226107. doi:10.1103/PhysRevLett.96.226107
26. Vlachová, J.; König, R.; Johannsmann, D. *Beilstein J. Nanotechnol.* **2015,** *6,* 845–856. doi:10.3762/bjnano.6.87
27. Huang, K.; Szlufarska, I. *Langmuir* **2012,** *28,* 17302–17312. doi:10.1021/la303381z
28. Shenderova, O.; Koscheev, A.; Zaripov, N.; Petrov, I.; Skryabin, Y.; Detkov, P.; Turner, S.; Van Tendeloo, G. *J. Phys. Chem. C* **2011,** *115,* 9827–9837. doi:10.1021/jp1102466
29. Kaszuba, M.; Corbett, J.; Watson, F. M.; Jones, A. *Philos. Trans. R. Soc., A* **2010,** *368,* 4439–4451. doi:10.1098/rsta.2010.0175
30. Lazarowich, R. J.; Taborek, P.; Yoo, B.-Y.; Myung, N. V. *J. Appl. Phys.* **2007,** *101,* 104909. doi:10.1063/1.2730563
31. Krim, J.; Indekeu, J. O. *Phys. Rev. E* **1993,** *48,* 1576–1578. doi:10.1103/PhysRevE.48.1576
32. Krim, J.; Heyvaert, I.; Van Haesendonck, C.; Bruynseraede, Y. *Phys. Rev. Lett.* **1993,** *70,* 57–60. doi:10.1103/PhysRevLett.70.57
33. Palasantzas, G.; Krim, J. *Phys. Rev. Lett.* **1994,** *73,* 3564–3567. doi:10.1103/PhysRevLett.73.3564
34. *QCM200 Quartz Crystal Microbalance Digital Controller - QCM25 5 MHz Crystal Oscillator,* Revision 2; Stanford Research Systems Inc., 2011.
35. Kanazawa, K. K.; Gordon, J. G. *Anal. Chem.* **1985,** *57,* 1770–1771. doi:10.1021/ac00285a062
36. Martin, S. J.; Granstaff, V. E.; Frye, G. C. *Anal. Chem.* **1991,** *63,* 2272–2281. doi:10.1021/ac00020a015
37. McHale, G.; Newton, M. I. *J. Appl. Phys.* **2004,** *95,* 373–380. doi:10.1063/1.1630373
38. Daikhin, L.; Urbakh, M. *Langmuir* **1996,** *12,* 6354–6360. doi:10.1021/la950763d
39. Daikhin, L.; Gileadi, E.; Katz, G.; Tsionsky, V.; Urbakh, M.; Zagidulin, D. *Anal. Chem.* **2002,** *74,* 554–561. doi:10.1021/ac0107610
40. Acharya, B.; Sidheswaran, M. A.; Yungk, R.; Krim, J. *Rev. Sci. Instrum.* **2017,** *88,* 025112. doi:10.1063/1.4976024
41. Johannsmann, D. Stratified Layer Systems. *The Quartz Crystal Microbalance in Soft Matter Research;* Soft and Biological Matter; Springer,: Cham , 2015; pp 221–246.
42. Hanaor, D. A. H.; Gan, Y.; Einav, I. *Tribol. Int.* **2016,** *93,* 229–238. doi:10.1016/j.triboint.2015.09.016
43. Acharya, B.; Chestnut, M.; Marek, A.; Smirnov, A. I.; Krim, J. *Tribol. Lett.* **2017,** *65,* 115. doi:10.1007/s11249-017-0898-5
44. Gåhlin, R.; Jacobson, S. *Wear* **1999,** *224,* 118–125. doi:10.1016/s0043-1648(98)00344-5
45. Shirvani, K. A.; Mosleh, M.; Smith, S. T. *J. Nanopart. Res.* **2016,** *18,* 248. doi:10.1007/s11051-016-3526-7
46. Krueger, A. *J. Mater. Chem.* **2011,** *21,* 12571–12578. doi:10.1039/C1JM11674F
47. Hees, J.; Heidrich, N.; Pletschen, W.; Sah, R. E.; Wolfer, M.; Williams, O. A.; Lebedev, V.; Nebel, C. E.; Ambacher, O. *Nanotechnology* **2013,** *24,* 025601. doi:10.1088/0957-4484/24/2/025601
48. Yoshikawa, T.; Reusch, M.; Zuerbig, V.; Cimalla, V.; Lee, K.-H.; Kurzyp, M.; Arnault, J.-C.; Nebel, C. E.; Ambacher, O.; Lebedev, V. *Nanomaterials* **2016,** *6,* 217. doi:10.3390/nano6110217
49. Franks, G. V.; Gan, Y. *J. Am. Ceram. Soc.* **2007,** *90,* 3373–3388. doi:10.1111/j.1551-2916.2007.02013.x
50. Cuddy, M. F.; Poda, A. R.; Brantley, L. N. *ACS Appl. Mater. Interfaces* **2013,** *5,* 3514–3518. doi:10.1021/am400909g
51. Yoshikawa, T.; Zuerbig, V.; Gao, F.; Hoffmann, R.; Nebel, C. E.; Ambacher, O.; Lebedev, V. *Langmuir* **2015,** *31,* 5319–5325. doi:10.1021/acs.langmuir.5b01060

52. Lefèvre, G.; Čerović, L.; Milonjić, S.; Fédoroff, M.; Finne, J.; Jaubertie, A. *J. Colloid Interface Sci.* **2009,** *337,* 449–455. doi:10.1016/j.jcis.2009.05.005
53. Nunn, N.; Mahbooba, Z.; Ivanov, M. G.; Ivanov, D. M.; Brenner, D. W.; Shenderova, O. *Diamond Relat. Mater.* **2015,** *54,* 97–102. doi:10.1016/j.diamond.2014.09.003
54. Lancaster, J. K. *Tribol. Int.* **1990,** *23,* 371–389. doi:10.1016/0301-679X(90)90053-R
55. Dunckle, C. G.; Altfeder, I. B.; Voevodin, A. A.; Jones, J.; Krim, J.; Taborek, P. *J. Appl. Phys.* **2010,** *107,* 114903. doi:10.1063/1.3436564
56. Berman, D.; Deshmukh, S. A.; Sankaranarayanan, S. K. R. S.; Erdemir, A.; Sumant, A. V. *Science* **2015,** *348,* 1118–1122. doi:10.1126/science.1262024
57. Gubarevich, A. V.; Usuba, S.; Kakudate, Y.; Tanaka, A.; Odawara, O. *Jpn. J. Appl. Phys., Part 2* **2004,** *43,* L920–L923. doi:10.1143/jjap.43.l920
58. Feng, Z.; Tzeng, Y.; Field, J. E. *J. Phys. D: Appl. Phys.* **1992,** *25,* 1418. doi:10.1088/0022-3727/25/10/006
59. Totolin, V.; Göcerler, H.; Rodríguez Ripoll, M.; Jech, M. *Lubr. Sci.* **2016,** *28,* 363–380. doi:10.1002/ls.1336
60. Totolin, V.; Göcerler, H.; Rodríguez Ripoll, M.; Jech, M. *Tribol. Lett.* **2017,** *65,* 20. doi:10.1007/s11249-016-0806-4

License and Terms

BEILSTEIN JOURNAL OF NANOTECHNOLOGY

Velocity dependence of sliding friction on a crystalline surface

Christian Apostoli[1], Giovanni Giusti[1], Jacopo Ciccoianni[1], Gabriele Riva[1], Rosario Capozza[2], Rosalie Laure Woulaché[3], Andrea Vanossi[4,5], Emanuele Panizon[5] and Nicola Manini[*1]

Full Research Paper

Open Access

Address:
[1]Dipartimento di Fisica, Università degli Studi di Milano, Via Celoria 16, 20133 Milano, Italy, [2]Istituto Italiano di Tecnologia, via Morego 30, 16163 Genova, Italy, [3]Laboratoire de Mécanique, Département de Physique, Faculté des Sciences, Université de Yaoundé I. B.P. 812, Yaoundé, Cameroun, [4]CNR-IOM Democritos National Simulation Center, Via Bonomea 265, 34136 Trieste, Italy and [5]International School for Advanced Studies (SISSA), Via Bonomea 265, 34136 Trieste, Italy

Email:
Nicola Manini* - nicola.manini@fisica.unimi.it

* Corresponding author

Keywords:
atomic-scale friction; contact; dissipation; friction; nanotribology; phonons; velocity dependence

Beilstein J. Nanotechnol. **2017,** *8,* 2186–2199.
doi:10.3762/bjnano.8.218

Received: 16 May 2017
Accepted: 18 September 2017
Published: 19 October 2017

This article is part of the Thematic Series "Nanotribology".

Guest Editor: E. Gnecco

Abstract

We introduce and study a minimal 1D model for the simulation of dynamic friction and dissipation at the atomic scale. This model consists of a point mass (slider) that moves over and interacts weakly with a linear chain of particles interconnected by springs, representing a crystalline substrate. This interaction converts a part of the kinetic energy of the slider into phonon waves in the substrate. As a result, the slider experiences a friction force. As a function of the slider speed, we observe dissipation peaks at specific values of the slider speed, whose nature we understand by means of a Fourier analysis of the excited phonon modes. By relating the phonon phase velocities with the slider velocity, we obtain an equation whose solutions predict which phonons are being excited by the slider moving at a given speed.

Introduction

Friction affects a wide variety of phenomena spanning broad ranges of length and time scales. Due to its practical and technological relevance, the study of friction was addressed even long before physics became a science. Fundamental steps in understanding its microscopic nature were achieved in the early 20th century [1-5]. Since the last decades of that century, major advancements in capturing the intimate relations between the atomistic dynamics and the dissipation mechanisms came as the result of the development of the atomic force microscope (AFM) and its friction force microscope (FFM) variant [6-8], as well as the extensive usage of atomistic molecular dynamics (MD) simulations and modeling

made possible by the vastly increased computing power availability [9-16].

Despite this substantial progress, several fundamental mechanisms of friction and dissipation still need clarification. In particular, nanofriction (the study of friction at the atomic scale) lacks a theoretical model capable of accounting quantitatively for the dissipation of energy, i.e., the transformation of the kinetic energy of a macroscopic ordered motion into the internal energy of disordered thermal phonons. Both standard basic models of nanotribology, namely the Prandtl–Tomlinson model [1,2,13] and the Frenkel–Kontorova model [13,15-18], implement dissipation through a phenomenological viscous damping term acting on the physical degrees of freedom of the model. Moreover, such damping terms, beside affecting the dynamics, are characterized by a damping rate γ whose value is left to the arbitrary choice of the researcher. Finite-temperature is often simulated in the standard Langevin scheme, where to the viscous term one adds suitable Gaussian-distributed random forces, whose amplitude, via the fluctuation–dissipation theorem, is also affected by the value of γ [19].

A few approaches try to get rid of the arbitrariness of damping terms, describing dissipation explicitly. Microcanonical conservative simulations, for example, can describe the energy transfer into internal vibrational energy omitting all unphysical damping terms altogether [20-25]. The disadvantage of this approach is that, due to the finite and relatively small number of degrees of freedom available in a practical MD simulation cell, the dissipated energy accumulates in the phonons in the simulated sample, leading to a progressive overheating. Therefore this simulation procedure cannot address a steady sliding regime, but can at most identify the leading instabilities occurring and the most strongly coupled internal modes of the system. Another kind of approach involves using microcanonical equations to simulate a relatively broad cell including and surrounding the sliding contact region, adding dissipation through a suitable thermostat affecting only the atoms at the outer boundary of this region [26-35]. The main difficulty here is to provide a satisfactory implementation of the thermostat that not only provides a correct canonical dynamics in equilibrium conditions, but also manages to dispose of the extra excitation energy carried by the traveling phonon waves generated at the sliding contact, with minimal reflections at the boundary interface between conservative and thermostated particles. Such an implementation is in the process of being achieved [36-38], although with a rather intricate formalism, and should eventually become the technique of choice when one attempts to predict the sliding properties of a given physical interface for which a reliable force field is available. A third approach involves an uniformly distributed viscous damping term acting however only on the degrees of freedom perpendicular to the sliding direction [10,39,40]. While this method is quite effective in the context of fluid boundary lubrication, in the context of dry friction and crystalline interfaces nontrivial couplings of longitudinal and transverse modes [32,41,42] may lead to undesired γ-dependent effects.

In the present work we propose a different, minimalist approach, very much in the spirit of the Prandtl–Tomlinson and Frenkel–Kontorova (FK) models. We introduce and characterize a minimal slider–substrate model that captures the microscopic essentials of sliding friction and dissipation mechanisms, without the need of introducing ad hoc uncontrolled dissipative terms. This model consists only of a point-like localized cursor representing, e.g., a sharp AFM tip, interacting with an atomistic elastic substrate. As the slider skates on the elastically deformable crystal, phonons are generated and propagate away from the point of interaction. In this way, the slider mechanical energy is converted into crystal vibrational energy without any artificial viscous damping term affecting the slider itself. Of course, without any mechanism for dissipating this vibrational energy, the elastic substrate would eventually heat up as discussed above. For this reason we do include a weak viscous damping term, but this term acts on the elastic substrate only. We make sure that the effect of this term is negligible for the target of this research: the energy transfer from the slider to the substrate. This model virtually allows us to dispose of the arbitrary viscous damping, and to study the intrinsic dissipation properties of a sliding interface, as a function of several physical quantities, the most interesting of which is the sliding speed. Earlier work also investigated the speed dependence of the kinetic friction force in several models [1,25,43-50]. Under suitable conditions, specific velocities emerged as characterized by large kinetic friction due to suitable resonant conditions, in particular when the washboard frequency matches some phonon modes of the harmonic chain in the FK model [25,43]. In the present model too, characteristic resonances emerge at special speeds, but the resulting resonances differ significantly from those found for the FK model which represents an extended (infinite) solid–solid interface excited at a single wavelength, that of the sinusoidal potential. The present model focuses rather on the excitations induced by a localized point-like contact, inspired by an AFM tip, which has therefore the potentiality to generate excitations at all wavelengths.

This paper is organized as follows. Section “The Model” introduces our model. In Section “The kinetic friction force” we evaluate the kinetic friction as a function of the slider velocity. On top of a generally decreasing friction with sliding velocity, we identify peculiar “resonant” friction peaks at specific sliding velocities; in particular Subsection “Understanding: phonon

phase velocities" draws a connection between the slider speed and the substrate phonon phase velocities, and proposes a relation that predicts the excited phonon modes when the slider advances at a given velocity, accounting for the observed dissipation peaks. In Section "Discussion and Conclusion" we discuss the obtained results, compare them to previous work, and sketch future extensions of the model. Appendix "The static friction force" reports and discusses the evaluation of the static friction threshold of this model.

The Model

We propose the model sketched, in its simplest form, in Figure 1. It consists of a slider plus a linear chain of N pointlike atoms. The chain atoms, of mass m and positions x_j, are connected by harmonic springs to their nearest neighbors. The total harmonic potential is

$$V_{\text{harm}} = \frac{1}{2}\sum_{j=1}^{N}\left(x_{j+1} - x_j - a\right)^2, \tag{1}$$

where K is the elastic constant of the springs and a is the equilibrium lattice spacing. The simulation is carried out inside a periodically repeated supercell of size $L = Na$, so that, e.g., in Equation 1 $x_{N+1} \equiv x_1$.

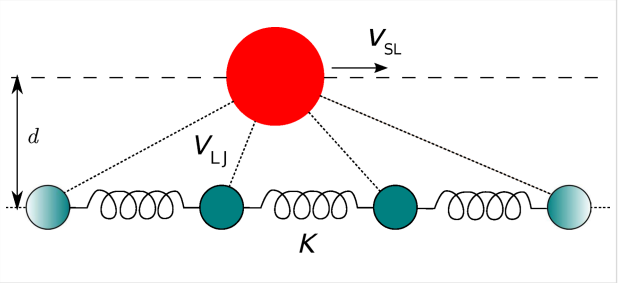

Figure 1: A sketch of the 1D slider-substrate model. The large sphere represents the slider, which moves along a fixed line (dashed) and interacts via Lennard–Jones forces with all atoms in the harmonic chain (smaller spheres).

The slider is also a pointlike particle, with horizontal position x_{SL} and mass m_{SL}. We usually take $m_{\text{SL}} > m$, but this condition is by no means required. The slider follows a guide at a fixed distance d from the chain and interacts with each chain atom through a Lennard–Jones (LJ) term. Indicating with $R_j = [d^2 + (x_{\text{SL}} - x_j)^2]^{1/2}$ the distance between the slider and the j-th particle, the total slider-chain interaction energy is

$$V_{\text{SL–C}} = \sum_{j=1}^{N} V_{\text{LJ}}\left(R_j\right), \tag{2}$$

where V_{LJ} is the LJ potential

$$V_{\text{LJ}} = \varepsilon\left[\left(\frac{\sigma}{R_j}\right)^{12} - 2\left(\frac{\sigma}{R_j}\right)^{6}\right], \tag{3}$$

with equilibrium distance σ. The total potential energy $V_{\text{harm}} + V_{\text{SL–C}}$ combined with the appropriate kinetic terms governs the model dynamics, which can be either classic or quantum. In Section "Discussion and Conclusion" we will discuss a few straightforward generalizations of this model, namely the removal of the constraint of a fixed slider–chain distance; a structured slider consisting of many atoms; the chain replaced by a 2D or, more realistically, 3D crystal.

A sinusoidal wave propagating in the chain follows the textbook dispersion relation [51] between its angular frequency ω and its 1D wave vector k:

$$\omega = 2\sqrt{\frac{K}{m}}\sin\left|\frac{ka}{2}\right|. \tag{4}$$

The corresponding long-wavelength speed of sound is

$$v_s = \left.\frac{\mathrm{d}\omega}{\mathrm{d}k}\right|_{k\to 0^+} = a\sqrt{\frac{K}{m}}. \tag{5}$$

As discussed in the Introduction, the chain atoms are also affected by a weak viscous force, so that the phonon waves that propagate in the crystal get dampened and eventually fade while they move away from the point where they were generated, namely in the vicinity of the slider. The viscous force that acts on the j-th atom of the chain is

$$F_{\text{diss},j} = -\gamma\dot{x}_j, \tag{6}$$

where γ is the damping coefficient. Thanks to this term, the oscillations generated by the slider are confined in a region smaller than the supercell, thus preventing the waves from coming back to the slider position.

In the present model all mechanical quantities can be expressed naturally in terms of the quantities a, m, and K characterizing the linear chain. Table 1 lists the natural units for the various mechanical quantities studied in the present work. For example, velocity is measured in units of the chain speed of sound v_s: this means that, e.g., a slider speed $|v_{\text{SL}}|$ exceeding unity is a supersonic speed.

Table 1: Natural units for several mechanical quantities in the model.

Physical quantity	Natural units
length	a
mass	m
spring constant	K
force	Ka
energy	Ka^2
time	$(m/K)^{1/2}$
speed	$a(K/m)^{1/2} \equiv v_s$
damping coefficient	$(mK)^{1/2}$

In most simulations, unless otherwise specified, we adopt the following standard set of parameters: $L = 500a$, i.e., a chain formed by $N = 500$ atoms; a weak slider–chain coupling $\varepsilon = 5 \times 10^{-4}\ Ka^2$; slider mass $m_{SL} = 10m$; and chain damping $\gamma = 0.1\ (mK)^{1/2}$. We take a rather small LJ radius $\sigma = 0.5a$, and adopt an even closer approach distance between the slider and the chain $d = 0.475a$. The effect of this $d < \sigma$ choice is to generate a periodic double-minimum effective potential experienced by the advancing slider in the limit where one could neglect the displacements of chain atoms, see the solid line of Figure 2. In contrast, a larger $d > \sigma$ would rather produce a potential of the type depicted by the dashed line of Figure 2: for simplicity, we defer the investigation of the $d > \sigma$ scenario to future work.

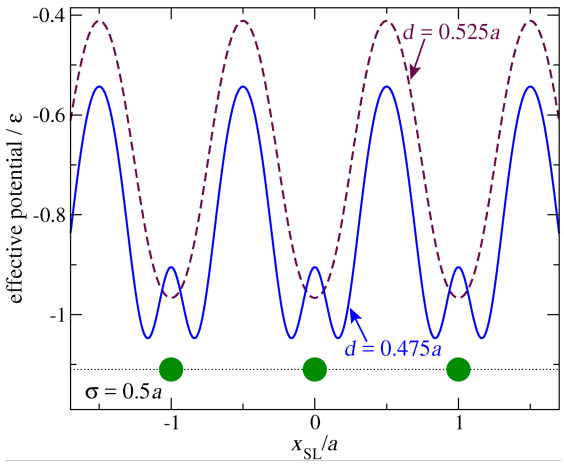

Figure 2: The potential-energy profile experienced by the slider as it moves along a hypothetical chain with atoms frozen at positions $x_j = ja$ (big circles), for a LJ parameter $\sigma = 0.5a$. Dashed curve: as obtained with $d = 0.525a > \sigma$; solid curve: with $d = 0.475a < \sigma$, the value adopted for the rest of this work.

The Kinetic Friction Force

Simulation protocols

To evaluate a meaningful estimate of the kinetic, or dynamic, friction force experienced by the advancing slider, we develop two alternative protocols [52,53]. In protocol A we first execute a "run-in" calculation at constant speed v_{SL}, that allows the initial shock waves induced by the sudden apparition of the slider near the chain to die out. Starting from the dynamical condition reached at the end of the first simulation, we then run a second simulation in which the slider is allowed to change its velocity as a consequence of the interaction with the chain and its own inertia like, e.g., in "ballistic" experiments where clusters deposited at surfaces are kicked around until they come to rest dissipating their kinetic energy into the substrate [49,54-56]. Figure 3 displays an example of the time dependence obtained in such second simulation. From the slider mean slowing rate during this second simulation, one can extract the kinetic friction force with the following method: time is divided into regular intervals, e.g., of 5000 time units, a very long time compared to the period of the fluctuations of v_{SL}; then a linear regression is performed over each interval; the (negative) slope of the straight line fitting v_{SL} as a function of time represents the slider average acceleration. The average dynamic friction force F_d experienced by the slider is then obtained by multiplying this acceleration by $(-m_{SL})$. Associating this value of F_d to the mean value of v_{SL} in the same time interval, one obtains the dependence $F_d(v_{SL})$. The faster and faster slider slowing rate displayed in Figure 3a indicates an increasing dynamic friction $F_d(v_{SL})$ as its speed v_{SL} decreases. As v_{SL} decreases and friction increases, the chain center-of-mass velocity v_{CM} oscillates more and more, a useful indicator of a larger and larger transfer of momentum from the slider to the chain. Of course the observed small-amplitude oscillations of v_{CM} are almost

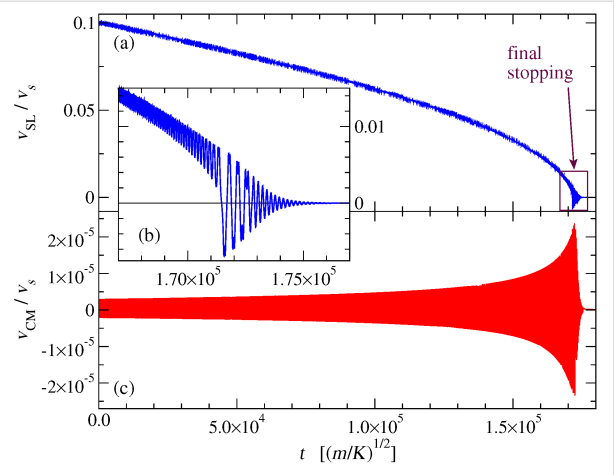

Figure 3: The time dependence (a) and (b) of the slider velocity v_{SL} and (c) of the chain center of mass v_{CM} for the second simulation (freely-slowing mode) of protocol A. The simulation is carried out until the slider finally stops and dissipates its residual energy in oscillations expanded in the inset (b), around a minimum of the effective potential of Figure 2, with chain phonon waves carrying this residual energy away, until the eventual complete arrest of the system. Note the increasing negative mean slope of the v_{SL} curve, indicating an increasing mean friction force F_d as v_{SL} decreases.

entirely the result of the oscillations induced in the few chain atoms directly interacting with the slider, with the vast majority of far-away atoms remaining essentially stationary. These center-of-mass oscillations are therefore an artifact of the finite size of the chain, and would vanish entirely in the macroscopic-size limit.

Protocol B is as follows: we execute a single calculation keeping v_{SL} constant, as if the slider was an AFM tip attached to an infinitely rigid AFM cantilever, wait until a steady-sliding regime is established, and discard the initial part affected by transients. For the remaining part of the simulation, we record the total force experienced by the slider as a function of time. This force has fluctuations as a result of collisions against the consecutive atoms of the chain. The period of these fluctuations is a/v_{SL}. We average this force over an integer number of these periods, and interpret the result as the average friction force F_d corresponding to the velocity v_{SL}. We start over a new simulation for every value of v_{SL} of interest.

While protocol A evaluates rigorously the friction force, allowing for all kinds of acceleration–deceleration effects related to individual slider–atom collisions, protocol B would coincide with protocol A only in the limit where the energy transferred in a single atomic collision is much smaller than the kinetic energy accumulated in the slider. The LJ parameter ε provides a conservative estimate of the energy transferred in the collision: the condition for a rigorous applicability of protocol B is

$$\varepsilon \ll \frac{1}{2} m_{SL} v_{SL}^2 . \tag{7}$$

This means that protocol B should yield results identical to protocol A for $v_{SL} \geq (2\ \varepsilon/m_{SL})^{1/2} \simeq 10^{-2}\ v_s$ for the standard simulation parameters introduced above. We have verified numerically that this is indeed the case. We have also verified numerically that in the considered weak-coupling regime, $F_d \propto \varepsilon^2$. This is in accord with the observation that the dissipated power $F_d v_{SL}$ must equal the average work per unit time done by the slider on the chain. The latter equals the product of the force exerted by the slider on each chain atom times that atom's velocity v_j. The force is of course proportional to the coupling ε and, to first order in $\varepsilon/(Ka^2)$, also v_j is proportional to ε, whence the $F_d \propto \varepsilon^2$ dependence at weak coupling.

Incidentally note that, in both protocols, the slider transfers not only energy but also momentum to the chain. Indeed the friction force F_d equals precisely the transfer of momentum per unit time from the slider to the chain. F_d is negative (leftward) when considered acting on the slider; due to the Newton's third law, the chain experiences a positive (rightward) force of precisely the same intensity. As a combined result of F_d and the damping force provided by the dissipative terms of Equation 6, in the steady regime the slider acquires a small but nonzero mean center-of-mass velocity v_{CM}. As a result, the slider speed relative to the chain is decreased relative to the imposed $v_{SL,abs}$, precisely by $\langle v_{CM} \rangle$. In the following, we denote by $v_{SL,abs}$ the slider velocity in the lab frame, and by v_{SL} the slider velocity in the frame of the chain center of mass:

$$v_{SL} = v_{SL,abs} - \langle v_{CM} \rangle . \tag{8}$$

In practice, we obtain $v_{CM}/v_{SL,abs} \ll 1$ for not-too-small $v_{SL,abs}$, so that this correction is irrelevant, and $v_{SL} \simeq v_{SL,abs}$. However at low speed this correction can become significant.

Control of the dissipation terms

First off, we need to identify a range for the dissipation parameter γ where the dissipative terms of Equation 6 become irrelevant to the frictional dynamics. Figure 4 displays the dependence of the sliding friction measured for $v_{SL} = 0.1\ v_s$, obtained repeating the simulations with different values of the damping parameter γ. This figure shows that for large and increasing γ, friction tends to decrease. This is expected, since in the unphysical strongly overdamped regime, it is harder and harder to displace the chain atoms away from their equilibrium positions, with the result that their effect on the slider resembles more and more closely that of a conservative effective potential, namely the one of Figure 2, which of course allows for no energy

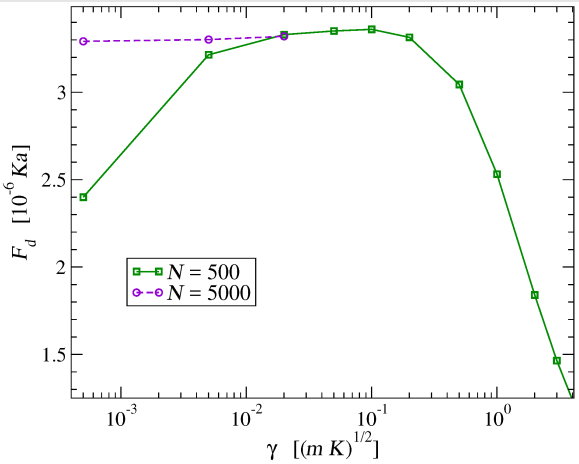

Figure 4: The dynamical friction force as a function of the damping coefficient γ that fixes the (unphysical) dissipation rate of the chain atoms. This is evaluated for $v_{SL} = 0.1\ v_s$ with protocol A (but protocol B provides identical data). Squares: simulations executed in a standard supercell of size $L = 500a$, with 500 atoms. Circles: similar simulations executed in a 10× longer supercell with 5000 atoms, where the waves emitted by the slider have a much longer space to decay fully before coming back to the contact point, even for smaller γ.

transfer, and no dissipation. As damping is decreased to the physically relevant underdamped region $\gamma < (mK)^{1/2}$, friction stabilizes to a physically significant γ-independent value. However, when γ is further decreased below approximately 10^{-2} $(mK)^{1/2}$, the waves produced at the slider–chain contact point become less and less damped, see Figure 5. When the γ value becomes too small, the phonon waves propagate all the way across the periodically repeated cell, eventually returning to the slider–chain contact point. As a result, the chain slides over an effectively "hot" substrate, generating an unphysical friction reduction related to thermolubricity [45,46,57-62]. As shown by the circles in Figure 4, a much longer chain provides enough space for the phonon waves to decay, thus allowing the phonon amplitude to be radically reduced before returning to slider-chain contact point, even with small γ. In the following we adopt $\gamma = 0.1(mK)^{1/2}$ as the standard value of the damping rate, unless otherwise indicated.

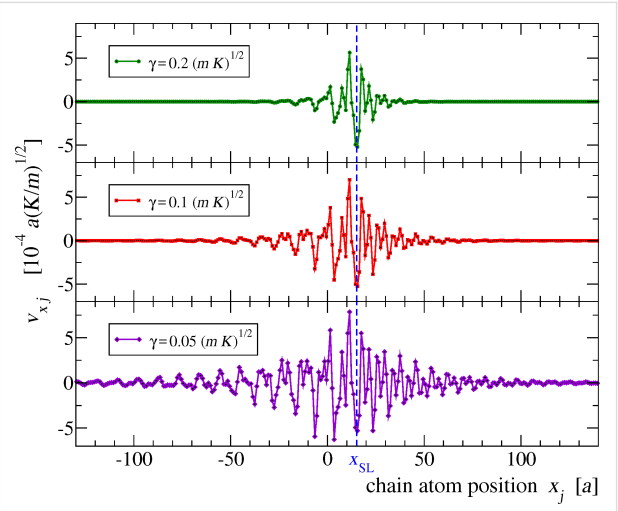

Figure 5: Three snapshots of the instantaneous velocities of a few chain atoms as a function of their position while interacting with the slider, whose instantaneous position x_{SL} is marked by a vertical dashed line. The three calculations are executed with the same $v_{SL} = 0.1\ v_s$, but with three different values of γ, which produce visibly different damping of the same excited phonon waves away from the interaction point.

Sliding-speed dependence of friction

Figure 6 shows the speed dependence of the kinetic friction F_d. The general trend is of a decreasing friction with speed. In particular, F_d drops dramatically to 0 when v_{SL} exceeds the speed of sound of the chain. In the region below the speed of sound (vertical dotted line) F_d stands on a relatively stable plateau. Several friction peaks then emerge in the region roughly between 10% and 20% v_s. When v_{SL} is further decreased, friction starts to rise approximately as Av_{SL}^{-1} (where A is a constant), although, with the standard parameters of Section "The Model", a deviation is observed quite early, for $v_{SL} \lesssim 0.03\ v_s$. This deviation is not particularly related to reaching the speed region where protocol B, introduced in Section "Simulation protocols" above, becomes unreliable. We have verified that this deviation is instead an artifact of the damping in the chain. By repeating the simulations with a longer chain ($L = 10^5 a$) and smaller damping $\gamma = 10^{-4}(mK)^{1/2}$, we find that the $F_d = Av_{SL}^{-1}$ regime persists down to $v_{SL} \simeq 10^{-3}\ v_s$. With the adopted value for the coupling ε, protocol A cannot determine friction reliably as a function of v_{SL} in this region of speeds, because v_{SL} itself oscillates widely in time as the slider nears stopping, see Figure 3b. However we reduced the coupling ε by one order of magnitude to $\varepsilon = 5 \times 10^{-5}\ Ka^2$, and verified that the points of the $N = 10^5$, $\gamma = 10^{-4}\ (mK)^{1/2}$ curve are perfectly reproducible, apart from a factor 10^{-2} smaller friction, thus confirming the $F_d = Av_{SL}^{-1}$ low-speed scaling.

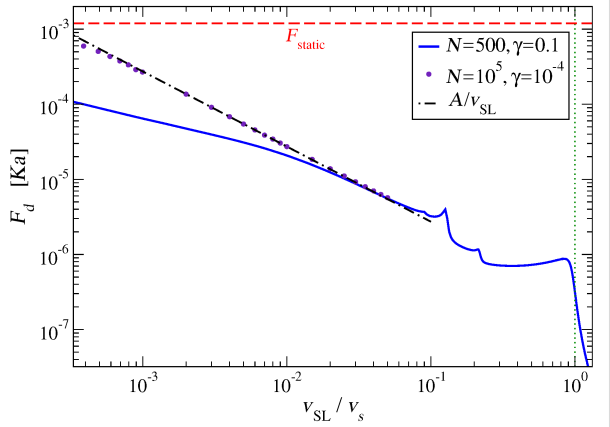

Figure 6: Dynamic friction force as a function of the slider speed v_{SL}. For comparison, the horizontal dashed line marks the static-friction threshold F_{static} obtained in Appendix "The static friction force", Equation 16. The vertical dotted line marks the speed of sound v_s. The data are obtained by means of protocol B; we verified that perfectly superposable curves can be obtained by means of protocol A as long as it can be effectively applied, i.e., as long as the friction force $F_d < 10^{-5}\ Ka$.

As shown in Figure 3, the simulations of this model do provide concrete realizations of the dynamic to static transition. Unfortunately, due to the wide oscillations displayed in Figure 3b, the transition from dynamic to static friction is just impossible to characterize in terms of a simple function $F_d(v_{SL})$. We evaluate the static friction for this model as detailed in Appendix "The static friction force". The comparison of F_d and F_{static} in Figure 6 confirms that of course this model is consistent with the well-known result that $F_d < F_{static}$.

We should now investigate the reason for the friction peaks at certain special subsonic velocities. For this purpose, we must identify what phonon modes are most strongly excited at each particular slider speed.

Phonon excitations

The friction force F_d of Figure 6 dissipates the slider kinetic energy by transforming it into phonon waves that travel away from the contact point, as illustrated in Figure 5. We analyze these phonon excitations for several values of v_{SL}. We must first detail the protocol of this analysis.

We run a simulation with fixed slider speed $v_{SL,abs}$. At a given time t after the end of the initial transient, we take a snapshot of the individual velocities v_j of the chain atoms, as in the example of Figure 7a. We then execute a spatial Fourier transform of these instantaneous velocities:

$$\tilde{v}(k,t)=\sum_{j=1}^{N} e^{ikaj} v_j(t), \quad \text{with } k=\frac{\pi}{a}\left(\frac{2n}{N}-1\right), \text{ and } n=1,\ldots,N. \tag{9}$$

Here i is the imaginary unit and k spans the first Brillouin zone (BZ) $(-\pi/a, \pi/a]$. Figure 7b displays $|\tilde{v}(k,t)|^2$ for the velocity pattern of Figure 7a. Observe first that the real values of v_j guarantee that $\tilde{v}(-k,t)=\tilde{v}^*(k,t)$, and therefore that $|\tilde{v}|^2$ is an even function of k, as is evident in Figure 7b. Due to this symmetry in all following figures reporting Fourier transforms we will display the positive half $[0, \pi/a]$ of the first BZ only.

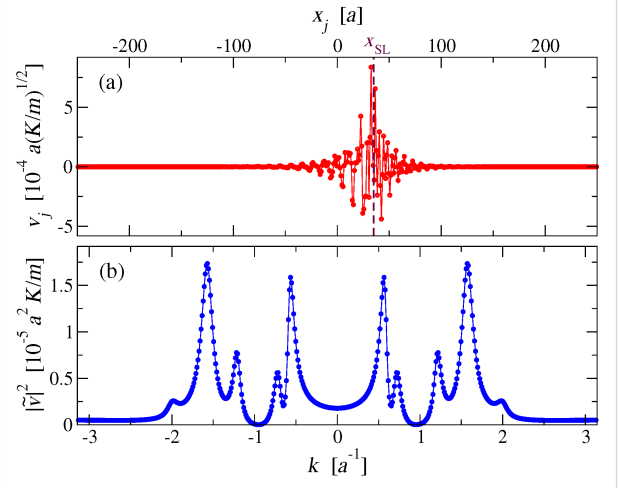

Figure 7: (a): A snapshot of the velocities of the chain particles while the slider, instantly at the vertical dashed-line position, advances at v_{SL} = 0.1 v_s. (b): The square modulus of the spatial Fourier transform $\tilde{v}(k, t)$ of the velocities, as defined in Equation 9.

The peaks of the Fourier transform highlight the phonons most excited by the interaction with the slider at that given instant in time. For a given v_{SL}, during the simulation the velocity pattern $v_j(t)$, and therefore its Fourier transform, evolve in time. We take advantage of the fact that the slider encounters the chain particles at a regular interval $T = a/v_{SL}$: in the steady state $v_j(t)$ is a periodic function of time but for a lattice translation, $v_{j+1}(t + T) = v_j(t)$. As a global translation (a shift in j) only affects the phase of $\tilde{v}(k, t)$, but not its amplitude, $|\tilde{v}(k,t)|^2$ is exactly periodic in time:

$$|\tilde{v}(k,t+T)|^2=|\tilde{v}(k,t)|^2, \text{ with } T=\frac{a}{v_{SL}}. \tag{10}$$

Figure 8 displays an example of this periodic time dependence of $|\tilde{v}(k,t)|^2$.

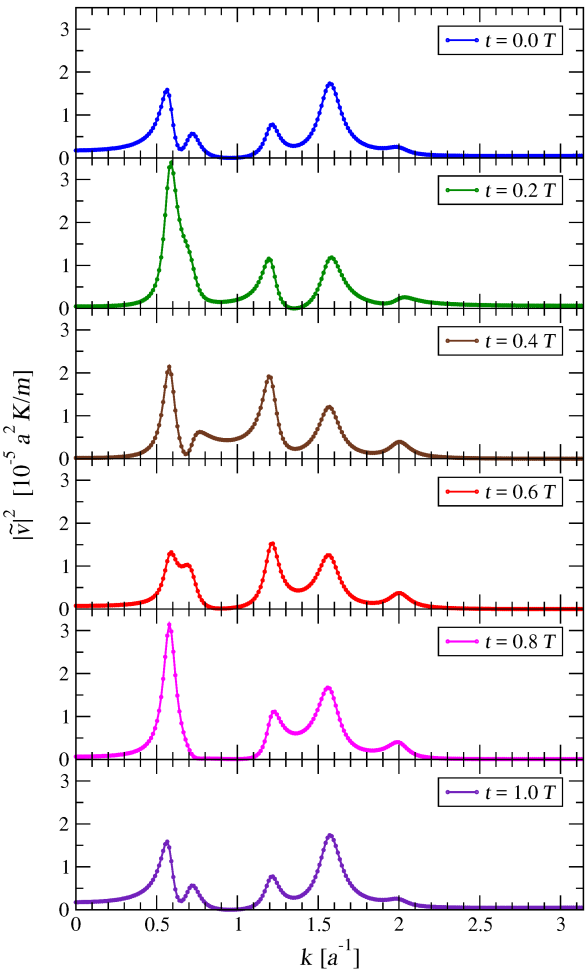

Figure 8: The square modulus of the Fourier transforms of the velocities $v_j(t)$, at six subsequent times. Here the slider velocity is v_{SL} = 0.1 v_s. Comparing the plots of $|\tilde{v}(k,0)|^2$ and $|\tilde{v}(k,T)|^2$, one sees that $|\tilde{v}|^2$ repeats itself identically after one entire period $T = a/v_{SL}$ = 10 $(m/K)^{1/2}$.

To obtain a time-independent description of the typical phonon-excitation spectrum at a given v_{SL}, we average the square modulus of $|\tilde{v}(k,t)|$ over a period T. We select M = 50 instants

of time, equally spaced within the period, and compute $\tilde{v}$ at each of them. Then we calculate the time-averaged Fourier transform as follows:

$$\left\langle |\tilde{v}|^2 \right\rangle (k) = \frac{1}{M} \sum_{l=1}^{M} \left| \tilde{v}\left(k, l\frac{T}{M}\right) \right|^2 . \qquad (11)$$

We verified that a finer sampling of the period (larger M) shows no significant difference in this average spectral intensity.

Figure 9 illustrates the resulting time-averaged power spectra $\left\langle |\tilde{v}|^2 \right\rangle (k)$, for a few sample velocities v_{SL}. Figure 9a shows that for supersonic v_{SL} the power spectrum is quite flat, with no sharp peak: most phonon modes are excited with comparable, rather weak, intensities; only those closest to $k = 0$ are left substantially unexcited. When v_{SL} is less than the speed of sound

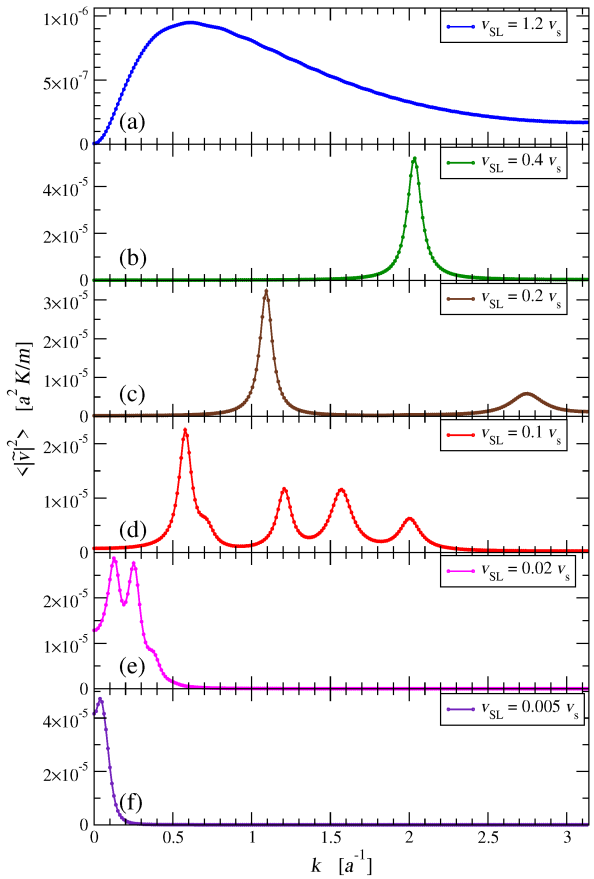

Figure 9: The time-averaged square modulus of the Fourier transform of the chain velocities, for a few characteristic values of v_{SL}: (a) supersonic speed; (b) single-peak subsonic region; (c) appearance of the second pair of peaks; (d) multi peak region near $v_{SL} \simeq 0.1\ v_s$; (e) small-speed collapse of the dissipation peaks toward $k = 0$; (f) full collapse to one peak at very small $v_{SL} \ll v_s$.

v_s, but greater than $\simeq 0.217\ v_s$, as in Figure 9b, the spectrum is dominated by a single peak. As v_{SL} is lowered below $\simeq 0.217\ v_s$, as in Figure 9c,d, multiple peaks appear, and, as v_{SL} decreases, their number increases progressively. As v_{SL} further decreases, Figure 9e, the positions of all peaks approach $k = 0$, where they gradually merge into a single peak, Figure 9f. Note that the spectral resolution is limited both by the finite chain length, with $\delta k = 2\pi/(Na)$, see Equation 9, and by the phonon localization induced by the damping term of Equation 6.

Figure 10 tracks the positions and intensities of the observed peaks of $\left\langle |\tilde{v}|^2 \right\rangle (k)$ as functions of v_{SL}. These data are obtained by fitting the functions $\left\langle |\tilde{v}|^2 \right\rangle (k)$ with sums of up to 7 Lorentzian curves. Figure 10 reports the centers and heights of the fitted Lorentzian terms.

Even in the supersonic region $v_{SL} > v_s$, where the phonon power spectrum is smooth and flat and lacks sharp peaks as in Figure 9a, we fit the spectrum with the sum of four Lorentzian curves. These four Lorentzian profiles do their best to interpolate that continuum spectrum. Not surprisingly, the Lorentzian centers and intensities, displayed at the right side of Figure 10, follow a rather erratic variation with v_{SL}, confirming that in the spectrum for supersonic sliding no sharp peak is actually present.

As v_{SL} decreases below approximately 90% of the speed of sound, initially a single prominent peak appears near the BZ boundary (Figure 9b), tracked in wave vector and intensity by the crosses in the central region of Figure 10a,b. As v_{SL} decreases below $0.217\ v_s$, more peaks appear near the BZ boundary too, as in the examples of Figure 9c,d, and tracked explicitly in Figure 10c,d. As v_{SL} is further decreased all peaks move down toward $k = 0$ and eventually merge for $v_{SL} \ll v_s$, due to the finite k-resolution (Figure 9e,f). Figure 10c clarifies a nontrivial feature of this velocity-dependent phonon spectrum: except for the single peak emerging at $v_{SL} \lesssim v_s$, all other new peaks appear in pairs.

Figure 11 highlights the relation between the appearance of new peaks in the chain phonon spectrum of excitations at certain speeds with jumps in the dynamic friction F_d as a function of v_{SL}. The important conclusion of this correlation is the following: dissipation increases suddenly for those values of v_{SL} where new phonon modes start to get excited.

Understanding: phonon phase velocities

Given the simplicity of this 1D model and the special weak-coupling regime investigated, we should be able to understand why certain phonons get excited at certain special speeds. We formulate the hypothesis that phonon modes get excited when

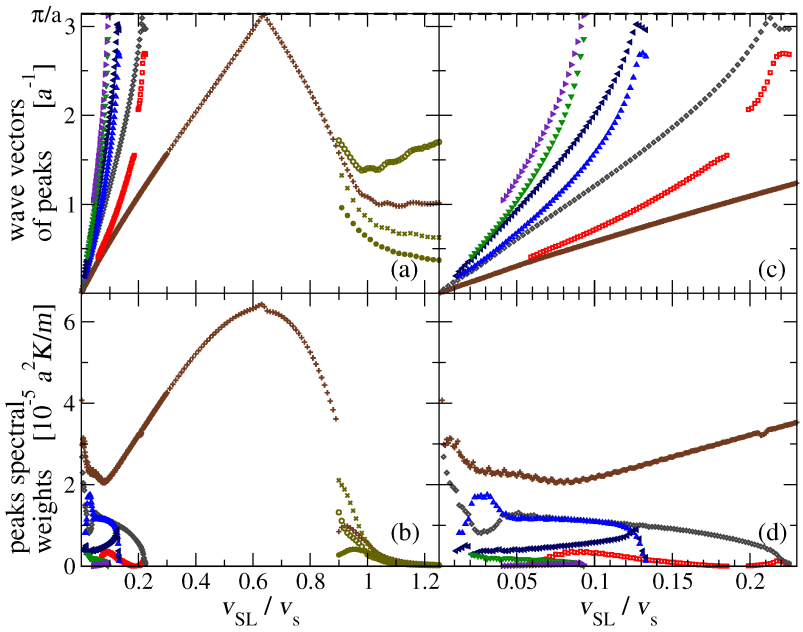

Figure 10: The positions (a) and heights (b) of the peaks of $\langle|\tilde{v}|^2\rangle(k)$ as functions of v_{SL}. Panels (c) and (d): detail of the $v_{SL} \leq 0.23\ v_s$ low-speed region for the same quantities.

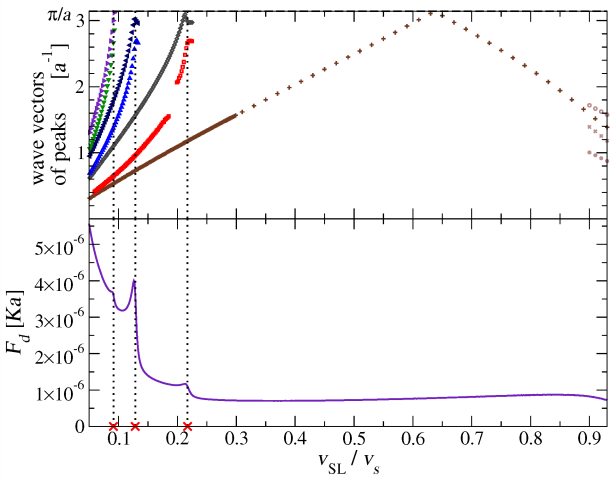

Figure 11: A direct comparison of the peak wave vectors of $\langle|\tilde{v}|^2\rangle(k)$, with the dynamic friction F_d as a function of v_{SL} over the interesting speed range of Figure 6. The dotted vertical lines highlight the relation of the peaks of F_d with the appearance of new pairs of excited phonons near the BZ boundary.

their phase velocities ω/|*k*| match the slider speed v_{SL}. We start by searching all values of *k* such that the phonon phase velocity matches a given speed v_{SL}:

$$\frac{\omega(k)}{|k|} = v_{SL}\,. \tag{12}$$

We substitute the simple dispersion relation ω(*k*) of Equation 4, and reformulate Equation 12 as:

$$2\sqrt{\frac{K}{m}}\left|\sin\left(\frac{ka}{2}\right)\right| = v_{SL}\,|k|. \tag{13}$$

This equation is put in dimensionless form by introducing $x \equiv \frac{1}{2}ka$, and the parameter $V \equiv v_{SL}\Big/\left(aK^{1/2}m^{-1/2}\right) = v_{SL}/v_s$:

$$\left|\sin(x)\right| = V\,|x|. \tag{14}$$

For a given *V* (or equivalently a given v_{SL}), the solutions *x* (or equivalently *k*) of Equation 14 (or equivalently Equation 13) provide the special wave vectors such that the phonon phase velocity matches the given speed v_{SL}.

Equation 14 can of course be solved numerically for any *V*. An example of graphic solution of Equation 13 is displayed in Figure 12a. The resulting wave vectors are scattered over several BZs. We then bring all the *k*-point solutions inside the first BZ, Figure 12b. Finally, we proceed to compare these solutions to the positions of the peaks of the power spectrum $\langle|\tilde{v}|^2\rangle(k)$ obtained by MD at that specific slider speed, Figure 12c. In the example of Figure 12, this procedure is followed for $v_{SL} = 0.12\ v_s$, showing that the solutions of Equation 13 match perfectly the positions of all observed peaks

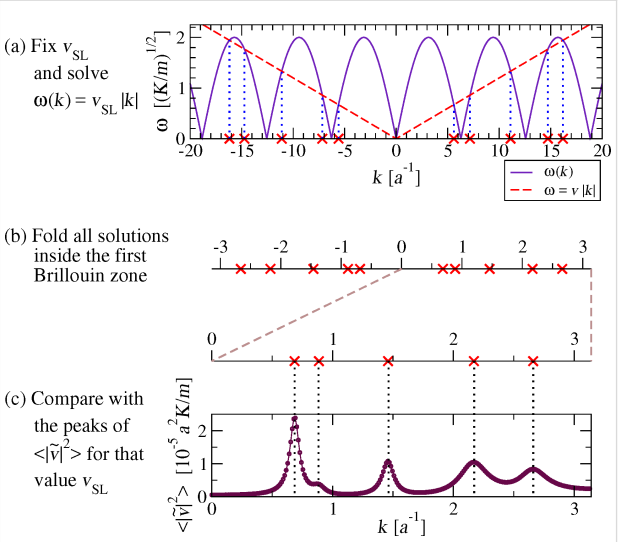

Figure 12: A scheme of the steps performed to identify the phonons whose phase velocity equals v_{SL}, and the comparison of the obtained wave vectors with the observed excited phonons peaks for the same slider velocity v_{SL}. In this example v_{SL} = 0.12 v_s.

in the spectrum. In particular, Figure 12a clarifies why, for decreasing v_{SL}, new excited phonon modes always arise near, but not quite at, the BZ boundary.

Figure 13 compares the positions of the peaks of $\langle|\tilde{v}|^2\rangle(k)$ obtained from the analysis of MD trajectories as in Figure 10, with the wave vectors of the phonons whose phase velocity equals v_{SL}, obtained by solving Equation 13. It is apparent that for $v_{SL} \lesssim 0.9\ v_s$ the two quantities match almost perfectly. We conclude that Equation 13 provides a reliable prediction of the

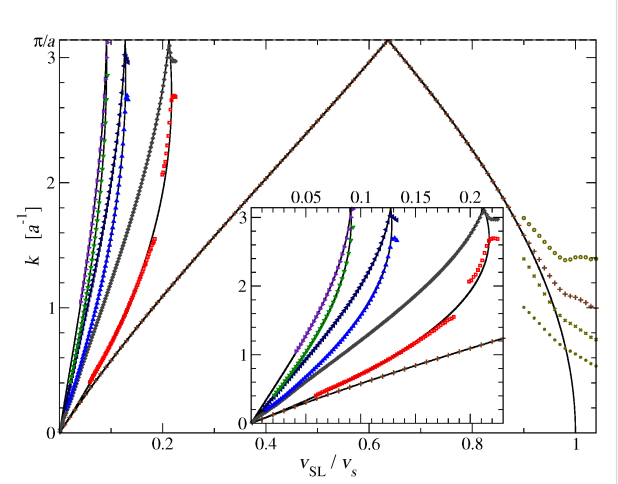

Figure 13: The positions of the observed peaks of $\langle|\tilde{v}|^2\rangle(k)$ (symbols), compared with the values of k of the phonons whose phase velocity is equal to v_{SL} (black solid lines), solutions of Equation 13. Inset: a blow up of the interval $0 \le v_{SL} \le 0.23\ v_s$.

wave vectors of the excited phonons for a given v_{SL}. Above the speed of sound v_s, Equation 13 has no solution and indeed the spectrum displays no sharp peak, see Figure 9a. Correspondingly the "nonresonant" friction is very small, see the right side of Figure 6.

In particular Equation 13 allows us to predict the number and wave vectors of the excited phonon modes when the slider is moving at a given velocity. The number N_{ph} of excited phonon modes at a given v_{SL} is null for any $v_{SL} > v_s$, it turns to unity for $0.217\ v_s < v_{SL} < v_s$, and then for smaller and smaller v_{SL} N_{ph} increases by two every time the dashed line of Figure 12a crosses one more sine hump. As a result, in the limit of small v_{SL}, N_{ph} is approximately

$$N_{ph}(v_{SL}) \simeq \frac{2v_s}{\pi v_{SL}}. \qquad (15)$$

We have then a number of excited phonons which is inversely proportional to v_{SL} for small v_{SL}. The comparison of Figure 11 suggests that an increasing number of excited phonon modes leads to an increasing kinetic friction F_d, see Figure 11. If a comparable power was dissipated in each of the excited phonon modes, then Equation 15 would be compatible with the power-law dependence $F_d(v_{SL}) \simeq A/v_{SL}$ that we observe in the low-speed regime in Figure 6. However there is no evidence that the same power is dissipated in each one of the phonon modes. In fact, Figure 10b,d shows that different modes draw different spectral weights. A systematic study of the intensities of the phonon excitations would probably be useful in understanding the $F_d(v_{SL}) \simeq A/v_{SL}$ behavior in detail.

Discussion and Conclusion

We introduce a new model, or rather a model class, that allows one to investigate friction at the very point where it is generated: the contact point. In the present paper we examine the main predictions of this model in its most basic incarnation: a point-like slider kept at a fixed distance to a 1D harmonic chain of masses and springs. The main result is that kinetic friction should depend on speed as a generally decreasing function, with several nontrivial features deviating from monotonicity: friction peaks arise every time a new "resonance condition" is fulfilled, namely that the phase velocity of some substrate phonon mode matches the slider speed. Recently published research also identified relations between dissipation peaks and the properties of a dispersion relation in a different model [63].

The present model can also be investigated in a spring-pulling scheme analogous to the Prandtl–Tomlinson model, to simulate the finite stiffness of an AFM cantilever. In that scheme a stick-

slip to smooth-sliding transition can also be investigated, especially at low speed (see Appendix "The static friction force"), allowing one to study in detail the nonlinear phenomena and mechanisms of phonon excitations that arise at slip times. The stick-slip regime and the associated nonlinear phenomena will of course be more significant when the model is studied in a realistic regime of intermediate to strong coupling $\varepsilon \approx Ka^2$. We defer this investigation to future work, which should provide a microscopic basis and the limits of applicability for the Prandtl–Tomlinson model. This simple 1D model, studied in the spirit of protocol B (fixed slider speed) for weak slider-chain coupling $\varepsilon \ll Ka^2$, should be suitable to address even by means of analytic perturbative many-body methods. We plan to pursue this investigation in the future.

The FK model and the present model both describe dissipation in terms of the excitations of the phonon modes of a linear harmonic chain. Therefore, the two models agree that no resonant energy transfer can occur for very large speed, and friction drops to 0, as at the right side of Figure 6. However, the frictional features demonstrated in the present work differ significantly from those found for the superlubric weak-corrugation regime of the FK model [25,43]. Specifically, in the FK model the condition for dissipation peaks, where center-mass translational energy is converted rapidly into internal phononic degrees of freedom, requires that the modulation dictated by the chain-potential lattice incommensurability resonates with the washboard frequency at the center-mass sliding velocity, due to the sinusoidal potential acting to perturb the entire harmonic chain at a single wave vector. That conditition reflects the extended nature of the contact, and may be suitable to describe friction as generated at crystalline incommensurate solid-solid interfaces. Instead, in the present model dissipation occurs simultaneously through whatever phonon has a phase velocity matching the slider speed, and resonant peaks arise as more and more phonons become available at slower speeds. In the current model, more suitable to describe the dissipation of an AFM tip, there is no equivalent to the relative spatial periodicity, with the effect that phonons at all wave vectors can virtually be excited simultaneously. As a result, the present model exhibits dissipation peaks of the same physical nature (i.e., phononic excitations) but in detail quite different from those of the FK model. Relatedly and importantly, the obtained low-speed behavior, with friction increasing and approaching the static limit when the sliding velocity decreases to 0 is opposite to that obtained for the single-wave vector FK model.

More refined incarnations of this model are interesting targets of future study. We mention just a few obvious generalizations: (i) remove the constraint of a fixed slider-chain distance, thus allowing for longitudinal-to-transverse energy transfer; (ii) replace the point slider with a more realistically structured slider consisting of several atoms, e.g., placed periodically, thus making contact with the FK model, or rather in a disordered structure; (iii) replace the 1D chain by a 2D [64], or a more realistic 3D harmonic crystal; (iv) adopt, rather than a harmonic crystal, a realistic force field modeling a specific substrate, with the target of predicting the frictional dynamic features of a specific interface as was done, e.g., in [49,65]; (v) energy dissipation implemented through suitably remote boundary-atom thermostats [30,31,33] rather than via an unphysical damping throughout the crystal.

In the present work we do our best to keep the chain as close as possible to its $T = 0$ ground state. The study of this or any of the generalizations of this model at finite temperature will also provide a playground to investigate all sorts of thermolubric effects [25,45,46,57-62]. It is presently unclear which of the predictions of the simple 1D model studied here will hold in the extended versions of the model, and at finite temperature. It will be particularly interesting to find out how dissipation changes when energy is transferred to a physically realistic density of phonon modes of 3D crystals, rather than 1D.

Appendix: the Static Friction Force

The solid curve of Figure 2 shows two kinds of nonequivalent equilibrium positions: immediately at the left and at the right of a chain atom. Obviously, the most robust of them against rightward sliding is the one of them sitting at the right of an atom, thus we probe the static friction there. For this purpose, we place the slider at that minimum, and run a simulation where we pull the slider through a spring of elastic constant K_{pull} extending from the slider to a support which moves at a constant velocity v_{pull} to the right. Figure 14a reports the positions of the support, the slider, and a few chain atoms as a function of time. At the beginning, the spring elongates (Figure 14b) while the slider remains stuck near the minimum. Meanwhile, as a result of the force between the slider and the atoms, the whole chain accelerates slowly to the right. If v_{pull} is large enough, there comes a time at which the pulling spring elongates enough for the pulling force to exceed the static friction threshold F_{static}, and the slider suddenly abandons its initial position near a certain atoms, oscillates around the support dissipating the elastic energy accumulated in the pulling spring, and eventually reaches a quasi-stationary "stick" configuration at a new local equilibrium position near the next atom at the right of the starting one. Then the stick-slip process repeats itself. Conversely, if v_{pull} is less than a certain critical value $v_{\text{pull c}}$, the whole chain speed advances at a speed asymptotically close to v_{pull}: the support, the slider, and the chain slide together at the same velocity and the spring never elongates enough for the elastic force to exceed F_{static}.

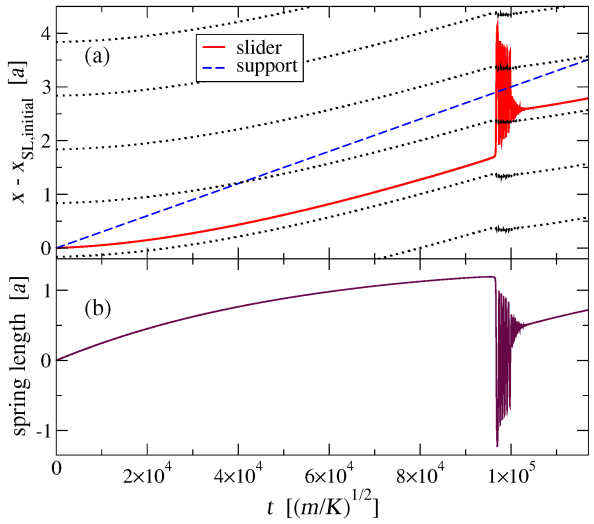

Figure 14: (a): The motion of the slider (solid line) as it is pulled by a spring having elastic constant $K_{pull} = 10^{-3}$ K connecting it to a support (dashed line) advancing at a constant speed $v_{pull} = 3 \times 10^{-5}$ v_s; the dotted lines mark the time evolution of the positions x_j of successive atoms in the chain. (b): The pulling spring length as a function of time: the spring elongates until the slider suddenly slips forward, oscillates around the next stick position, and dissipates the energy accumulated in the pulling spring by emitting phonons. The process then repeats itself.

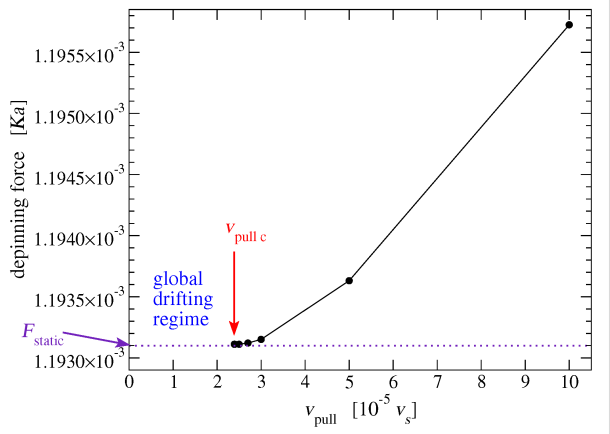

Figure 15: For smaller and smaller support velocity v_{pull}, the maximum elastic force experienced by the slider just before it overtakes one atom of the chain provides a better and better estimation of the static friction F_{static}. By moving closer and closer to the minimum $v_{pull\ c}$, we obtain a quantitative estimate of the actual F_{static}, see Equation 16. In these simulations, the pulling elastic constant $K_{pull} = 10^{-3}$ K.

In simulations with v_{pull} greater than the (hitherto undetermined) critical speed $v_{pull\ c}$, the pulling spring length reaches a maximum value before the slider abandons its equilibrium position. By multiplying this maximum elongation by K_{pull}, we obtain the maximum pulling force experienced by the slider, which systematically overestimates F_{static}. We repeat this calculation for decreasing values of v_{pull}, and record the resulting estimations of F_{static} in Figure 15. Our resulting best estimation for the static friction is

$$F_{static} \simeq 1.1931 \times 10^{-3}\, Ka. \tag{16}$$

The transition from the sliding regime to the low-speed global drift mode, Figure 15, provides the following estimation for $v_{pull\ c} = (2.385 \pm 0.005) \times 10^{-5}\ v_s$. An even better estimation of $v_{pull\ c}$ can be obtained from F_{static} by a simple relation with the damping terms of Equation 6 hindering the chain advancement. In low-speed $v_{pull} < v_{pull\ c}$ regime the chain, the slider and the pulling support all drift rightward together at the same speed v_{pull}. This constant-speed advancement requires a null total force acting on the chain. Accordingly, the total force $F_{SL-chain}$ that the slider exerts on the chain must be equal in strength but opposite in direction to the total damping force of Equation 6, which is $N\gamma v_{pull}$:

$$F_{SL\text{-}chain} = N\gamma v_{pull}. \tag{17}$$

The maximum speed v_{pull} for which this situation occurs is $v_{pull\ c}$, which corresponds to the maximum possible value of $F_{SL-chain}$, namely F_{static}. Then, at the depinning transition Equation 17 requires

$$v_{pull\ c} = \frac{F_{static}}{N\gamma}. \tag{18}$$

In the conditions of our simulations we obtain

$$v_{pull\ c} \simeq 2.3862 \times 10^{-5} v_s\ , \tag{19}$$

perfectly compatible with the previous estimation. While, according to Equation 18, $v_{pull\ c}$ is strongly dependent on simulation details such as N and γ, F_{static} is not, and is therefore a physically significant quantity. The obtained F_{static} value is of course dependent on the precise slider-substrate interaction, which in the present model is tuned by the σ and d lengths, and by the LJ coupling energy ε. For small $\varepsilon \ll Ka^2$, F_{static} is essentially proportional to ε.

Acknowledgements

We acknowledge useful discussions with A. Fasolino, G. E. Santoro, and E. Tosatti. Work in Trieste was carried out under ERC Grant 320796 MODPHYSFRICT. The COST Action MP1303 is also gratefully acknowledged.

References

1. Prandtl, L. *Z. Angew. Math. Mech.* **1928,** *8,* 85. doi:10.1002/zamm.19280080202
2. Tomlinson, G. A. *Philos. Mag.* **1929,** *7,* 905. doi:10.1080/14786440608564819
3. Frenkel, Y.; Kontorova, T. *Phys. Z. Sowjetunion* **1938,** *13,* 1.
4. Kontorova, T.; Frenkel, Y. *Zh. Eksp. Teor. Fiz.* **1938,** *8,* 89.
5. Bowden, F. P.; Tabor, D. *The Friction and Lubrication of Solids;* Oxford University Press: New York, NY, U.S.A., 1950.
6. Binnig, G.; Quate, C. F.; Gerber, C. *Phys. Rev. Lett.* **1986,** *56,* 930. doi:10.1103/PhysRevLett.56.930
7. Mate, C. M.; McClelland, G. M.; Erlandsson, R.; Chiang, S. *Phys. Rev. Lett.* **1987,** *59,* 1942. doi:10.1103/PhysRevLett.59.1942
8. Hirano, M.; Shinjo, K.; Kaneko, R.; Murata, Y. *Phys. Rev. Lett.* **1997,** *78,* 1448. doi:10.1103/PhysRevLett.78.1448
9. Persson, B. N. J. *Sliding Friction: Physical Principles and Applications;* Springer: Berlin, Germany, 2000. doi:10.1007/978-3-662-04283-0
10. Robbins, M.; Müser, M. Computer Simulations of Friction, Lubrication and Wear. In *Modern Tribology Handbook;* Bhushan, B., Ed.; CRC Press: Boca Raton, FL, U.S.A., 2001; p 717.
11. Müser, M. H. Theory and Simulation of Friction and Lubrication. In *Computer Simulations in Condensed Matter Systems: From Materials to Chemical Biology Vol. 2;* Ferrario, M.; Ciccotti, G.; Binder, K., Eds.; Lecture Notes in Physics, Vol. 704; Springer: Berlin, Germany, 2006; p 65.
12. Mate, C. M. *Tribology on the Small Scale: A Bottom Up Approach to Friction, Lubrication, and Wear (Mesoscopic Physics and Nanotechnology);* Oxford University Press: Oxford, United Kingdom, 2008.
13. Vanossi, A.; Manini, N.; Urbakh, M.; Zapperi, S.; Tosatti, E. *Rev. Mod. Phys.* **2013,** *85,* 529. doi:10.1103/RevModPhys.85.529
14. Gnecco, E.; Meyer, E., Eds. *Fundamentals of Friction and Wear on the Nanoscale,* 2nd ed.; Springer: Berlin, Germany, 2015. doi:10.1007/978-3-319-10560-4
15. Manini, N.; Braun, O. M.; Vanossi, A. Nanotribology: Nonlinear Mechanisms of Friction. In *Fundamentals of Friction and Wear on the Nanoscale,* 2nd ed.; Gnecco, E.; Meyer, E., Eds.; Springer: Berlin, Germany, 2015; pp 175 ff. doi:10.1007/978-3-319-10560-4_10
16. Manini, N.; Braun, O. M.; Tosatti, E.; Guerra, R.; Vanossi, A. *J. Phys.: Condens. Matter* **2016,** *28,* 293001. doi:10.1088/0953-8984/28/29/293001
17. Floría, L. M.; Mazo, J. J. *Adv. Phys.* **1996,** *45,* 505. doi:10.1080/00018739600101557
18. Braun, O. M.; Kivshar, Y. S. *The Frenkel-Kontorova Model: Concepts, Methods, and Applications;* Springer: Berlin, Germany, 2004. doi:10.1007/978-3-662-10331-9
19. Gardiner, C. *Handbook of Stochastic Methods for Physics, Chemistry and the Natural Sciences;* Springer: Berlin, Germany, 1985.
20. Consoli, L.; Knops, H. J. F.; Fasolino, A. *Phys. Rev. Lett.* **2000,** *85,* 302. doi:10.1103/PhysRevLett.85.302
21. Consoli, L.; Knops, H. J. F.; Fasolino, A. *Phys. Rev. E* **2001,** *64,* 016601. doi:10.1103/PhysRevE.64.016601
22. Consoli, L.; Knops, H.; Fasolino, A. *Europhys. Lett.* **2002,** *60,* 342. doi:10.1209/epl/i2002-00270-x
23. Franchini, A.; Bortolani, V.; Santoro, G.; Brigazzi, M. *Phys. Rev. E* **2008,** *78,* 046107. doi:10.1103/PhysRevE.78.046107
24. Bortolani, V.; Franchini, A.; Santoro, G.; Brigazzi, M. *Tribol. Lett.* **2010,** *39,* 251. doi:10.1007/s11249-010-9631-3
25. van den Ende, J. A.; de Wijn, A. S.; Fasolino, A. *J. Phys.: Condens. Matter* **2012,** *24,* 445009. doi:10.1088/0953-8984/24/44/445009
26. Magalinskii, V. B. *Sov. Phys. - JETP* **1959,** *9,* 1381.
27. Rubin, R. J. *J. Math. Phys.* **1960,** *1,* 309. doi:10.1063/1.1703664
28. Zwanzig, R. *J. Stat. Phys.* **1973,** *9,* 215. doi:10.1007/BF01008729
29. Li, X.; E, W. *Phys. Rev. B* **2007,** *76,* 104107. doi:10.1103/PhysRevB.76.104107
30. Kantorovich, L. *Phys. Rev. B* **2008,** *78,* 094304. doi:10.1103/PhysRevB.78.094304
31. Kantorovich, L.; Rompotis, N. *Phys. Rev. B* **2008,** *78,* 094305. doi:10.1103/PhysRevB.78.094305
32. Braun, O. M.; Manini, N.; Tosatti, E. *Phys. Rev. B* **2008,** *78,* 195402. doi:10.1103/PhysRevB.78.195402
33. Benassi, A.; Vanossi, A.; Santoro, G. E.; Tosatti, E. *Phys. Rev. B* **2010,** *82,* 081401. doi:10.1103/PhysRevB.82.081401
34. Benassi, A.; Vanossi, A.; Santoro, G. E.; Tosatti, E. *Tribol. Lett.* **2012,** *48,* 41. doi:10.1007/s11249-012-9936-5
35. Pastewka, L.; Sharp, T. A.; Robbins, M. O. *Phys. Rev. B* **2012,** *86,* 075459. doi:10.1103/PhysRevB.86.075459
36. Stella, L.; Lorenz, C. D.; Kantorovich, L. *Phys. Rev. B* **2014,** *89,* 134303. doi:10.1103/PhysRevB.89.134303
37. Ness, H.; Stella, L.; Lorenz, C. D.; Kantorovich, L. *Phys. Rev. B* **2015,** *91,* 014301. doi:10.1103/PhysRevB.91.014301
38. Ness, H.; Genina, A.; Stella, L.; Lorenz, C. D.; Kantorovich, L. *Phys. Rev. B* **2016,** *93,* 174303. doi:10.1103/PhysRevB.93.174303
39. Thompson, P. A.; Robbins, M. O. *Phys. Rev. A* **1990,** *41,* 6830. doi:10.1103/PhysRevA.41.6830
40. Thompson, P. A.; Robbins, M. O. *Science* **1990,** *250,* 792. doi:10.1126/science.250.4982.792
41. Heuberger, M.; Drummond, C.; Israelachvili, J. *J. Phys. Chem. B* **1998,** *102,* 5038. doi:10.1021/jp9823143
42. Castelli, I. E.; Manini, N.; Capozza, R.; Vanossi, A.; Santoro, G. E.; Tosatti, E. *J. Phys.: Condens. Matter* **2008,** *20,* 354005. doi:10.1088/0953-8984/20/35/354005
43. Strunz, T.; Elmer, F.-J. *Phys. Rev. E* **1998,** *58,* 1601. doi:10.1103/PhysRevE.58.1601
44. Strunz, T.; Elmer, F.-J. *Phys. Rev. E* **1998,** *58,* 1612. doi:10.1103/PhysRevE.58.1612
45. Gnecco, E.; Bennewitz, R.; Gyalog, T.; Loppacher, C.; Bammerlin, M.; Meyer, E.; Güntherodt, H.-J. *Phys. Rev. Lett.* **2000,** *84,* 1172. doi:10.1103/PhysRevLett.84.1172
46. Reimann, P.; Evstigneev, M. *Phys. Rev. Lett.* **2004,** *93,* 230802. doi:10.1103/PhysRevLett.93.230802
47. Fusco, C.; Fasolino, A. *Phys. Rev. B* **2005,** *71,* 045413. doi:10.1103/PhysRevB.71.045413
48. Furlong, O. J.; Manzi, S. J.; Pereyra, V. D.; Bustos, V.; Tysoe, W. T. *Tribol. Lett.* **2010,** *39,* 177. doi:10.1007/s11249-010-9632-2
49. Guerra, R.; Tartaglino, U.; Vanossi, A.; Tosatti, E. *Nat. Mater.* **2010,** *9,* 634. doi:10.1038/nmat2798
50. Müser, M. H. *Phys. Rev. B* **2011,** *84,* 125419. doi:10.1103/PhysRevB.84.125419
51. Ashcroft, N.; Mermin, M. *Solid State Physics;* Holt-Saunders: Philadelphia, PA, U.S.A., 1976.
52. Giusti, G. Meccanismi microscopici di dissipazione in un modello unidimensionale. Bachelor Thesis, University Milan, 2015. http://materia.fisica.unimi.it/manini/theses/giusti.pdf
53. Apostoli, C. Phonon analysis of the dynamic to static friction crossover in a 1D model. Bachelor Thesis, University Milan, 2017. http://materia.fisica.unimi.it/manini/theses/apostoli.pdf

54. Luedtke, W. D.; Landman, U. *Phys. Rev. Lett.* **1999,** *82,* 3835. doi:10.1103/PhysRevLett.82.3835
55. Lebedeva, I. V.; Knizhnik, A. A.; Popov, A. M.; Ershova, O. V.; Lozovik, Y. E.; Potapkin, B. V. *Phys. Rev. B* **2010,** *82,* 155460. doi:10.1103/PhysRevB.82.155460
56. Jafary-Zadeh, M.; Reddy, C. D.; Sorkin, V.; Zhang, Y.-W. *Nanoscale Res. Lett.* **2012,** *7,* 148. doi:10.1186/1556-276X-7-148
57. Sang, Y.; Dubé, M.; Grant, M. *Phys. Rev. Lett.* **2001,** *87,* 174301. doi:10.1103/PhysRevLett.87.174301
58. Dudko, O. M.; Filippov, A. E.; Klafter, J.; Urbakh, M. *Chem. Phys. Lett.* **2002,** *352,* 499. doi:10.1016/S0009-2614(01)01469-5
59. Riedo, E.; Gnecco, E.; Bennewitz, R.; Meyer, E.; Brune, H. *Phys. Rev. Lett.* **2003,** *91,* 084502. doi:10.1103/PhysRevLett.91.084502
60. Krylov, S. Y.; Jinesh, K. B.; Valk, H.; Dienwiebel, M.; Frenken, J. W. M. *Phys. Rev. E* **2005,** *71,* 65101. doi:10.1103/PhysRevE.71.065101
61. Jinesh, K. B.; Krylov, S. Y.; Valk, H.; Dienwiebel, M.; Frenken, J. W. M. *Phys. Rev. B* **2008,** *78,* 155440. doi:10.1103/PhysRevB.78.155440
62. Pierno, M.; Bignardi, L.; Righi, M. C.; Bruschi, L.; Gottardi, S.; Stöhr, M.; Ivashenko, O.; Silvestrelli, P. L.; Rudolf, P.; Mistura, G. *Nanoscale* **2014,** *6,* 8062. doi:10.1039/c4nr01079e
63. de Wijn, A. S.; Fasolino, A.; Filippov, A. E.; Urbakh, M. *J. Phys.: Condens. Matter* **2016,** *28,* 105001. doi:10.1088/0953-8984/28/10/105001
64. Ciccoianni, J. Meccanismi microscopici di dissipazione in un modello bidimensionale. Bachelor Thesis, University Milan, 2015. http://materia.fisica.unimi.it/manini/theses/ciccoianni.pdf
65. Gigli, L.; Manini, N.; Benassi, A.; Tosatti, E.; Vanossi, A.; Guerra, R. *2D Mater.* **2017,** *4,* 045003. doi:10.1088/2053-1583/aa7fdf

License and Terms

BEILSTEIN JOURNAL OF NANOTECHNOLOGY

Numerical investigation of the tribological performance of micro-dimple textured surfaces under hydrodynamic lubrication

Kangmei Li[1], Dalei Jing[2], Jun Hu[*1], Xiaohong Ding[2] and Zhenqiang Yao[3,4]

Full Research Paper

Open Access

Address:
[1]School of Mechanical Engineering, Donghua University, 2999 North Renmin Road, Shanghai, 201620, China, [2]School of Mechanical Engineering, University of Shanghai for Science and Technology, 516 Jungong Road, Shanghai, 200093, China, [3]State Key Laboratory of Mechanical System and Vibration, Shanghai Jiao Tong University, 800 Dongchuan Road, Shanghai, 200240, China, and [4]School of Mechanical Engineering, Shanghai Jiao Tong University, 800 Dongchuan Road, Shanghai, 200240, China

Email:
Jun Hu[*] - hujun@dhu.edu.cn

* Corresponding author

Keywords:
CFD simulation; hydrodynamic lubrication; micro-dimple array; surface texture; tribological performance

Beilstein J. Nanotechnol. **2017,** *8,* 2324–2338.
doi:10.3762/bjnano.8.232

Received: 15 May 2017
Accepted: 12 October 2017
Published: 06 November 2017

This article is part of the Thematic Series "Nanotribology".

Guest Editor: E. Gnecco

Abstract

Surface texturing is an important approach for controlling the tribological behavior of friction pairs used in mechanical and biological engineering. In this study, by utilizing the method of three-dimensional computational fluid dynamics (CFD) simulation, the lubrication model of a friction pair with micro-dimple array was established based on the Navier–Stokes equations. The typical pressure distribution of the lubricant film was analyzed. It was found that a positive hydrodynamic pressure is generated in the convergent part of the micro-dimple, while a negative hydrodynamic pressure is generated in the divergent part. With suitable parameters, the total integration of the pressure is positive, which can increase the load-carrying capacity of a friction pair. The effects of the micro-dimple parameters as well as fluid properties on tribological performance were investigated. It was concluded that under the condition of hydrodynamic lubrication, the main mechanism for the improvement in the tribological performance is the combined effects of wedging and recirculation. Within the range of parameters investigated in this study, the optimum texture density is 13%, while the optimum aspect ratio varies with the Reynolds number. For a given Reynolds number, there exists a combination of texture density and aspect ratio at which the optimum tribological performance could be obtained. Conclusions from this study could be helpful for the design of texture parameters in mechanical friction components and even in artificial joints.

Introduction

The wear caused by friction is considered to be the main reason for the failure of mechanical systems and the major source of energy loss [1]. Various methods have been developed to reduce friction and wear. One of the most promising solutions is the introduction of surface texturing on a friction pair. The benefits of surface texturing and the effects of texturing parameters on tribological performance have been experimentally and theoretically investigated over the past two decades. Experimental investigations by means of friction tests were performed to study the influence of surface texturing on load-carrying capacity, friction forces and the friction coefficient [2-4]. Meanwhile, theoretical models were established to describe the mechanism behind surface texturing to improve the tribological performance of lubricated contacts [5-9]. In Kligerman and Etsion's study [5], the pressure distribution in the uniform clearance between the annular surfaces is obtained from a solution of the Reynolds equation for compressible viscous gas in a laminar flow. Wang et al. [6] calculated the dimensionless load of a SiC thrust bearing based on the Reynolds equation and compared the results with the experimental results. Rahmani et al. [7] presented a method of integrating the Reynolds equation for partially textured slider bearings to achieve the optimum texturing parameters. In Meng and Khonsari's study [9], the Stokes equations and the energy equation were solved for the microtextured parallel surfaces to gain insight into the role of the viscosity wedge on the pressure distribution and the load-carrying capacity.

From the experimental and theoretical studies, it was found that properly designed surface texture acts as micro-hydrodynamic bearings on the friction pair, which help to reduce friction and increase the load-carrying capacity. In addition, the surface texturing also provides extra space to reserve lubricant and entrap wear debris. Furthermore, parametric studies were conducted for various applications such as thrust bearings [10-12], journal bearings [13], engine cylinders [14-17] and mechanical seals [3,18]. It was concluded that there are optimal texturing parameters with which the friction pair exhibits optimal tribological performance.

As shown in this literature survey, most theoretical studies are based on the Reynolds equation. In some cases, textured surfaces under hydrodynamic lubrication can be accurately modeled by the Reynolds equation. However, the Reynolds equation is not accurate when inertial effects are important, for instance, when the Reynolds number is high, when the textures a have high aspect ratio, or when the texture depth exceeds 10% of the film thickness [19-21]. In these cases, the general Navier–Stokes (N-S) equations have to be adopted in order to account for the role of convective inertia in generating lift from surface textures.

Due to the development of more efficient algorithms and computational techniques in recent years, the mechanisms and effects of surface texturing on improving tribological performance could be numerically investigated using CFD based on the N-S equations.

Based on a two-dimensional CFD method, the tribological performance of surface with groove-shaped texture was studied. Sahlin et al. [22] successfully compared the lubrication characteristics of groove texture with arc-shaped cross section against that with spline-shaped cross section. The pressure distribution of the film and the fluid field status in grooves were investigated. Moreover, the effects of groove depth, groove width and Reynolds number on load-carrying capacity were studied. Brajdic-Mitidieri et al. [23] investigated the effect of groove-shaped texture on the lubrication characteristics of unparallel sliding surfaces. It was found that surface texturing not only reduces the friction coefficient significantly, but also improves the load-carrying capacity. Li and Chen [20] studied the lubrication characteristics of parallel surfaces with rectangle-shaped grooves. The results calculated using the two-dimensional CFD method were compared against those based on the Reynolds equations. It was found that when the groove depth is greater than ten percent of the film thickness, the method based on the Reynolds equations is no longer applicable. Shi and Ni [24] developed a two-dimensional CFD model to investigate the effects of groove texture on fully lubricated sliding with cavitation. The effects of cavitation pressure, sliding speed, sliding pitch angle and texture scale were discussed. Ramesh et al. [25] solved the N-S equations by using two-dimensional CFD and predicted the texture-induced lift. The results showed good correlation between the experiments and the CFD analysis. The above-described studies are all focused on groove-textured surfaces using a two-dimensional method.

It was reported that the tribological performance of a dimple-textured surface is better than that of groove-textured surface in terms of the friction coefficient [26]. A two-dimensional method is more suitable to simulate the hydrodynamic lubrication of a groove-textured surface, in which case the cross section of the surface is identical along the groove length. Due to the geometrical complexity of the micro-dimple array, however, the commonly used two-dimensional CFD technique is not able to simulate the lubrication behavior accurately. Therefore, the three-dimensional CFD method was proposed. Han et al. [27] studied the tribological characteristics of the micro-dimple array by using a three-dimensional CFD technique. The

effects of micro-dimple size and the Reynolds number on film pressure, friction force as well as the friction coefficient were investigated and the optimum range for the micro-dimple depth was recommended.

Published papers regarding hydrodynamic lubrication of micro-dimple textured surfaces using three-dimensional CFD are very limited. Moreover, although some general guidelines for finding the optimal texturing parameters exist, the effects of texturing parameters on the tribological performance are highly dependent on contact and operating conditions [28]. Therefore, it is necessary to put more efforts into numerically investigating the hydrodynamic lubrication of micro-dimple textured surface.

In this study, the three-dimensional CFD method based on the N-S equations is proposed. The purpose of this study is to simulate the tribological behavior of a friction pair with a micro-dimple array under the condition of hydrodynamic lubrication. The pressure and velocity distribution are obtained using the finite volume method. Negative pressure is permitted and cavitation is not yet considered. The main mechanism for the improvement of the tribological performance by micro-dimple texturing is investigated and the optimum combination of texture density and aspect ratio for a given Reynolds number is discussed.

Modeling

Geometrical modeling

In this study, the lubricant is filled between the upper flat surface and the lower surface in each compartment of the micro-dimple array. Because the micro-dimple array is composed of many identical micro-dimples which are linearly arranged with equal intervals, the fluids can also be divided into many identical units. Figure 1 shows the three-dimensional geometric model of the fluid in the micro-dimple array and details of a single micro-dimple unit.

As shown in Figure 2, due to the symmetrical characteristic of each micro-dimple unit, only half of the fluid in the micro-dimple unit is chosen as the computational domain. The coordinate system and geometrical parameters of the computational domain used in this study are also shown in Figure 2. The origin of the coordinate system is located on the revolution axis of the micro-dimple and is $h_0/2$ away from the upper surface. The x, y and z axes are defined as the direction vertical to the symmetry plane, the flow direction and the direction of lubrication film thickness, respectively. l is the characteristic length of a micro-dimple unit, h_0 is the thickness of lubricant film, which is identical to the gap between the friction pairs, h is the depth of the micro-dimple and d is the diameter of dimple.

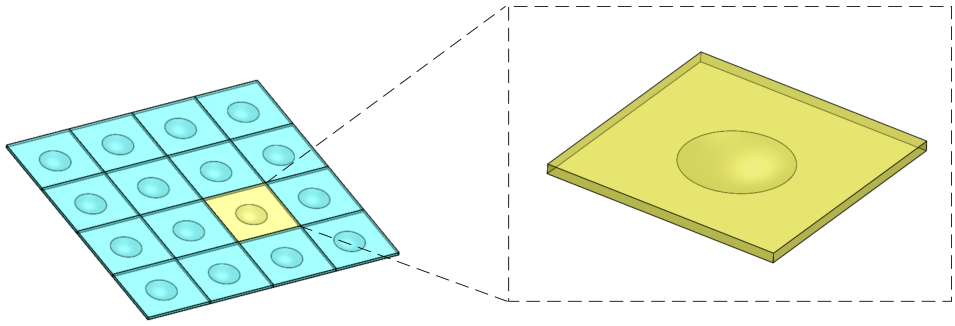

Figure 1: Three-dimensional geometric model of fluid in a micro-dimple array and a single micro-dimple unit.

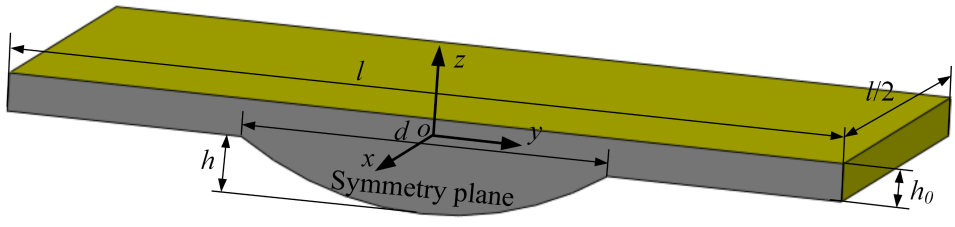

Figure 2: The computational domain.

Mathematical modeling

Governing equations

In order to solve the hydrodynamic lubrication problem for a friction pair with micro-dimple texturing more accurately, the N-S equations, which are the equations of momentum conservation considering inertia terms, are used as the governing equations. In addition, the behavior of the lubricant in a micro-dimple array satisfies the law of mass conservation.

For the purpose of facilitating modeling and analysis, the following assumptions were made: 1) The body force is considered negligible (e.g., gravity or magnetic force); 2) No slip of lubricant is supposed to occur on the boundary, which means the velocity of lubricant close to the friction pair surface is identical with that of the friction pair surface; 3) The isothermal condition is considered and the lubricant is assumed to be an incompressible Newtonian fluid.

Based on these assumptions, the N-S equations and the continuation equation could be simplified. Furthermore, in order to reduce the number of independent variables, the dimensionless variables are defined as follows:

$$\begin{aligned} &x^* = x/l; y^* = y/l; z^* = z/h_0; \\ &u^* = u/v_0; v^* = v/v_0; w^* = w/(v_0 l/h_0); \\ &p^* = p/p_0 \end{aligned} \tag{1}$$

where u, v and w are the velocities of the fluid along the x, y, and z axes, respectively; η is the dynamic viscosity; p is pressure; v_0 is the characteristic velocity of the lubricant and p_0 is the characteristic pressure.

By substituting the above dimensionless variables into the simplified N-S equations [29], the dimensionless N-S equations can be expressed as the following. Along the direction of the x-axis:

$$\begin{aligned} &\frac{\rho {v_0}^2}{l}\left(u^*\frac{\partial u^*}{\partial x^*}+v^*\frac{\partial u^*}{\partial y^*}+\left(\frac{l}{h_0}\right)^2 w^*\frac{\partial u^*}{\partial z^*}\right) \\ &=-\frac{p_0}{l}\frac{\partial p^*}{\partial x^*}+\left(\frac{\eta v_0 l}{{h_0}^3}\right)\frac{\partial^2 u^*}{\partial {z^*}^2}+\left(\frac{\eta v_0}{l^2}\right)\left(\frac{\partial^2 u^*}{\partial {x^*}^2}+\frac{\partial^2 u^*}{\partial {y^*}^2}\right) \end{aligned} \tag{2}$$

where ρ is density of the fluid. By letting $p_0 = \eta v_0 l/{h_0}^2$ and defining the Reynolds number as $Re = \rho v_0 h_0/\eta$, the above equation can be simplified as:

$$\begin{aligned} &Re\left(\frac{h_0}{l}\right)\left(u^*\frac{\partial u^*}{\partial x^*}+v^*\frac{\partial u^*}{\partial y^*}+\left(\frac{l}{h_0}\right)^2 w^*\frac{\partial u^*}{\partial z^*}\right) \\ &=-\frac{\partial p^*}{\partial x^*}+\left(\frac{l}{h_0}\right)\frac{\partial^2 u^*}{\partial {z^*}^2}+\left(\frac{h_0}{l}\right)^2\left(\frac{\partial^2 u^*}{\partial {x^*}^2}+\frac{\partial^2 u^*}{\partial {y^*}^2}\right) \end{aligned} \tag{3}$$

In a similar way, the equations along the y and z-axis could be obtained as follows:

$$\begin{aligned} &Re\left(\frac{h_0}{l}\right)\left(u^*\frac{\partial v^*}{\partial x^*}+v^*\frac{\partial v^*}{\partial y^*}+\left(\frac{l}{h_0}\right)^2 w^*\frac{\partial v^*}{\partial z^*}\right) \\ &=-\frac{\partial p^*}{\partial y^*}+\left(\frac{l}{h_0}\right)\frac{\partial^2 v^*}{\partial {z^*}^2}+\left(\frac{h_0}{l}\right)^2\left(\frac{\partial^2 v^*}{\partial {x^*}^2}+\frac{\partial^2 v^*}{\partial {y^*}^2}\right) \end{aligned} \tag{4}$$

$$\begin{aligned} &Re\left(\frac{h_0}{l}\right)\left(u^*\frac{\partial w^*}{\partial x^*}+v^*\frac{\partial w^*}{\partial y^*}+\left(\frac{l}{h_0}\right)^2 w^*\frac{\partial w^*}{\partial z^*}\right) \\ &=-\frac{\partial p^*}{\partial z^*}+\frac{\partial^2 w^*}{\partial {z^*}^2}+\left(\frac{h_0}{l}\right)^2\left(\frac{\partial^2 w^*}{\partial {x^*}^2}+\frac{\partial^2 w^*}{\partial {y^*}^2}\right) \end{aligned} \tag{5}$$

The dimensionless continuity equation could be expressed as:

$$\frac{\partial u^*}{\partial x^*}+\frac{\partial v^*}{\partial y^*}+\frac{\partial w^*}{\partial z^*}=0. \tag{6}$$

Equations 3–6 could be used to describe the behavior of the fluid in micro-dimple unit under the condition of hydrodynamic lubrication. Due to the complexity of the governing equations, however, it is difficult to obtain an analytical solution. Therefore, a numerical simulation is adopted in this study to solve the problem.

Characterization of tribological properties

The effect of the micro-dimple array on the tribological performance of a friction pair under the condition of hydrodynamic lubrication can be characterized by the following tribological characteristics: (1) dimensionless average film carrying force; (2) dimensionless average film shear force; (3) friction coefficient.

The film carrying force is calculated by integrating the pressure on the upper wall over the total calculation domain and can be expressed by

$$F_z = \iint p(x, y)\,\mathrm{d}x\,\mathrm{d}y, \tag{7}$$

where F_z is the film carrying force and $p(x,y)$ is the pressure distribution function. The dimensionless form of the average film carrying force is obtained by

$$F_z^* = \frac{F_z}{p_0 S_\mathrm{t}} = \frac{F_z h_0^2}{S_\mathrm{t}\eta v_0 l}, \tag{8}$$

where S_t is the area of the upper wall of the calculation domain, that is, the area of the micro-dimple unit. A high dimensionless average film carrying force indicates a good load-carrying capacity of the friction pair.

In a similar way, as shown in Equation 9, the film shear force is calculated by integrating the shear stress along the y-axis on the upper wall over the total calculation domain:

$$F_y = \iint \tau' \mathrm{d}x\,\mathrm{d}y, \tag{9}$$

where F_y is shear force and τ' is the shear stress. The dimensionless form of the average film shear force can be obtained by

$$F_y^* = \frac{F_y}{p_0 S_\mathrm{t}} = \frac{F_y h_0^2}{S_\mathrm{t}\eta v_0 l}. \tag{10}$$

The friction coefficient is defined as the ratio of the dimensionless average film shear force to the dimensionless average film carrying force and can be expressed as

$$f = \frac{F_y^*}{F_z^*}, \tag{11}$$

where f represents the friction coefficient. A low friction coefficient means small shear force with large carrying force, which indicates good behavior of the comprehensive tribological performance under the condition of hydrodynamic lubrication.

Numerical simulation

Meshing

The three-dimensional model of the computational domain was meshed by using GAMBIT software. In order to obtain a high-quality mesh, the model was divided into three domains (see Figure 3). The micro-dimple was located in domain two and domain three.

In order to guarantee the accuracy of calculation and the rate of convergence, the meshing operation follows several criteria: (1) the use of structured grids, as far as possible; (2) the ratio of the length of the longest element edge to the length of the shortest element edge should be controlled below 5:1; (3) the skewness should be controlled to be no more than 0.9; (4) because the entry, exit and interior of the dimple are the areas of most concern, the mesh density of the model increases gradually from domain one to domain three; (5) the dimen-

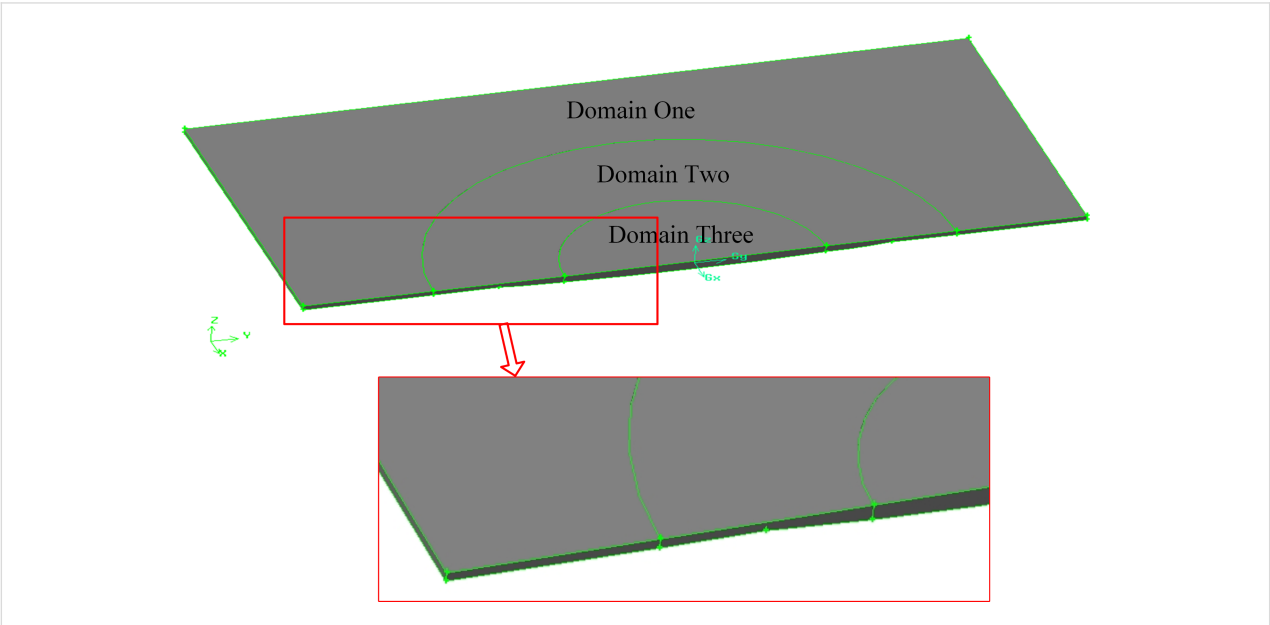

Figure 3: The division of the fluid domain in the micro-dimple unit.

sional difference between neighboring elements should be controlled to be as small as possible.

The meshing is challenging in particular for shallow dimples and for a small film thickness. A smaller dimple depth requires very small grid volumes in order to have enough volume in the vertical direction. When combined with the volume aspect ratio limits, a large number of volumes are required to fill the horizontal extent of the dimple. Since the mesh size has a great effect on the accuracy and efficiency of the numerical simulation, the grid independence analysis was carried out to develop the proper meshing strategy. The variation of the mesh size may affect the film pressure distribution and therefore the load-carrying capacity. Thus, the dimensionless average film carrying force, F_z*, was considered as the main indicator of grid independence. The mesh sizes were chosen to suit the geometry of each case so that further mesh refinement did not change the dimensionless average film carrying force by more than 0.01%.

Based on the typical dimple unit geometry characterized by l = 2400 μm, d = 1200 μm, h = 20 μm and h_0 = 20 μm, the grid independence analysis was performed as follows. Six sets of mesh sizes were selected for calculation (see Table 1). The variations of the dimensionless average film carrying force, F_z*, and the computing time, T, of the simulation with different average mesh sizes are shown in Figure 4.

Table 1: Mesh sizes for the grid independence analysis.

Case number	Average mesh size (μm)		
	Domain one	Domain two	Domain three
1	12	10	8
2	10	8	6
3	8	6	4
4	6	5	4
5	6	4	3
6	5	4	3

It is noted from Table 1 that the average mesh size decreases gradually from case 1 to case 6. As shown in Figure 4, from case 1 to case 6, F_z* decreases and tends to be stable while T increases constantly. From case 4 to case 6, the value of F_z* converged within a satisfactory tolerance of about 0.01% to a constant value. Meanwhile, the value of T for case 4 is in the acceptable range. Therefore, the average mesh sizes for case 4 were chosen for meshing this model. Figure 5 shows the meshed model of the micro-dimple unit with a total grid number of 416,670.

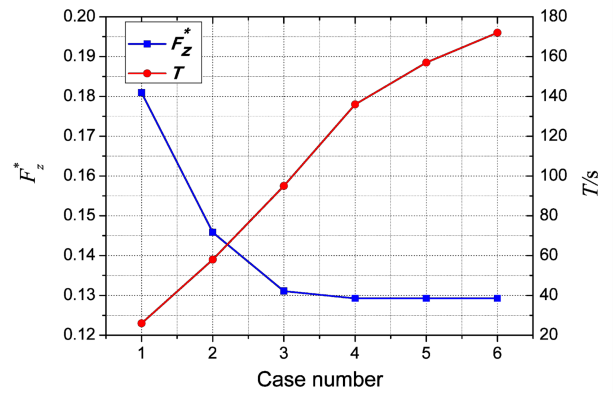

Figure 4: Variations of the dimensionless average film carrying force and the computing time.

Boundary conditions

As shown in Figure 5, the upper and lower walls of the simulation model are set as no-slip boundaries. The upper wall moves along the positive direction of the y-axis with a velocity of v_0, while the lower wall is assumed stationary. The inlet and outlet of the model along the y-axis are set as periodic boundary conditions. That is, the values of the variables of the inlet are the same as those of the outlet. The two walls along the x-axis are set as symmetrical boundary conditions.

Calculation

The model is calculated by utilizing commercial CFD software, and the FLUENT and SIMPLE algorithms were adopted for solving. The key parameters used in the CFD simulation are listed in Table 2.

In Table 2, the texture density is defined as the ratio of the micro-dimple area to the friction pair area. Because the micro-dimple array could be divided into many identical micro-dimple units, the texture density can be expressed as

$$\rho_t = \frac{S_\mathrm{d}}{S_\mathrm{t}} \times 100\% = \frac{\pi d^2}{4l^2} \times 100\%, \quad (12)$$

where S_d is the area of a single micro-dimple and S_t is the area of a single micro-dimple unit. The aspect ratio, λ, is defined as the ratio of the micro-dimple depth to the micro-dimple diameter.

Results and Discussion

Film pressure distribution of the micro-dimple unit

The typical pressure distribution on the upper wall of the lubricant in the micro-dimple unit is shown in Figure 6. Moreover, Figure 7 shows the pressure distribution on the middle section

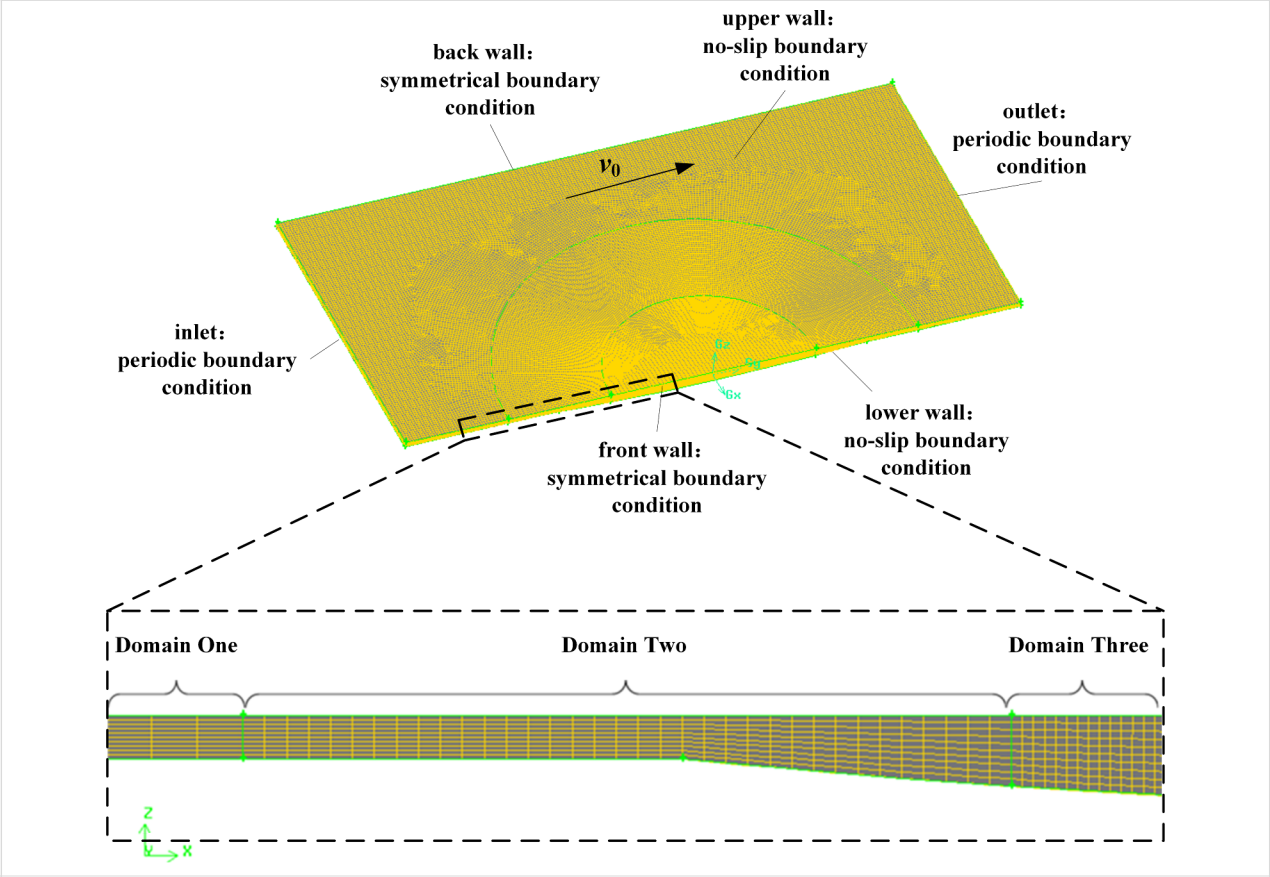

Figure 5: The typical meshed model of a micro-dimple unit.

Table 2: Parameters of the CFD simulation.

Texture density, ρ_t	5%, 13%, 20%, 50%
Aspect ratio, λ	0.017, 0.033, 0.05, 0.075, 0.1, 0.125, 0.2
Reynolds number, *Re*	5, 50, 250

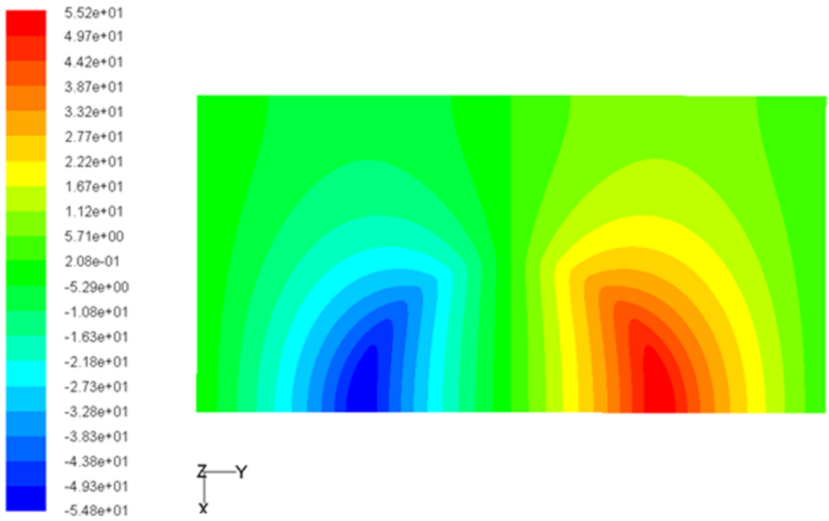

Figure 6: Pressure distribution on the upper wall of the lubricant in the micro-dimple unit.

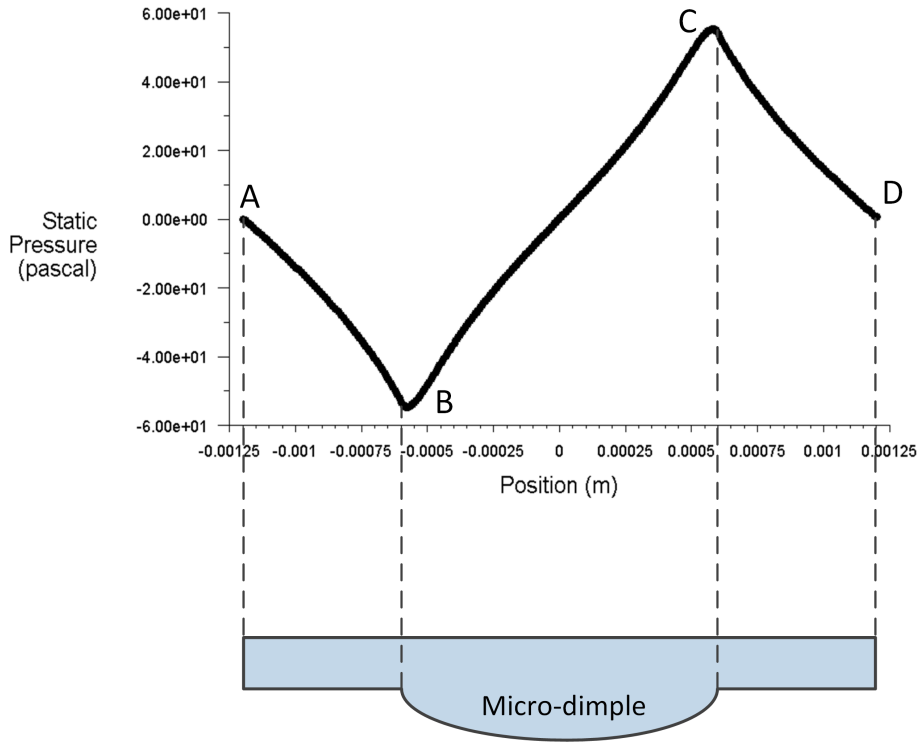

Figure 7: Pressure distribution of the cross-sectional area of the lubricant in a micro-dimple unit.

of the micro-dimple unit. From Figure 6 and Figure 7, it is can be seen that when the lubricant flows into the micro-dimple unit from point A to point D, the pressure decreases gradually and reaches a minimum at the entry of the micro-dimple (point B). Then the pressure starts to increase and reaches a maximum at the exit of the micro-dimple (point C). From point C to point D, the pressure decreases to a value at point D, which is identical as that at point A.

Positive hydrodynamic pressure is generated in the convergent part of the gap while negative hydrodynamic pressure is generated in the divergent part. With suitable parameters (e.g., shape and size of the micro-dimple unit, film thickness and velocity of fluid), the magnitude of the positive pressure could be greater than that of the negative pressure, which makes the total integration of the pressure in the micro-dimple unit become positive. This phenomenon is called the wedging effect of a micro-dimple. In this case, the hydrodynamic pressure in the micro-dimple unit offers extra carrying force, which helps increase the load-carrying capacity of the friction pair.

The effect of Reynolds number on the dimensionless pressure distribution

In this study, the Reynolds number is changed by modifying the moving velocity of the upper wall. The three-dimensional pressure distribution on the upper wall under different Reynolds numbers is shown in Figure 8. Figure 9 presents the two-dimensional pressure distribution on the middle section of the micro-dimple unit. From Figure 8 and Figure 9, it can be seen that the Reynolds number affects the dimensionless pressure distribution significantly. The magnitude of the positive and negative pressure increases with Reynolds number. The increase rate of the positive pressure, however, is higher than that of the negative pressure. This result indicates that a large Reynolds number leads to a high hydrodynamic pressure.

Effect of texture density and aspect ratio on the dimensionless average film carrying force

Figure 10a–c shows the effect of texture density and aspect ratio on the dimensionless average film carrying force with Reynolds numbers of 5, 50, and 250, respectively (the texture density of 5%, 13%, 20% and 50% are abbreviated as tex5%, tex13%, tex20% and tex50%, respectively).

It is found that for a given Reynolds number and aspect ratio, the dimensionless average film carrying force at a texture density of 13% is higher than that at a texture density of 5%, 20% and 50%. This indicates that there exists an optimum texture density which leads to a maximum carrying force. Meanwhile, it can be seen that with a given Reynolds number and texture density, there also exists an optimum aspect ratio at which the film carrying force reaches a maximum. However, the optimum

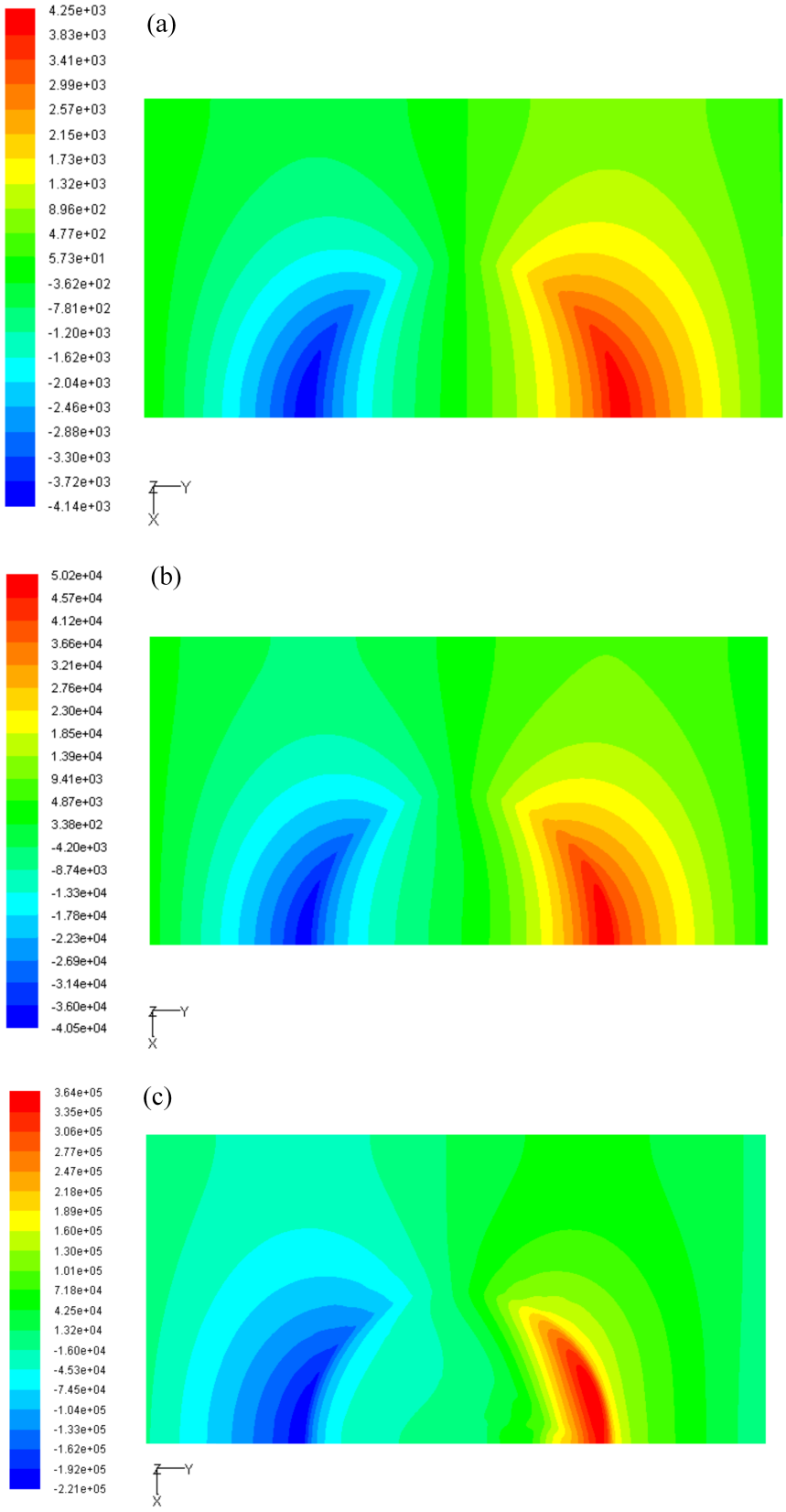

Figure 8: The pressure distribution on the upper wall for (a) *Re* = 5, (b) *Re* = 50 and (c) *Re* = 250.

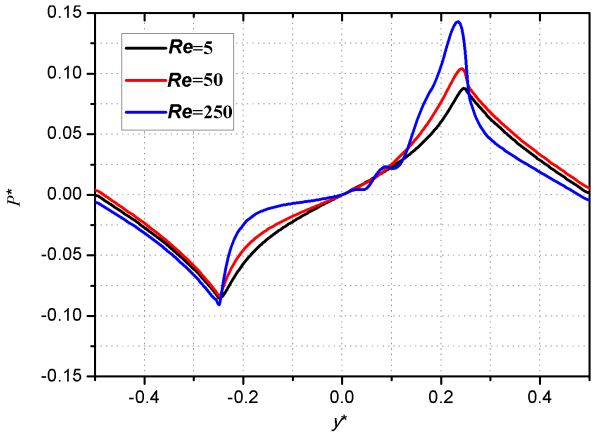

Figure 9: Effect of Reynolds number on the pressure distribution on the middle section of the micro-dimple unit.

aspect ratio is not constant but changes with the Reynolds number. The existence of an optimum texture density and optimum aspect ratio is also observed and proved using experimental and analytical methods in previously published investigations [3,6,30].

The reason for the existence of an optimum aspect ratio could be explained as follows. By assuming that the diameter of the micro-dimple is constant, a large aspect ratio means a large micro-dimple depth. The inertia force of the lubricant in the micro-dimple unit increases with the depth, which can enhance the wedging effect that is helpful for improving the load-carrying capacity. However, when the depth increases to a certain value, recirculation starts to occur at the bottom of the micro-dimple due to the interaction between the fluid and the wall of micro-dimple. In terms of energy conversion, part of the energy transferred from the moving film upper wall to the fluid is dissipated by being converted to the kinetic energy of recirculation. Therefore, the load-carrying capacity is reduced. This phenomenon could be called the recirculation effect. Due to the joint result of the wedging effect and the recirculation effect, there is an optimum value of the aspect ratio which leads to the best load-carrying capacity of the micro-dimple unit.

To further investigate the recirculation effect, the velocity streamlines on the middle section of the micro-dimple unit with different aspect ratios are compared in Figure 11. The arrow direction indicates the direction of velocity and the arrow size stands for the velocity magnitude.

With a small aspect ratio, the direction of the fluid velocity at the bottom of the micro-dimple is identical with that on the upper wall (see Figure 11a). When the aspect ratio is increased, it is found that the direction of fluid flow at the bottom of the

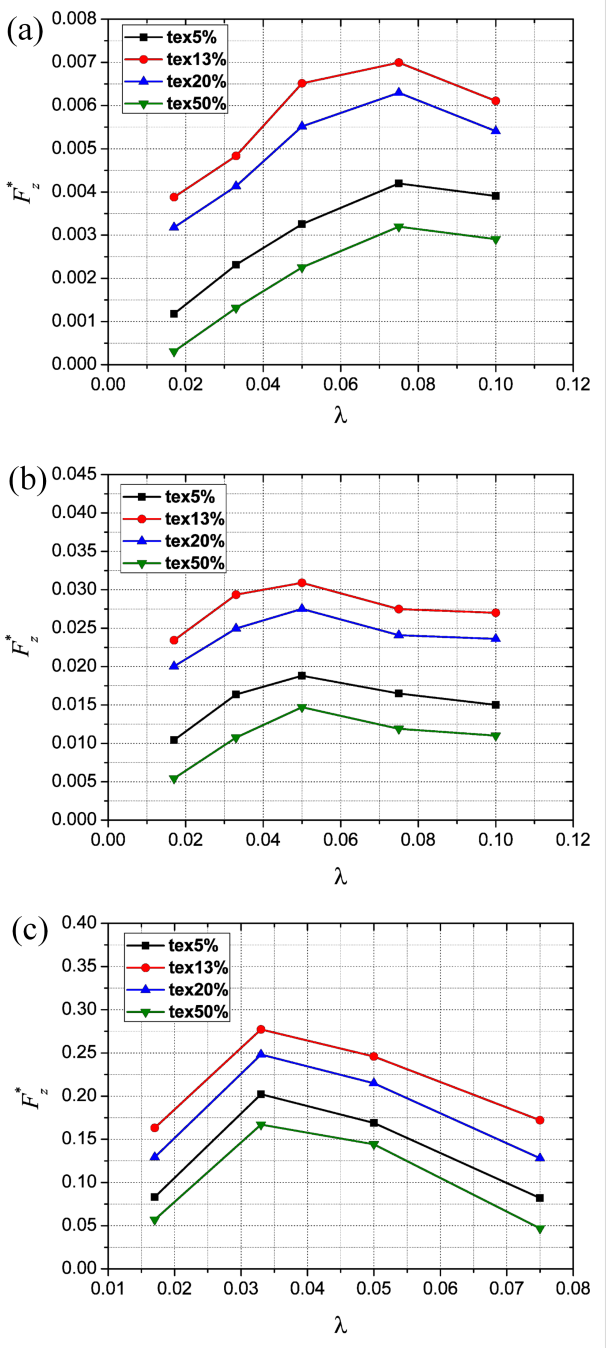

Figure 10: Effect of texture density and aspect ratio on the dimensionless average film carrying force for (a) *Re* = 5, (b) *Re* = 50 and (c) *Re* = 250.

micro-dimple is reversed to that of the upper wall, which implies the generation of a recirculation zone in the micro-dimple (see Figure 11b). With a further increase of the aspect ratio, the range of the recirculation zone increases. This means that more energy is converted to kinetic energy of recirculation, resulting in a more adverse effect on the load-carrying capacity of the micro-dimple (see Figure 11c,d).

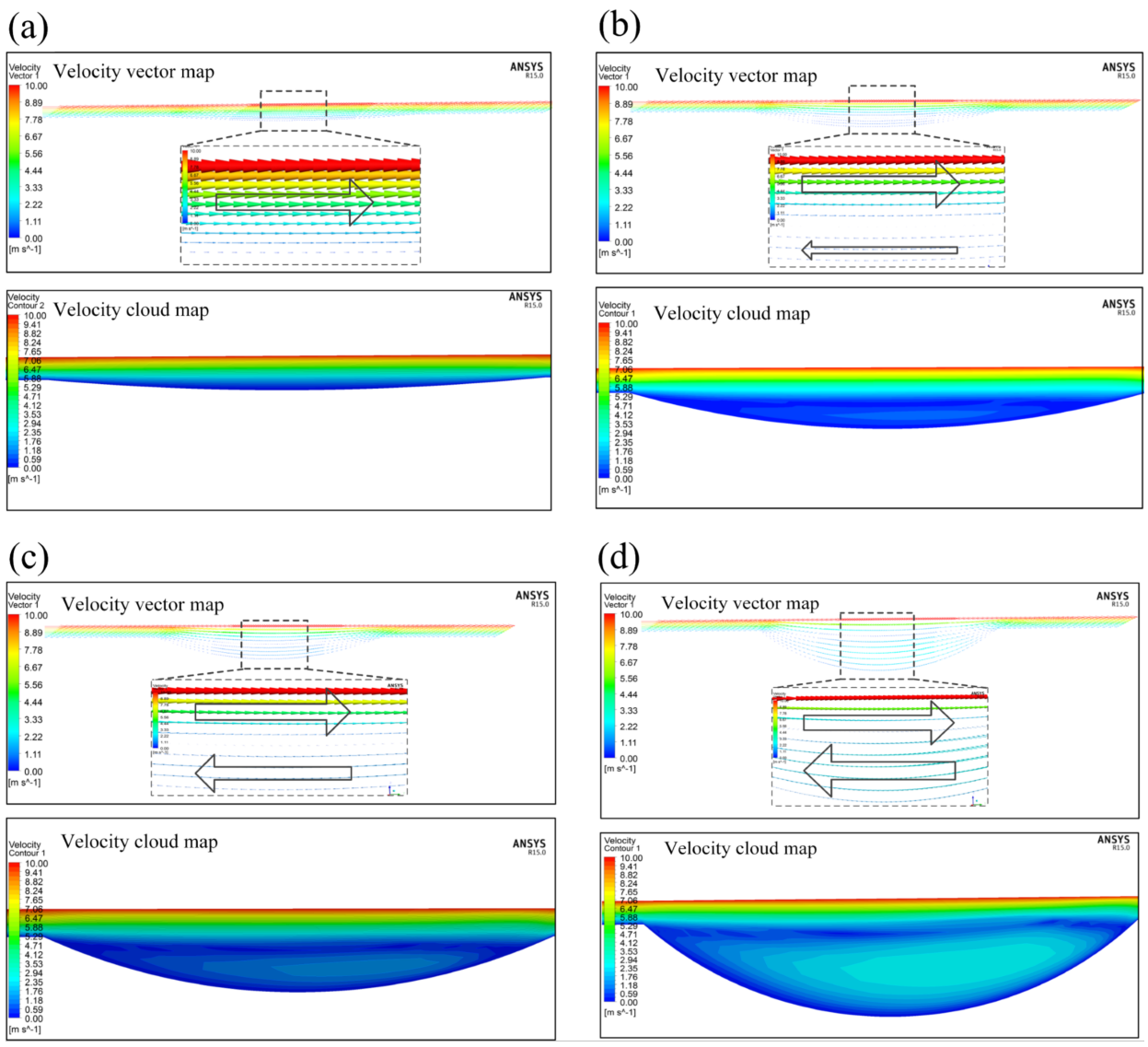

Figure 11: Variation of the fluid velocity in the micro-dimple unit with (a) λ = 0.025, (b) λ = 0.075, (c) λ = 0.1 and (d) λ = 0.2 (texture density: 20%).

Effect of texture density and aspect ratio on the dimensionless average film shear force

Figure 12a–c shows the effects of the texture density and aspect ratio on the dimensionless average film shear force with Reynolds numbers of 5, 50 and 250, respectively.

At a given Reynolds number and aspect ratio, with the increase of texture density, the dimensionless average film shear force decreases first and then starts to increase after reaching a minimum. It is noted that the variation trend of the dimensionless average shear force is opposite to that of the dimensionless average film carrying force. In addition, with a given Reynolds number and texture density, the variation of aspect ratio has very limited effect on dimensionless average shear force.

Effect of texture density and aspect ratio on friction coefficient

The effect of texture density and aspect ratio on the friction coefficient with Reynolds numbers of 5, 50 and 250 is shown in Figure 13a–c, respectively. Due to the insignificant impact of texture density and aspect ratio on the dimensionless average film shear force, it is found that the variation trend of the friction coefficient is reverse to that of the dimensionless average film carrying force. There also exists an optimum texture density and optimum aspect ratio which leads to the best tribological performance. Within the range of parameters investigated in this study, the optimum texture density was found to be 13% while the optimum aspect ratio varies with the Reynolds number.

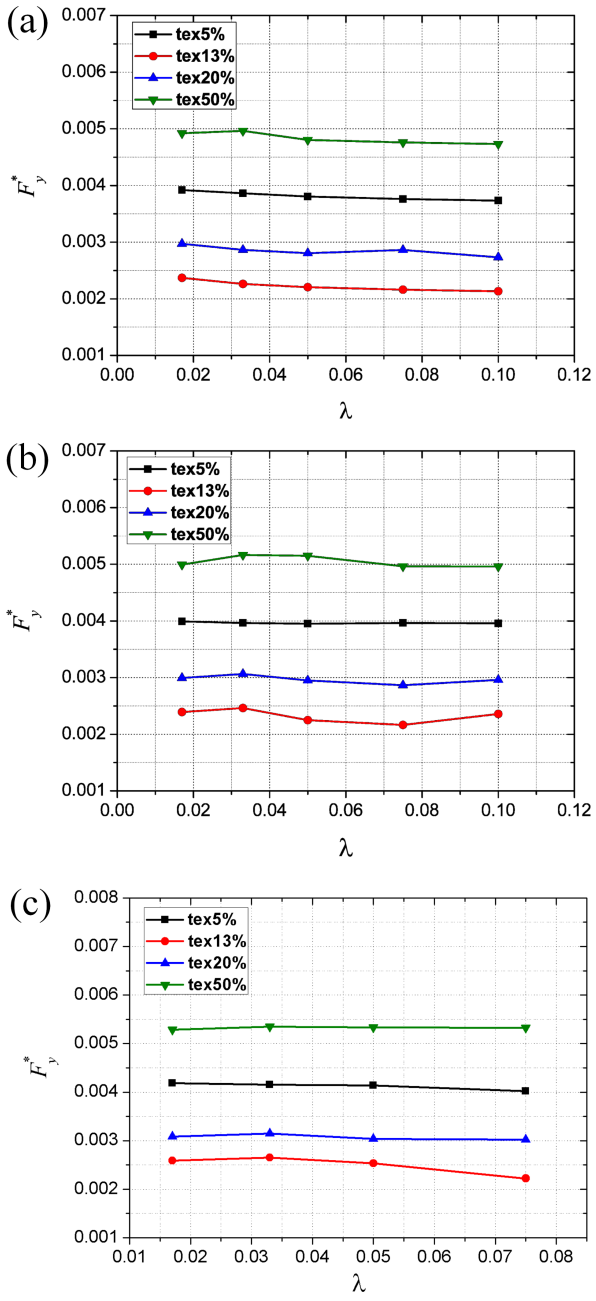

Figure 12: Effect of texture density and aspect ratio on the dimensionless average film shear force for (a) *Re* = 5, (b) *Re* = 50 and (c) *Re* = 250.

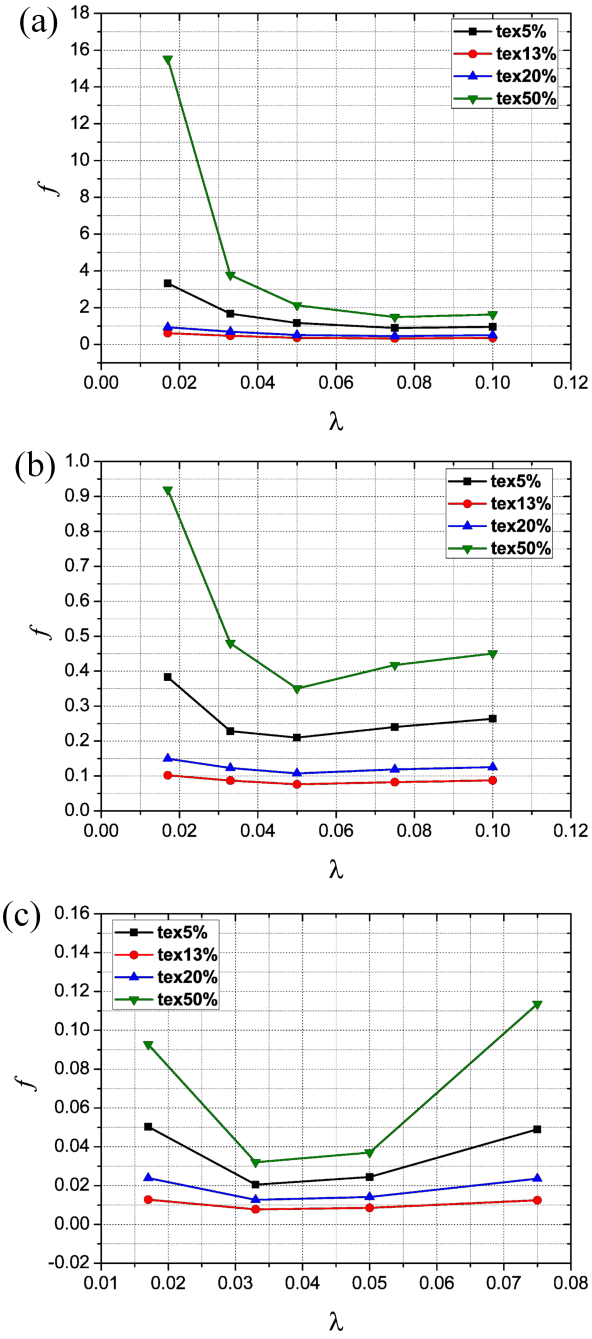

Figure 13: Effect of texture density and aspect ratio on the friction coefficient for (a) *Re* = 5, (b) *Re* = 50 and (c) *Re* = 250.

The above conclusion is in good agreement with other experimental investigations [31] in which the effect of texture density on the friction coefficient was studied. It was found that the lowest friction coefficient was achieved with a texture density of 10.4% when comparing against those with a texture density of 2.6%, 15.5% and 22.9%.

Effect of Reynolds number on the tribological characteristics of the friction pair

Figure 14a–c illustrates the trend variation of the tribological characteristics with Reynolds number for the cases with a texture density of 13% and aspect ratio of 0.017, 0.033 and 0.05.

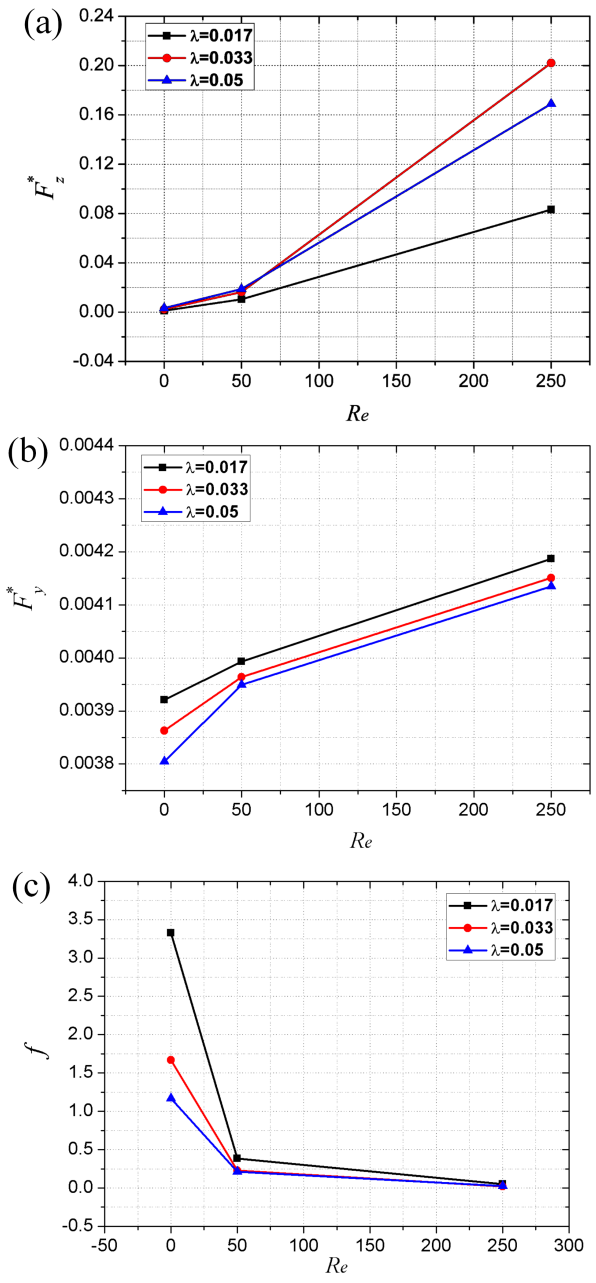

Figure 14: Effect of Reynolds number on (a) the dimensionless average film carrying force, (b) the dimensionless average film shear force and (c) the friction coefficient.

It can be seen from Figure 14a that the dimensionless average film carrying force obviously increases with Reynolds number. In addition, the increasing rate of the carrying force increases with the value of the Reynolds number. As shown in Figure 8a–c, with an increase in the Reynolds number, the maximum magnitude, as well as the distributed area of positive pressure, increases more significantly than that of the negative pressure. As a result, the total integration of the pressure over the area of film upper wall (which stands for the film carrying force) increases with the Reynolds number.

Although the dimensionless average film shear force increases with Reynolds number as well, the increase rate is very small as compared to that of the dimensionless average film carrying force (see Figure 14b). When the Reynolds number increases from 5 to 50, and from 50 to 250, the dimensionless average carrying force increases by 606% and 1135%, respectively. However, the dimensionless average film shear force increases by only 3% and 5%, respectively. These conclusions about the effect of the Reynolds number on the carrying force and shear force are consistent with those in another study [27]. As a result, the variation of the friction coefficient with Reynolds number is reverse to that of the dimensionless average film carrying force (see Figure 14c).

Effect of Reynolds number on optimum texture density and optimum aspect ratio

Figure 15 shows the variation of the optimum texture density and the optimum aspect ratio with Reynolds number. It is found that, within the parameter range of this study, the optimum texture density is independent of the Reynolds number and the micro-dimple array, where a texture density of 13% is found to exhibit the optimum hydrodynamic lubrication performance in all cases. The optimum dimple aspect ratio decreases with increased Reynolds number. For a given industrial application, the operating condition could be characterized by a corresponding Reynolds number. Therefore, for a given Reynolds number, the preferred dimensional parameters of micro-dimple texturing could be obtained according to the combination of optimum texture density and optimum aspect ratio, which leads to the best tribological performance.

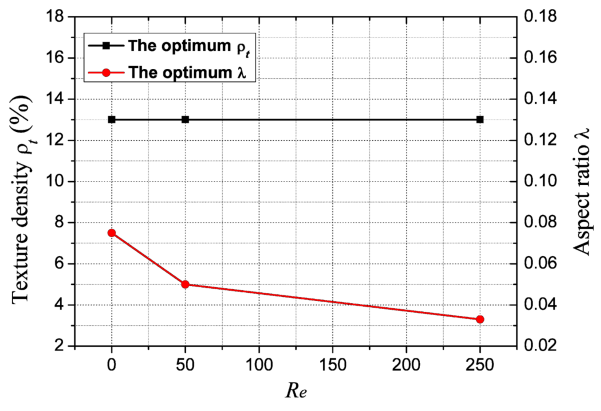

Figure 15: Effect of Reynolds number on the optimum texture density and optimum aspect ratio.

Conclusion

By utilizing a three-dimensional CFD simulation method, the tribological performance of a micro-dimple array under the condition of hydrodynamic lubrication was investigated. This study focused on the influence of the micro-dimple array parameters and fluid properties on the film pressure distribution and tribological characteristics. The main conclusions are as follows.

With proper dimensional parameters, such as texture density and aspect ratio, the total integration of the film pressure could be positive. As a result, the micro-dimple texture could provide extra carrying force, which is helpful for improving the tribological performance of a friction pair. The wedging effect of the micro-dimple texturing is beneficial for the load-carrying capacity, while the recirculation effect is disadvantage in this sense. The main mechanism for the improvement of the tribological performance is the comprehensive results of these two effects. For a certain Reynolds number, there exists the combination of an optimum texture density and optimum aspect ratio with which the maximum hydrodynamic lubrication coefficient could be obtained. In this case, the optimum tribological performance under the condition of hydrodynamic lubrication is achieved. And finally, it was concluded that within the parameters used in this study, when the Reynolds number is increased, the optimum aspect ratio decreases while the optimum texture density does not change.

The conclusions drawn in this study could be the basis for further numerical studies in specific applications such as thrust bearings, engine cylinders and mechanical seals. Our future work will focus on implementing more complex boundary conditions and thermal effects for specific applications.

Acknowledgements

The authors gratefully acknowledge the sponsorship from the National Natural Science Foundation of China (Grant No. 51605296), Shanghai Sailing Program (Grant No. 16YF1408300) and Young Teachers Training Program of Shanghai College (Grant No. ZZsl15029).

References

1. Bhushan, B. *Introduction to tribology;* Wiley: New York, U. S. A., 2013. doi:10.1002/9781118403259
2. Baum, M. J.; Heepe, L.; Gorb, S. N. *Beilstein J. Nanotechnol.* **2014,** *5,* 83–97. doi:10.3762/bjnano.5.8
3. Uddin, M. S.; Ibatan, T.; Shankar, S. *Lubr. Sci.* **2017,** *29,* 153–181. doi:10.1002/ls.1362
4. Baum, M. J.; Heepe, L.; Fadeeva, E.; Gorb, S. N. *Beilstein J. Nanotechnol.* **2014,** *5,* 1091–1103. doi:10.3762/bjnano.5.122
5. Kligerman, Y.; Etsion, I. *Tribol. Trans.* **2001,** *44,* 472–478. doi:10.1080/10402000108982483
6. Wang, X.; Kato, K.; Adachi, K.; Aizawa, K. *Tribol. Int.* **2003,** *36,* 189–197. doi:10.1016/S0301-679X(02)00145-7
7. Rahmani, R.; Mirzaee, I.; Shirvani, A.; Shirvani, H. *Tribol. Int.* **2010,** *43,* 1551–1565. doi:10.1016/j.triboint.2010.02.016
8. Fesanghary, M.; Khonsari, M. M. *Tribol. Int.* **2013,** *67,* 254–262. doi:10.1016/j.triboint.2013.08.001
9. Meng, X.; Khonsari, M. M. *Tribol. Int.* **2017,** *107,* 116–124. doi:10.1016/j.triboint.2016.11.007
10. Brizmer, V.; Kligerman, Y.; Etsion, I. *Tribol. Trans.* **2003,** *46,* 397–403. doi:10.1080/10402000308982643
11. Etsion, I.; Halperin, G.; Brizmer, V.; Kligerman, Y. *Tribol. Lett.* **2004,** *17,* 295–300. doi:10.1023/B:TRIL.0000032467.88800.59
12. Etsion, I. *Tribol. Lett.* **2004,** *17,* 733–737. doi:10.1007/s11249-004-8081-1
13. Brizmer, V.; Kligerman, Y. *J. Tribol.* **2012,** *134,* 031702. doi:10.1115/1.4006511
14. Golloch, R.; Merker, G. P.; Kessen, U.; Brinkmann, S. *TriboTest* **2005,** *11,* 307–324. doi:10.1002/tt.3020110403
15. Kligerman, Y.; Etsion, I.; Shinkarenko, A. *J. Tribol.* **2005,** *127,* 632–638. doi:10.1115/1.1866171
16. Yin, B.; Li, X.; Fu, Y.; Yun, W. *Lubr. Sci.* **2012,** *24,* 293–312. doi:10.1002/ls.1185
17. Kim, B.; Chae, Y. H.; Choi, H. S. *Tribol. Int.* **2014,** *70,* 128–135. doi:10.1016/j.triboint.2013.10.006
18. Etsion, I.; Burstein, L. *Tribol. Trans.* **1996,** *39,* 677–683. doi:10.1080/10402009608983582
19. Dobrica, M. B.; Fillon, M. *Proc. Inst. Mech. Eng., Part J* **2009,** *223,* 69–78. doi:10.1243/13506501JET433
20. Li, J.; Chen, H. *J. Tribol.* **2007,** *129,* 963–967. doi:10.1115/1.2768619
21. Qiu, M.; Bailey, N. B.; Stoll, R.; Raeymaekers, B. *Tribol. Int.* **2014,** *72,* 83–89. doi:10.1016/j.triboint.2013.12.008
22. Sahlin, F.; Glavatskih, S. B.; Almqvist, T.; Larsson, R. In *ASME/STLE 2004 International Joint Tribology Conference,* Long Beach, California, U. S. A., Oct 24–27, 2004; pp 1657–1665.
23. Brajdic-Mitidieri, P.; Gosman, A. D.; Ioannides, E.; Spikes, H. A. *J. Tribol.* **2005,** *127,* 803–812. doi:10.1115/1.2032990
24. Shi, X.; Ni, T. *Tribol. Int.* **2011,** *44,* 2022–2028. doi:10.1016/j.triboint.2011.08.018
25. Ramesh, A.; Akram, W.; Mishra, S. P.; Cannon, A. H.; Polycarpou, A. A.; King, W. P. *Tribol. Int.* **2013,** *57,* 170–176. doi:10.1016/j.triboint.2012.07.020
26. Nakano, M.; Korenaga, A.; Korenaga, A.; Miyake, K.; Murakami, T.; Ando, Y.; Usami, H.; Sasaki, S. *Tribol. Lett.* **2007,** *28,* 131–137. doi:10.1007/s11249-007-9257-2
27. Han, J.; Fang, L.; Sun, J.; Ge, S. *Tribol. Trans.* **2010,** *53,* 860–870. doi:10.1080/10402004.2010.496070
28. Gropper, D.; Wang, L.; Harvey, T. J. *Tribol. Int.* **2016,** *94,* 509–529. doi:10.1016/j.triboint.2015.10.009
29. Versteeg, H. K.; Malalasekera, W. *An introduction to computational fluid dynamics: the finite volume method;* Pearson Education: New Jersey, U. S. A., 2007.
30. Tang, W.; Zhou, Y.; Zhu, H.; Yang, H. *Appl. Surf. Sci.* **2013,** *273,* 199–204. doi:10.1016/j.apsusc.2013.02.013
31. Yu, H. The Optimal Design of Surface Texturing Based on Hydrodynamic Lubrication. Ph.D. Thesis, Nanjing University of Aeronautics & Astronautics, China, 2010.

BEILSTEIN JOURNAL OF NANOTECHNOLOGY

Exploring wear at the nanoscale with circular mode atomic force microscopy

Olivier Noel*[1], Aleksandar Vencl[2] and Pierre-Emmanuel Mazeran[3]

Full Research Paper

Open Access

Address:
[1]IMMM, UMR CNRS 6283, Le Mans Université, Av. O. Messiaen, 72085 cedex 09, Le Mans, France, [2]Faculty of Mechanical Engineering, University of Belgrade, Kraljice Marije 16, 11120 Belgrade 35, Serbia and [3]Sorbonne universités, Université de Technologie de Compiègne, UMR CNRS 7337, Roberval, Centre de recherche de Royallieu – CS 60 319 – 60 203 Compiègne cedex, France

Email:
Olivier Noel* - Olivier.noel@univ-lemans.fr

* Corresponding author

Keywords:
circular mode atomic force microscopy; composite materials; image processing; nanowear; wear mechanisms

Beilstein J. Nanotechnol. **2017,** *8,* 2662–2668.
doi:10.3762/bjnano.8.266

Received: 24 May 2017
Accepted: 24 November 2017
Published: 11 December 2017

This article is part of the Thematic Series "Nanotribology".

Guest Editor: E. Gnecco

Abstract

The development of atomic force microscopy (AFM) has allowed wear mechanisms to be investigated at the nanometer scale by means of a single asperity contact generated by an AFM tip and an interacting surface. However, the low wear rate at the nanoscale and the thermal drift require fastidious quantitative measurements of the wear volume for determining wear laws. In this paper, we describe a new, effective, experimental methodology based on circular mode AFM, which generates high frequency, circular displacements of the contact. Under such conditions, the wear rate is significant and the drift of the piezoelectric actuator is limited. As a result, well-defined wear tracks are generated and an accurate computation of the wear volume is possible. Finally, we describe the advantages of this method and we report a relevant application example addressing a Cu/Al_2O_3 nanocomposite material used in industrial applications.

Introduction

Wear remains a prominent economical issue [1-5] as it generates industrial maintenance and limits the lifetime of numerous mechanical systems. Another major concern is the ecological impact of wear. For instance, wear is responsible for the production of microparticles from the abrasion of roads, brakes or car engines [6]. The use of lubricants to reduce wear is also a source of pollution as they are often in the form of unfriendly environmental chemicals discarded into the environment [7].

Advances in tribology have allowed for a better understanding of wear mechanisms at the macroscale [8,9]. In particular, different wear mechanisms such as abrasion, adhesion, surface fatigue, and tribochemical reactions [10] are known to depend on the tribological systems and the operating conditions. For example, the straightforward Archard's law predicts that the wear volume is proportional to the normal load and the sliding distance and the inverse of the hardness of the material [11].

Exploring wear at the nanoscale becomes more and more mandatory with the development of the nanotechnology and its applications [12]. In addition, emerging numerical simulations of nanowear mechanisms are quite demanding in experimental validations [13,14]. The development of atomic force microscopy (AFM) in the 90's has opened the field of tribology at the nanoscale. One of the main advantages of AFM is that a single asperity contact between a nanometer-sized AFM tip and an interacting surface can be generated [15,16]. Although AFM is used as a versatile technique, it was first dedicated to imaging and not to the measurement of tribological properties. Classical wear experiments with the AFM hinge on the slow linear scanning of the sample surface with the AFM tip with a constant normal load. Under such conditions, producing a significant wear is long and fastidious due to the low sliding velocity. In addition, the typical AFM scanning velocity, in the µm/s range, does not allow well-defined wear tracks to be obtained as the piezoelectric actuator thermal drift continuously moves the sample under the probe. As a significant impediment, one ends up with mostly large and low-depth wear tracks for which the wear volume is difficult to compute. In this case, the determination of relevant wear laws is difficult or even impossible. Finally, only a few proper experimental studies of nanoscale studies of wear (nanowear) have been reported in the literature [17-20], whereas AFM has been widely used for measuring nanoscale friction [21,22].

In this paper, we propose a new experimental methodology based on circular mode AFM (CM-AFM) to explore wear mechanisms and laws at the nanoscale. It consists of wearing the material with the AFM tip with a suitable circular motion at a high frequency. Following this process, a well-defined wear track obtained within a reasonable time may be easily revealed by AFM imaging. We also describe an original wear track image treatment that allows the wear volume and its uncertainties to be computed. Finally, an application of this methodology and computation for exploring wear of a specific copper-based composite with alumina nanoparticles is reported and discussed.

Results and Discussion

The CM-AFM: a powerful nanotribometer for wear experiments

In classical wear experiments based on AFM, the probe linearly scans back and forth along the surface of the material while a constant normal load is applied on the contact (Figure 1A). With this problematic methodology, stop periods generated during the scan and a slow, nonconstant sliding velocity prohibit performing the experiments in a stationary regime. Recently, a new AFM mode called the CM-AFM [23-26] was implemented to overcome some of the limitations of the conventional wear experimental set-up using an AFM. In CM-AFM, the electronic driving unit of a conventional AFM has been modified to impose a relative circular displacement of an AFM tip in contact with the plane of a given material (Figure 1B). The circular displacement is provided by way of injecting two sinusoidal voltage components in phase quadrature on the piezoelectric actuator of the AFM in both directions of the plan of the sample.

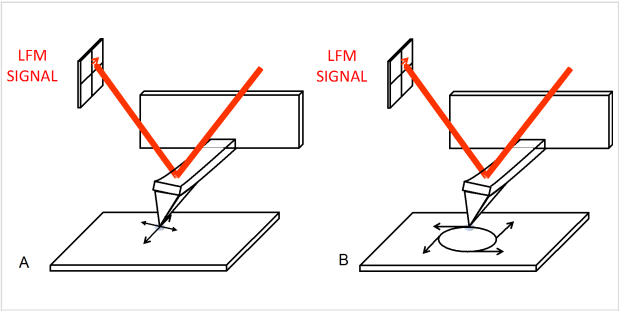

Figure 1: Schematic of the wear-induced atomic force microscopy (AFM) experimental protocols using (A) conventional scanning and (B) circular mode AFM circular displacement.

With such a driving scheme, the sliding velocity of the nanocontact is constant and continuous. Stop periods do not occur during the experiment and real stationary regimes are successfully achieved. In addition, with CM-AFM, the sliding velocity is driven by the frequency and the amplitude of external sinusoidal voltages applied to the scanner. Therefore, wear experiments may be achieved at high sliding velocities (>6 mm/s) as compared to sliding velocity values that are implemented in classical AFM wear experiments (100 µm/s maximum). The only limitation for high sliding velocities is the resonance frequency of the scanner and its lateral extension. For example, for a conventional AFM scanner whose resonance frequency is about 500 Hz and considering a 4 µm diameter circular displacement (which is obtained by applying an external voltage of 10 V applied to a scanner of lateral extension of 100 µm), a maximum sliding velocity close to 6 mm/s may be achievable. Performing wear experiments at high sliding velocities also limits the drift during the experiment as it is possible to obtain a significant wear rate in a short time (Figure 2).

In our experimental set-up using a commercial AFM (DI3100 from Bruker), the diameter of the circular displacement ranges from 0.16 µm to 3 µm. Thus, the CM-AFM allows local probing of materials. In this way, it is possible to investigate wear of metallic materials while avoiding the grain boundary effects. Considering the CM-AFM, the lateral force signal (also referred as the lateral force microscopy (LFM) signal proportional to the friction force) of the cantilever stemming from the circular displacement of the contact features a sinusoidal signal

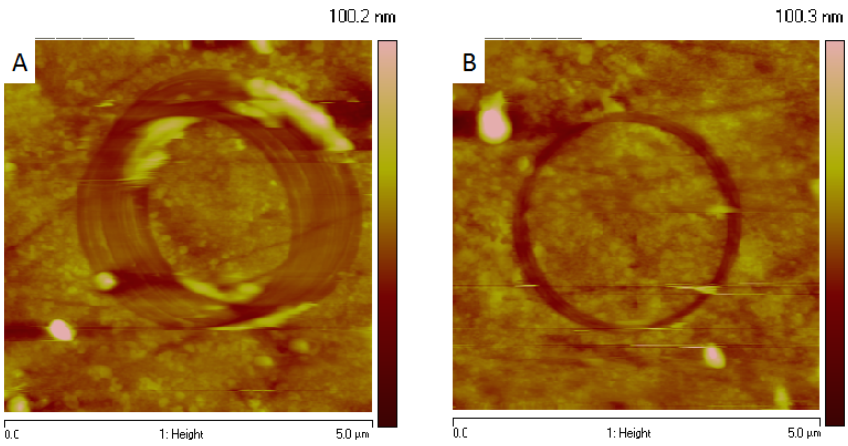

Figure 2: Atomic force microscopy (AFM) contact mode topographic images of wear tracks resulting from wear experiments on copper-based composites (the counter-body is a silicon nitride probe) at a constant normal load of 180 nN with constant sliding distance and sliding velocities of (A) 100 µm/s and (B) 1 mm/s. To maintain a constant sliding distance, the wear duration is 100 min for the experiment in (A) and 10 min for the experiment in (B). It is clearly demonstrated that a long wear time results in a large and low-depth wear track due to the drift.

with the same frequency as the relative circular displacement of the contact. Then a lock-in amplifier is used to register the real-time amplitude of the LFM signal of the cantilever (or friction force) during the wear experiment in order to determine prospective variations of the friction properties during the experiment. For example, this option may be advantageously implemented for investigating the correlation between friction, energy dissipation and worn material at the local scale or to exhibit local heterogeneity of the material.

To summarize, CM-AFM applied to wear experiments regarding different applications such as tribochemistry and wear of thin films presents numerous advantages compared to conventional AFM wear experiments: (1) sliding velocity values are much higher than the conventional ones, thus achieving a significant wear volume in a short time; (2) the drift of the piezoelectric scanner is reduced because of the short experiment duration (due to the high scanning velocity), together with average x- and y-voltage values applied on the scanner being zeroed; (3) the wear volume can be easily computed as the wear track is well-defined; (4) as the wear track is circular, it can be easily detected and unlikely to be confused with surface scratches; (5) another valuable consequence of the circular motion is that the probe, if worn during the experiment, is submitted to an isotropic wear; (6) the circular displacement allows for the exploration of wear in all directions of the surface material, which may be of major interest to investigate wear anisotropy; and (7) if wear debris are generated during the wear process, the circular motion of the tip favors rejection of this debris to the outer part of the wear track or at the exact position where this wear debris was generated, leading to an easy determination of the real wear volume. In the case of a back and forth displacement, the scanning imposed on the tip used in classical AFM nanowear experiments may result in accumulation of debris located within the wear track, which cannot be discerned from non-worn material.

Wear volume calculation at the nanoscale

The wear volume is calculated following a five-step procedure: 1) topographic AFM images are recorded in contact mode before and after the wear experiment, at the same location of the sample (Figure 3A,B); 2) as the wear track depth is of the same order of magnitude as the peak-to-valley roughness, it is necessary to subtract the height of these two AFM images to highlight the wear track; 3) relevant subtraction of the images must take into account the drift that occurs during the wear experiments. Therefore, both images are shifted by a few pixels in the two directions of the plane of the image and the standard deviation of the height of the pixels is computed. An optimized shift for eliminating the drift should lead to a standard deviation of the height of the pixels of the difference image converging to zero. Due to the nonconstant value of the drift along an image, the nonlinearity of the piezoelectric actuator, and the pixel size, the shifting imaging process will not be perfect. The resulting image is not perfectly flat outside the wear track, but the process considerably reduces the effect of the roughness for determining the wear volume (Figure 3C); 4) once the difference image is computed, the average height is calculated as a function of the distance from the center of the circular wear track (Figure 3D); 5) the baseline (red line) is determined by fitting the portion of the profile excluding the wear track with polynomial algorithms of order 1 to 4. The difference in height between the experimental and the four different fitted curves is integrated to compute the volume of the wear track. The

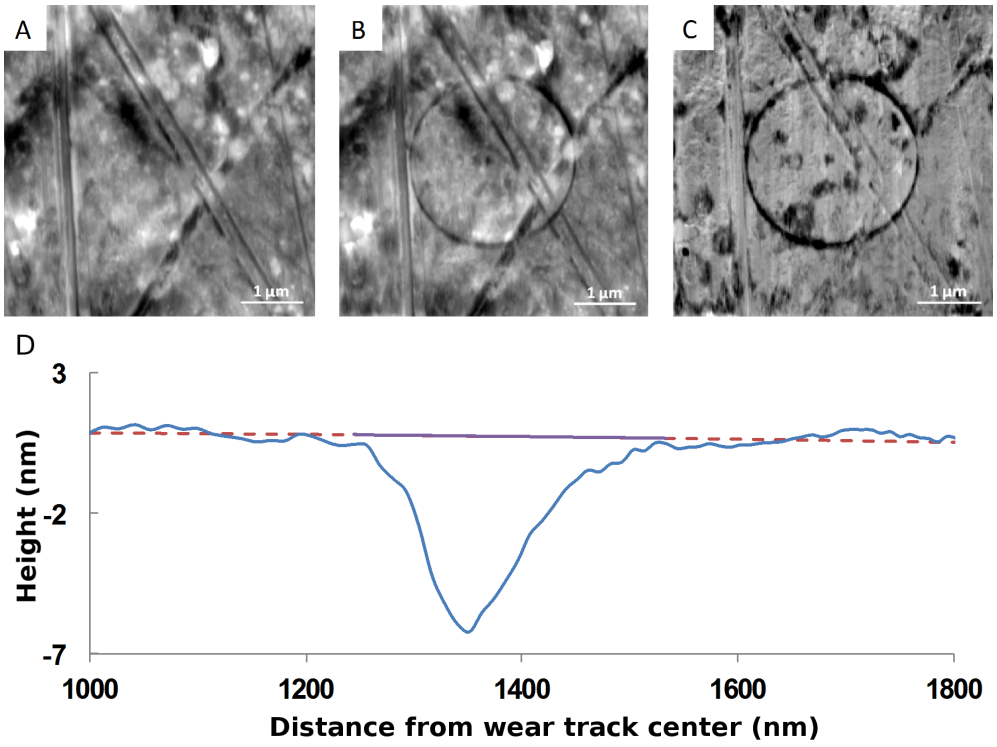

Figure 3: Summary of the steps for computing the wear volume from AFM topographic images (image size: 5 × 5 µm): A and B (grey scale is 35 nm) and B shows the AFM topographic images, before and after wear respectively, for a given location on a copper-based composite (the counter-body is a silicon nitride probe); C (grey scale is 16 nm) is the height difference of the topographic images (B) − (A). The drift correction has been previously determined; the bottom image D is the average height as a function of the distance from the center of the wear track circle. The baseline (dotted red line) in this example is obtained by a polynomial fit of order 4 of the profile without considering the wear track. The wear volume is calculated by integrating the surface under the full purple line.

minimum and maximum wear volume values of these different results are determined in order to estimate the uncertainties.

The image processing is fundamental for obtaining a clear description of the wear process. It is clearly illustrated in Figure 4 where the wear track on the image before the image processing (image B in Figure 4) is hardly distinguishable from the background. After having applied the image processing (image C), the circular wear track clearly contrasts with the background and details such as wear debris accumulation (not visible on the topographic image A before the wear experiment) become visible and help to understand the wear process.

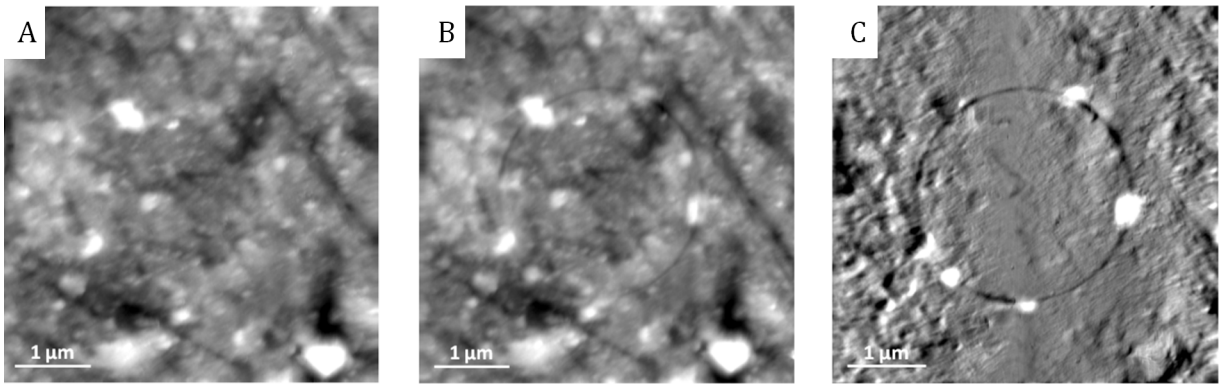

Figure 4: A and B (grey scale is 35 nm) are the AFM contact mode topographic images before and after the wear experiment; C (grey scale is 12 nm) is the height difference (B) − (A) obtained on a copper-based composite (image size: 5 × 5 µm).

Application of CM-AFM to study wear of a Cu-based nanocomposite

An application example to assess the promising potential of CM-AFM to explore wear of materials at the nanoscale is addressed with a copper-based nanocomposite (see the Experimental section for details). This material is of industrial relevance as it is widely used in electrical sliding contacts such as those in railway overhead current collection system, lead frames in large-scale integrated circuitd, welding electrodes, transfer switches and electrical contact material.

Experimental details about the wear experiments with CM-AFM and the recording of the topographic images are described in the Experimental section. In particular, all wear experiments are carried out at different locations on the sample and tips of different nature were used to access to a broad range of cantilever stiffness. Experimental images as shown in Figure 3C and in Figure 4 also show that the material is not uniformly worn along the circular wear track. Wear is more intensive at some random locations of the material, evidencing heterogeneous wear (as in Figure 3C) or production of wear debris accumulation (as in Figure 4). This makes clear that CM-AFM is able to locally analyze wear mechanisms and wear properties of the material.

Figure 5 reports the evolution of the wear volume against sliding time with a given sliding velocity (880 µm/s) and two different applied normal loads, respectively 1 µN and 3 µN.

This result shows that the wear volume varies linearly with the sliding distance (running-in regime) until reaching 16 min of wear, where a plateau (steady-state regime) indicates that the wear volume is almost independent of the sliding time. This trend is similar for both values of the applied load (1 µN and 3 µN). Wear profiles (Figure 3D) obtained with the analysis procedure show also that the AFM tip conforms to the nanocomposite wear track during the wear process. The plateau could not be attributed to the wear of the probe during the wear process. At least, if the tip wear occurs, its worn volume contribution is negligible compared to the sample worn volume. One should rather consider that while the probe is going deeper and deeper into the wear track, the contact pressure is decreasing as the surface contact between the AFM tip and the substrate is increased. Consequently, the shear stress applied to the contact appears to be not high enough to wear the material.

The wear depths determined from the wear profiles (Figure 3D for example) are in the nanometer range. One can calculate from Figure 5 in the steady-state regime for an applied load of 3 µN that about 100 atoms of copper per micrometer of sliding have been removed. Then an atom-by-atom or atomic cluster by atomic cluster or nanograin-by-nanograin removal process may be involved in the wear mechanism. However, SEM imaging was of satisfactory resolution to precisely distinguish the morphology of the wear track and to confirm any of these assumptions.

In the running-in regime, the evolution of the wear rate as a function of the applied normal load is depicted in Figure 6.

These results show that for high loads, the behavior follows an Archard-like wear law since the wear volume or wear rate is proportional to the applied load. For small applied loads, the wear rate is almost zero and it is necessary to reach a threshold load (of approximately 50 nN) to get a significant wear volume.

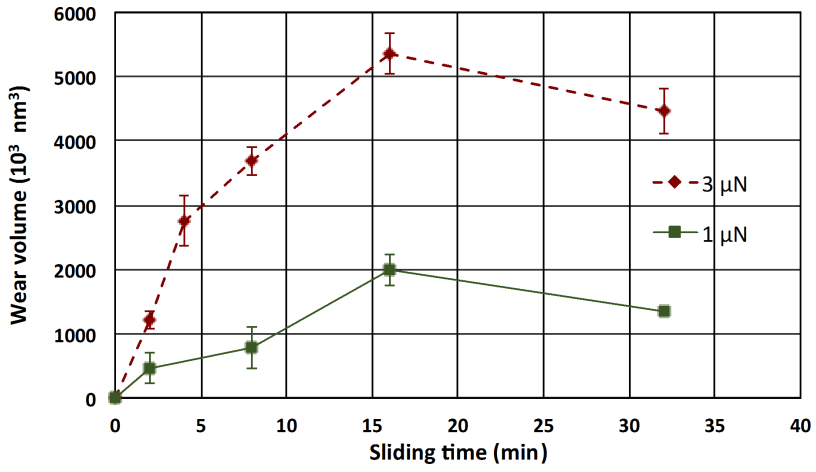

Figure 5: Wear volume as a function of the sliding time at a sliding velocity of 880 µm/s and a normal load of 1 µN (green squares) and 3 µN (red diamonds). Experiments were carried with a diamond-like carbon (DLC) probe. Error bars are the standard deviation and the data result from an average between the maximum wear volume and the minimum wear volume issued from the calculation described in the Experimental section.

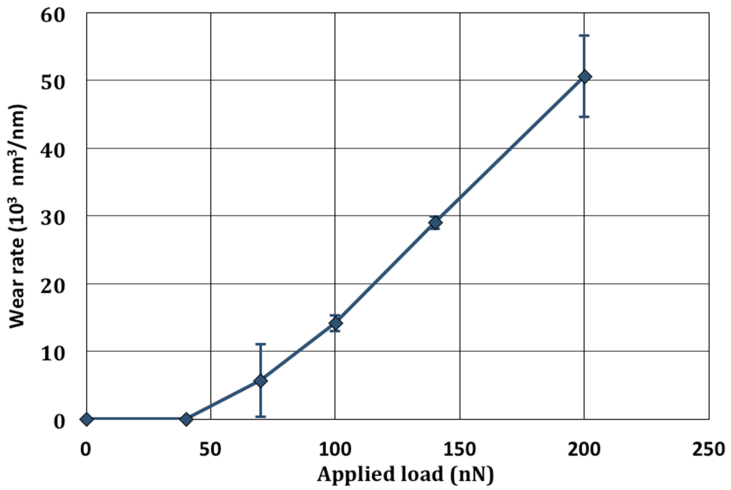

Figure 6: Wear rate as a function of the applied normal load with a given sliding velocity (880 µm/s) and a 2 min duration wear. Experiments were carried with the Si_3N_4 probe.

Conclusion

This paper reported on an original approach for generating and quantitatively measuring nanoscale wear tracks resulting from the sliding contact between an AFM tip and an interacting sample (counter-body). Using the AFM circular mode with a high sliding velocity allows a significant and valuable decrease of the drift together with a well-defined wear track and consequent wear. Accordingly, quantitative wear volumes at the nanoscale are accessible using an image processing method. The used strategy to calculate the wear volume consists of attenuating the roughness of the surface that is of the same order as the nanometer dimension of the wear track (which may interfere in the calculation of the wear volume) by subtracting relevant topographic images after and before wear. Finally, this methodology has been applied to a copper-based nanocomposite sample using both diamond-like carbon and silicon nitride tips in the µN load range. The results show that even if wear loss remains locally heterogeneous and erratic, their related trends regarding Cu/Al_2O_3 nanocomposites at the nanoscale may be obtained.

Experimental

The investigated copper-based nanocomposite was produced by powder metallurgy technology and contained approximately 4.7 wt % of nanometer-sized Al_2O_3 particles (the average diameter was less than 100 nm) [26]. The surface roughness, R_a, of the samples, determined from AFM topographic images of 5 × 5 µm, is 2.9 ± 0.6 nm.

Wear experiments were performed with the CM-AFM mode implemented on a DI-3100 Nanoscope V controller Bruker AFM, in air, at ambient temperature and at a relative humidity of 30%. The AFM tips were either a unique DLC coating tip with a rectangular cantilever (from NT-MDT) or a unique silicon nitride (Si_3N_4) probe with a triangular cantilever. Both nominal tip radius values were 100 nm and 70 nm for the DLC and Si_3N_4 probes, respectively, and the cantilever stiffness was 12 N/m and 0.4 N/m, respectively (as determined by the thermal noise method [27,28]). For each set of wear experiments, a unique AFM tip was used. After each measurement, force curves on a silicon wafer were performed to verify the state of the tip. Every data point represented in Figure 5 and Figure 6 was obtained by doing wear measurements at different locations on the sample. Scanning electronic microscopy images of the probes after wear showed that no significant wear of the AFM tip occurred after the set of experiments. Such facts were also confirmed by the adhesion force measurements before each wear experiment, with quite similar resulting values. Another piece of evidence highlighting that the probe is not damaged is given by the AFM topographic images before and after each experiment, which were recorded with the same AFM tip that was used for wear experiments. In case of damaged tips, the features of the surface would have been dilated due to tip self-imaging [19]. For improving the imaging processing, AFM topographic images before and after wear were always recorded from the left to the right and from top to bottom directions. Proceeding in such a way reduces the nonlinearity behavior of the piezoelectric actuator with regards to imaging.

Acknowledgements

The authors are grateful to COST through the action MP1303 and Campus France through the program PHC Pavle Savic for funding this work. Aleksandar Vencl also acknowledges project TR 35021, supported by the Republic of Serbia, Ministry of Education, Science and Technological Development.

References

1. Belot, J. M.; Rigaut, B. Importance économique de l'usure. *CETIM informations no 141;* 1994; pp 29–32.
2. Jost, H. P. *Wear* **1990,** *136,* 1–17. doi:10.1016/0043-1648(90)90068-L
3. Igarashi, J. *J. Jpn. Soc. Tribol.* **2003,** *48,* 265–271.
4. Yoshitsugu, K. *Wear* **1997,** *207,* 63–66. doi:10.1016/S0043-1648(96)07472-8
5. Sivebaek, I.-M. Lubrication and wear in diesel engine injection equipment fuelled by dimethyl ether (DME). Ph.D. Thesis, Technical University of Denmark, 2003.
6. Surveillance & informations sur la qualité de l'air en île de France, Airparif Internal Report, 2015.
7. Holmberg, K.; Andersson, P.; Erdemir, P. *Tribol. Int.* **2012,** *47,* 221–234. doi:10.1016/j.triboint.2011.11.022
8. Peterson, M. B.; Winer, W. O. *Wear control handbook;* American Society of Mechanical Engineers: New York, NY, U.S.A., 1980.
9. Goryacheva, I. G. *Contact Mechanics in Tribology;* Kluwer Academic Publishers: Dordrecht, Netherlands, 1998.
10. Kandeva-Ivanova, M.; Vencl, A.; Karastoyanov, D. *Advanced Tribological Coatings for Heavy-Duty Applications: Case Studies;* Prof. Marin Drinov Publishing House of Bulgarian Academy of Sciences: Sofia, Bulgaria, 2016.
11. Archard, J. F. *J. Appl. Phys.* **1953,** *24,* 981–988. doi:10.1063/1.1721448
12. Bhushan, B. *Handbook of Micro/Nanotribology;* CRC Press, Inc.: Boca Raton, FL, U.S.A., 1999.
13. Eder, S. J.; Feldbauer, G.; Bianchi, D.; Cihak-Bayr, U.; Betz, G.; Vernes, A. *Phys. Rev. Lett.* **2015,** *115,* 025502. doi:10.1103/PhysRevLett.115.025502
14. Aghababaei, R.; Warner, D. H.; Molinari, J.-F. *Nat. Commun.* **2016,** *7,* 11816. doi:10.1038/ncomms11816
15. Mazeran, P.-E. *Mat. Sci. Eng. C* **2006,** *26,* 751–755. doi:10.1016/j.msec.2005.09.055
16. Gotsmann, B.; Lantz, M. A. *Phys. Rev. Lett.* **2008,** *101,* 125501. doi:10.1103/PhysRevLett.101.125501
17. Jacobs, T. D. B.; Carpick, R. W. *Nat. Nanotechnol.* **2013,** *8,* 108–112. doi:10.1038/nnano.2012.255
18. Schirmeisen, A. *Nat. Nanotechnol.* **2013,** *8,* 81–82. doi:10.1038/nnano.2013.4
19. Liu, J.; Jiang, Y.; Grierson, D. S.; Sridharan, K.; Shao, Y.; Jacobs, T. D. B.; Falk, M. L.; Carpick, R. W.; Turner, K. T. *ACS Appl. Mater. Interfaces* **2017,** *9,* 35341–35348. doi:10.1021/acsami.7b08026
20. Loubet, J. L.; Belin, M.; Durand, R.; Pascal, H. *Thin Solid Films* **1994,** *253,* 194–198. doi:10.1016/0040-6090(94)90319-0
21. Mate, M. *Tribology on the Small Scale, A Bottom Up Approach to Friction, Lubrication, and Wear;* Oxford University Press: Oxford, United Kingdom, 2008.
22. Gnecco, E.; Meyer, E., Eds. *Fundamentals of Friction and Wear on the Nanoscale;* Springer: Berlin, Germany, 2015. doi:10.1007/978-3-319-10560-4
23. Nasrallah, H.; Mazeran, P.-E.; Noël, O. *Rev. Sci. Instrum.* **2011,** *82,* 113703. doi:10.1063/1.3658049
24. Noel, O.; Mazeran, P. E.; Nasrallah, H. U. S. Patent 008997261B2. CM-AFM International Patent PCT/FR2011/051024; Japanese Patent JP2013-508547.
25. Noel, O.; Mazeran, P.-E.; Nasrallah, H. *Phys. Rev. Lett.* **2012,** *108,* 015503. doi:10.1103/PhysRevLett.108.015503
26. Vencl, A.; Rajkovic, V.; Zivic, F. Friction and wear properties of copper-based composites reinforced with micro- and nano-sized Al_2O_3 particles. In *Proceedings of the 8th International Conference on Tribology,* BALKANTRIB '14, Sinaia, Romania; pp 357–364.
27. Butt, H.-J.; Jaschke, M. *Nanotechnology* **1995,** *6,* 1. doi:10.1088/0957-4484/6/1/001
28. Lübbe, J.; Temmen, M.; Rahe, P.; Kühnle, A.; Reichling, M. *Beilstein J. Nanotechnol.* **2013,** *4,* 227–233. doi:10.3762/bjnano.4.23

License and Terms

BEILSTEIN JOURNAL OF NANOTECHNOLOGY

Friction force microscopy of tribochemistry and interfacial ageing for the SiO_x/Si/Au system

Christiane Petzold, Marcus Koch and Roland Bennewitz*

Full Research Paper

Open Access

Address:
INM – Leibniz Institute for New Materials, Campus D2 2, 66123 Saarbrücken, Germany

Email:
Roland Bennewitz* - roland.bennewitz@leibniz-inm.de

* Corresponding author

Keywords:
contact ageing; friction; nanotribology; tribochemistry; wear

Beilstein J. Nanotechnol. **2018,** *9,* 1647–1658.
doi:10.3762/bjnano.9.157

Received: 19 February 2018
Accepted: 23 May 2018
Published: 05 June 2018

This article is part of the Thematic Series "Nanotribology".

Guest Editor: E. Gnecco

Abstract

Friction force microscopy was performed with oxidized or gold-coated silicon tips sliding on Au(111) or oxidized Si(100) surfaces in ultrahigh vacuum. We measured very low friction forces compared to adhesion forces and found a modulation of lateral forces reflecting the atomic structure of the surfaces. Holding the force-microscopy tip stationary for some time did not lead to an increase in static friction, i.e., no contact ageing was observed for these pairs of tip and surface. Passivating layers from tip or surface were removed in order to allow for contact ageing through the development of chemical bonds in the static contact. After removal of the passivating layers, tribochemical reactions resulted in strong friction forces and tip wear. Friction, wear, and the re-passivation by oxides are discussed based on results for the temporal development of friction forces, on images of the scanned area after friction force microscopy experiments, and on electron microscopy of the tips.

Introduction

Contact ageing, the strengthening of contacts after formation, is an important phenomenon in tribology, with impact ranging from the nano-scale (NEMS and MEMS) [1,2] to the macro-scale (sliding of rock in earthquakes) [3,4]. Different microscopic mechanisms for contact ageing have been identified, e.g., material creep [5], structural changes in the interfacial contact [6,7] or an increase in number of chemical bonds [8,9]. The frictional strength may also grow in time by rotation of the contacting surfaces into a preferred misorientation defined by dislocation structure [10], for which friction maxima have been predicted [11].

Friction force microscopy (FFM) is a key method to investigate the microscopic mechanisms underlying friction, wear, and lubrication as it allows for measurements of static and kinetic friction of single nanometer-scale contacts. In FFM, an ultrasharp tip is scanned across the surface line by line probing a square frame. Lateral forces acting on the sliding contact are determined as deflection of a cantilever spring holding the tip.

Single-asperity contact ageing between silica tip and surface has been directly observed in ambient atmosphere by FFM [8]. It has been explained by an increase in the number of covalent

bonds across the contact facilitated by the presence of water [12,13]. Ageing of well-defined contacts between metallic nanoparticles and surfaces has also been quantified by displacement of the particles in a FFM experiment [7].

Contact ageing may proceed at very different timescales for different materials. The initial phase of contact strengthening is often reported to depend logarithmically on the duration of the static contact [5,8]. Cold welding of two Au surfaces in air is a rather slow process (seconds to minutes) [5], while contact ageing between chemically reactive surfaces may occur very fast (nanoseconds to milliseconds) [14].

Here, we report FFM experiments in ultrahigh vacuum that address contact ageing and atomic-scale friction for contacts formed by Si, SiO_x, and Au. We found that no contact ageing was observed for oxidized silicon tips sliding on Au(111) or on oxidized Si(100) surfaces. We therefore deliberately increased the adhesive forces between probes and surfaces. In an attempt to allow for the successive formation of chemical bonds in contact ageing experiments, we removed passivating layers, in particular oxide films, from surface and tip. The control of surface oxidation required the implementation of all experiments in ultrahigh vacuum. We report on tribochemical processes between Si, SiO_x, and Au, which were initiated by removal of the passivating layers.

Experimental

Tip and sample preparation

Friction force microscopy experiments were performed with uncoated ("SiO_x/Si") and gold-coated ("Au/Si") silicon tips and cantilevers with a nominal spring constant of k_{nom} = 0.2 N/m (PPP-CONTR, PPP-CONTAu; Nanosensors, Switzerland). The cantilevers were fixed with conductive glue (H21D; Epoxy Technology, Inc., USA) to a metal tip holder. In order to remove water and physisorbed hydrocarbons, holder and cantilever were transferred into the preparation chamber of an ultrahigh vacuum system ($p = 10^{-10}$ mbar) and heated to 120 °C for several hours until the pressure had stabilized. The holder was then transferred into the measurement chamber with the FFM experiment. Normal and lateral spring constant of each cantilever were calculated from the resonance frequency and the dimensions of cantilevers and tips. The tip height was assessed individually from SEM images of the cantilevers before use.

A Au(111) single crystal (MaTeck GmbH, Jülich, Germany) was prepared by repeating a sputter–heating cycle (20 min Ar sputtering at 25 μA/1 keV followed by 1 h annealing at 850 °C) until a sharp (111) pattern was observed by low-energy electron diffraction (LEED). The n-Si(100) sample was cleaved from a wafer and fixed mechanically to a sample holder. The Si was either heated to 120 °C for several hours in the preparation chamber to remove water and physisorbed hydrocarbons ("oxidized Si(100)"), or heated to high temperatures to remove the surface oxide ("reactive Si(100)"). Removal of the oxide layer was achieved by heating with electric current flow through the sample, heating it first to about 600 °C for 8 h (red glow). The current was then increased until the sample was glowing bright orange and no further increase in temperature could be detected when increasing the current (sample temperatures between 1000 and 1300 °C were measured, depending on the sample size and surface oxide). This maximum temperature was kept for about 5 min. The temperature was recorded with a pyrometer (Impac IGA 140; LumaSense Technologies GmbH, Germany). The sample was allowed to cool to room temperature before transferring it to the measurement chamber.

Friction force microscopy experiments were performed with a VT-AFM (Scienta Omicron GmbH, Taunusstein, Germany) under ultrahigh vacuum conditions ($p < 10^{-9}$ mbar). While sliding an AFM tip at the end of a soft micro-manufactured cantilever beam perpendicularly to its length axis over the sample surface we recorded the torsional deflection of the cantilever, which allowed for the calculation of frictional forces. The scan rate was kept at 34 ms·line^{-1} if not stated otherwise.

Slide–hold–slide experiments

Contact ageing between tip and flat surface was investigated in slide–hold–slide experiments similar to those reported in [8], but under UHV conditions at low loads (ca. 0 nN, i.e., the load was controlled by adhesion). As the name "slide–hold–slide" suggests, a tip was slid in contact over a surface, then held stationary for a defined duration of time, and then slid again in the opposite direction. Stationary contact times were varied between nominally 0 and 100 s. In order to realize very short hold times, we further applied different sliding velocities in scanning FFM frames such that the stationary contact duration at the turning points varied between 252 μs and 3.9 ms. Hold times and velocities were varied randomly in order to identify possible systematic errors. The stationary contact in FFM is prone to unwanted movements caused by creep of the piezo actuator and by instrumental drift upon temperature changes. To minimize movement during hold times, the system was allowed to stabilize for prolonged times after turning on the light source for detecting the cantilever bending and after piezo repositioning. Furthermore, the temperature in the laboratory was kept stable to less than ±1 °C. The relative tip movement was monitored during hold periods by recording normal and lateral force signals with an external data recorder (LTT24, Labortechnik Tasler GmbH, Würzburg, Germany). Atomic stick–slip events revealed that the system was drifting by about 1 atom per 10 s in direction of sliding in our experiments.

Friction force measurements

The friction and wear of five tip–sample material pairs were investigated, namely Au/Si–oxidized Si(100), Au/Si–reactive Si(100), Au/Si–Au(111), SiO_x/Si–reactive Si(100), and SiO_x/Si–Au(111). By activating the tip apex a tribochemical reaction between tip and surface was triggered and the changes in friction were recorded during subsequent scanning. Activating the tip apex in a controlled manner was essential for the experiments. Methods to activate different tips are summarized in Table 1.

Table 1: Methods for activating the tip apices. The more controlled method is listed first.

tip	activation
SiO_x/Si	sliding on reactive Si(100); Ar plasma sputtering (10 s) and impacting the surface with a force pulse or an applied voltage pulse
Au/Si	sliding on reactive Si(100); Ar plasma sputtering (10 s) and prolonged static contact on Au(111) for cold welding and subsequent pull-off

Friction force experiments were performed in the following sequence: First, an overview image (1 μm^2) was recorded with an intact sharp tip. Then a sequence of frames (200 × 200 nm^2) was scanned in the center of the previous scan area until the friction forces had stabilized. Finally, an overview scan (1 μm^2) was recorded to reveal topographical changes in the area of the friction sequence. The whole sequence was performed first with tips with intact passivating layer and then repeated with activated tips.

Electron microscopy (SEM, TEM)

Contamination and modification of the AFM tips were examined by scanning electron microscopy (10 kV acceleration voltage) using secondary-electron and backscattered-electron signals (Quanta 400 FEG; FEI, Eindhoven, Netherlands). The tips were examined before transferring them into the preparation chamber (already glued to the tip holder) for sharpness, tip height, and contaminations, and after friction experiments for changes of the tip shape, material transfer, and tip height.

One Au/Si tip apex was analyzed by transmission electron microscopy (TEM; JEM-2100(HR) LaB_6, JEOL GmbH, Eching, Germany, 200 kV acceleration voltage) after activation on Au(111) and sliding experiments. The tip was cut using a focused ion beam (Versa3D; FEI, Eindhoven, Netherlands) to a thickness that allowed for TEM analysis. The FIB lamella was produced by first depositing a layer of platinum, starting with an electron beam at 2 kV and subsequently using the Ga ion beam at 30 kV until the platinum layer had reached a thickness of about 2.5 µm. The lamella was cut with the Ga ion beam at 30 kV and 7 nA. Finally, the lamella was cleaned from both sides at 2 kV and 0.26 nA using the Ga ion beam.

Results

Atomic-scale friction on oxidized Si(100) and on Au(111)

Sliding an intact Au/Si tip against a non-reactive surface (Au(111) or oxidized Si(100)) typically resulted in friction values in the range of 10–30 pN, while with SiO_x/Si tips the friction was found to be ten times higher (Table 2). Irregular stick–slip signals were detected in the fast scan direction when probing oxidized Si(100) (Figure 1a) and regular stick–slip was detected for the fast scan direction on Au(111) (Figure 1b). For both surfaces a characteristic stick–slip distance in the range of the expected atomic distances (250 pm for Si(100); 170 pm for Au(111)) was observed reproducibly in subsequent scan frames. Larger scan frames recorded on Au(111) sometimes exhibited the herringbone reconstruction (Figure 1c), which is also stable under contact-mode scanning [15].

Table 2: Friction values for intact tips sliding against non-reactive surfaces.

tip	surface	
	oxidized Si(100)	Au(111)
SiO_x/Si	0.25 nN	0.33 nN
Au/Si	0.02 nN	0.01 nN

No contact ageing for passivated tips sliding against non-reactive surfaces

With passivated tips sliding on non-reactive surfaces, we did not observe any static friction peak exceeding the kinetic friction for either of the holding times nor for the turning point at different scan velocities. As examples, we present the lateral force signal of a SiO_x/Si tip sliding against Au(111) for holding times between 0 and 100 s (Figure 2a) and the lateral force signals of a SiO_x/Si tip scanning over an oxidized Si(100) at different velocities (Figure 2b). As we did not observe any static friction peak, overall no contact ageing was found for these non-reactive contacts in vacuum.

Occasionally, we observed first signs of a stronger tip–surface interaction at varying positions and scan velocities, prevalently at the turning points of the scanning motion. The sign for a strong interaction was a sudden increase in friction force where the tip was stuck in contact (Figure 2c). After such isolated large stick–slip events, the kinetic friction remained increased

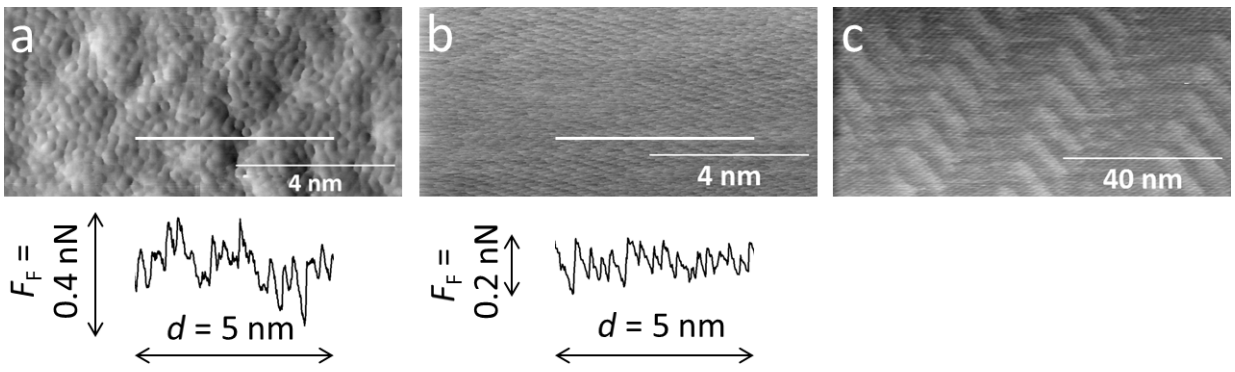

Figure 1: Friction force maps for a) an oxidized Si(100) surface scanned with an intact Ar-sputter cleaned SiO_x/Si tip, b) Au(111), and c) the topography of the Au(111) herringbone reconstruction scanned with an intact SiO_x/Si tip. One line was extracted from a) and b) to visualize the stick–slip pattern on Si(100) and on Au(111).

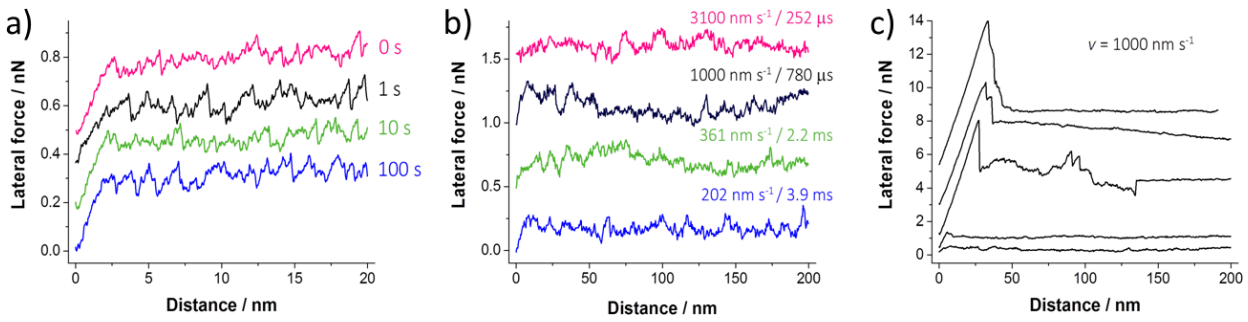

Figure 2: Graphs exemplifying the absence of contact ageing for slide–hold–slide experiments under UHV conditions. All curves are offset for better clarity. a) Variation of the holding times (0–100 s) for a SiO_x/Si tip sliding against a Au(111) surface. The static friction did not exceed the kinetic friction for any holding time. b) Variation of scanning velocity and, thus, of the holding time at the turning points (252 µs to 3.9 ms) for a SiO_x/Si tip sliding against an oxidized Si(100) surface. c) Examples for irregularly large stick–slip events observed during scanning, prevalently at the turning points of the scanning movement. Scan lines are extracted from various positions of two scan frames for a SiO_x/Si tip sliding against an oxidized Si(100) surface at a sliding velocity of 1 µm·s^{-1}. The line with the lowest friction corresponds to the black line in Figure 2b. The kinetic friction remained increased after large stick–slip events.

compared to experiments where no friction peaks were observed. Thus, it was not possible to perform systematic slide–hold–slide experiments starting from the same level of friction in each repetition. The stronger interaction occurred at arbitrary positions across the scan frame during repeated scanning, but in most cases the increased stickiness appeared first at the turning points (Figure 2c).

Tribochemical characteristics of the tip–surface pairings

We suggest that the intermittent friction peaks (Figure 2c) were caused by chemical bonding between tip and surface after local damage of a passivating layer on tip and/or surface. To clarify the origin of the large stick–slip events and of the increase of kinetic friction we removed the protective oxide layer from either the tip or the surface and created a tribochemical system of Au, Si, and SiO_x (Table 1). Different aspects of tip–surface interactions are illustrated by the average friction forces (Figure 3), single lateral force traces from the scanning sequences (Figure 4), surface topography images recorded before and after the sliding sequences (Figure 5), and electron microscopy images of the tips before and after the experiments (Figure 6).

In general, the onset of tip activation was evident by a sudden increase in friction (Figure 3a,b). Results for the tip–surface interactions of the different tips and surfaces are presented in this section. Friction of a Au/Si tip sliding on oxidized Si(100) is illustrated by the black squares in Figure 3. Initially (section 1 in Figure 3) a low friction force of about 0.02 nN was measured for the intact tip sliding against the intact oxide surface. Friction decreased slightly with scanning time until stabilizing after about 10 scans (Figure 4a). We attribute this decrease to structural changes at the sliding interface caused by tip–surface interactions, as scanning the same area ten times left an elevation of about 10 pm in height (Figure 5a,b). This eleva-

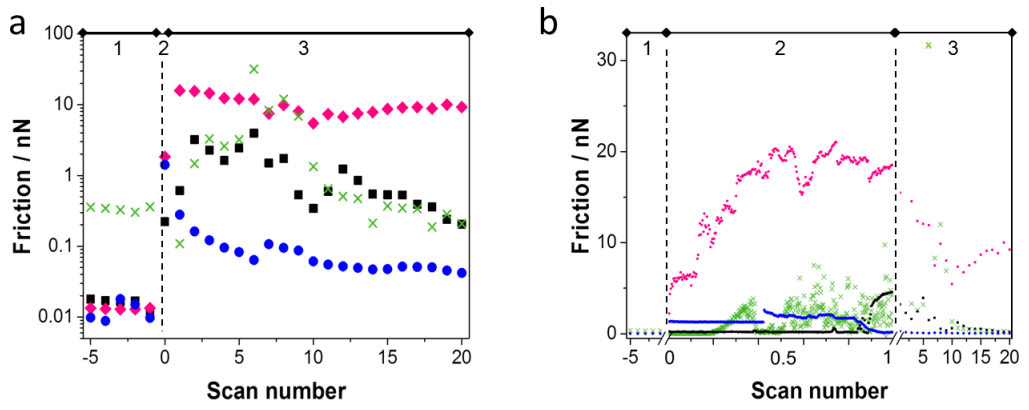

Tip	Surface		
	1	2	3
SiOx/Si	Au(111)	reactive Si(100)	Au(111)
Au/Si	oxidized Si(100)	reactive Si(100)	
Au/Si	Si(100) oxide		
Au/Si	Au(111)		

Figure 3: Development of friction for different tip–surface pairs upon activation of the interface. 1 – Control experiment with intact surface and tip; 2 – onset of activation; 3 – friction values for scanning sequences after activation. a) Emphasis on average friction values per scan before and after activation. b) Emphasis on the onset of the interfacial reaction showing the average friction values per scan line for the frame in which the activation occurred.

tion is less than the diameter of Si (111 pm) and Au atoms (144 pm). We thus exclude material transfer and rather assume structural changes at the atomic scale. We did not observe any shape changes at the tip apex by SEM analysis after a total sliding distance of about 4.8 mm (Figure 6a).

The same Au/Si tip was activated by Ar sputter cleaning and impacting on the surface of oxidized Si(100) (Table 1). Continued sliding on oxidized Si(100) in a different area then resulted in a sudden increase in friction towards the end of the first scan frame (section 2 in Figure 3b, Figure 5c), where friction forces increased to about 3 nN. Friction decreased during the following scans (section 3 in Figure 3). This decrease of friction proceeded by localized changes of the surface. It started from a circular area of decreased friction in the scan center that became wider until the friction was reduced to about 0.2 nN in the entire scan area after 20 scans (Figure 4b). An overview scan of the area revealed material transfer to the oxidized Si(100) surface (Figure 5c,d) with an elevation of about 10 nm. The tip apex was worn by about 325 nm after a sliding length of 10 mm after tip activation (Figure 6b). We did not observe material transfer to the tip apex by electron microscopy.

The initial friction forces measured for another non-activated Au/Si tip sliding against oxidized Si(100) (pink diamonds in Figure 3) were again below 20 pN. Changing the sample and sliding this Au/Si tip against reactive Si(100) resulted in a very rapid increase of friction forces (section 2 in Figure 3b) to more than 20 nN. Friction remained at this level throughout the scanning sequence (section 3 in Figure 3). The tip apex was worn flat by 530 nm after a total of 10 mm sliding distance with no material transferred to the tip (Figure 6c). Observing changes of the topography of the reactive Si(100) surface was not possible as the tip adhered strongly to the surface, leading to artifacts in the topography measurement (similar to Figure 5f).

The initial friction between a SiO_x/Si tip and an oxidized Si(100) surface (green crosses in section 1 in Figure 3) was about ten times higher than the friction between Au/Si tips and oxidized Si(100) (black and pink symbols). Interestingly, the onset of the tribochemical reaction between this SiO_x/Si tip and a reactive Si(100) surface (green crosses in section 2 of Figure 3) was later and the increase in friction slower compared to the Au/Si tip on reactive Si(100) (pink diamonds in section 2, Figure 3b). It was possible to scan one entire frame on reactive Si(100) before friction increased gradually during the second scan to about 5 nN and later to more than 10 nN (Figure 4c, Figure 5e,f). The maximum friction after four scan frames was still lower than for a Au/Si tip on reactive Si(100). Again, the friction did not decrease for continued sliding on

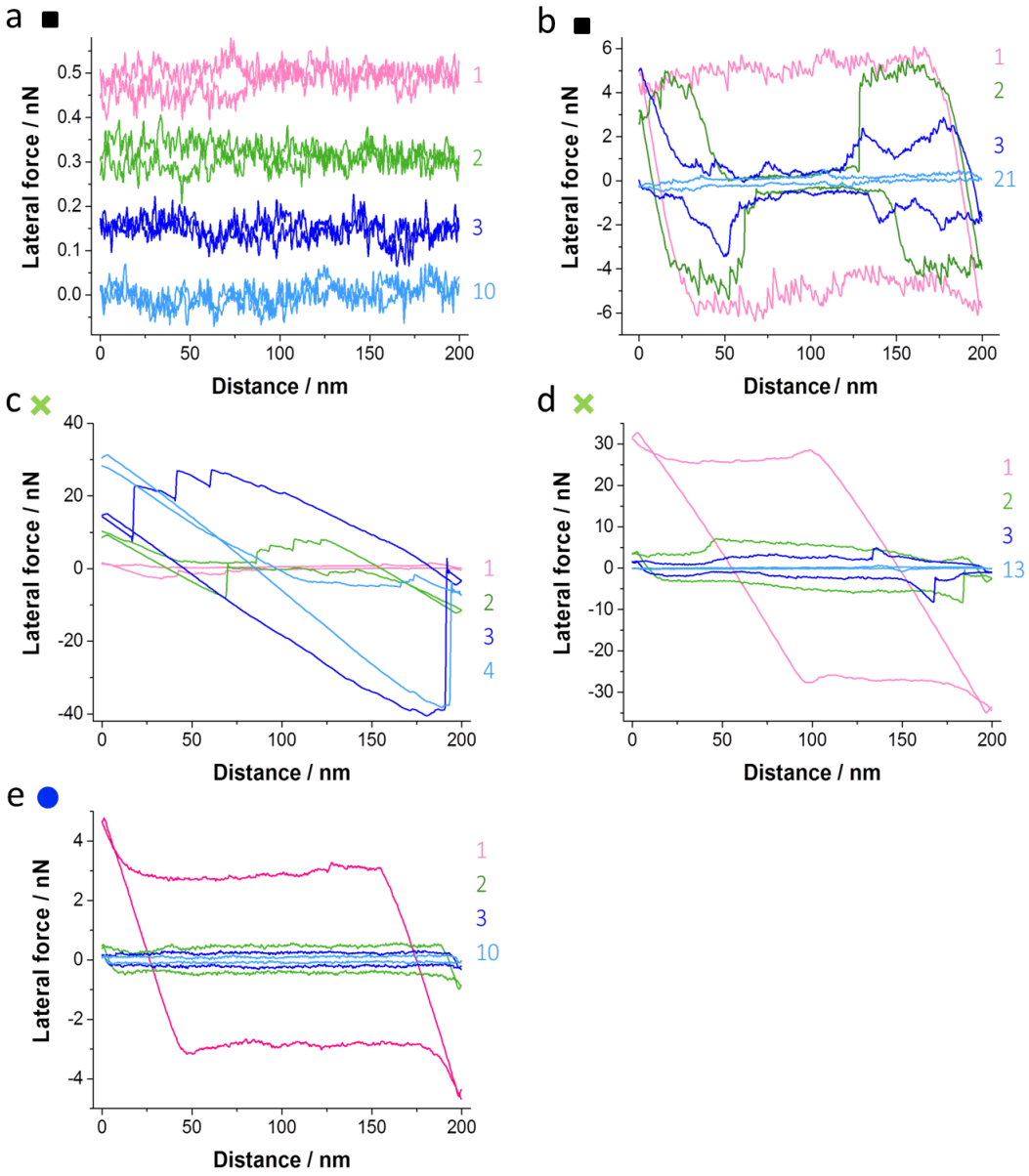

Figure 4: Lateral force loops of the same line from different scan frames. The respective scan number is indicated in the graphs. a) Au/Si tip–oxidized Si(100); friction was very low and decreased with scan frame. The curves are offset for clarity. b) Activated Au/Si tip–oxidized Si(100); the initially high and uniform friction decreased non-uniformly over the surface until it reached a low level and even distribution. c) SiO_x/Si tip–reactive Si(100); the friction increased unevenly with scan frame. d) Activated SiO_x/Si tip–Au(111); the friction decreased from a very high level within 13 scan frames. e) Activated Au/Si tip–Au(111); the friction decreased within ten scan frames and the lateral force remained uniform.

reactive Si(100) (results not shown). This activated SiO_x/Si tip was subsequently used for a sliding experiment against Au(111). After an initial increase of friction forces to 32 nN, we found a rapid decrease to a level comparable to that of Au/Si tips sliding on oxidized Si(100) (Figure 3, green crosses in segment 3; Figure 4d). The scanning produced a square hole with material shifted to its borders (Figure 5g,h). Electron microscopy of the tip apex revealed material transfer from the Au(111) surface to the tip (Figure 6d). The tip was worn by 880 nm after a sliding distance of 17.7 mm.

Scanning a Au/Si tip against the Au(111) surface at low loads resulted in low friction of about 0.01 nN (blue dots in Figure 3a, section 1) and modification of surface topography by displacement of surface atoms (Figure 5i,j). To compare tribochemical reactions of SiO_x/Si and Au/Si tips with the Au(111) surface, a sputter-cleaned Au/Si tip was activated by leaving it in stationary contact for 48 h until cold welding had occurred and adhesive forces between tip and surface had become larger than the force detection range of the cantilever. We found that the tip was reactive after pulling it off the surface, indicating a partial

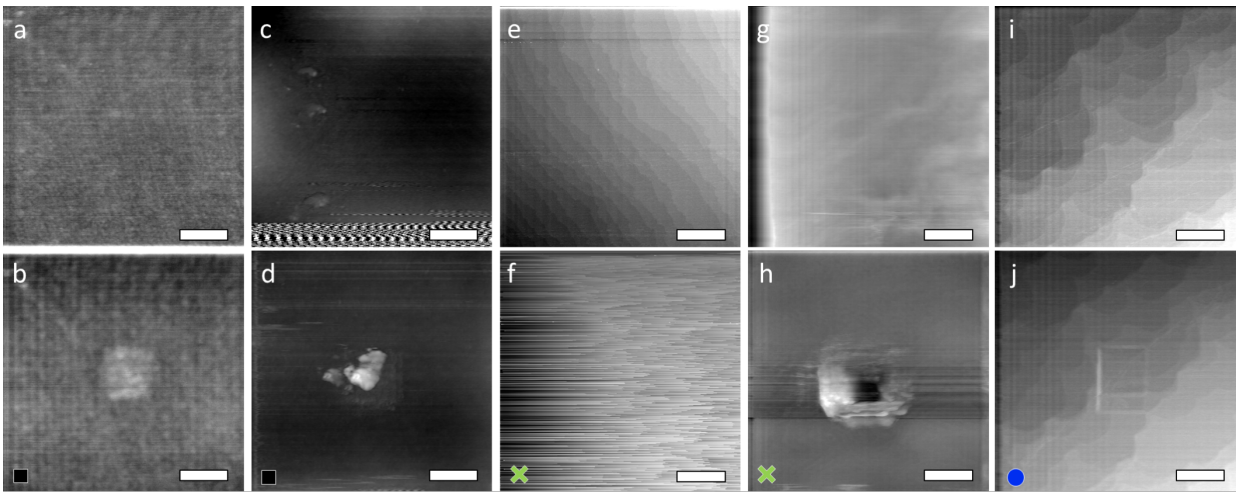

Figure 5: Surface topography of the same area before (upper row) and after (lower row) the friction sequences were recorded in the center of the frames. Scale bars: 200 nm. a, b) Control experiment with an intact Au/Si tip on an oxidized Si(100) surface. Eleven frames were scanned in the center of the scan. The square in the center was elevated by 10 pm. c, d) Activated Au/Si tip on oxidized Si(100). The onset of the tribochemical reaction is revealed in panel c) as intermittent increase in friction causing distortion of the topography measurement. A feature with a height of about 10 nm had evolved in the central area after scanning 21 frames in the image center (panel d)). e, f) Intact SiO_x/Si tip on reactive Si(100). Monatomic steps were observed in panel e); after scanning four frames the topography measurement became hampered by high adhesive friction (panel f)). g, h) Activated SiO_x/Si tip on Au (111). After 15 scans in the center, the topography had changed significantly. The height of the pile-up around the square depression is about 5.8 nm (panel h)). i, j) Intact Au/Si tip sliding on Au(111); despite low normal forces applied and low friction force measured, scanning ten frames in the center resulted in topographical changes. The scanning area had been offset after five scans; therefore two overlapping squares can be distinguished. The height of the pile-up at the left edge of the squares is about 1.15 nm (panel j)).

removal of the Au coating. The friction force was increased to 1.4 nN followed by an increase to about 3 nN while scanning the first frame (blue circles in section 2, Figure 3). In the following sequence of scan frames, friction decreased faster and to lower values than for the activated tips described above (section 2 in Figure 3b, Figure 4e). After a total sliding distance of 260 mm the tip apex was worn by about 370 nm. The electron microscopy images of the Au/Si tip slid against Au(111) show a rim of gold with an irregularly shaped border (Figure 6e) rather than a very sharp border as in the tips worn flat against Si(100) oxide and reactive Si(100) (Figure 6b and Figure 6c, respectively).

The lateral force loops in Figure 4 provide additional details on how friction developed for the tip–surface pairings. The friction force F_F (also given in Figure 3) is calculated from the lateral forces F_L measured in forward (FW) and backward (BW) direction as $F_F = (\overline{F_{L,BW} - F_{L,FW}})/2$, where the average of lateral forces is taken over each scan line. Figure 4 presents the same scan line from subsequent scan frames. The lateral force loops for the Au/Si tip sliding on oxidized Si(100) (Figure 4a) show a very low initial friction (2 pN) and even a decrease of friction from scan 1 to scan 10 to a friction value of 0.2 pN. When the same tip was activated (Figure 4b), friction first increased to about 5 nN and then decreased in the course of the scanning sequence to 0.1 nN in a non-uniform manner. Patches of low friction grew from one scan frame to the next, indicating the formation of a low-friction layer with weak an irregular stick–slip pattern on the surface. When sliding a SiO_x/Si tip against reactive Si(100), the friction increased with sliding time (Figure 4c). Large stick–slip events extended across almost the entire scanning distance (scans 3 and 4 in Figure 4c) due the strong tip–sample adhesion. Sliding activated tips against Au(111) always resulted in a decrease of friction, both for activated SiO_x/Si tips (Figure 4d) and activated Au/Si tips (Figure 4e).

Additional information about the friction processes can be obtained by comparing topography features before and after the sliding sequences (Figure 5). An intact Au/Si tip left an elevated square with a height of only some picometers on oxidized Si(100) (Figure 5a,b), but on Au(111) it moved Au atoms to the four sides of the scan frame (Figure 5i,j). From an activated Au/Si tip material was transferred to the oxidized Si(100) surface (Figure 5c,d) up to a height of 10 nm, while an activated SiO_x/Si tip created a square depression with large pile-up on all sides on the Au(111) surface (Figure 5g,h).

Electron microscopy of the tips after sliding on the various surfaces reveals distinct differences in shape and material transfer for different tip–surface pairings (Figure 6). No changes at the tip apex were observed after sliding an intact Au/Si tip on oxidized Si(100) for 4.8 mm (Figure 6a). A tip wear of 325 nm was measured when the same tip was activated before sliding

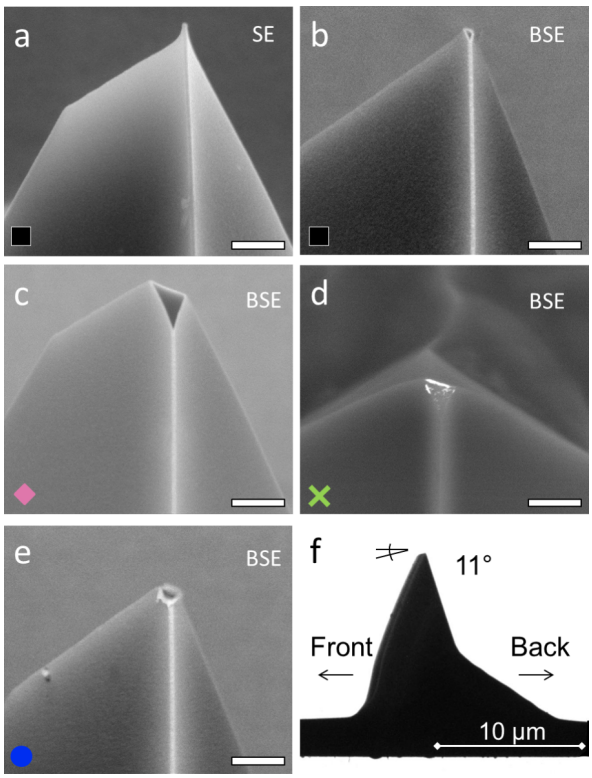

Figure 6: Scanning electron microscopy (SEM) images (secondary electrons (SE), back-scattered electrons (BSE)) of tip apices used in the experiments. The scale bars in panels a) to e) correspond to 500 nm. a) Au/Si tip after sliding for a distance of 4.8 mm on oxidized Si(100), with no detectable wear. b) Au/Si tip after activation and sliding for a distance of 20 mm on oxidized Si(100); the tip was worn by 325 nm. c) Au/Si tip after sliding for a distance of 10 mm on reactive Si(100); the height difference to the intact tip was about 530 nm. d) SiO_x/Si tip after sliding for a distance of 17.7 mm on reactive Si(100) and Au(111); the tip was worn by 880 nm and Au was transferred from the surface to the tip apex (white contrast). e) Au/Si tip after activation and sliding for a distance of 260 mm on Au(111); tip wear was 370 nm. f) TEM side view of a non-coated AFM tip after sliding. The angle of the worn tip apex corresponds to the angle between cantilever holder and surface of 11°.

for 20 mm on oxidized Si(100) (Figure 6b). Prolonged stationary contact with Au(111) after sputtering resulted in activation of a Au/Si tip. After sliding this tip for 260 mm on Au(111), the tip was worn by 370 nm (Figure 6e). The largest wear was measured for tips that had been sliding against reactive Si(100); the Au/Si tip was worn by 530 nm after a sliding length of 10 mm (Figure 6c), and the SiO_x/Si tip was worn by 880 nm after a sliding length of 17.7 mm (Figure 6d). A wear rate was determined by estimating the wear volume as that of a cone with the base area equal to the flat area of the worn tip, with the height of the measured height loss, and the apex radius of the un-worn tip. The wear rates are summarized in Table 3 for the cases described above. We refrain from including the normal force into the calculation of the wear rate since the unknown contribution of adhesion is significant in these nanoscale experiments. The highest wear rate was found for the tips that had been in contact with reactive Si(100). Material transfer was found in one case, for the activated SiO_x/Si tip after sliding on Au(111) (Figure 6d). The coatings of the Au/Si tips that were slid against reactive or oxidized Si(100) had a sharp border (Figure 6b,c), while the Au coating of the Au/Si tip that was slid against Au(111) had an irregularly shaped border (Figure 6e). When viewed from the side, the wear of the tip apices corresponded to the sliding angle of about 11° between cantilever and surface (Figure 6f).

TEM analysis of the damaged Au/Si tip after sliding on Au(111)

The cross section of a Au/Si tip that had been sliding against Au(111) (Figure 6e) was analyzed by transmission electron microscopy (TEM). The Au coating and the Si bulk can be clearly distinguished in the images (Figure 7a,b). In some areas a crystalline lattice was resolved (lattice spacing of 2.4 Å in the Au layer and 1.9 Å in the Si bulk are indicated in Figure 7c,d). The Au coating consisted of crystal grains of different orientation. Tip wear proceeded through the Au coating and the SiO_x layer (Figure 7a). Low amounts of Cr were detected by EDX analysis, especially in the Au layer, while no adhesive Cr layer could be distinguished between Si and Au. An amorphous layer (marked with asterisk in Figure 7) with a thickness of about 13 nm covers the surface that had been in sliding contact with Au(111). A rather sharp border marks the transition from amorphous Si to crystalline Si (Figure 7d). If the amorphous layer contained significant amounts of oxygen, it would appear brighter than the crystalline silicon. This was not the case and we conclude that the amorphization is a mechanical process that

Table 3: Wear rate estimated from SEM tip images. Please refer to the description in the text for details on the surfaces and the tip activation, for example by intermittent sliding on reactive Si(100).

tip	surface	V_{worn} / 10^6 nm^3	d / mm	wear rate / 10^5 nm^3·mm^{-1}
Au/Si (black squares)	Si(100) oxide	3.5	20	1.7
Au/Si (purple diamonds)	Si(100)	15.7	10	15.7
SiO_x/Si (green crosses)	Au(111)	66.3	17.7	37.5
Au/Si (blue circles)	Au(111)	6.1	260	0.2

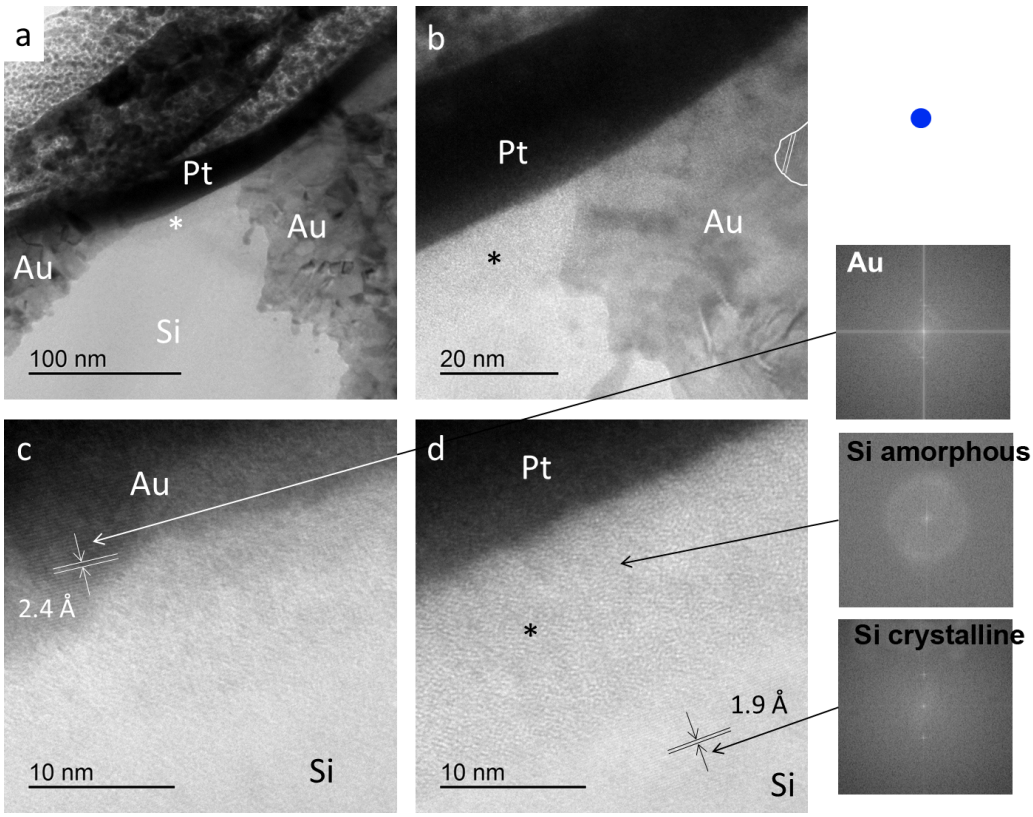

Figure 7: TEM images of a cross section through the apex of a Au/Si tip that had been sliding against Au(111). a) Overview showing the Pt protective coating that was added prior to FIB cutting, the Au cantilever coating and the Si bulk. The contact area is worn flat and the asterisk marks an amorphous layer in the contact region. b) Detail of panel a) showing the amorphous Si with its sharp boundary to crystalline Si as well as crystallites (highlighted) in the Au layer. c) Close-up resolving the crystal lattice in the Au coating layer. The lattice distance was measured to be 2.4 Å. d) Detail of the amorphous layer (*) and the crystalline Si bulk with a lattice distance of 1.9 Å. Fourier transformations of the Au lattice in panel c) and the Si amorphous layer and the crystalline Si from panel d) are provided in the right part of the figure.

does not require oxidation to occur. Fourier transformation of the images (right side of Figure 7) revealed crystalline order for the tip material lattice and amorphous short-range structure for the layer that was transformed by the sliding contact.

Discussion

We start by discussing the absence of contact ageing in our slide–hold–slide experiments by AFM in ultrahigh vacuum. Previous experimental results had suggested the formation of a liquid-like Au neck in nanometer-scale single-asperity contacts on gold surfaces by diffusion of Au atoms along surface and contact [15-19]. We assumed that the neck formation by diffusion would manifest itself as contact ageing in slide–hold–slide experiments on the time scale of seconds, similar to the development of grain boundaries in the fusion of gold nanoparticles [16]. In our experiments, the holding time before sliding was varied between 252 µs (v = 3.1 µm·s^{-1}) and 100 s. As our system was drifting by only one atomic distance per 10 s, we should be able to detect effects of the holding times up to 10 s. No static friction peak was observed for any of the holding times for SiO_x/Si tips sliding against Au(111). Au atoms are very mobile on Au(111) surfaces; at room temperature a Au atom may diffuse several micrometers within nanoseconds [20]. We conclude that contact ageing on Au(111) that results from Au atom diffusion is too fast to be observed with our experiment, or that the neck formation by Au diffusion does not result in increased static friction as the neck follows the AFM tip movement without additional friction. In this case we may even ask if the neck actually follows the tip movement or, considering the fast diffusion rates of Au, if it is rather re-forming continuously in a liquid-like manner.

We also investigated contact ageing for SiO_x/Si tips on oxidized Si(100) surfaces, a system for which contact ageing in slide–hold–slide experiments in ambient atmosphere has been reported [8]. While we could reproduce the result in ambient atmosphere, we did not observe any static friction peak in ultrahigh vacuum for holding times up to 100 s. The absence of contact ageing in vacuum is in agreement with the explanation that contact ageing in air is caused by a successive formation of

hydroxide bonds between the oxide surfaces, which requires the presence of water [12,13,21].

When probing Au(111) with an intact, passivated tip we found regular stick–slip patterns in the lateral force signal, which resembled the atomic structure of the (111) surface. Despite the small friction forces in the piconewton range, scanning resulted in pile-up of atoms at the edges of the scan frame. It is striking that the observation of atomic stick–slip friction does not imply sliding on a perfect rigid atomic lattice but rather a tip interacting with a dynamic surface of displaceable atoms. This description is in full agreement with the explanation of the absence of contact ageing by a liquid-like nature of the contact. An irregular atomic-scale stick–slip pattern was observed for the oxidized Si(100) surface. The irregularities were likely caused by the nanoscale topography of the oxide surface. Patterns with larger characteristic slip length and signs of stronger tip–surface interactions were recently reported for similar tip–surface pairings at low pressure [22]. The difference between the observations could be caused by the difference in water and oxygen content between experiments in low vacuum and in ultrahigh vacuum with extended surface cleaning, as water and oxygen cause the formation of hydroxide bonds between two SiO_x surfaces [8,12].

Since we did not observe contact ageing for the intact tips, we developed several techniques for controlled removal of passivating layers from the tip apex or the counter surfaces. The onset of chemical interactions between tip and surface was very sudden and resulted in a strong increase in friction forces. Significant static friction peaks appeared, mainly at the turning points of the scanning motion but also at random positions in the scan frames. Once the tip had been stuck to a position on the surface and a significant static friction peak had been observed, the kinetic friction remained increased during the subsequent sliding compared to experiments where no static friction peaks were encountered. The static friction peaks varied in magnitude and could not be reproduced by repeating the scan at the same position. We conclude that sticking of the contact and breaking loose changed the local surface chemistry as well as structure and chemistry of the tip. AFM-based slide–hold–slide experiments require that structure and chemistry of the tip–surface interface are similar at the beginning of each holding phase [7,8]. This prerequisite could not be met by our AFM experiments on reactive SiO_x/Si and SiO_x/Si/Au systems in ultrahigh vacuum.

The onset of reactivity between tip and surface occurred faster when sliding Au/Si tips on reactive Si(100) than for SiO_x/Si tips. The difference can be explained by the thickness of the oxide layer on the tip, which is thinner for Au coated tips than for the oxide-sharpened SiO_x/Si tips. Furthermore, the highly reactive Cr that is used in Au-coated tips as thin adhesive layer could play a role in the chemical activation and act as a catalyst.

Strong friction was observed as sign of reactive tip–sample interactions after removal of passivating layers. The further development of friction after tip activation depended crucially on the presence of atoms that could re-passivate the interface. The effects of passivation have been shown in pioneering study on UHV AFM by Howald et al., who achieved stable sliding on reactive Si(111) after covering the tip by PTFE [23]. For our tips, sliding contacts with clean Si(100) stayed reactive and were subject to adhesive wear, as impressively shown by the SEM images of the worn tips. The removal of the oxide layer and later of the Si from the sliding tip can possibly be enhanced by the formation of volatile silane with residual H_2 molecules in the UHV chamber and with H atoms passivating Si(100), as we did not find any wear debris on the tips or on the surfaces. Wear rates of sharp AFM tips after sliding distances of up to 1 μm against diamond have been calculated earlier [24]. The wear volumes and sliding distances were much smaller than in our experiments but the wear rates of (5–100) × 10^5 $nm^3 \cdot mm^{-1}$ are comparable with the present results. The initial wear rates in [24] are expected to decrease with sliding distance due to reduced pressure at the interface and cannot be extrapolated linearly [25].

When two reactive surfaces were in sliding contact we measured very high lateral forces. The AFM tips were worn flat with an angle imposed by the geometry of the AFM. The flat was smooth and no wear debris was found. Therefore an adhesive wear process where single atoms were removed through formation and breaking of chemical bonds is a most likely microscopic scenario [24,25].

A reactive contact sliding on oxidized Si(100) or Au(111) will be passivated within a few scan frames. As the effective contact time for each position while scanning was in the range of microseconds, the passivating reaction occurred on this fast time scale. Intermediary formation of gold silicide at the sliding interface is expected only at higher temperature [26,27] but may be facilitated by frictional energy and by shear mixing. Eutectic AuSi will segregate at room temperature and can thus not be detected after the experiments. We rather suggest that for re-passivation Si reacts with oxygen-containing species on oxidized Si(100) and Au(111) surfaces.

Higher friction forces were measured after activation and re-passivation compared to the initial values. They were likely caused by the increased contact area [28] and the modified geometry of the tip, the flat end of which was worn to be perfectly

parallel with the surface. The results of Figure 3 and Figure 4 reveal details on the transfer of material in the scanning process. Both on oxidized Si(100) and on Au(111), scanning with passivated, intact tips led to very subtle atomic-scale rearrangements on the surface despite minimal friction forces. Neither the atomic roughening of the oxidized Si(100) nor the displacement of gold atoms to the edges of the scanning frame on Au(111) caused a significant contact ageing. While there was significant loss of material from the tip due to wear, no corresponding volume was found on the surfaces when imaging after the scanning sequences. Transfer of surface material to the tip was observed only for gold and after scanning on Au(111) surfaces. The transferred gold was spread across the worn contact for SiO_x/Si tips and stuck to the Au coating in the case of Au/Si tips.

Amorphization of the Si tip apex after sliding contact with silicon oxide in air and vacuum has been reported before [29-31] and was confirmed here for sliding contacts in UHV by TEM analysis of the tip. The thickness of the amorphous layer on our tip was in the same range as described for scratching experiments on oxidized Si [29-31]. Upon scratching in air, the amorphization is accompanied by changes in chemical composition towards a higher oxide content [30] and by distortions of the crystalline structure below the scratch [29]. Our TEM images indicate that the friction-induced amorphization proceeds with similar results for silicon in UHV, probably without significant oxidation. Precise determination of the chemical composition in nanometer-sized regions of the tip apex lamella by EDX or from scattering results in TEM remains a challenge, in particular as the sample is exposed to air during preparation and transfer.

Conclusion

In summary, we investigated nanometer-scale friction phenomena between oxidized and clean silicon surfaces and gold surfaces by means of friction force microscopy in ultrahigh vacuum. We did not observe any contact ageing for oxidized silicon tips sliding on gold surfaces or on oxidized silicon surfaces, although we found evidence for atomic rearrangement in the course of scanning. We conclude that the contact formation with the gold surface is too fast and the contact too compliant to reveal contact ageing as holding-time-dependent static friction. For friction between oxidized silicon surfaces, the chemical bond formation leading to contact ageing does not occur in the absence of water in UHV. Both systems show very low lateral forces compared to pull-off forces, modulated by the atomic structure of the surface.

When passivating layers are removed from tips or surfaces, tribochemical reactions cause a strong increase in friction and significant tip wear in the Si/SiO_x/Au system. On reactive, clean Si(100) we found persistent adhesive wear, while the presence of oxidized silicon led to a re-passivation of the sliding interface within a few scan frames.

Acknowledgements

We thank Birgit Heiland from INM for FIB-cutting the AFM tip. This work was financially supported by Deutsche Forschungsgemeinschaft. We acknowledge the continuing support of this project by Eduard Arzt.

ORCID® iDs

Roland Bennewitz - https://orcid.org/0000-0002-5464-8190

References

1. Zaghloul, U.; Bhushan, B.; Pons, P.; Papaioannou, G. J.; Coccetti, F.; Plana, R. *J. Colloid Interface Sci.* **2011,** *358,* 1–13. doi:10.1016/j.jcis.2011.03.005
2. Bhushan, B. *Microelectron. Eng.* **2007,** *84,* 387–412. doi:10.1016/j.mee.2006.10.059
3. Marone, C. *Int. J. Rock Mech. Min. Sci.* **1997,** *34,* 187.e1–187.e17. doi:10.1016/S1365-1609(97)00054-3
4. Fulton, P. M.; Rathbun, A. P. *Earth Planet. Sci. Lett.* **2011,** *308,* 185–192. doi:10.1016/j.epsl.2011.05.051
5. Budakian, R.; Putterman, S. J. *Phys. Rev. B* **2002,** *65,* 235429. doi:10.1103/PhysRevB.65.235429
6. Gosvami, N. N.; Feldmann, M.; Peguiron, J.; Moseler, M.; Schirmeisen, A.; Bennewitz, R. *Phys. Rev. Lett.* **2011,** *107,* 144303. doi:10.1103/PhysRevLett.107.144303
7. Feldmann, M.; Dietzel, D.; Tekiel, A.; Topple, J.; Grütter, P.; Schirmeisen, A. *Phys. Rev. Lett.* **2016,** *117,* 025502. doi:10.1103/PhysRevLett.117.025502
8. Li, Q.; Tullis, T. E.; Goldsby, D.; Carpick, R. W. *Nature* **2011,** *480,* 233–236. doi:10.1038/nature10589
9. Blass, J.; Albrecht, M.; Wenz, G.; Guerra, R.; Urbakh, M.; Bennewitz, R. *J. Phys. Chem. C* **2017,** *121,* 15888–15896. doi:10.1021/acs.jpcc.7b05412
10. Chan, S.-W.; Balluffi, R. W. *Acta Metall.* **1985,** *33,* 1113–1119. doi:10.1016/0001-6160(85)90205-6
11. Merkle, A. P.; Marks, L. D. *Tribol. Lett.* **2007,** *26,* 73–84. doi:10.1007/s11249-006-9191-8
12. Liu, Y.; Szlufarska, I. *Phys. Rev. Lett.* **2012,** *109,* 186102. doi:10.1103/PhysRevLett.109.186102
13. Tian, K.; Gosvami, N. N.; Goldsby, D. L.; Liu, Y.; Szlufarska, I.; Carpick, R. W. *Phys. Rev. Lett.* **2017,** *118,* 076103. doi:10.1103/PhysRevLett.118.076103
14. Guerra, R.; Benassi, A.; Vanossi, A.; Ma, M.; Urbakh, M. *Phys. Chem. Chem. Phys.* **2016,** *18,* 9248–9254. doi:10.1039/C6CP00661B
15. Gosvami, N. N.; Filleter, T.; Egberts, P.; Bennewitz, R. *Tribol. Lett.* **2010,** *39,* 19–24. doi:10.1007/s11249-009-9508-5
16. Casillas, G.; Ponce, A.; Velázquez-Salazar, J. J.; José-Yacamán, M. *Nanoscale* **2013,** *5,* 6333–6337. doi:10.1039/c3nr01501g
17. Landman, U.; Luedtke, W. D.; Burnham, N. A.; Colton, R. J. *Science* **1990,** *248,* 454–461. doi:10.1126/science.248.4954.454
18. Pashley, D. W.; Stowell, M. J.; Jacobs, M. H.; Law, T. J. *Philos. Mag. A* **1964,** *10,* 127–158. doi:10.1080/14786436408224212

19. Merkle, A. P.; Marks, L. D. *Wear* **2008,** *265,* 1864–1869. doi:10.1016/j.wear.2008.04.032
20. Liu, C. L.; Cohen, J. M.; Adams, J. B.; Voter, A. F. *Surf. Sci.* **1991,** *253,* 334–344. doi:10.1016/0039-6028(91)90604-Q
21. Li, A.; Liu, Y.; Szlufarska, I. *Tribol. Lett.* **2014,** *56,* 481–490. doi:10.1007/s11249-014-0425-x
22. Craciun, A. D.; Gallani, J. L.; Rastei, M. V. *Nanotechnology* **2016,** *27,* 055402. doi:10.1088/0957-4484/27/5/055402
23. Howald, L.; Lüthi, R.; Meyer, E.; Güntherodt, H.-J. *Phys. Rev. B* **1995,** *51,* 5484–5487. doi:10.1103/PhysRevB.51.5484
24. Jacobs, T. D. B.; Carpick, R. W. *Nat. Nanotechnol.* **2013,** *8,* 108–112. doi:10.1038/nnano.2012.255
25. Gotsmann, B.; Lantz, M. A. *Phys. Rev. Lett.* **2008,** *101,* 125501. doi:10.1103/PhysRevLett.101.125501
26. Adachi, T. *Surf. Sci.* **2002,** *506,* 305–312. doi:10.1016/S0039-6028(02)01429-2
27. Yokota, Y.; Hashimoto, H.; Saito, N.; Endoh, H. *Jpn. J. Appl. Phys., Part 2* **1986,** *25,* L168. doi:10.1143/JJAP.25.L168
28. Enachescu, M.; van den Oetelaar, R. J. A.; Carpick, R. W.; Ogletree, D. F.; Flipse, C. F. J.; Salmeron, M. *Tribol. Lett.* **1999,** *7,* 73–78. doi:10.1023/A:1019173404538
29. Guo, J.; Song, C.; Li, X.; Yu, B.; Dong, H.; Qian, L.; Zhou, Z. *Nanoscale Res. Lett.* **2012,** *7,* 152. doi:10.1186/1556-276X-7-152
30. Yu, B.; Dong, H.; Qian, L.; Chen, Y.; Yu, J.; Zhou, Z. *Nanotechnology* **2009,** *20,* 465303. doi:10.1088/0957-4484/20/46/465303
31. Yu, B.; Qian, L.; Dong, H.; Yu, J.; Zhou, Z. *Wear* **2010,** *268,* 1095–1102. doi:10.1016/j.wear.2010.01.007

License and Terms

BEILSTEIN JOURNAL OF NANOTECHNOLOGY

Recent highlights in nanoscale and mesoscale friction

Andrea Vanossi[1,2], Dirk Dietzel[3], Andre Schirmeisen[3], Ernst Meyer[4], Rémy Pawlak[4], Thilo Glatzel[4], Marcin Kisiel[4], Shigeki Kawai[5] and Nicola Manini[*6]

Review

Open Access

Address:
[1]CNR-IOM Democritos National Simulation Center, Via Bonomea 265, 34136 Trieste, Italy, [2]International School for Advanced Studies (SISSA), Via Bonomea 265, 34136 Trieste, Italy, [3]Institute of Applied Physics, University of Giessen, 33492 Giessen, Germany, [4]Department of Physics, University of Basel, Klingelbergstr. 82, CH-4056 Basel, Switzerland, [5]International Center for Materials Nanoarchitectonics, National Institute for Materials Science, 1-1, Namiki, Tsukuba, Ibaraki 305-0044, Japan and [6]Dipartimento di Fisica, Università degli Studi di Milano, via Celoria 16, 20133 Milano, Italy

Email:
Nicola Manini[*] - nicola.manini@fisica.unimi.it

* Corresponding author

Keywords:
atomic force microscopy; dissipation; friction; mesoscale; nanomanipulation; nanoscale; scale bridging; structural lubricity; superlubricity

Beilstein J. Nanotechnol. **2018,** *9,* 1995–2014.
doi:10.3762/bjnano.9.190

Received: 16 April 2018
Accepted: 27 June 2018
Published: 16 July 2018

This article is part of the Thematic Series "Nanotribology".

Guest Editor: E. Gnecco

Abstract

Friction is the oldest branch of non-equilibrium condensed matter physics and, at the same time, the least established at the fundamental level. A full understanding and control of friction is increasingly recognized to involve all relevant size and time scales. We review here some recent advances on the research focusing of nano- and mesoscale tribology phenomena. These advances are currently pursued in a multifaceted approach starting from the fundamental atomic-scale friction and mechanical control of specific single-asperity combinations, e.g., nanoclusters on layered materials, then scaling up to the meso/microscale of extended, occasionally lubricated, interfaces and driven trapped optical systems, and eventually up to the macroscale. Currently, this “hot” research field is leading to new technological advances in the area of engineering and materials science.

Introduction

Friction, the force that resists the relative lateral motion of bodies in contact, and the related dissipation phenomena are being investigated extensively due to their importance in applications, from everyday life to advanced technology. At the macroscopic scale, friction between sliding bodies depends on their surface roughness. But studies of atomically flat surfaces in vacuum demonstrate that the actual origin of friction is at the atomic scale. The friction force results from the sum of atomic-scale forces, including all kinds of interactions including Coulombic forces, covalent bonding and van der Waals forces. As a result, in vacuum, friction depends heavily on the arrangement, be it crystalline or amorphous, and the chemical nature of

the surface atoms of the contacting bodies. For this reason, research in the last quarter of a century has focused on the mechanisms occurring at the atomic scale, which are ultimately responsible for the microscopic processes governing friction. Major advances in experimental techniques, including the development and widespread adoption of scanning microscopes and particularly the atomic force microscope (AFM) [1], accompanied by new theoretical concepts and models, have brought this field to an advanced state of maturity, although open problems and issues remain numerous. For example, the concept of superlubricity [2,3] was introduced theoretically and proven experimentally in several contexts, several of which are reviewed in the following, but it still fails to deliver concrete breakthroughs in applications. The state of the art of the field advancement in the early 2010's and the fundamentals of theory, simulations, and experimental techniques were assessed in a few review works and volumes [4-8]. In the years 2013–2017, the European Union has sponsored a collaborative effort in this field, through COST Action MP1303. The resulting flourishing international collaboration has led to remarkable progress of this field. The present review summarizes the most relevant results in fundamental tribology from the past five years, with focus of those obtained within this COST-supported collaboration, and on friction phenomena resolved down to the nanometer or at least micrometer scale. While we try to cover the most recent research and those that to our taste and knowledge seem the most exciting results, a complete review even of purely atomic-scale research would exceed our resources, and take us too far in extent.

We organize the selected topics in sections as follows: We first report on the progress in nanomanipulation, i.e., controlled movements at the nanometer scale. The successive section focuses on nano-confined lubrication. Then section "Trapped optical systems: ions and colloids" reviews recent experiments and theory exploring the depinning and sliding mechanisms in analog model systems controlled by forces generated by electromagnetic fields. A successive section "Controlling friction and wear at the nanometer scale" addresses novel frictional systems allowing some degree of friction control and/or tuning. Section "Multiscale bridging" summarizes recent efforts towards establishing a quantitative link among the vastly different length and time scales involved in tribology. The section "Conclusion" summarizes our view of the developments of the field foreseeable in the near future.

Review

Controlled nanomovements

Friction force microscopy (FFM) is a well-defined AFM operation mode in which tiny lateral forces acting on the tip, as it scans across the surface, are recorded [9]. Atomic forces involving few-atom contacts can provide direct information on the crystal structure itself. Particularly when the FFM tip is subject to stick–slip advancement, this mode becomes especially efficient for resolving structural features. By mapping the power dissipated by these lateral forces, FFM can even detect such elusive structures as moiré patterns on a lattice-mismatched crystal overlayer [10-12]. One of the most frequent motivations to utilize FFM as a tool in nanotribology is its ability to mimic a single-asperity contact by the junction between a sharp AFM tip and the substrate. Such single-asperity contacts are widely considered as the most fundamental building blocks of friction, as pointed out in well-established interface models, where interfaces are considered as a complex system of single-asperity contacts [13,14].

Consequently, FFM has received tremendous attention since its invention 30 years ago. To date an ever growing number of studies has explored the fundamental mechanisms of single-asperity friction in which, e.g., the influence of parameters such as temperature [15-17], sliding velocity [18-22], chemical composition [23,24] and normal load [25-29] was analyzed. Additionally, effects such as contact ageing [30-33] or the dependence of friction on the scan direction over crystalline surfaces [34-38] were explored.

To address many properties over a broad range of experimental conditions it is sufficient to use simple theoretical models that describe qualitatively the tribological contact in terms of few atoms only, or even consider a single-atom contact. In this context, especially the concept of thermally-activated stick–slip [18] has become a universal starting point to describe nanoscopic friction phenomena.

In recent years however, growing interest was directed toward extended but still atomically flat nanocontacts where friction is not only determined by the interaction between a single slider atom and the substrate, but is instead crucially influenced by the collective behavior of the atoms forming the two contacting bodies. This kind of behavior becomes crucial for the intriguing concept of structural lubricity, where collective force cancellation effects can result in ultra-low friction for incommensurate interfaces [39-41]. Note that "superlubricity" and "structural lubricity" are often used synonymous throughout the literature, although the latter term should be considered to be more accurate [42].

The experimental analysis of structural lubricity has long since been difficult, because well-defined junctions between conventional AFM tips and substrates cannot readily be found for single-asperity contacts. Instead, the detailed structure and composition of AFM tips is often ill-defined and therefore obstructs

any systematic analysis of problems where accurate interface structures are required [43]. As a consequence, a growing number of studies is now focusing on friction of sliding nanoobjects, where well-defined interfaces are made accessible for structures prepared by thermal evaporation [44-48] or lithographic techniques [49-54]. Alternatively, molecular-scale structures such as PTCDA [55], polyfluorene chains [56], graphene nanoflakes on graphene [57] or graphene nanoribbons (GNRs) on single crystals [58] can be analyzed (see [59] for a detailed review on single-molecule manipulation in nanotribology). These experimental efforts are accompanied by increasing theoretical work, where the analysis of specific nanoscale systems and systematic variation of their key characteristics provides fundamental insight into a large variety of tribological phenomena.

To experimentally assess the interfacial friction of sliding nanostructures, FFM still remains the primary tool. However, the AFM is now applied as a manipulation tool with which friction becomes accessible by measuring the additional lateral force component originating from the interface between nanostructure and substrate [43]. Only for very small structures, dynamic NC-AFM techniques are required in which the interfacial friction can be quantified based on the frequency shift induced by the resistance of the structure against movement [55,58,60,61]. Occasionally, AFM nanomanipulation is also combined with scanning electron microscopy, which then allows for a very defined interaction with the nanostructures and in situ monitoring of their movement [62-64].

An instructive example of the capabilities of such AFM-assisted nanomanipulation approaches was demonstrated in [65], where an AFM tip positioned on top of a MoO_3 nanocrystal provided continuous controlled manipulation of the nanocrystal. As shown in Figure 1, during the movement of the particle a gradual decrease of friction was observed which could be related to thermolubricity spurred by dissipated heat trapped in the nanocrystal due to its confined size and layered structure.

In recent years, analyzing systems showing structural lubricity has been a primary field of application for nanomanipulation techniques. Here, especially the sublinear contact-area dependence of friction has been recognized as a unique fingerprint of structural lubricity, which reflects the underlying physical mechanism of collective force cancellations of slider atoms moving on the potential energy surface of the substrate. These cancellation effects become more and more effective, when the particle size increases, ultimately leading to a sublinear relation between friction and contact area described by $F \propto A^{\gamma}$, with F the friction force, A the contact area, and $\gamma < 1$ the scaling exponent [66-68].

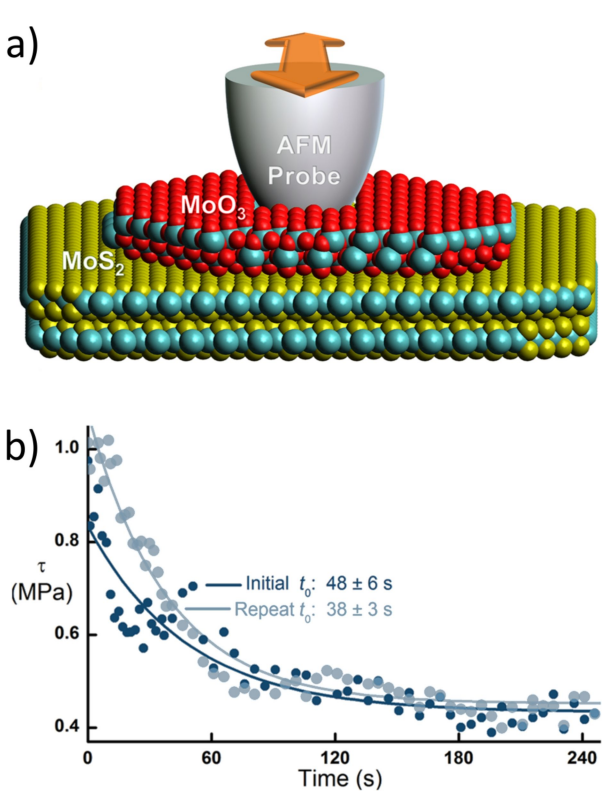

Figure 1: a) Scheme of a MoO_3 nanocrystal on MoS_2. The AFM tip is firmly positioned on top on the nanocrystal and can facilitate continuous manipulation of the structure. b) Friction of the MoO_3 nanostructure as a function of the time obtained by continuous recording of friction loops. The initial friction decreases with time (as described by the time constants) until a stationary friction level is reached. This effect can be attributed to thermolubricity related to the friction-driven temperature increase at the interface. Reprinted with permission from [65], copyright 2017 American Chemical Society.

A first experimental verification of this effect has been provided by UHV nanomanipulation experiments of gold and antimony nanoparticles on highly oriented pyrolithic graphite (HOPG) [46], where the precise value of γ was found to depend sensitively on the crystallinity of the particles. As predicted theoretically [66,67], γ = 0.5 was found for the case of amorphous Sb nanoparticles, whereas crystalline gold nanoparticles can be described by an effective scaling exponent of approximately half this value. This difference can be understood simply by considering how force cancellation effects become less effective for amorphous interfaces with irregular positioning of slider atoms [46].

While the absolute contact area is of crucial importance to describe the interfacial friction, it was found that also the exact shape of a nanoparticle is a key parameter to describe its tribological behavior. Unfortunately, this parameter usually cannot be determined precisely due to the limited spatial resolution of most nanomanipulation experiments, but recent theoretical

studies have pointed out its significance, especially with respect to its influence of the relative orientation between particle and substrate. It was shown that, e.g., the succession of orientational maxima of the potential energy barrier for sliding depends sensitively on the shape of the particle [68,69]. Perfectly geometrical structures such as Au triangles on HOPG show sharp and defined maxima as a function of the relative rotation angle, whereas rounded edges smoothen out the angular corrugation and additionally increase the scaling exponent γ. Hence, shape effects play an important role to explain friction fluctuations associated to particle reorientation observed in nanomanipulation experiments [69].

In part, these shape effects can be related to the particular role that the edge plays within the force-cancellation mechanisms of structural lubricity. This crucial importance of the edge was also demonstrated by molecular dynamics (MD) simulations for Kr islands adsorbed on Pb(111). Here, depending on size and shape of the islands, the edge generates a barrier for the unpinning and successive advancement of the edge dislocations lines (often also called "solitons" or "kinks"), which is required for the overall depinning of the island and thus defines the static friction [70]. An important influence of the edge was also found for GNRs sliding on gold (see subsection "Manipulation of graphene nanoribbons on gold" below), where edge-dominated friction effects lead to a small overall influence of length [71,72].

To unambiguously identify friction effects governed by structural lubricity in experiments, especially the sublinear contact-area dependence has been used in a number of works [46-49,58]. The contact areas of the analyzed systems in these works spanned several orders of magnitude ranging from a few square nanometers for GNRs [58] to almost the square micrometer range for sheared graphite stacks [49].

Once the exact tribological scenario is identified, further interface effects can be derived from sliding nanosystems. This was demonstrated, e.g., for sheared graphite stacks [49], where nanomanipulation experiments also allowed the authors to determine the adhesion forces between the sliding graphite surfaces, simply by distinguishing between reversible displacement forces related to the conservative adhesion energy and irreversible friction forces. The same mechanisms of adhesion-driven forces in combination with structural lubricity have recently been observed for other systems as well. First, adhesion was found as the driving force for the formation of graphene nanoribbons by a self tearing process after nanoindentation experiments [73]. Secondly, also the self-retracting motion of graphene nanostacks can be explained if tiny friction forces, i.e., superlubric friction [3], are overcome by the adhesion-driven forces [50,51]. At the same time, the self-retracting motion of graphene stacks, which can reach speeds in excess of 10 m/s [74], allows one to identify further key criteria of structural lubricity such as, e.g., the locked state that is encountered once a commensurate configuration between stacked graphite layers has been established upon realignment [51].

Achieving ultra-low friction by exploiting structural lubricity is not only interesting from a fundamental scientific point of view, but also holds alluring perspectives for technology [3]. However, for a long time, technical exploitation was considered difficult due to the influence of interface contamination, which can effectively mediate the contact between incommensurate surfaces [66] and lead to the breakdown of superlubricity. This effect was held responsible, e.g., for the frictional behavior of Sb-nanoparticles on HOPG, where early UHV experiments only yielded a small fraction of particles sliding superlubrically [44].

Only recently, several systems have been discovered in which structural superlubricity can be observed under ambient conditions. For graphene stacks the self-retracting motion was found to remain a robust feature even under ambient conditions, which indicates that contamination cannot enter the interface [50,51]. Moreover, recent studies have highlighted that structural lubricity can also be observed for nanoparticle systems under ambient conditions. More specifically, a sublinear dependence of friction on the area was found both for gold [47] (Figure 2) and platinum particles [48] on HOPG. Ab initio simulations additionally elucidated how interface contamination is prevented by sufficiently large energy barriers and how absolute friction values are compatible with the atomic interactions upon application of the scaling laws. A recent study has pointed out that mechanical cleaning of interfaces can become possible by enhanced diffusion upon oscillating lateral movement within the contact [54]. Graphene interfaces, for which this effect was demonstrated experimentally, may thus be a good candidate to achieve structural lubricity in technological applications [75]. Indeed, ultra-low friction was recently observed for micro- and macroscale systems based on incommensurate sliding between graphene-covered spheres or "nanoscrolls" and substrates [76,77]. Also a decrease of friction shear stress with increasing number of layers has been observed for graphene over Si/SiO_2 in vacuum, nitrogen, and air [78]. In addition, the shear strength and the interface adhesion energy for graphene on Si/SiO_2 was proven to always exceed those of the graphene/Ni(111) interface [78]. The weakly lattice-mismatched graphite/hBN interface is also predicted to be promising for ultra-low-friction applications [79,80].

In most experiments described above the nanostructures can be viewed approximately as rigid bodies sliding on rigid sub-

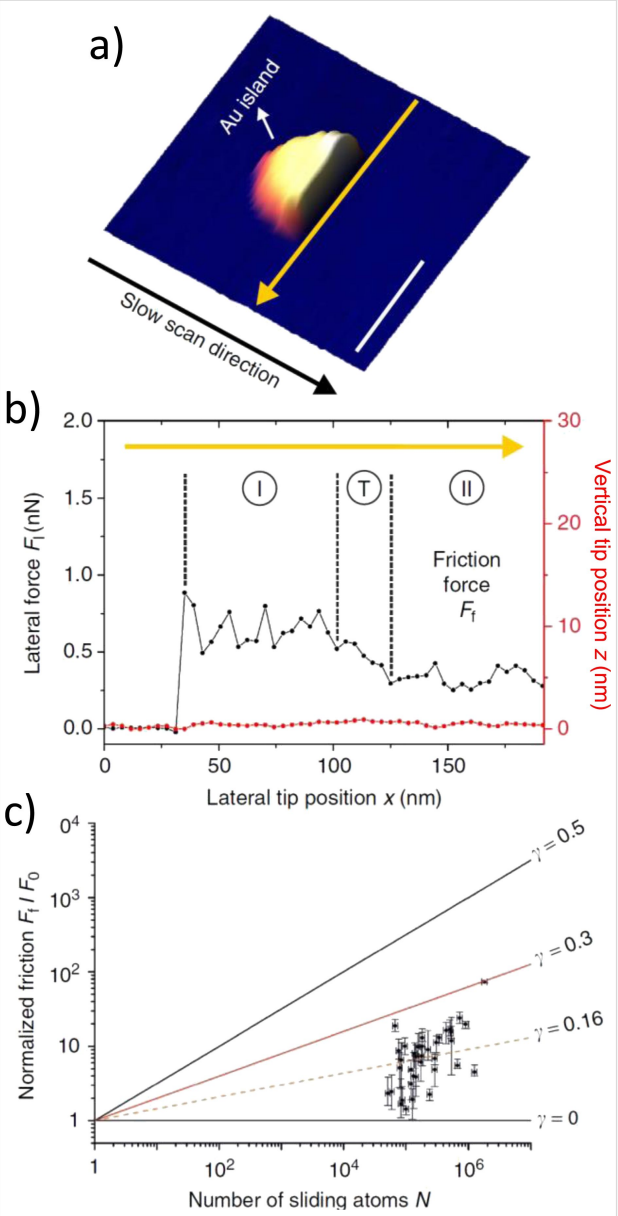

Figure 2: a) Example of a nanomanipulation during which half of a nanoparticle is scan-imaged, before the tip pushes it out of the image frame along the fast scan axis (yellow arrow). b) Friction trace observed during the manipulation. The AFM tip makes contact with the particle at $x \approx 30$ nm. The stable lateral force level observed in region II has then been used as a measure for the interfacial friction between particle and substrate. c) Dependence of friction on the contact area obtained for an ensemble of Au nanoparticles. The absolute values fall well into the range anticipated by application of scaling laws for the specific material combination. Reprinted with permission from [47], copyright 2016 Springer Nature.

strates. However, this fully rigid system is just an idealization. Deviations due to the compliant nature of actual nanostructures can have significant influence on friction and may ultimately lead to the breakdown of structural lubricity. In this context, the effect of surface compliance is conventionally described in terms of an Aubry-type transition [39,81], where the increased atomic interface corrugation induced by increased normal load eventually leads to an interface adaption between the slider and the substrate. Recently, such an Aubry transition was observed in idealized "model" systems consisting of chains of atomic ions [82] or of colloidal particles [83] driven across an optical lattice of varying depth (see section "Trapped optical systems: ions and colloids" for more details). However, in more conventional nanomanipulation experiments such a transition could not yet be actively induced, most probably due to insufficient normal forces [50,76,84].

Nonetheless, this does not mean that interface-relaxation effects play no role even for relatively rigid sliding nanostructures. A first indication stems from nanomanipulation experiments performed for Sb nanoparticles on HOPG, where distinct contact-ageing effects were demonstrated. By characterizing the ageing dynamics as a function of the temperature, of the sliding velocity, and of the hold time in nanoparticle stick–slip experiments [85,86], contact ageing was characterized as a thermally activated process [87]. Atomic-scale interface relaxations, either by single-atom displacements or by the formation and growth of commensurate patches at the interface [88], can serve as a likely explanation for the ageing effects for which the overall behavior of the nanoparticles still remains compatible with the concept of structural lubricity, especially for high sliding speeds, equivalent to short ageing times.

Ageing is understood to play an important role also in the transition from static friction to sliding, which can occur through precursor events. These phenomena were investigated in macroscopic-friction experiments [89,90] and simulated by means of several theoretical approaches [91-99].

Notice however that a different behavior was observed for Sb particles on MoS_2. Here, only small particles adhere to the sublinear superlubric scaling law, while larger particles show a linear scaling between friction and area, equivalent to a constant shear stress [100]. This can be explained by an enhanced interaction between the Sb atoms and the substrate, as was found by ab initio simulations [100]. According to MD simulations, a critical length scale exists for nanoparticles above which dislocations are formed at the interface and sliding is governed by the motion of these dislocations. This ultimately marks the transition from sublinear to linear scaling between friction and area [101] leading to a size-dependent breakdown of structural lubricity. As anticipated, the critical length scale depends sensitively on the ratio between the slider elasticity and the interaction forces with the substrate. Consequently, this transition was experimentally observed only for the MoS_2 substrate, while all particles sliding on HOPG remained in the regime of structural lubricity (Figure 3).

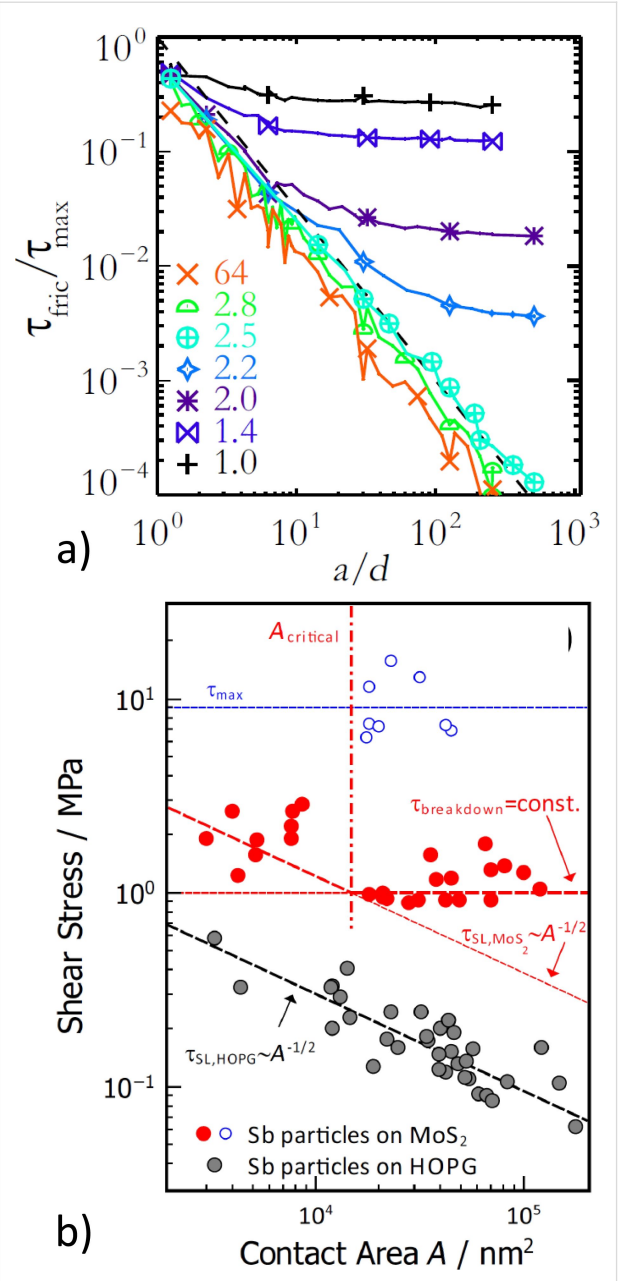

Figure 3: Dependence of nanoparticle shear stress on the contact area. a) Relative shear stress obtained from MD simulations as a function of the particle radii normalized by the lattice constant *d*. Calculations have been performed for different shear moduli *G* of the particles: low values of *G* result in a saturation of the shear stress. Reprinted with permission from [101], copyright 2016 American Physical Society. b) Experimental data obtained for Sb nanoparticles sliding on HOPG (gray) and MoS_2 (red). While a constant decrease of shear stress with particle size is observed for the HOPG substrate, a saturating shear stress is found on MoS_2. Reprinted with permission from [100], copyright 2017 American Chemical Society.

The important role of particle size was further highlighted in theory works [102,103]. Here it was found that besides the size and the shape of the contact area, also the absolute thickness of particles can be of importance. This was demonstrated by MD simulations for gold clusters on HOPG, where a significant reduction of static friction was found by simply increasing the cluster thickness. As a result, the nanostructure becomes elastically stiffer, which goes along with a reduced tendency to become pinned to the surface [104]. Due to the thickness effect, flat 2D islands can exhibit a significantly different tribologic behavior compared to thick 3D particles. Following this perspective, the slider dimensionality can even be further reduced. This was done in [105] in which the sliding of a 1D chain on top of a periodic surface potential was simulated as an edge-driven Frenkel–Kontorova model. Similar to [101], a critical length scale was identified, above which superlubricity breaks down, due to local commensuration induced by overall interface relaxations. On the other hand, for heterogeneous contacts formed between hexagonal boron nitride clusters and graphene, a recent study has pointed out how kinetic friction can drastically decrease when the slider enters a regime of soliton-supported smooth sliding beyond a certain contact area [79].

Confined systems and lubrication

Several research groups have been investigating the frictional properties of nanoscale systems confined between two sliding blocks. This intendedly vague indication of “systems” includes liquid lubricants in the boundary-lubrication regime, but also solid lubricants such as graphite or graphene or MoS_2 flakes.

Focusing initially on liquid lubrication, research has investigated the possibility of controlling friction in unconventional fluids, in particular the room-temperature ionic liquids (RTILs). The RTIL microscopic structuring [106,107], and in particular their layering near surfaces [108-113] induced by the interplay of the surface-induced confinement and the structural correlations of charged and hydrophobic molecular sections, has potential implications for the nanoscale lubrication properties of the resulting interfaces. These properties can be affected not only by the interlocking of the RTIL molecular structure with the surface corrugation, but also by the surface charge, which is tunable (within reason) by the application of electric fields, with the effect of modifying the ordering of the boundary layers. Sliding in a confined geometry has been investigated with the surface-force balance and an impressive evidence of layering effects on friction was demonstrated [114]. RTILs are being also investigated as additives in liquid lubrication [115].

Modeling has investigated the role of the molecular shape of the ions [116,117] and the layer-by-layer squeeze-out phenomenon under load [118]. Simulations [119] agree with experiment that friction depends sensitively on the number or residual confined layers in the interface. At a given number of layers, friction shows a relatively modest increase with load. A systematic in-

vestigation of friction as a function of load and charging [120] concluded that friction increases when the applied surface potential changes from negative values to positive values, and that, for negative surface potential, friction depends on the alkyl-chain length of the cation of the RTIL. Assuming well-ordered anchored molecular layers, the effects of molecular dipolar charges on friction were investigated in a model [121], predicting a friction peak when a suitable resonance condition is reached as a function of an applied electric field. Different anions play a complex role depending on the surface potential, and related to the steric constraints they pose in relation to their partner cations. Steric effects in boundary lubrications were also investigated in the context of confined molecular fluids that were not electrically charged [122-125].

Progress was also reported regarding the friction involved in layered crystalline lubricants. By MD simulations and theoretical arguments two (even commensurate) crystalline surfaces lubricated by mobile, rotating graphene flakes were proven to exhibit stable superlubric sliding when they are dressed by randomly-oriented pinned graphene patches: The resulting effectively incommensurate states were shown to be compatible with thermal fluctuations [126], going beyond previous conclusions based on a simpler model [127]. Simulations also investigated the role of graphene as lubricant and anti-wear agent [128,129]. An extremely low friction was demonstrated as long as load remains weak. At larger load graphene breaks down, the superlubric behavior is lost, and the ordinarily regime of large friction and rapid wear is recovered.

Also in the context of simulations, a special "quantized" sliding-velocity regime [130-134] was identified and characterized by the confined solid lubricant advancing at a fixed fraction of the sliding speed. This quantized velocity was understood as due to the moiré pattern of solitons generated by the lattice mismatch between the lubricant and one of the sliders being dragged forward by the other slider [135,136]. This phenomenon, besides being identified in the simple ideal 1D geometry [137-140] was also demonstrated in 2D [141,142] and 3D [143] realistic numerical simulations, but it still awaits experimental confirmation.

Trapped optical systems: ions and colloids

One of the main challenges and difficulties in unraveling the fundamental frictional mechanisms, and their connection to the physical response of the system at a larger scale, as recorded, e.g., by a suitable experimental setup, relates to the intimate buried nature of the sliding interface, where many hidden degrees of freedom concur collectively in giving rise to the complex, often nonlinear, tribologic process [7,144,145]. Moreover, the severity of the task is sometimes affected by the practical lack of well-characterized mating surfaces and well-defined operative conditions. All these aspects, together with the impossibility of tuning physical properties of real materials, make testing and comparison with theoretical predictions a mission that is far from trivial. In this view, the field of atomic-scale friction, and nanotribology in general, can now take advantage of the possibilities offered by handling nano/micro-sized particles with optically generated potentials, disclosing the opportunity both to directly visualize the detailed intimate mechanisms at play and to tune the parameters across relatively broad ranges in well-controlled setups [146,147]. While the framework of the Prandtl–Tomlinson and the Frenkel–Kontorova models [145] provides a solid theoretical understanding for the pinning/depinning transition, a systematic experimental investigation of how the relevant physical parameters (such as lattice mismatch, substrate-interaction strength, adsorbate rigidity, driving force, and temperature) influence the frictional response, e.g., from a statically pinned state to an intermittent stick–slip dynamics to a sliding regime (possibly characterized by superlubric motion) has not been explicitly carried out.

Recently, thanks to state-of-the-art experimental setups [82,148-150], artificial tribology emulators have taken friction experiments to the single-particle limit. Inspired by earlier theoretical suggestions [151-154], a laser-cooled Coulomb crystal of ions, set into motion across a periodic optical lattice under the action of an external electric field, demonstrates the feasibility to control friction. By changing the structural mismatch between ion and substrate, as predicted by many-particle models, highly dissipative stick–slip can be tuned to a nearly frictionless dynamical state already at the level of just a few interacting atoms [148], revealing intriguing potential implications even into the quantum many-body regime [155].

By tuning the optical substrate corrugation from low to high, or effectively change the mutual interaction strength within a setup of two deformable chains, the spatially resolved position of the trapped cold ions allows one to observe several peculiar features of the celebrated Aubry structural phase transition in frustrated systems [39], from a free-sliding arrangement of the chain to a pinned fractal-like atomic configuration [82,150]. Compared to standard experimental tribology techniques with inherent limitations of the dynamic range, time resolution, and control at the single-atom level, another important achievement of these ion-crystal systems in an optical lattice consists in the capability to span essentially five orders of magnitude in sliding speed. This is achieved while maintaining a full control of dissipation and temperature, thus emulating perfectly the Prandtl–Tomlinson model [149]. Along this research line, characteristic dissipation frictional peaks at specific values of the

slider velocity, recently investigated within a 1D theoretical approach [156,157], could be potentially observed in experiments here.

Exploiting the versatility of trapped optical systems, new light is cast on elemental frictional processes in tribologically meaningful 2D extended contact geometries by charged colloidal systems driven across laser-interference-generated corrugation profiles the spatial structure and intensity of which can be tuned with remarkable freedom. While AFM, surface-force apparatus (SFA), and quartz-crystal microbalance (QCM) experiments measure the system frictional response in terms of crucial, but averaged, physical quantities, colloidal friction provides an unprecedented real-time insight into the dynamical mechanisms at play in 2D contacts, excitingly probing what each mobile particle in the sliding layer is doing instant after instant at the interface.

In short, charged polystyrene spheres in aqueous solution repel each other, forming, under confinement, a 2D hexagonal crystal [158-163]. This crystal is driven across an either commensurate or incommensurate laser-generated hexagonal corrugation potential profile. Driving results in the advancement of mobile localized superstructures (namely solitons or kinks and antisolitons or antikinks) [164]. Those density modulations in periodic overlayers that are out of registry with their substrates (Figure 4) play a crucial role in tribology. Experiments [164] agree with theory and numerical simulations [165-168] in showing the radical change of the static-friction threshold from the highly pinned regime of the lattice-matched colloidal layer to a practically superlubric frictional sliding observed in the case of overlayer/substrate lattice mismatch. Nucleation dynamics characterizes the depinning mechanism of a stiff commensurate colloidal monolayer [167]. In contrast, if the interface is characterized by a lattice mismatch, the presence/absence of static friction depends on the system parameters. For small substrate corrugation the network of solitons supports a free-sliding superlubric interface; with increasing corrugation the layer switches to a statically pinned configuration after crossing a well-defined, Aubry-like, dynamical and structural phase transition, with the static friction force increasing from zero to finite [146,164,168,169]. The critical corrugation for this transition depends significantly on the relative angular orientation of colloid and substrate. A slightly misaligned orientation is energetically favored, as discussed in a recent work [170]. Indeed, the competition between the superlubric orientationally twisted phase and the pinned phase consisting of an array of aligned islands leads to a first-order transition [171]. Experiments confirm this theory, showing the first-order transition with a coexistence region as a function of the corrugation-potential amplitude [83].

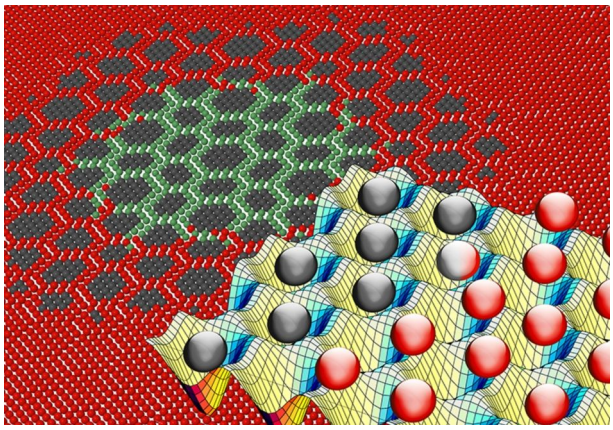

Figure 4: Front perspective: a snapshot of a MD-simulated frictional interface between a colloidal monolayer and an optical periodic substrate potential representing the surface corrugation. Background: the overlayer/substrate lattice mismatch (an experimentally tunable parameter) generates a network of localized solitonic structures (highlighted by the particle colors), the mobility of which rules the tribological response of the monolayer.

By flashing the corrugation amplitude periodically in time, it is possible to investigate synchronization phenomena including harmonic and even subharmonic Shapiro steps [172-174]. By extending this method to an optical substrate with quasiperiodic as opposed to periodic hexagonal symmetry [175], the colloidal approach can address questions such as the onset of static friction with the associate Aubry-like transition, and even the possible occurrence of directional locking in overlayers driven on quasicrystalline landscapes [176].

Controlling friction and wear on the nanometer scale

Molecular layers play an important role in the reduction of friction and wear at the macro scale. The addition of boundary lubricants is necessary to prevent damaging metallic adhesive forces between the machine parts in relative motion (cold welding). Unfortunately, under high load these molecular layers are often worn after relatively short time. Therefore, the typical engineering response is to avoid the boundary-lubrication regime as well as possible by the usage of thicker oil layers in the elasto-hydrodynamic regime. Although the elasto-hydrodynamic regime is the basis of most moving machinery parts, it has the disadvantages of a relatively large viscous drag and the risk of a transition to the boundary regime under certain, sometimes uncontrolled conditions. Just recently, a few systems based on layered materials, such as graphene or molybdenum chalcogenides have shown low-friction properties for extended periods of time. Early examples of superlubricity at the nano- and microscale and even at the macroscale were observed [44,77,177,178].

In addition to the role of friction in energy conservation, the control and reduction of adhesion has a great technological impact. For example, the treatment of surfaces with molecular layers can have beneficial effects as it is well known from PTFE-coated surfaces. There is a need of alternative coatings for modern touch screens to prevent fingerprints and other contaminants. Surfaces for medical applications are very demanding to keep the contamination with multi-resistant bacteria at the lowest possible levels.

The question to be addressed here is: Is it possible to influence friction and wear by mechanical, optical, electrical or magnetic stimuli? For instance, previous experiments on the nanometer scale have shown that electrical fields can be used to change frictional properties by orders of magnitude [179]. Molecular layers can be studied relatively to their frictional, adhesive and elastic properties and how can these mechanical properties be controlled by external means. In the future, we may be able to synthesize smart lubricants that can change their lubrication properties on demand. By irradiation with the appropriate wavelength these novel materials might change from a high-friction to a low-friction state. Analogous concepts can be envisaged for friction anisotropy [180] and for adhesion.

Manipulation of graphene nanoribbons on gold

A number of nano-mechanics experiments were performed with graphene nanoribbons (GNRs) manipulated by the tip of a force microscope [58]. The structure of the GNR was determined by means of high-resolution force microscopy (CO-terminated tip), with a method developed by Gross and co-workers [181,182]. The metallic tip was approached to the GNR until a bond was formed to the ribbon, and the ribbon was subsequently pulled along the Au(111) surface. Lateral force variations were determined by a combination of experiments and theoretical calculations (Figure 5). The GNR was found to move under quite small lateral forces (10–100 pN), and these forces do not increase systematically with the length of the GNR. This is indeed a transparent case of structural superlubricity, where the incommensurate nature of the contact leads to small lateral forces with a minimum of energy dissipation. In this case, the low friction is depending on the high elastic modulus of graphene, which ensures that the graphene lattice remains nearly unaltered relative to the gold lattice. Therefore, an incommensurate contact is maintained during movement along the gold surface. An important prerequisite of these experiments is to operate the instrument under ultrahigh-vacuum conditions, where contaminants can be avoided. In the case of Kawai et al. [58], the GNRs were

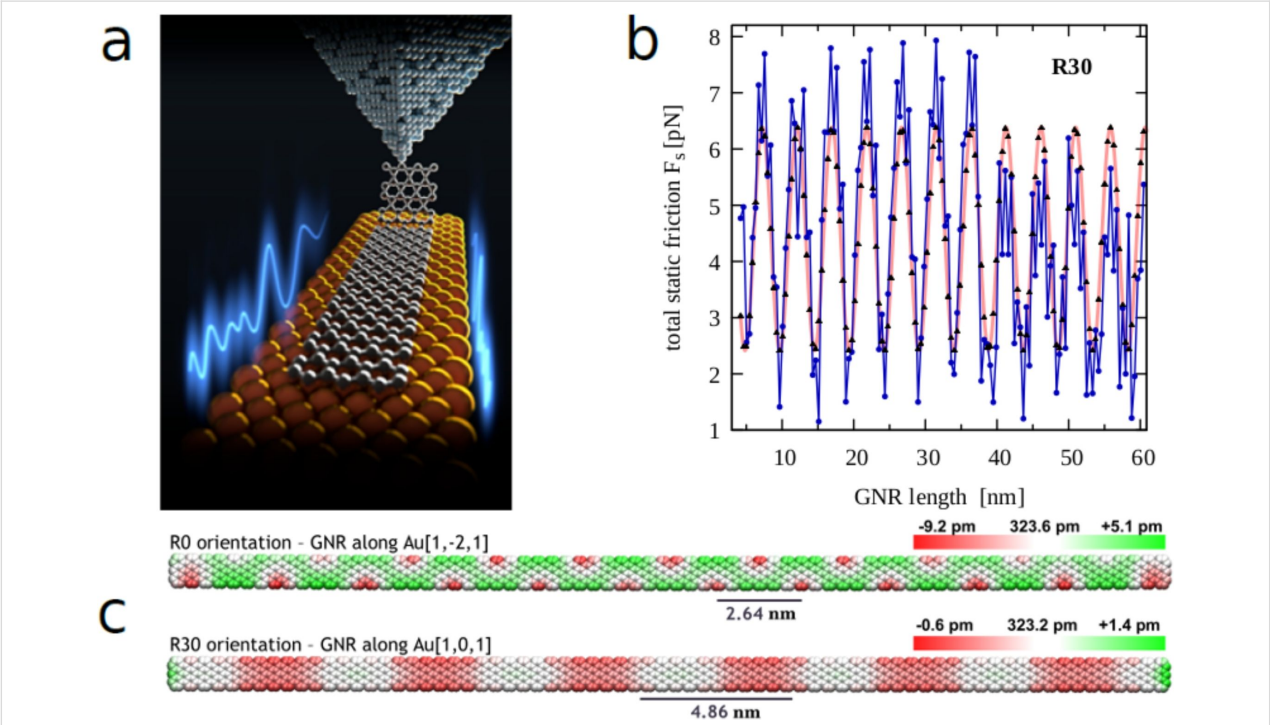

Figure 5: a) A graphene nanoribbon manipulated along a Au(111) surface. A probing tip lifts the GNR vertically, detaches it partially, and subsequently moves it along the horizontal direction. A simultaneous measurement of the lateral forces shows that the incommensurability of the GNR–Au contact grants superlubric sliding [58]. b) The simulated static force as function of the GNR length [71]. This force is not growing with the length, but is oscillating with the periodicity of the moiré pattern. This mild dependence of friction on the contact size is characteristic of superlubric conditions. The length and orientation of a GNR are under direct experimental control: Experiments are also consistent with friction not systematically increasing with the GNR length. c) The moiré pattern of GNR in the orientation [1−21] (R0) and [−101] (R30) over the Au(111) surface. Experimentally, R30 is preferred and exhibits the smallest lateral forces. Panels **b)** and **c)** are adapted from [71].

grown by on-surface chemistry through evaporating a precursor of 10,10'-dibromo-9,9'-bianthryl monomers. By suitable annealing, dehalogenation as well as cyclodehydrogenation can be achieved, which leads to clean, defect-free GNRs. Therefore, ideal contacts, free of contaminants, can be grown on the gold surface. The GNRs are observed to move preferentially in the [−101] direction, where the moiré pattern forming with Au(111) has a relatively long period. The residual lateral forces are mostly related to uncompensated edge sections of the GNR [71]. As a result, it is found that, rather than growing with the GNR length, the lateral force is oscillating with the same periodicity as the moiré pattern (Figure 5b,c). If one starts to perform similar experiments under ambient pressure, it appears probable that a contamination layer influences the friction processes. This "third body" consists of molecules or atoms that easily can move laterally and will lock into position, thus forming an effectively commensurate contact, with increased friction. It is obvious that this contamination effect is one of the major limitations for large-scale applications of structural superlubricity. However, Cihan et al. achieved structural superlubricity of gold islands (4000–130,000 nm^2) on graphite even under ambient conditions [47], as discussed in Section "Controlled nanomovements" (see Figure 2).

Pawlak et al. investigated the sliding of a single molecule on a Cu(111) surface in order to shed light on the interplay between intra-molecular mechanics and friction [183]. The experiment was realized by attaching a single porphyrin molecule functionalized by two *meso*-(3,5-dicyanophenyl) and two *meso*-(3,5-di-*tert*-butylphenyl) peripheral rings to the AFM apex, which was then dragged over the surface, as sketched in Figure 6a. Despite the complex molecular structure attached to the tip, atomic-scale patterns and sawtooth modulations were systematically obtained in the force channel, as shown in Figure 6b and Figure 6c. This indicates the formation of a well-defined tip–sample junction during the experiment. According to the authors, the tendency of the cyano end groups to form coordination bonds with Cu atoms of both the tip and the surface plays an important role in the formation of the single-point contact with the copper surface. Of the many internal degrees of freedom of a porphyrin molecule, the σ-bond connecting the porphyrin leg in contact to the surface to the macrocycle was postulated to be the dominant molecular spring dictating the friction response. Using the Prandtl–Tomlinson model parameterized using density-functional theory calculations including the internal degrees of freedom of the molecule and its interactions with the underlying surface, the friction patterns were numerically reproduced as a result of the bond-length and bond-angle variations of the porphyrin leg while sliding.

Controlling friction and wear by the application of mechanical oscillations and electrostatic forces

One way to control friction is to apply an AC voltage between the probing tip and surface [179]. In this experiment, an oscilla-

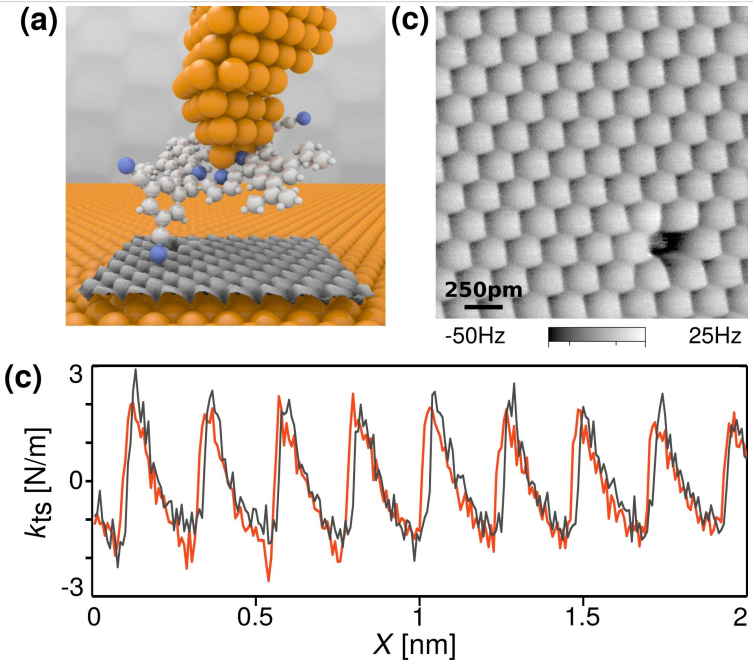

Figure 6: Single-molecule tribology. a) Schematic drawing of the experiment: A single porphyrin molecule is attached to the AFM apex and dragged over a Cu(111) surface. b) By recording the mechanical response of the sliding molecule, the AFM scan maps the atomic lattice of Cu(111). c) Tip–sample stiffness trace extracted from the image showing a stick–slip modulation. Reprinted with permission from [183], copyright 2016 American Chemical Society.

tion frequency in the region of the contact resonance was applied. Under these conditions, moderate voltages of a few volts are sufficient to create variations of the normal force that are sufficient to move the contact zone without measurable sticking force. Essentially, the friction control is the result of a modulation of the effective lateral energy barrier height by changing the distance between the contacting bodies. Since the resonance frequency of small nanometer-sized contacts is in the range from megahertz to gigahertz, the contact may move fast enough to cross the barrier during the short time when its height is negligible. Experimentally, it was found that time periods of a few microseconds are long enough to observe sliding without stick–slip. Alternative ways to oscillate the contact are mechanical oscillations of the AFM tip, generated either with one of the flexural modes or even with torsional modes [184]. Theoretical works have shown that lateral oscillations can lead to increased diffusion [185,186].

Another phenomenon involving oscillations is related to the interplay between the washboard frequency and the actuated oscillating frequency. In this context Lantz et al. made an interesting observation: Through the application of a small electrostatic force modulation to a micromechanical device (Millipede device), they achieved the sliding of ultra-sharp contacts for distances as long as several hundreds of meters, without any measurable wear [187]. By comparison, the lack of actuation leads to conditions under which significant atomic-scale wear was observed, leading to blunted tip radii after such long sliding distances. Therefore, the suppression of the sticking phase by the application of actuation seems also favorable for the operation of micromechanical devices in which wear is a critical issue.

At separations of several nanometers one talks about the phenomenon of non-contact friction. At first sight, this type of dissipation appears rather academic. However, the fundamental damping mechanisms of friction, which relate the energy released after instabilities of atomic stick–slip to thermal vibrations, are found to be intimately related to non-contact friction. Energy can get dissipated into phononic and/or electronic channels. In a number of examples, it was found that non-contact friction can be tuned over orders of magnitudes by changing the applied voltage and/or the distance [188-192].

An example of particular interest is that of charge-density waves (CDW) where a superstructure is formed by a charge redistribution. Langer et al. have observed that the damping coefficient can be drastically changed on $NbSe_2$, when the probing tip is locally disturbing the charge density waves [188] (Figure 7). At a certain threshold, the CDW shows a phase slip, which then leads to dissipation.

Another example where non-contact friction can be influenced by external parameters are the measurements of superconduc-

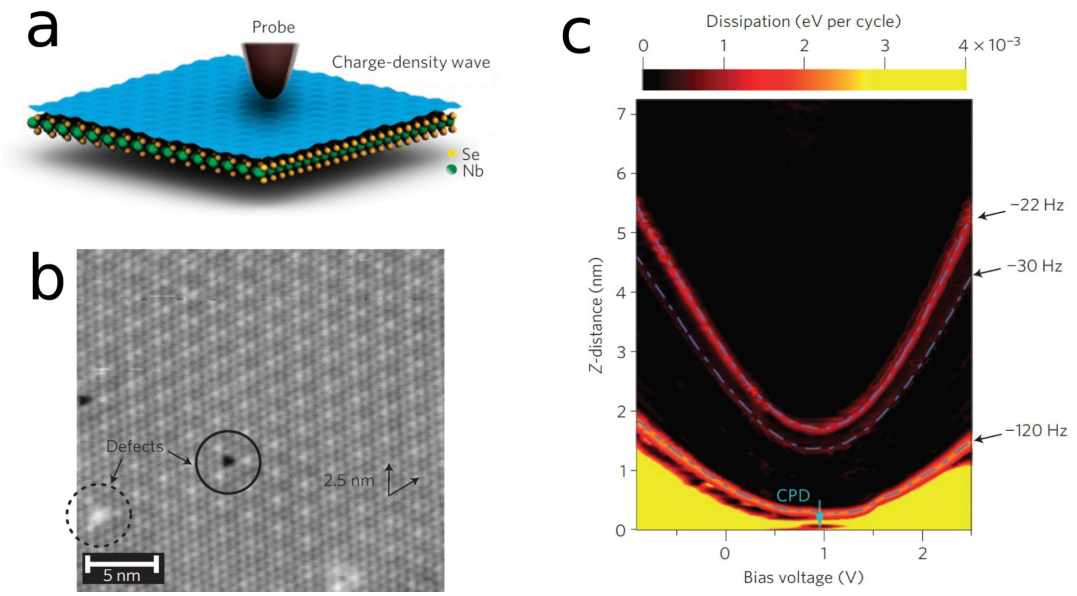

Figure 7: Non-contact friction experiments of $NbSe_2$. At certain voltages and distances, one finds dramatically increased non-contact friction. This is related to the local disturbance of the charge-density wave, which leads to phase slips. a) Schematics of the probing tip above the charge-density wave system. b) STM image of the $NbSe_2$-surface revealing the CDW. c) Non-contact friction dissipation as a function of distance and voltage. Reprinted with permission from [188], copyright 2013 Springer Nature.

tors across the critical temperature [189]. In this case, the electronic friction is reduced below the critical temperature T_c, because the electrons are bound in Cooper pairs, thus suppressing the electronic-friction channel. Thus, the residual non-contact dissipation is dominated by phononic contributions. Electronic friction is found to be proportional to $(V - V_{cpd})^2$, where V is the tip–substrate bias voltage and V_{cpd} is the contact potential difference, whereas the phononic contribution is proportional to $(V - V_{cpd})^4$ [193]. Park et al. observed the influence of electronic friction on semiconductive surfaces in contact mode and found differences between p- and n-doped areas [190].

A nanocar race

One of the most impressive ways to demonstrate the control of motion is to manipulate single molecules by the action of a probing tip. The first molecular race was held in Toulouse in April 2017. The task was to move single molecules by the action of a probing tip along a track of 100 nm on a Au(111) surface (Figure 8). The method to move the molecules is based on inelastic tunneling through which the electrons induce molecular vibrations, which then lead to increased diffusion. Depending on the polarity of the applied bias voltage and the effective charge of the molecule, the molecule motion induced by the tip is "field-assisted", which means that the molecule will either be attracted (negative bias voltage in the case of the molecule in Figure 8) or repelled (positive bias voltage) from the tip position. Typical sliding distances per manipulation step are less than a 0.6–0.8 nm in the attractive mode and up to 2–3 nm in the repulsive mode. The pilots from the University of Basel, Rémy Pawlak and Tobias Meier, were able to efficiently steer a single molecule along the 100 nm racetrack over a time of five hours, thus achieving an average speed of 20 nm/h. The Swiss team ranked first at this international competition, but most importantly some fundamental knowledge about the motion of single molecules on surfaces was gained, which is relevant for nanotribology [59,194]. For successfully "driving" a nanocar, a detailed understanding of the energetics of the molecule on different surface locations, which are closely related to atomic friction processes, is required. In particular, it turned out that molecules interact more strongly on elbow sites of the Au(111) herringbone reconstruction compared to valley sites. This interaction is so strong, that the molecules cannot be moved away from this region anymore. During the race, these elbow sites had to be avoided. This high degree of control is useful for future nanotechnology fabrication processes in which single atoms or molecules have to be driven to specific locations to assemble more complex nanodevices.

Prospects in tuning friction with photo-assisted reactions

The influence of light exposure on properties such as friction and adhesion is rarely explored. For instance, it is known that certain surfaces, such as titanium oxide, exhibit photocatalytic properties and might become water- and dirt-repellent under UV-light exposure. In solution, photoinduced conformational changes of molecules are also well-known photochromic reactions. However, little is known whether such phenomena operated on the molecular level are reversible at surfaces. By controlling the properties of a molecule adsorbed on a surface by light exposure, one could imagine to control friction and adhesion properties. High-resolution force microscopy has achieved a high degree of fidelity. It is possible to resolve the internal structure of molecules, including their bond order [181,182]. In preliminary experiments [195], it was possible to observe the conformational changes of single adsorbed molecules due to the presence of single Fe atoms acting as catalytic

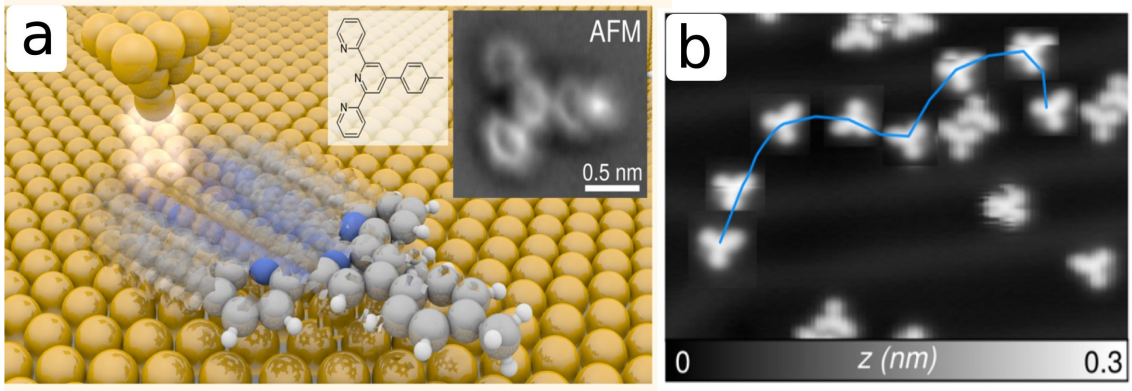

Figure 8: The "Swiss Nanodragster" (SND), a 4'-(*p*-tolyl)-2,2':6',2"-terpyridine molecule, was moved across an Au(111) surface on the occasion of the first nanocar race held in Toulouse in April 2017. The required distance of 100 nm of controlled motion was covered through the application of voltage pulses. a) Schematics of the manipulation of the molecule. Left inset: Structure of the SND molecule. Right inset: High-resolution AFM image of the SND molecule. b) A sequence of manipulation steps, as observed by STM imaging between the manipulation steps. Reprinted with permission from [59], copyright 2017 American Chemical Society.

centers (Figure 9). Future experiments in this line, for example using other photo-chromic groups integrated in molecules such as azobenzene or spiropyran groups, should enable us to modify conformation, structure and chemical properties of the molecular layers on surfaces under photon irradiation. High-resolution force microscopy will provide detailed information about these conformation changes, and will allow us to understand this process and the task of the related functional molecular groups. Then, the frictional properties of these films in the different conformations (e.g., trans and cis) will be intensively studied to understand how this conformation switching affects energy dissipation.

Multiscale bridging

The current standard phenomenological theories of frictional interfaces, which are essential for modeling macroscopic frictional dynamics, are not yet fully linked to the atomistic processes and interfacial geometries at the atomistic scales. Bridging over the widely separated time and length scales by establishing quantitative connections between small-scale processes and macroscopically observed phenomena is a major challenge of current tribology in particular, and, more in general, of materials modeling [196-200].

A first line of ongoing research efforts focuses on enriching the descriptions of mesoscopic sliding friction beyond the single-asperity level. In relevant multi-contact systems, both single-asperity dynamics and collective interaction mechanisms should play a crucial role. In [201], the authors discuss a minimal model of slip instabilities ("earthquakes"), which reproduces two main empirical seismological laws, the Gutenberg–Richter law [202,203] and the Omori aftershock law [204]. This approach, inspired by discrete spring-block models [205-207], demonstrates that the simultaneous incorporation of two minimal ingredients, namely the ageing of contacts at the sliding interface and the elasticity of the sliding plates, are needed to account for both laws within the same frictional model. The authors of [201] suggested that insight gained from spring-block frictional models could offer explanations for statistical properties of macroscopic frictional systems, and extended it to investigate the load dependence of friction for viscoelastic materials [208].

A second aspect of this effort is investigating and controlling the mechanisms of energy dissipation due to wear and plastic deformations, and in particular in making contact between atomistic studies of friction with macroscopic friction and wear tests. A nontrivial connection between the macroscopic and microscopic scales in frictional systems has been obtained by means of MD simulations of the wear process of a rough Fe surface by multiple hard abrasive particles [209]. By quantifying the nanoscopic abrasion depth as a function of time, Barwell's macroscopic wear law [210] was shown to be applicable even at the atomic scale. It has been further shown that in this multi-asperity system the term describing the friction force as a function of the actual nanoscopic contact area (the so-called Bowden–Tabor term), predicts the kinetic friction even in a condition involving wear. As a result, the Derjaguin–Amontons–Coulomb [211,212] friction law is recovered following the linear dependence of the contact area on the applied load.

A third type of approach to multiple spatial length scales focuses on a statistical analysis of the complex geometry of the contact between two rough surfaces, extending over several decades in length scales, understanding its effects on friction and on the flow of a fluid between the surfaces. For example, in [213] the authors study the friction force and the real contact area of a viscoelastic solid (rubber) in sliding contact with hard, randomly rough substrates. These surfaces can be seen as self-affine fractals involving roughness over many orders of magnitude in length. The numerically exact calculations performed in this work show that the friction coefficient and the contact area are well described by an analytic theory previously developed

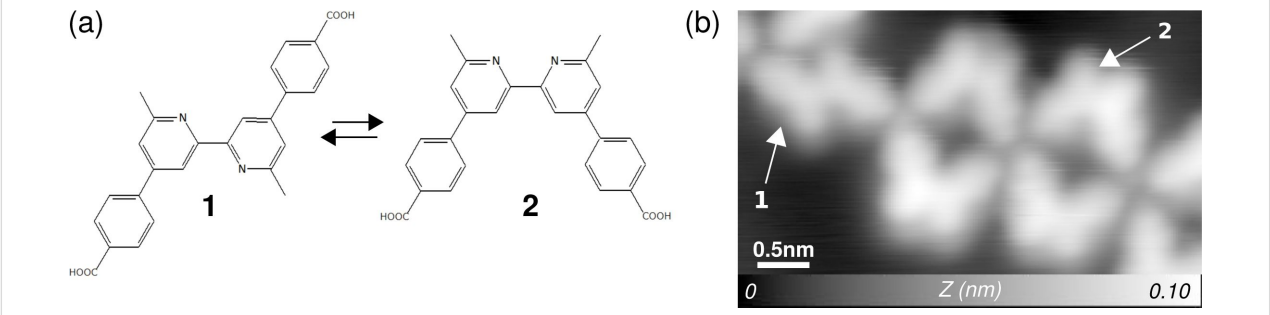

Figure 9: Example of a change of conformation potentially triggered at surfaces. a) Trans (**1**) and cis (**2**) isomers. By depositing and/or annealing, the molecule can be turned from trans to cis and vice versa. b) After the deposition of Fe atoms, the molecules can be switched from trans into cis conformation.

by the authors, in particular when the contact pressure is large. This approach demonstrates the power of scale-bridging and multi-scale approaches to friction in a context even extending beyond standard tribology [214,215]. Alternative approaches based on finite-element methods are also providing promising results for rubber–asphalt friction [216-218].

Frictional interfaces separating two dissimilar materials exhibit a well-known coupling of variations of interfacial slip and normal stress. This coupling bears major implications on the stability, failure mechanisms, and directionality for the rupture of these interfaces. However, interfaces separating identical materials are traditionally not assumed to feature such a coupling, due to symmetry considerations. In [219], the authors combined theory and experiment in order to show that even interfaces separating bodies composed of macroscopically identical materials but lacking geometrical reflection symmetry generally feature this kind of coupling as well. This new framework is applied to two basic problems: Firstly, the new effect was shown to account for a distinct, and hitherto unexplained, experimentally observed weakening of the frictional cracks induced by the normal stress; secondly, the new effect was shown to be able to destabilize the otherwise stable frictional sliding under homogeneous conditions for velocity-strengthening interfaces. The resulting framework could find a wide range of applications in tribology.

Further progress in multiscale coupling may be achieved by targeted investigations of the anisotropic frictional behavior of nanowires and/or nanotubes [56,58,71,72,220]. These objects with a micro/mesoscale in one dimension and a nanoscale in others may play a role as possible candidates for bridging tribological properties at different length scales. Also mesoscale models for boundary lubrication [221] may provide hints about how the microscale and the mesoscale may connect. Finally, direct comparison of microfriction and macrofriction measurements conducted with the same materials [222] may also provide hints to how the sliding regimes on microscale and macroscale can be brought into the same picture.

Conclusion

From the sliding of an atomically sharp AFM tip, over squeaking door hinges, up in scale to the extended and intermittent evolution of a geophysical fault, friction finds its ubiquitous place in nature – spanning vastly different scales of time, size, and energy, in widely scattered areas of science and technology. Besides many intriguing fundamental aspects of out-of-equilibrium dissipative phenomena, the ability to specify, by design, the desired level of friction in a sliding apparatus or even to make it vary at will, from small to large, surely has far-reaching practical and technological implications, with long-term essential effects on the protection of the environment and on sustainable development, and conservation of energy and materials. In particular, a reduction of friction and wear would have a huge impact on energy consumption and, consequently, CO_2 emission. Estimates show that 30% of the fuel energy in automobiles is consumed due to friction losses. By the use of new technologies, a friction reduction of up to 60% seems feasible, which would lead to annual economic savings of 576,000 million euros, fuel saving of 385,000 million liters and a CO_2 reduction of 960 million tons [223].

The fundamental investigation of friction at the atomic scale yields groundbreaking insight for the development of novel working principles and architectures, which will have an impact on the fabrication of microdevices. Progress in understanding, and thus controlling friction, is necessary for industrial applications of emerging nanotechnologies and will later on become enabling for a number of the important challenges that our societies face, in sectors including energy and transportation as mentioned above, but also health.

The present work attempts to cover in some detail the tremendous developments that the field of friction investigation from the atomic scale up to the macroscale has seen in the last few years. Surely the picture provided here is incomplete, because even significant theoretical [224-230] and experimental [231-241] advancements, in particular progress in engineering efforts on the macroscale, are not covered.

In some detail, our overview over the friction of sliding nanoobjects highlights a number of important trends in nanotribology. This research is, first of all, driven by the curiosity to understand the fundamental mechanisms governing friction of extended nanocontacts. By applying either experimental or theoretical nanomanipulation approaches, several concurring effects are analyzed systematically. Especially the intriguing concept of structural superlubricity has spurred considerable interest. Structural superlubricity [2,3] was observed repeatedly under well-defined conditions of ultrahigh vacuum, where contamination effects are excluded. In structural superlubric contacts, frictional forces are kept under control by compensations associated to poorly compliant perfectly crystalline incommensurate surfaces, giving origin to moiré (solitonic) patterns. Such patterns were both calculated and observed, and correlated to the variations of lateral forces, especially for the manipulations of nanoclusters over surfaces, where friction is dominated precisely by the marginal uncompensated sections of the solitonic pattern, which are present near the cluster edges. This determines the fundamental and general characteristics of superlubricity: the weak scaling with contact size, and the nontrivial influence of contact shape and orientation. Recent

research focuses on the breakdown mechanisms of superlubricity. Most prominently, two different classes of effects are distinguished and investigated, namely the role played by interface contaminations [47], and that of interface relaxation, for different system dimensions and/or relative interaction strengths. In future studies, both breakdown mechanisms require further evaluation, especially by experiments. Initial steps toward technological applications of sliding nanostructures in the superlubric regime have already been taken. Currently, the most promising interface involves graphene sheets, which seem to be fairly stable against both interface contamination and intrinsic breakdown mechanisms.

Beyond superlubricity, attempts to control friction with external parameters such as normal load and electric fields, were found to affect profoundly and in an intrinsically nonlinear fashion the nanotribological properties of interfaces. The biggest open challenge now is to scale up these concepts to make them work at the level of real-life macroscopic sliding interfaces. The first step in this scale-up will most likely involve micro-electromechanical systems (MEMS).

Acknowledgements

We wish to acknowledge valuable discussions, collaborations and support by E. Bouchbinder, O.M. Braun, A. Fasolino, A. Foster, E. Gnecco, R. Guerra, O. Noel, S. Perkin, I.M. Sivebæk, E. Tosatti, and M. Urbakh. Collaboration was fostered by the COST Action MP1303, which is therefore gratefully acknowledged. AV and NM acknowledge support from the ERC Grant 320796 MODPHYSFRICT. EM acknowledges financial support from the Swiss Nanoscience Institute and the Swiss National Science foundation. SK acknowledges financial support by Japan Society for the Promotion of Science (JSPS) KAKENHI Grant Number 15K21765, and by the Japan Science and Technology Agency (JST) 'Precursory Research for Embryonic Science and Technology (PRESTO)' for a project of 'Molecular technology and creation of new functions'.

ORCID® iDs

Ernst Meyer - https://orcid.org/0000-0001-6385-3412
Thilo Glatzel - https://orcid.org/0000-0002-3533-4217
Nicola Manini - https://orcid.org/0000-0003-4374-6374

References

1. Binnig, G.; Quate, C. F.; Gerber, C. *Phys. Rev. Lett.* **1986,** *56,* 930–933. doi:10.1103/physrevlett.56.930
2. Berman, D.; Erdemir, A.; Sumant, A. V. *ACS Nano* **2018,** *12,* 2122–2137. doi:10.1021/acsnano.7b09046
3. Martin, J. M.; Erdemir, A. *Phys. Today* **2018,** *71,* 40–46. doi:10.1063/pt.3.3897
4. Persson, B. N. J. *Sliding Friction: Physical Principles and Applications;* Springer: Berlin, Germany, 1998. doi:10.1007/978-3-662-04283-0
5. Mate, C. M. *Tribology on the Small Scale: A Bottom Up Approach to Friction, Lubrication, and Wear;* Oxford University Press: Oxford, United Kingdom, 2008. doi:10.1093/acprof:oso/9780198526780.001.0001
6. Krim, J. *Adv. Phys.* **2012,** *61,* 155–323. doi:10.1080/00018732.2012.706401
7. Vanossi, A.; Manini, N.; Urbakh, M.; Zapperi, S.; Tosatti, E. *Rev. Mod. Phys.* **2013,** *85,* 529–552. doi:10.1103/revmodphys.85.529
8. Gnecco, E.; Meyer, E., Eds. *Fundamentals of Friction and Wear on the Nanoscale;* Springer: Berlin, Germany, 2015. doi:10.1007/978-3-319-10560-4
9. Bennewitz, R. *Mater. Today* **2005,** *8,* 42–48. doi:10.1016/s1369-7021(05)00845-x
10. Maier, S.; Pfeiffer, O.; Glatzel, T.; Meyer, E.; Filleter, T.; Bennewitz, R. *Phys. Rev. B* **2007,** *75,* 195408. doi:10.1103/physrevb.75.195408
11. Maier, S.; Gnecco, E.; Baratoff, A.; Bennewitz, R.; Meyer, E. *Phys. Rev. B* **2008,** *78,* 045432. doi:10.1103/physrevb.78.045432
12. Negri, C.; Manini, N.; Vanossi, A.; Santoro, G. E.; Tosatti, E. *Phys. Rev. B* **2010,** *81,* 045417. doi:10.1103/physrevb.81.045417
13. Greenwood, J. A.; Williamson, J. B. P. *Proc. R. Soc. London, Ser. A* **1966,** *295,* 300. doi:10.1098/rspa.1966.0242
14. Bowden, F. P.; Tabor, D. *Proc. R. Soc. London, Ser. A* **1939,** *169,* 391–413. doi:10.1098/rspa.1939.0005
15. Schirmeisen, A.; Jansen, L.; Hölscher, H.; Fuchs, H. *Appl. Phys. Lett.* **2006,** *88,* 123108. doi:10.1063/1.2187575
16. Zhao, X.; Hamilton, M.; Sawyer, W. G.; Perry, S. S. *Tribol. Lett.* **2007,** *27,* 113–117. doi:10.1007/s11249-007-9220-2
17. Barel, I.; Urbakh, M.; Jansen, L.; Schirmeisen, A. *Phys. Rev. Lett.* **2010,** *104,* 066104. doi:10.1103/physrevlett.104.066104
18. Gnecco, E.; Bennewitz, R.; Gyalog, T.; Loppacher, C.; Bammerlin, M.; Meyer, E.; Güntherodt, H.-J. *Phys. Rev. Lett.* **2000,** *84,* 1172–1175. doi:10.1103/physrevlett.84.1172
19. Evstigneev, M.; Schirmeisen, A.; Jansen, L.; Fuchs, H.; Reimann, P. *Phys. Rev. Lett.* **2006,** *97,* 240601. doi:10.1103/physrevlett.97.240601
20. Jansen, L.; Hölscher, H.; Fuchs, H.; Schirmeisen, A. *Phys. Rev. Lett.* **2010,** *104,* 256101. doi:10.1103/physrevlett.104.256101
21. Zwörner, O.; Hölscher, H.; Schwarz, U. D.; Wiesendanger, R. *Appl. Phys. A: Mater. Sci. Process.* **1998,** *66* (Suppl. 1), S263. doi:10.1007/s003390051142
22. Chen, J.; Ratera, I.; Park, J. Y.; Salmeron, M. *Phys. Rev. Lett.* **2006,** *96,* 236102. doi:10.1103/physrevlett.96.236102
23. Meyer, E.; Overney, R.; Brodbeck, D.; Howald, L.; Lüthi, R.; Frommer, J.; Güntherodt, H.-J. *Phys. Rev. Lett.* **1992,** *69,* 1777–1780. doi:10.1103/physrevlett.69.1777
24. Overney, R. M.; Meyer, E.; Frommer, J.; Brodbeck, D.; Lüthi, R.; Howald, L.; Güntherodt, H.-J.; Fujihira, M.; Takano, H.; Gotoh, Y. *Nature* **1992,** *359,* 133–135. doi:10.1038/359133a0
25. Lantz, M. A.; O'Shea, S. J.; Welland, M. E.; Johnson, K. L. *Phys. Rev. B* **1997,** *55,* 10776–10785. doi:10.1103/physrevb.55.10776
26. Schwarz, U. D.; Zwörner, O.; Köster, P.; Wiesendanger, R. *Phys. Rev. B* **1997,** *56,* 6987–6996. doi:10.1103/physrevb.56.6987
27. Schwarz, U. D.; Zwörner, O.; Köster, P.; Wiesendanger, R. *Phys. Rev. B* **1997,** *56,* 6997. doi:10.1103/physrevb.56.6997
28. Meyer, E.; Lüthi, R.; Howald, L.; Bammerlin, M.; Guggisberg, M.; Güntherodt, H.-J. *J. Vac. Sci. Technol., B: Microelectron. Nanometer Struct.–Process., Meas., Phenom.* **1996,** *14,* 1285. doi:10.1116/1.589082

29. Enachescu, M.; Van Den Oetelaar, R. J. A.; Carpick, R. W.; Ogletree, D. F.; Flipse, C. F. J.; Salmeron, M. *Phys. Rev. Lett.* **1998,** *81,* 1877. doi:10.1103/physrevlett.81.1877
30. Petzold, C.; Koch, M.; Bennewitz, R. *Beilstein J. Nanotechnol.* **2018,** *9,* 1647–1658. doi:10.3762/bjnano.9.157
31. Mazo, J. J.; Dietzel, D.; Schirmeisen, A.; Vilhena, J.; Gnecco, E. *Phys. Rev. Lett.* **2017,** *118,* 246101. doi:10.1103/physrevlett.118.246101
32. Gosvami, N. N.; Feldmann, M.; Peguiron, J.; Moseler, M.; Schirmeisen, A.; Bennewitz, R. *Phys. Rev. Lett.* **2011,** *107,* 144303. doi:10.1103/physrevlett.107.144303
33. Li, Q.; Tullis, T. E.; Goldsby, D.; Carpick, R. W. *Nature* **2011,** *480,* 233–236. doi:10.1038/nature10589
34. Overney, R. M.; Takano, H.; Fujihira, M.; Paulus, W.; Ringsdorf, H. *Phys. Rev. Lett.* **1994,** *72,* 3546–3549. doi:10.1103/physrevlett.72.3546
35. Bluhm, H.; Schwarz, U. D.; Meyer, K.-P.; Wiesendanger, R. *Appl. Phys. A: Mater. Sci. Process.* **1995,** *61,* 525–533. doi:10.1007/bf01540254
36. Shindo, H.; Shitagami, K.; Sugai, T.; Kondo, S.-i. *Phys. Chem. Chem. Phys.* **1999,** *1,* 1597–1600. doi:10.1039/a808691e
37. Park, J. Y.; Ogletree, D. F.; Salmeron, M.; Ribeiro, R. A.; Canfield, P. C.; Jenks, C. J.; Thiel, P. A. *Science* **2005,** *309,* 1354. doi:10.1126/science.1113239
38. Balakrishna, S. G.; de Wijn, A. S.; Bennewitz, R. *Phys. Rev. B* **2014,** *89,* 245440. doi:10.1103/physrevb.89.245440
39. Peyrard, M.; Aubry, S. *J. Phys. C: Solid State Phys.* **1983,** *16,* 1593–1608. doi:10.1088/0022-3719/16/9/005
40. Hirano, M.; Shinjo, K. *Phys. Rev. B* **1990,** *41,* 11837–11851. doi:10.1103/physrevb.41.11837
41. Hirano, M.; Shinjo, K.; Kaneko, R.; Murata, Y. *Phys. Rev. Lett.* **1991,** *67,* 2642–2645. doi:10.1103/physrevlett.67.2642
42. Müser, M. H. *Europhys. Lett.* **2004,** *66,* 97–103. doi:10.1209/epl/i2003-10139-6
43. Dietzel, D.; Schwarz, U. D.; Schirmeisen, A. *Friction* **2014,** *2,* 114–139. doi:10.1007/s40544-014-0054-2
44. Dietzel, D.; Ritter, C.; Mönninghoff, T.; Fuchs, H.; Schirmeisen, A.; Schwarz, U. D. *Phys. Rev. Lett.* **2008,** *101,* 125505. doi:10.1103/physrevlett.101.125505
45. Ritter, C.; Heyde, M.; Stegemann, B.; Rademann, K.; Schwarz, U. *Phys. Rev. B* **2005,** *71,* 085405. doi:10.1103/physrevb.71.085405
46. Dietzel, D.; Feldmann, M.; Schwarz, U. D.; Fuchs, H.; Schirmeisen, A. *Phys. Rev. Lett.* **2013,** *111,* 235502. doi:10.1103/physrevlett.111.235502
47. Cihan, E.; Ipek, S.; Durgun, E.; Baykara, M. Z. *Nat. Commun.* **2016,** *7,* 12055. doi:10.1038/ncomms12055
48. Özoğul, A.; İpek, S.; Durgun, E.; Baykara, M. Z. *Appl. Phys. Lett.* **2017,** *111,* 211602. doi:10.1063/1.5008529
49. Koren, E.; Lortscher, E.; Rawlings, C.; Knoll, A. W.; Duerig, U. *Science* **2015,** *348,* 679–683. doi:10.1126/science.aaa4157
50. Vu, C. C.; Zhang, S.; Urbakh, M.; Li, Q.; He, Q.-C.; Zheng, Q. *Phys. Rev. B* **2016,** *94,* 081405. doi:10.1103/physrevb.94.081405
51. Liu, Z.; Yang, J.; Grey, F.; Liu, J. Z.; Liu, Y.; Wang, Y.; Yang, Y.; Cheng, Y.; Zheng, Q. *Phys. Rev. Lett.* **2012,** *108,* 205503. doi:10.1103/physrevlett.108.205503
52. Zheng, Q.; Jiang, B.; Liu, S.; Weng, Y.; Lu, L.; Xue, Q.; Zhu, J.; Jiang, Q.; Wang, S.; Peng, L. *Phys. Rev. Lett.* **2008,** *100,* 067205. doi:10.1103/physrevlett.100.067205
53. Liu, Y.; Grey, F.; Zheng, Q. *Sci. Rep.* **2014,** *4,* 4875. doi:10.1038/srep04875
54. Ma, M.; Sokolov, I. M.; Wang, W.; Filippov, A. E.; Zheng, Q.; Urbakh, M. *Phys. Rev. X* **2015,** *5,* 031020. doi:10.1103/physrevx.5.031020
55. Langewisch, G.; Falter, J.; Fuchs, H.; Schirmeisen, A. *Phys. Rev. Lett.* **2013,** *110,* 036101. doi:10.1103/physrevlett.110.036101
56. Kawai, S.; Koch, M.; Gnecco, E.; Sadeghi, A.; Pawlak, R.; Glatzel, T.; Schwarz, J.; Goedecker, S.; Hecht, S.; Baratoff, A.; Grill, L.; Meyer, E. *Proc. Natl. Acad. Sci. U. S. A.* **2014,** *111,* 3968. doi:10.1073/pnas.1319938111
57. Feng, X.; Kwon, S.; Park, J. Y.; Salmeron, M. *ACS Nano* **2013,** *7,* 1718–1724. doi:10.1021/nn305722d
58. Kawai, S.; Benassi, A.; Gnecco, E.; Söde, H.; Pawlak, R.; Feng, X.; Müllen, K.; Passerone, D.; Pignedoli, C. A.; Ruffieux, P.; Fasel, R.; Meyer, E. *Science* **2016,** *351,* 957–961. doi:10.1126/science.aad3569
59. Pawlak, R.; Meier, T.; Renaud, N.; Kisiel, M.; Hinaut, A.; Glatzel, T.; Sordes, D.; Durand, C.; Soe, W.-H.; Baratoff, A.; Joachim, C.; Housecroft, C. E.; Constable, E. C.; Meyer, E. *ACS Nano* **2017,** *11,* 9930–9940. doi:10.1021/acsnano.7b03955
60. Ternes, M.; Lutz, C. P.; Hirjibehedin, C. F.; Giessibl, F. J.; Heinrich, A. J. *Science* **2008,** *319,* 1066–1069. doi:10.1126/science.1150288
61. Klocke, M.; Wolf, D. E. *Beilstein J. Nanotechnol.* **2014,** *5,* 2048–2057. doi:10.3762/bjnano.5.213
62. Vlassov, S.; Polyakov, B.; Oras, S.; Vahtrus, M.; Antsov, M.; Šutka, A.; Smits, K.; Dorogin, L. M.; Lõhmus, R. *Nanotechnology* **2016,** *27,* 335701. doi:10.1088/0957-4484/27/33/335701
63. Polyakov, B.; Vlassov, S.; Dorogin, L. M.; Butikova, J.; Antsov, M.; Oras, S.; Lõhmus, R.; Kink, I. *Beilstein J. Nanotechnol.* **2014,** *5,* 133–140. doi:10.3762/bjnano.5.13
64. Polyakov, B.; Vlassov, S.; Dorogin, L.; Butikova, J.; Smits, K.; Antsov, M.; Oras, S.; Zabels, R.; Lohmus, R. *Phys. Scr.* **2015,** *90,* 094007. doi:10.1088/0031-8949/90/9/094007
65. Sheehan, P. E.; Lieber, C. M. *Nano Lett.* **2017,** *17,* 4116–4121. doi:10.1021/acs.nanolett.7b00871
66. Müser, M. H.; Wenning, L.; Robbins, M. O. *Phys. Rev. Lett.* **2001,** *86,* 1295–1298. doi:10.1103/physrevlett.86.1295
67. Müser, M. H. Theoretical Studies of Superlubricity. In *Fundamentals of Friction and Wear on the Nanoscale,* 2nd ed.; Gnecco, E.; Meyer, E., Eds.; Springer: Berlin, Germany, 2015; pp 209–232. doi:10.1007/978-3-319-10560-4_11
68. de Wijn, A. S. *Phys. Rev. B* **2012,** *86,* 085429. doi:10.1103/physrevb.86.085429
69. Dietzel, D.; de Wijn, A. S.; Vorholzer, M.; Schirmeisen, A. *Nanotechnology* **2018,** *29,* 155702. doi:10.1088/1361-6528/aaac21
70. Varini, N.; Vanossi, A.; Guerra, R.; Mandelli, D.; Capozza, R.; Tosatti, E. *Nanoscale* **2015,** *7,* 2093–2101. doi:10.1039/c4nr06521b
71. Gigli, L.; Manini, N.; Benassi, A.; Tosatti, E.; Vanossi, A.; Guerra, R. *2D Mater.* **2017,** *4,* 045003. doi:10.1088/2053-1583/aa7fdf
72. Gigli, L.; Manini, N.; Tosatti, E.; Guerra, R.; Vanossi, A. *Nanoscale* **2018,** *10,* 2073–2080. doi:10.1039/c7nr07857a
73. Annett, J.; Cross, G. L. W. *Nature* **2016,** *535,* 271–275. doi:10.1038/nature18304
74. Yang, J.; Liu, Z.; Grey, F.; Xu, Z.; Li, X.; Liu, Y.; Urbakh, M.; Cheng, Y.; Zheng, Q. *Phys. Rev. Lett.* **2013,** *110,* 255504. doi:10.1103/physrevlett.110.255504
75. Marchetto, D.; Held, C.; Hausen, F.; Wählisch, F.; Dienwiebel, M.; Bennewitz, R. *Tribol. Lett.* **2012,** *48,* 77–82. doi:10.1007/s11249-012-9945-4

76. Liu, S.-W.; Wang, H.-P.; Xu, Q.; Ma, T.-B.; Yu, G.; Zhang, C.; Geng, D.; Yu, Z.; Zhang, S.; Wang, W.; Hu, Y.-Z.; Wang, H.; Luo, J. *Nat. Commun.* **2017,** *8,* 14029. doi:10.1038/ncomms14029
77. Berman, D.; Deshmukh, S. A.; Sankaranarayanan, S. K. R. S.; Erdemir, A.; Sumant, A. V. *Science* **2015,** *348,* 1118–1122. doi:10.1126/science.1262024
78. Paolicelli, G.; Tripathi, M.; Corradini, V.; Candini, A.; Valeri, S. *Nanotechnology* **2015,** *26,* 055703. doi:10.1088/0957-4484/26/5/055703
79. Mandelli, D.; Leven, I.; Hod, O.; Urbakh, M. *Sci. Rep.* **2017,** *7,* 10851. doi:10.1038/s41598-017-10522-8
80. Guerra, R.; van Wijk, M.; Vanossi, A.; Fasolino, A.; Tosatti, E. *Nanoscale* **2017,** *9,* 8799–8804. doi:10.1039/c7nr02352a
81. Aubry, S. The New Concept of Transitions by Breaking of Analyticity in a Crystallo- graphic Model. In *Solitons and Condensed Matter Physics;* Bishop, A. R.; Schneider, T., Eds.; Springer Series in Solid State Sciences, Vol. 8; Springer: Berlin, Germany, 1978; pp 264–277. doi:10.1007/978-3-642-81291-0_28
82. Bylinskii, A.; Gangloff, D.; Counts, I.; Vuletić, V. *Nat. Mater.* **2016,** *15,* 717–721. doi:10.1038/nmat4601
83. Brazda, T.; Silva, A.; Manini, N.; Vanossi, A.; Guerra, R.; Tosatti, E.; Bechinger, C. *Phys. Rev. X* **2018,** *8,* 011050. doi:10.1103/physrevx.8.011050
84. Dietzel, D.; Feldmann, M.; Fuchs, H.; Schwarz, U. D.; Schirmeisen, A. *Appl. Phys. Lett.* **2009,** *95,* 053104. doi:10.1063/1.3193551
85. Feldmann, M.; Dietzel, D.; Fuchs, H.; Schirmeisen, A. *Phys. Rev. Lett.* **2014,** *112,* 155503. doi:10.1103/physrevlett.112.155503
86. Feldmann, M.; Dietzel, D.; Tekiel, A.; Topple, J.; Grütter, P.; Schirmeisen, A. *Phys. Rev. Lett.* **2016,** *117,* 025502. doi:10.1103/physrevlett.117.025502
87. Liu, Y.; Szlufarska, I. *Phys. Rev. Lett.* **2012,** *109,* 186102. doi:10.1103/physrevlett.109.186102
88. Khomenko, A. V.; Prodanov, N. V.; Persson, B. N. J. *Condens. Matter Phys.* **2013,** *16,* 33401. doi:10.5488/cmp.16.33401
89. Rubinstein, S. M.; Cohen, G.; Fineberg, J. *Nature* **2004,** *430,* 1005–1009. doi:10.1038/nature02830
90. Rubinstein, S. M.; Barel, I.; Reches, Z.; Braun, O. M.; Urbakh, M.; Fineberg, J. *Pure Appl. Geophys.* **2011,** *168,* 2151–2166. doi:10.1007/s00024-010-0239-1
91. Capozza, R.; Rubinstein, S. M.; Barel, I.; Urbakh, M.; Fineberg, J. *Phys. Rev. Lett.* **2011,** *107,* 024301. doi:10.1103/physrevlett.107.024301
92. Capozza, R.; Urbakh, M. *Phys. Rev. B* **2012,** *86,* 085430. doi:10.1103/physrevb.86.085430
93. Taloni, A.; Benassi, A.; Sandfeld, S.; Zapperi, S. *Sci. Rep.* **2015,** *5,* No. 8086. doi:10.1038/srep08086
94. Kammer, D. S.; Pino Muñoz, D.; Molinari, J. F. *J. Mech. Phys. Solids* **2016,** *88,* 23–34. doi:10.1016/j.jmps.2015.12.014
95. Putelat, T.; Dawes, J. H. P.; Champneys, A. R. *Proc. R. Soc. A* **2017,** *473,* 20160606. doi:10.1098/rspa.2016.0606
96. Tarasov, B. G.; Guzev, M. A.; Sadovskii, V. M.; Cassidy, M. J. *Int. J. Fract.* **2017,** *207,* 87–97. doi:10.1007/s10704-017-0223-1
97. Bonfanti, S.; Taloni, A.; Negri, C.; Sellerio, A. L.; Manini, N.; Zapperi, S. *J. Phys. Chem. Lett.* **2017,** *8,* 5438–5443. doi:10.1021/acs.jpclett.7b02414
98. Costagliola, G.; Bosia, F.; Pugno, N. M. *ACS Biomater. Sci. Eng.* **2017,** *3,* 2845–2852. doi:10.1021/acsbiomaterials.6b00709
99. Costagliola, G.; Bosia, F.; Pugno, N. M. *J. Mech. Phys. Solids* **2018,** *112,* 50–65. doi:10.1016/j.jmps.2017.11.015
100. Dietzel, D.; Brndiar, J.; Štich, I.; Schirmeisen, A. *ACS Nano* **2017,** *11,* 7642–7647. doi:10.1021/acsnano.7b02240
101. Sharp, T. A.; Pastewka, L.; Robbins, M. O. *Phys. Rev. B* **2016,** *93,* 121402. doi:10.1103/physrevb.93.121402
102. Koren, E.; Duerig, U. *Phys. Rev. B* **2016,** *93,* 201404. doi:10.1103/physrevb.93.201404
103. Koren, E.; Duerig, U. *Phys. Rev. B* **2016,** *94,* 045401. doi:10.1103/physrevb.94.045401
104. Guerra, R.; Tosatti, E.; Vanossi, A. *Nanoscale* **2016,** *8,* 11108–11113. doi:10.1039/c6nr00520a
105. Ma, M.; Benassi, A.; Vanossi, A.; Urbakh, M. *Phys. Rev. Lett.* **2015,** *114,* 055501. doi:10.1103/physrevlett.114.055501
106. Triolo, A.; Russina, O.; Bleif, H.-J.; Di Cola, E. *J. Phys. Chem. B* **2007,** *111,* 4641–4644. doi:10.1021/jp067705t
107. Manini, N.; Cesaratto, M.; Del Pópolo, M. G.; Ballone, P. *J. Phys. Chem. B* **2009,** *113,* 15602–15609. doi:10.1021/jp907924z
108. Atkin, R.; Warr, G. G. *J. Phys. Chem. C* **2007,** *111,* 5162–5168. doi:10.1021/jp067420g
109. Wakeham, D.; Hayes, R.; Warr, G. G.; Atkin, R. *J. Phys. Chem. B* **2009,** *113,* 5961–5966. doi:10.1021/jp900815q
110. Hayes, R.; Warr, G. G.; Atkin, R. *Phys. Chem. Chem. Phys.* **2010,** *12,* 1709. doi:10.1039/b920393a
111. Ballone, P.; Del Popolo, M. G.; Bovio, S.; Podestà, A.; Milani, P.; Manini, N. *Phys. Chem. Chem. Phys.* **2012,** *14,* 2475. doi:10.1039/c2cp23459a
112. Dragoni, D.; Manini, N.; Ballone, P. *ChemPhysChem* **2012,** *13,* 1772–1780. doi:10.1002/cphc.201100947
113. Smith, A.; Lee, A.; Perkin, S. *Phys. Rev. Lett.* **2017,** *118,* 096002. doi:10.1103/physrevlett.118.096002
114. Smith, A. M.; Lovelock, K. R. J.; Gosvami, N. N.; Welton, T.; Perkin, S. *Phys. Chem. Chem. Phys.* **2013,** *15*. doi:10.1039/c3cp52779d
115. Amorim, P. M.; Ferraria, A. M.; Colaço, R.; Branco, L. C.; Saramago, B. *Beilstein J. Nanotechnol.* **2017,** *8,* 1961–1971. doi:10.3762/bjnano.8.197
116. Fajardo, O. Y.; Bresme, F.; Kornyshev, A. A.; Urbakh, M. *Sci. Rep.* **2015,** *5,* No. 7698. doi:10.1038/srep07698
117. Fajardo, O. Y.; Bresme, F.; Kornyshev, A. A.; Urbakh, M. *J. Phys. Chem. Lett.* **2015,** *6,* 3998. doi:10.1021/acs.jpclett.5b01802
118. Capozza, R.; Vanossi, A.; Benassi, A.; Tosatti, E. *J. Chem. Phys.* **2015,** *142,* 064707. doi:10.1063/1.4907747
119. Capozza, R.; Benassi, A.; Vanossi, A.; Tosatti, E. *J. Chem. Phys.* **2015,** *143,* 144703. doi:10.1063/1.4933010
120. Li, H.; Rutland, M. W.; Atkin, R. *Phys. Chem. Chem. Phys.* **2013,** *15,* 14616. doi:10.1039/c3cp52638k
121. de Wijn, A. S.; Fasolino, A.; Filippov, A. E.; Urbakh, M. *J. Phys.: Condens. Matter* **2016,** *28,* 105001. doi:10.1088/0953-8984/28/10/105001
122. Braun, O. M.; Manini, N.; Tosatti, E. *Phys. Rev. B* **2008,** *78,* 195402. doi:10.1103/physrevb.78.195402
123. Sivebaek, I. M.; Samoilov, V. N.; Persson, B. N. J. *Phys. Rev. Lett.* **2012,** *108,* 036102. doi:10.1103/physrevlett.108.036102
124. Sivebaek, I. M.; Persson, B. N. J. *Tribol. Lett.* **2016,** *62,* 5. doi:10.1007/s11249-016-0656-0
125. Sivebaek, I. M.; Persson, B. N. J. *Nanotechnology* **2016,** *27,* 445401. doi:10.1088/0957-4484/27/44/445401
126. de Wijn, A. S.; Fasolino, A.; Filippov, A. E.; Urbakh, M. *EPL* **2011,** *95,* 66002. doi:10.1209/0295-5075/95/66002
127. Filippov, A. E.; Dienwiebel, M.; Frenken, J. W. M.; Klafter, J.; Urbakh, M. *Phys. Rev. Lett.* **2008,** *100,* 046102. doi:10.1103/physrevlett.100.046102

128. Klemenz, A.; Pastewka, L.; Balakrishna, S. G.; Caron, A.; Bennewitz, R.; Moseler, M. *Nano Lett.* **2014,** *14,* 7145–7152. doi:10.1021/nl5037403
129. Bai, L.; Srikanth, N.; Zhao, B.; Liu, B.; Liu, Z.; Zhou, K. *J. Phys. D: Appl. Phys.* **2016,** *49,* 485302. doi:10.1088/0022-3727/49/48/485302
130. Santoro, G. E.; Vanossi, A.; Manini, N.; Divitini, G.; Tosatti, E. *Surf. Sci.* **2006,** *600,* 2726–2729. doi:10.1016/j.susc.2005.12.084
131. Vanossi, A.; Manini, N.; Divitini, G.; Santoro, G. E.; Tosatti, E. *Phys. Rev. Lett.* **2006,** *97,* 056101. doi:10.1103/physrevlett.97.056101
132. Cesaratto, M.; Manini, N.; Vanossi, A.; Tosatti, E.; Santoro, G. E. *Surf. Sci.* **2007,** *601,* 3682–3686. doi:10.1016/j.susc.2007.07.009
133. Vanossi, A.; Santoro, G. E.; Manini, N.; Cesaratto, M.; Tosatti, E. *Surf. Sci.* **2007,** *601,* 3670–3675. doi:10.1016/j.susc.2007.07.015
134. Manini, N.; Cesaratto, M.; Santoro, G. E.; Tosatti, E.; Vanossi, A. *J. Phys.: Condens. Matter* **2007,** *19,* 305016. doi:10.1088/0953-8984/19/30/305016
135. Vanossi, A.; Manini, N.; Caruso, F.; Santoro, G. E.; Tosatti, E. *Phys. Rev. Lett.* **2007,** *99,* 206101. doi:10.1103/physrevlett.99.206101
136. Manini, N.; Vanossi, A.; Santoro, G. E.; Tosatti, E. *Phys. Rev. E* **2007,** *76,* 046603. doi:10.1103/physreve.76.046603
137. Vanossi, A.; Santoro, G.; Manini, N.; Tosatti, E.; Braun, O. *Tribol. Int.* **2008,** *41,* 920–925. doi:10.1016/j.triboint.2007.11.008
138. Manini, N.; Santoro, G. E.; Tosatti, E.; Vanossi, A. *J. Phys.: Condens. Matter* **2008,** *20,* 224020. doi:10.1088/0953-8984/20/22/224020
139. Woulaché, R. L.; Vanossi, A.; Manini, N. *Phys. Rev. E* **2013,** *88,* 012810. doi:10.1103/physreve.88.012810
140. Jia, L.-P.; Duan, W.-S. *Indian J. Phys.* **2016,** *90,* 457–460. doi:10.1007/s12648-015-0779-4
141. Castelli, I. E.; Manini, N.; Capozza, R.; Vanossi, A.; Santoro, G. E.; Tosatti, E. *J. Phys.: Condens. Matter* **2008,** *20,* 354005. doi:10.1088/0953-8984/20/35/354005
142. Castelli, I. E.; Capozza, R.; Vanossi, A.; Santoro, G. E.; Manini, N.; Tosatti, E. *J. Chem. Phys.* **2009,** *131,* 174711. doi:10.1063/1.3257738
143. Vigentini, A.; Van Hattem, B.; Diato, E.; Ponzellini, P.; Meledina, T.; Vanossi, A.; Santoro, G.; Tosatti, E.; Manini, N. *Phys. Rev. B* **2014,** *89,* 094301. doi:10.1103/physrevb.89.094301
144. Manini, N.; Braun, O. M.; Vanossi, A. Nanotribology: Nonlinear Mechanisms of Friction. In *Fundamentals of Friction and Wear on the Nanoscale;* Gnecco, E.; Meyer, E., Eds.; Springer: Berlin, Germany, 2015; pp 175–208. doi:10.1007/978-3-319-10560-4_10
145. Manini, N.; Braun, O. M.; Tosatti, E.; Guerra, R.; Vanossi, A. *J. Phys.: Condens. Matter* **2016,** *28,* 293001. doi:10.1088/0953-8984/28/29/293001
146. Vanossi, A.; Tosatti, E. *Nat. Mater.* **2012,** *11,* 97–98. doi:10.1038/nmat3229
147. Mandelli, D.; Tosatti, E. *Nature* **2015,** *526,* 332–333. doi:10.1038/526332a
148. Bylinskii, A.; Gangloff, D.; Vuletić, V. *Science* **2015,** *348,* 1115–1118. doi:10.1126/science.1261422
149. Gangloff, D.; Bylinskii, A.; Counts, I.; Jhe, W.; Vuletić, V. *Nat. Phys.* **2015,** *11,* 915–919. doi:10.1038/nphys3459
150. Kiethe, J.; Nigmatullin, R.; Kalincev, D.; Schmirander, T.; Mehlstäubler, T. E. *Nat. Commun.* **2017,** *8,* 15364. doi:10.1038/ncomms15364
151. García-Mata, I.; Zhirov, O. V.; Shepelyansky, D. L. *Eur. Phys. J. D* **2007,** *41,* 325–330. doi:10.1140/epjd/e2006-00220-2
152. Benassi, A.; Vanossi, A.; Tosatti, E. *Nat. Commun.* **2011,** *2,* 236. doi:10.1038/ncomms1230
153. Pruttivarasin, T.; Ramm, M.; Talukdar, I.; Kreuter, A.; Häffner, H. *New J. Phys.* **2011,** *13,* 075012. doi:10.1088/1367-2630/13/7/075012
154. Mandelli, D.; Vanossi, A.; Tosatti, E. *Phys. Rev. B* **2013,** *87,* 195418. doi:10.1103/physrevb.87.195418
155. Zanca, T.; Pellegrini, F.; Santoro, G. E.; Tosatti, E. *Proc. Natl. Acad. Sci. U. S. A.* **2018,** *115,* 3547–3550. doi:10.1073/pnas.1801144115
156. Apostoli, C.; Giusti, G.; Ciccoianni, J.; Riva, G.; Capozza, R.; Woulaché, R. L.; Vanossi, A.; Panizon, E.; Manini, N. *Beilstein J. Nanotechnol.* **2017,** *8,* 2186–2199. doi:10.3762/bjnano.8.218
157. Panizon, E.; Santoro, G. E.; Tosatti, E.; Riva, G.; Manini, N. *Phys. Rev. B* **2018,** *97,* 104104. doi:10.1103/physrevb.97.104104
158. Mangold, K.; Leiderer, P.; Bechinger, C. *Phys. Rev. Lett.* **2003,** *90,* No. 158302. doi:10.1103/physrevlett.90.158302
159. Baumgartl, J.; Brunner, M.; Bechinger, C. *Phys. Rev. Lett.* **2004,** *93,* 168301. doi:10.1103/physrevlett.93.168301
160. Baumgartl, J.; Zvyagolskaya, M.; Bechinger, C. *Phys. Rev. Lett.* **2007,** *99,* 205503. doi:10.1103/physrevlett.99.205503
161. Mikhael, J.; Roth, J.; Helden, L.; Bechinger, C. *Nature* **2008,** *454,* 501–504. doi:10.1038/nature07074
162. Pertsinidis, A.; Ling, X. S. *Phys. Rev. Lett.* **2008,** *100,* 028303. doi:10.1103/physrevlett.100.028303
163. Mikhael, J.; Schmiedeberg, M.; Rausch, S.; Roth, J.; Stark, H.; Bechinger, C. *Proc. Natl. Acad. Sci. U. S. A.* **2010,** *107,* 7214–7218. doi:10.1073/pnas.0913051107
164. Bohlein, T.; Mikhael, J.; Bechinger, C. *Nat. Mater.* **2012,** *11,* 126–130. doi:10.1038/nmat3204
165. Vanossi, A.; Manini, N.; Tosatti, E. *Proc. Natl. Acad. Sci. U. S. A.* **2012,** *109,* 16429–16433. doi:10.1073/pnas.1213930109
166. Hasnain, J.; Jungblut, S.; Dellago, C. *Soft Matter* **2013,** *9,* 5867. doi:10.1039/c3sm50458a
167. Hasnain, J.; Jungblut, S.; Tröster, A.; Dellago, C. *Nanoscale* **2014,** *6,* 10161–10168. doi:10.1039/c4nr01790k
168. Vanossi, A.; Manini, N.; Tosatti, E. Driven Colloidal Monolayers: Static and Dynamic Friction. In *Fundamentals of Friction and Wear on the Nanoscale,* 2nd ed.; Gnecco, E.; Meyer, E., Eds.; Springer: Berlin, Germany, 2015; pp 427–449. doi:10.1007/978-3-319-10560-4_19
169. Mandelli, D.; Vanossi, A.; Invernizzi, M.; Paronuzzi, S.; Manini, N.; Tosatti, E. *Phys. Rev. B* **2015,** *92,* 134306. doi:10.1103/physrevb.92.134306
170. Mandelli, D.; Vanossi, A.; Manini, N.; Tosatti, E. *Phys. Rev. Lett.* **2015,** *114,* 108302. doi:10.1103/physrevlett.114.108302
171. Mandelli, D.; Vanossi, A.; Manini, N.; Tosatti, E. *Phys. Rev. B* **2017,** *95,* 245403. doi:10.1103/physrevb.95.245403
172. Shapiro, S. *Phys. Rev. Lett.* **1963,** *11,* 80–82. doi:10.1103/physrevlett.11.80
173. Paronuzzi Ticco, S. V.; Fornasier, G.; Manini, N.; Santoro, G. E.; Tosatti, E.; Vanossi, A. *J. Phys.: Condens. Matter* **2016,** *28,* 134006. doi:10.1088/0953-8984/28/13/134006
174. Brazda, T.; July, C.; Bechinger, C. *Soft Matter* **2017,** *13,* 4024–4028. doi:10.1039/c7sm00393e
175. Bohlein, T.; Bechinger, C. *Phys. Rev. Lett.* **2012,** *109,* 058301. doi:10.1103/physrevlett.109.058301
176. Reichhardt, C.; Olson Reichhardt, C. J. *Phys. Rev. Lett.* **2011,** *106,* 060603. doi:10.1103/physrevlett.106.060603
177. Dienwiebel, M.; Verhoeven, G. S.; Pradeep, N.; Frenken, J. W. M.; Heimberg, J. A.; Zandbergen, H. W. *Phys. Rev. Lett.* **2004,** *92,* 126101. doi:10.1103/physrevlett.92.126101

178. Erdemir, A.; Ramirez, G.; Eryilmaz, O. L.; Narayanan, B.; Liao, Y.; Kamath, G.; Sankaranarayanan, S. K. R. S. *Nature* **2016,** *536,* 67–71. doi:10.1038/nature18948
179. Socoliuc, A.; Gnecco, E.; Maier, S.; Pfeiffer, O.; Baratoff, A.; Bennewitz, R.; Meyer, E. *Science* **2006,** *313,* 207. doi:10.1126/science.1125874
180. Takoutsing, C. S.; Djuidjé Kenmoé, G.; Kofané, T. C. *Tribol. Lett.* **2017,** *65,* 107. doi:10.1007/s11249-017-0889-6
181. Gross, L.; Mohn, F.; Moll, N.; Liljeroth, P.; Meyer, G. *Science* **2009,** *325,* 1110–1114. doi:10.1126/science.1176210
182. Gross, L.; Mohn, F.; Moll, N.; Schuler, B.; Criado, A.; Guitián, E.; Peña, D.; Gourdon, A.; Meyer, G. *Science* **2012,** *337,* 1326–1329. doi:10.1126/science.1225621
183. Pawlak, R.; Ouyang, W.; Filippov, A. E.; Kalikhman-Razvozov, L.; Kawai, S.; Glatzel, T.; Gnecco, E.; Baratoff, A.; Zheng, Q.; Hod, O.; Urbakh, M.; Meyer, E. *ACS Nano* **2016,** *10,* 713–722. doi:10.1021/acsnano.5b05761
184. Roth, R.; Fajardo, O. Y.; Mazo, J. J.; Meyer, E.; Gnecco, E. *Appl. Phys. Lett.* **2014,** *104,* 83103. doi:10.1063/1.4866427
185. Tshiprut, Z.; Filippov, A. E.; Urbakh, M. *Phys. Rev. Lett.* **2005,** *95,* 016101. doi:10.1103/physrevlett.95.016101
186. Guerra, R.; Vanossi, A.; Urbakh, M. *Phys. Rev. E* **2008,** *78,* 036110. doi:10.1103/physreve.78.036110
187. Lantz, M. A.; Wiesmann, D.; Gotsmann, B. *Nat. Nanotechnol.* **2009,** *4,* 586–591. doi:10.1038/nnano.2009.199
188. Langer, M.; Kisiel, M.; Pawlak, R.; Pellegrini, F.; Santoro, G. E.; Buzio, R.; Gerbi, A.; Balakrishnan, G.; Baratoff, A.; Tosatti, E.; Meyer, E. *Nat. Mater.* **2014,** *13,* 173–177. doi:10.1038/nmat3836
189. Kisiel, M.; Gnecco, E.; Gysin, U.; Marot, L.; Rast, S.; Meyer, E. *Nat. Mater.* **2011,** *10,* 119–122. doi:10.1038/nmat2936
190. Park, J. Y.; Ogletree, D. F.; Thiel, P. A.; Salmeron, M. *Science* **2006,** *313,* 186. doi:10.1126/science.1125017
191. Stipe, B. C.; Mamin, H. J.; Stowe, T. D.; Kenny, T. W.; Rugar, D. *Phys. Rev. Lett.* **2001,** *87,* 096801. doi:10.1103/physrevlett.87.096801
192. Saitoh, K.; Hayashi, K.; Shibayama, Y.; Shirahama, K. *Phys. Rev. Lett.* **2010,** *105,* 236103. doi:10.1103/physrevlett.105.236103
193. Volokitin, A. I.; Persson, B. N. J.; Ueba, H. *Phys. Rev. B* **2006,** *73,* 165423. doi:10.1103/physrevb.73.165423
194. Pawlak, R.; Kawai, S.; Meier, T.; Glatzel, T.; Baratoff, A.; Meyer, E. *J. Phys. D: Appl. Phys.* **2017,** *50,* 113003. doi:10.1088/1361-6463/aa599d
195. Freund, S.; Pawlak, R.; Moser, L.; Hinhaut, A.; Steiner, R.; Marinakis, N.; Constable, E. C.; Meyer, E.; Housecroft, C. E. *arXiv* **2018,** No. 1807.04011. http://arxiv.org/abs/1807.04011
196. Luan, B. Q.; Hyun, S.; Molinari, J. F.; Bernstein, N.; Robbins, M. O. *Phys. Rev. E* **2006,** *74,* 046710. doi:10.1103/physreve.74.046710
197. E, W.; Ren, W.; Vanden-Eijnden, E. *J. Comput. Phys.* **2009,** *228,* 5437–5453. doi:10.1016/j.jcp.2009.04.030
198. Braun, O. M. *Tribol. Lett.* **2010,** *39,* 283–293. doi:10.1007/s11249-010-9648-7
199. McGee, E.; Smith, R.; Kenny, S. D. *Int. J. Mater. Res.* **2007,** *98,* 430–437. doi:10.3139/146.101489
200. Pastewka, L.; Sharp, T. A.; Robbins, M. O. *Phys. Rev. B* **2012,** *86,* 075459. doi:10.1103/physrevb.86.075459
201. Braun, O. M.; Tosatti, E. *Phys. Rev. E* **2014,** *90,* No. 032403. doi:10.1103/physreve.90.032403
202. Gutenberg, B.; Richter, C. F. *Bull. Seismol. Soc. Am.* **1954,** *46,* 105.
203. Gutenberg, B.; Richter, C. F. *Ann. Geophys. (C. N. R. S.)* **1956,** *9,* 1.
204. Omori, F. *J. Coll. Sci., Imp. Univ. Tokyo* **1894,** *7,* 111.
205. Burridge, R.; Knopoff, L. *Bull. Seismol. Soc. Am.* **1967,** *57,* 341.
206. Carlson, J. M.; Langer, J. S.; Shaw, B. E. *Rev. Mod. Phys.* **1994,** *66,* 657–670. doi:10.1103/revmodphys.66.657
207. Braun, O. M.; Barel, I.; Urbakh, M. *Phys. Rev. Lett.* **2009,** *103,* 194301. doi:10.1103/physrevlett.103.194301
208. Braun, O. M.; Steenwyk, B.; Warhadpande, A.; Persson, B. N. J. *EPL* **2016,** *113,* 56002. doi:10.1209/0295-5075/113/56002
209. Eder, S. J.; Feldbauer, G.; Bianchi, D.; Cihak-Bayr, U.; Betz, G.; Vernes, A. *Phys. Rev. Lett.* **2015,** *115,* 025502. doi:10.1103/physrevlett.115.025502
210. Barwell, F. *Wear* **1958,** *1,* 317–332. doi:10.1016/0043-1648(58)90004-8
211. Vernes, A.; Eder, S.; Vorlaufer, G.; Betz, G. *Faraday Discuss.* **2012,** *156,* 173. doi:10.1039/c2fd00120a
212. Eder, S. J.; Vernes, A.; Betz, G. *Langmuir* **2013,** *29,* 13760–13772. doi:10.1021/la4026443
213. Scaraggi, M.; Persson, B. N. J. *J. Phys.: Condens. Matter* **2015,** *27*. doi:10.1088/0953-8984/27/10/105102
214. Persson, B. N. J. *Tribol. Lett.* **2016,** *63,* 42. doi:10.1007/s11249-016-0728-1
215. Tiwari, A.; Dorogin, L.; Tahir, M.; Stöckelhuber, K. W.; Heinrich, G.; Espallargas, N.; Persson, B. N. J. *Soft Matter* **2017,** *13,* 9103–9121. doi:10.1039/c7sm02038d
216. Lang, R.; Falk, K.; Kaliske, M. *Proc. Appl. Math. Mech.* **2016,** *16,* 539–540. doi:10.1002/pamm.201610258
217. Falk, K.; Lang, R.; Kaliske, M. *Tire Sci. Technol.* **2016,** *44,* 226–247. doi:10.2346/tire.16.440401
218. Wagner, P.; Wriggers, P.; Veltmaat, L.; Clasen, H.; Prange, C.; Wies, B. *Tribol. Int.* **2017,** *111,* 243–253. doi:10.1016/j.triboint.2017.03.015
219. Aldam, M.; Bar-Sinai, Y.; Svetlizky, I.; Brener, E.; Fineberg, J.; Bouchbinder, E. *Phys. Rev. X* **2016,** *6,* 041023. doi:10.1103/physrevx.6.041023
220. Lucas, M.; Zhang, X.; Palaci, I.; Klinke, C.; Tosatti, E.; Riedo, E. *Nat. Mater.* **2009,** *8,* 876–881. doi:10.1038/nmat2529
221. Lyashenko, I. A.; Borysiuk, V. N.; Popov, V. L. *Beilstein J. Nanotechnol.* **2017,** *8,* 1889–1896. doi:10.3762/bjnano.8.189
222. Curtis, C. K.; Marek, A.; Smirnov, A. I.; Krim, J. *Beilstein J. Nanotechnol.* **2017,** *8,* 2045–2059. doi:10.3762/bjnano.8.205
223. Holmberg, K.; Andersson, P.; Erdemir, A. *Tribol. Int.* **2012,** *47,* 221–234. doi:10.1016/j.triboint.2011.11.022
224. Bonelli, F.; Manini, N.; Cadelano, E.; Colombo, L. *Eur. Phys. J. B* **2009,** *70,* 449–459. doi:10.1140/epjb/e2009-00239-7
225. Braun, O. M.; Peyrard, M. *Phys. Rev. E* **2011,** *83,* 046129. doi:10.1103/physreve.83.046129
226. Jafary-Zadeh, M.; Reddy, C.; Sorkin, V.; Zhang, Y.-W. *Nanoscale Res. Lett.* **2012,** *7,* 148. doi:10.1186/1556-276x-7-148
227. van den Ende, J. A.; de Wijn, A. S.; Fasolino, A. *J. Phys.: Condens. Matter* **2012,** *24,* 445009. doi:10.1088/0953-8984/24/44/445009
228. Vanossi, A.; Benassi, A.; Varini, N.; Tosatti, E. *Phys. Rev. B* **2013,** *87,* 045412. doi:10.1103/physrevb.87.045412
229. Norell, J.; Fasolino, A.; de Wijn, A. S. *Phys. Rev. E* **2016,** *94,* No. 023001. doi:10.1103/physreve.94.023001
230. Volokitin, A. I. *Phys. Rev. B* **2016,** *94,* 235450. doi:10.1103/physrevb.94.235450

231. Schirmeisen, A.; Schwarz, U. D. *ChemPhysChem* **2009,** *10,* 2373–2382. doi:10.1002/cphc.200900378
232. Dietzel, D.; Feldmann, M.; Herding, C.; Schwarz, U. D.; Schirmeisen, A. *Tribol. Lett.* **2010,** *39,* 273–281. doi:10.1007/s11249-010-9643-z
233. Dietzel, D.; Mönninghoff, T.; Herding, C.; Feldmann, M.; Fuchs, H.; Stegemann, B.; Ritter, C.; Schwarz, U. D.; Schirmeisen, A. *Phys. Rev. B* **2010,** *82,* 035401. doi:10.1103/physrevb.82.035401
234. Brndiar, J.; Turanský, R.; Dietzel, D.; Schirmeisen, A.; Štich, I. *Nanotechnology* **2011,** *22,* 085704. doi:10.1088/0957-4484/22/8/085704
235. Paliy, M.; Braun, O. M.; Consta, S. *J. Phys. Chem. C* **2012,** *116,* 8932–8942. doi:10.1021/jp210761f
236. Zhang, R.; Ning, Z.; Xu, Z.; Zhang, Y.; Xie, H.; Ding, F.; Chen, Q.; Zhang, Q.; Qian, W.; Cui, Y.; Wei, F. *Nano Lett.* **2016,** *16,* 1367–1374. doi:10.1021/acs.nanolett.5b04820
237. Manini, N.; Mistura, G.; Paolicelli, G.; Tosatti, E.; Vanossi, A. *Adv. Phys.: X* **2017,** *2,* 569–590. doi:10.1080/23746149.2017.1330123
238. Chandrabhan, S. R.; Jayan, V.; Parihar, S. S.; Ramaprabhu, S. *Beilstein J. Nanotechnol.* **2017,** *8,* 1476–1483. doi:10.3762/bjnano.8.147
239. Prieto, G.; Bakoglidis, K. D.; Tuckart, W. R.; Broitman, E. *Beilstein J. Nanotechnol.* **2017,** *8,* 1760–1768. doi:10.3762/bjnano.8.177
240. Li, K.; Jing, D.; Hu, J.; Ding, X.; Yao, Z. *Beilstein J. Nanotechnol.* **2017,** *8,* 2324–2338. doi:10.3762/bjnano.8.232
241. Noel, O.; Vencl, A.; Mazeran, P.-E. *Beilstein J. Nanotechnol.* **2017,** *8,* 2662–2668. doi:10.3762/bjnano.8.266

License and Terms